DEVELOPMENT AND CHARACTERIZATION OF MgB_4O_7 FOR OPTICALLY STIMULATED LUMINESCENCE DOSIMETRY

By

TIMOTHY DAVID GUSTAFSON

Bachelor of Science
Bethel University
St. Paul, Minnesota, USA
2012

Submitted to the Faculty of the
Graduate College of the
Oklahoma State University
in partial fulfillment of
the requirements for
the Degree of
DOCTOR OF PHILOSOPHY
December 2018

DEVELOPMENT AND CHARACTERIZATION OF

MGB4O7 FOR OPTICALLY STIMULATATED

LUMINESCENCE DOSIMETRY

Dissertation Approved:

Eduardo G. Yukihara, Ph.D.

Dissertation Adviser

Stephen W.S. McKeever, Ph.D.

John W. Mintmire, Ph.D.

Don A. Lucca, Ph.D.

ACKNOWLEDGEMENTS

I would like to express my deep gratitude to Dr. Eduardo Yukihara for his mentorship and training. It has been a delight to learn from one who leads by example by having a high standard for himself. I am forever thankful and grateful for his patient encouraging of my development as a scientist.

I never thought when I met Dr. Stephen McKeever as an undergrad intern that the lab he showed me would become my academic home for a time. Thank you for taking the time out of your busy schedule to show an undergrad around. It spoke volumes.

Thank you to the other members of my dissertation committee, Dr. John Mintmire and Dr. Don Lucca. I appreciate the feedback throughout the years and to this manuscript.

Thank you to the department of physics staff. Your helpfulness has saved me from many headaches. Thank you for the work behind the scene that makes the department function.

To my lab mates both past and present, thank you for the many conversations. Your help in discussing ideas has been invaluable. You have been more than just colleagues but friends. A special thanks to Adam and Nishan whom had the greatest influence on me.

To my families, thank you for your support and encouragement. You have helped provide me with the foundational tools I have drawn on time and again through this process.

To my darling wife, Laura, thank you for your patience and sacrifice to allow me to chase my dreams. I look forward to our next adventure together.

Name: TIMOTHY DAVID GUSTAFSON

Date of Degree: DECEMBER 2018

Title of Study: DEVELOPMENT AND CHARACTERIZATION OF MGB4O7 FOR OPTICALLY STIMULATED LUMINESCENCE DOSIMETRY

Major Field: PHYSICS

Abstract: The objective of this study was to investigate MgB_4O_7 for optically stimulated luminescence (OSL) dosimetry. First, detailed characterization of MgB_4O_7:Ce,Li, shown in literature recently as a potential OSL material, was conducted to find avenues for improvement to the material. These studies include characterization of luminescence centers and dosimetric properties of the material. The MgB_4O_7 material was improved through changes to the synthesis, which includes modifying the annealing procedure and addition of a third codopant. The focus of these studies was to find a material with greater OSL sensitivity and reduced sensitization compared with the original material. The final material was eight times brighter than the original material and showed less than a third of the sensitization of the original material. Finally, attempts were made to determine mechanisms for various behaviors in MgB_4O_7. The behaviors of interest were the mechanisms for sensitization and the location ground state energies of lanthanides in MgB_4O_7. Understanding the mechanisms for sensitization allows for sensitization to be eliminated through readout modification. Determining the ground state energies allows for trap engineering within the material that was not useful for OSL but could be useful for other applications.

TABLE OF CONTENTS

LIST OF TABLES

LIST OF FIGURES

CHAPTER 1

INTRODUCTION

The objective of this work was to develop MgB_4O_7 for optically stimulated luminescence (OSL) dosimetry. This was pursued by characterizing MgB_4O_7:Ce,Li that had been presented in literature as a potential OSL dosimetry material (Souza et al., 2017; Yukihara et al., 2017), improving that material via changes to synthesis, and furthering the understanding of the trapping and recombination mechanisms in this material.

OSL is an important technique for personal dosimetry (Akselrod et al., 1999; McKeever and Akselrod, 1999; Sommer et al., 2007) and luminescence dating (Murray and Wintle, 2000). There has also been growing interest in OSL for medical dosimetry (Ahmed et al., 2014; Andersen et al., 2009; Bøtter-Jensen et al., 2003; Viamonte et al., 2008) and emergency dosimetry applications (Bailiff et al., 2016; Sholom et al., 2011). Much of the interest has been a result of the convenience of light stimulation over the controlled heating required in thermoluminescence (TL) dosimetry.

Currently, the only materials produced commercially are Al_2O_3:C (Landauer, Inc.) and BeO (Brush Ceramics Products, Materion Co.). However, BeO is not produced for dosimetry specifically. Both materials are highly sensitive for radiation measurement, but neither material has intrinsic neutron sensitivity and instead rely on neutron converters like Li_2CO_3 for neutron dosimetry (Yukihara et al., 2008).

Application of Al_2O_3:C to 2D dosimetry has been challenging because of the long luminescence lifetime (~35 ms) of the main luminescence centers in this material,

F-centers (Akselrod et al., 1998). The most convenient approach for OSL imaging, used forexample in computed radiograph (Rowlands, 2002), relies on laser scanning, so residual luminescence from the previous readout site results in pixel bleeding (Ahmed et al., 2016b; Yukihara and Ahmed, 2015). This can be addressed by a correction algorithm but increases noise in the image (Ahmed et al., 2016b). A system for 2D dosimetry based on BeO has been developed (Jahn et al., 2010; Jahn et al., 2011), but no advantage over the Al_2O_3:C system has been shown. Some of the difficulty could be that 2D films for OSL dosimetry are produced by embedding or adhering powder of the OSL material to a plastic film, and BeO is toxic in powder form. 2D OSL dosimetry would benefit from a nontoxic material with a fast luminescence center.

MgB_4O_7 (MBO) has been known as a TL material for nearly 40 years (Prokić, 1980). OSL properties have been found for the material doped with cerium more recently (Souza et al., 2017; Yukihara et al., 2017). This host material is nontoxic, has a near-tissue-equivalent effective atomic number (Z_{eff} = 8.2), a fast luminescence center when doped with cerium (Ce^{3+}, 10's of ns), and intrinsic neutron sensitivity (Yukihara et al., 2017).

In this work, we investigated the material we had published in far greater detail, now looking for avenues of improvement. We examined luminescence centers, TL, and OSL properties. Next, with the information gained, we sought to improve the brightness of the OSL signal through modification of the synthesis procedure: elimination of Mn^{2+} contamination that was found to be a competing recombination center to Ce^{3+}, modification of the annealing treatment, and addition of codopants to introduce new traps in the material that would empty and recombine at a cerium site. Finally, studies were conducted to determine the mechanism for sensitization in the material, improve TL and OSL curve fittings, and develop a model describing the ground state energies of lanthanides in MBO.

The work here shows improvement of the original MBO material to one that is competitive in brightness to Al_2O_3:C. The new material developed in this work shows linear dose response up a higher dose than Al_2O_3:C. Study of the luminescence centers confirmed Ce^{3+} as the recombination center for OSL, which should mean the lifetime of the luminescence is short (~10's ns). Thus, this could be a candidate material for 2D OSL dosimetry. The presence of boron in the host means that the improved material remains of interest for neutron dosimetry. Overall, the improved material is a strong candidate for OSL dosimetry applications.

This thesis is organized according to the following structure. First, background is provided for relevant luminescence phenomena, OSL materials, the MBO host material, and other relevant analysis techniques (Chapter 2). The materials and methods used are presented in Chapter 3. Then, results of detailed study of the original MBO material are presented in Chapter 4. Chapter 5 shows attempts made to improve the material's OSL brightness through synthesis modification. Chapter 6 shows development of a model for sensitization, discussion of TL and OSL curve fitting, and application of the chemical shift model to MBO to describe the ground state energies of lanthanides in MBO. Overall conclusions to this work are given in Chapter 7.

CHAPTER 2

BACKGROUND

This chapter introduces the underlying physics of luminescence processes in solids, its application in radiation dosimetry, and provides an overview of the properties and limitations of existing luminescence materials used in dosimetry. Then, we discuss a luminescence material, MgB_4O_7, which has been identified for potential application in optically stimulated luminescence (OSL) dosimetry due to its potential to circumvent some of the limitations of existing OSL materials. Next, material analysis techniques used to characterize this material are discussed. Then, the chemical shift model is discussed. Finally, an outline for the studies presented in this work is given.

2.1 ***Luminescence processes in solids***

Light is taken for granted in daily life, yet it is wonderfully complex, and its sources are diverse. Solids are one of those sources of light. The red-hot glow of metal or the yellow light of an incandescent bulb is a familiar image. Scientific progress identified this glow as blackbody radiation, which is a function of the temperature of the light-emitting material. Another familiar image is some glow-in-the-dark item or a rock that will glow many colors under a black light, despite looking normal under room light. These phenomena are types of luminescence called fluorescence and phosphorescence.

As fluorescence and phosphorescence have been found to be more complicated than blackbody radiation, they have opened new avenues to investigate the luminescent

mechanisms in solids (Blasse and Grabmaier, 1994; Chen and McKeever, 1997).Radioluminescence (RL), the material's luminescence under irradiation, has been used to characterize defects in the crystal (Wright and Garlick, 1954). Photoluminescence (PL) gives information on the energy levels of defects or optical centers within the crystalline lattice, or on optical transitions between the delocalized bands and the optical centers. PL can show the same luminescence centers as RL, but it can provide evidence of charge transfer to a band as well (Marfunin, 1979). Some materials phosphoresce at room temperature so slowly that additional stimulation is needed to reduce the lifetime. Two techniques used to observe slow phosphorescence in previously irradiated materials are thermoluminescence (TL) and optically stimulated luminescence (OSL). TL uses thermal stimulation to induce luminescence, whereas OSL uses optical stimulation (Chen and McKeever, 1997). In the following sections we give a basic description of these luminescence processes.

2.1.1 Thermoluminescence

Thermally stimulated luminescence (TSL) or thermoluminescence (TL) is light emission from an insulator or semiconductor during heating that is distinct from blackbody radiation (McKeever, 1985). Blackbody radiation is a result of the temperature of an object, whereas TL requires excitation of the material for light emission. The excitation of the material can be ionizing radiation or even sufficiently energetic photons (e.g. UV light) depending on the material.

During excitation, an electron-hole pair forms or an electron moves to an excited state in the material. If the relaxation of the material to its ground state is rapid, of the order of nanoseconds, the phenomenon is called fluorescence. Phosphorescence and TL have a longer lifetime to return to equilibrium than fluorescence. TL and phosphorescence both are characterized by a charge carrier entering a metastable state and subsequent thermal

release. At a given ambient temperature, a phosphorescent process is one that will detrap, whereas a TL process is one that will require additional thermal stimulation above that ambient temperature to return the sample to equilibrium in an observable amount of time (McKeever, 1985).

The TL mechanism can be explained by the application of the band gap model from solid-state physics. Band theory in solids describes the allowed energy states (quantum states) for electrons as bands where many allowed energy states are closely bunched (Kittel, 1996). Two of these bands of states, the valence band and the conduction band, are relevant to describing many optical and electronic properties of a solid. The valence band is comprised of energy levels of valence electrons, which are the outermost electrons of an atom and involved in chemical bonding. The conduction band is comprised of non-localized electron states. For the materials here, semiconductors and insulators, there is a gap between these two bands for which there are no electron states. The amount of energy needed to move an electron from the uppermost state of the valence band to the lowest state of the conduction band is called the band gap or energy gap (Bube, 1960). When an electron is excited to the conduction band, a hole is left behind in the valence band which is also delocalized.

Electrons are usually in the lower energy band, the valence band. When excited, the electrons can transition up to the conduction band. Eventually, they will relax back to the valence band. In a perfect crystal, there are no acceptable electron or hole states within the bandgap, so charge carriers can only be present in the valence or conduction bands. However, impurities in a material can introduce states within the bandgap. TL theory relies on the presence of impurities creating states within the bandgap that will behave as traps for the charges or recombination centers.

To examine the TL process, we can start with the simplest possible model, the one trap one recombination (OTOR) model, shown in Figure 2-1 (Chen and McKeever, 1997).

The transitions shown in Figure 2-1 are as follows. Transition *a* is excitation of electrons from the valence band to the conduction band due to the irradiation of the material. Transition *b* shows the trapping of electrons at trapping centers. Transition *c* shows stimulation of electrons out of a trap to the conduction band. Transition *d* is the recombination of electrons with holes at a recombination center. Transition *e* is the trapping of a hole at a recombination center. The recombination center is, by definition, a sufficiently deep trap such that the hole escapes only by recombination with an electron rather than thermal or optical stimulation. Transition *f* is a direct recombination of electrons in the conduction band with holes in the valence band.

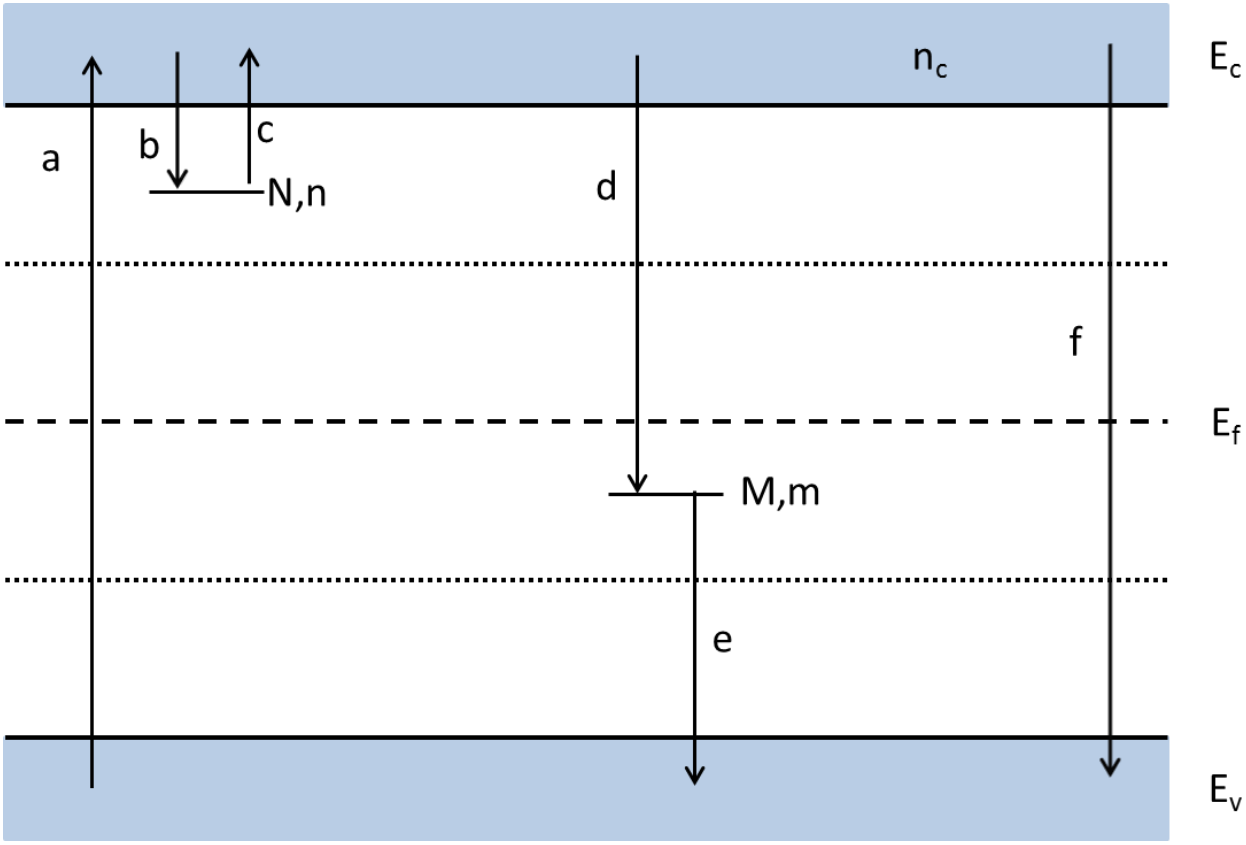

Figure 2-1: Energy band model for the OTOR model with electron transitions: (a) excitation of electrons from the valence to the conduction band via ionizing radiation, (b) trapping of electrons from the conduction band in an electron trap, (c) release of electron from a trap due to stimulation, (d) recombination of electron with hole at a recombination center, (e)

trapping of a hole at a recombination center, (f) direct recombination. Based on Chen and McKeever (1997).

The TL process can be modeled mathematically by writing rate equations tracking the electron populations in the electron trap and conduction band, as well as the hole populations in the recombination center and valence band (McKeever, 1985):

$$\frac{dn_c}{dt} = -A_n\, n_c\, (N - n) + np - A_r\, n_c\, m + G - A_d n_c m_v \quad \textbf{(2.1)}$$

$$\frac{dn}{dt} = A_n\, n_c\, (N - n) - np \quad \textbf{(2.2)}$$

$$\frac{dm}{dt} = A_r\, n_c\, m - A_m m_v (M - m) \quad \textbf{(2.3)}$$

$$\frac{dm_v}{dt} = A_m m_v (M - m) + G - A_d n_c m_v \quad \textbf{(2.4)}$$

In the above equations: n is the trapped electron concentration (number per unit volume); n_c is the concentration of electrons in the conduction band; m is the concentration of holes at the recombination center; m_v is the concentration of holes in the valence band; G is the rate of excitation due to irradiation and has a value of 0 since irradiation has concluded; N is the concentration of electron traps; M is the concentration of recombination centers; A_n is the trapping probability for an electron at an electron trap site; A_r is the recombination probability for electron-hole recombination at a recombination center; A_m is the trapping probability for a hole at a recombination center; A_d is the probability of direct recombination of a delocalized electron and a delocalized hole which has a value close to 0; p is the probability of an electron being released from a trap due to stimulation. For TL, p is given by $p = s\, exp(-E/kT)$ where s is the attempt to escape frequency, E is the energy for the trap depth, T is the temperature, and k is Boltzmann's constant.

The rate equations are not solvable analytically. Thus, either numerical solutions are evaluated or simplifying assumptions must be made. The main simplification assumes a pair of inequalities, called quasi-static equilibrium (Chen and McKeever, 1997). The first assumption is that $n_c << n$, the number of electrons in the conduction band is much less than the trapped population. The second assumption is that the change of the conduction band electron population is small compared to the change in the trapped electron population, that is $dn_c/dt << dn/dt$. Under these assumptions, the TL intensity can now be expressed as $-dn/dt$ or $-dm/dt$. This allows the General One-Trap (GOT) equation for TL intensity to be written as in Eq. (2.5) (Levy, 1985).

$$I_{TL} = -\frac{dn}{dt} \cong -\frac{dm}{dt} = \frac{ns*Exp(-\frac{E}{kT})mA_r}{(N-n)A_n+mA_r} \quad \textbf{(2.5)}$$

Typically, a TL measurement is done by holding the sample at a constant temperature (isothermal decay) or by heating it at a constant heating rate, which generates the so-called TL curve. For the model described above, the TL curve consists of a single TL peak (Figure 2-2a) associated with the trapping center shown in Figure 2-1. In real materials, however, multiple TL peaks reveal a multiplicity of trapping centers.

To arrive at functions of the TL intensity with respect to temperature that show order of interaction, further assumptions are made about the likelihood of recombination compared to retrapping. If it is assumed that recombination is far more likely than retrapping, that is $(N-n)A_n << mA_r$, Eq. (2.8), called the first-order expression, is obtained (Randall and Wilkins, 1945a, 1945b). This is found be solving Eq. (2.6) for n via integration and a change of variables from time to temperature by assuming a linearly increasing temperature such that $T(t) = T_0 + \beta t$.

$$I_{TL} = -\frac{dn}{dt} \cong -\frac{dm}{dt} = ns\ exp(-\frac{E}{kT}) \quad \textbf{(2.6)}$$

Otherwise, if retrapping is more likely than recombination, that is $(N-n)A_n >> mA_r$, Eq. (2.9), called the second-order expression, is obtained (Garlick and Gibson, 1948). This is found by solving Eq. (2.7) for n by integration and the same change of variables from time to temperature assuming a linearly increasing temperature such that $T(t) = T_0 + \beta t$.

$$I_{TL} = -\frac{dn}{dt} \cong -\frac{dm}{dt} = \frac{ns\ exp(-\frac{E}{kT})mA_r}{(N-n)A_n} \quad \textbf{(2.7)}$$

In both solutions, the first-order in Eq. (2.8) and second-order in Eq. (2.9), n_0 is the initial trapped population and T' is a dummy variable for integration over temperature, and β is the heating rate.

$$I_{TL} = n_0 s\ exp(-E/kT)\ exp(-\frac{s}{\beta}\int_{T_0}^{T} exp(-E/kT')dT') \quad \textbf{(2.8)}$$

$$I_{TL} = \frac{n_0^2 A_r}{NA_n} s\ exp(-E/kT)[1 + \frac{n_0 s A_r}{\beta N A_n}\int_{T_0}^{T} exp(-E/kT')dT']^{-2} \quad \textbf{(2.9)}$$

The integral, in each expression, is unsolvable analytically so numerical solutions or approximations (Balarin, 1975, 1977; Gorbachev, 1975; Kitis et al., 1998) are made. The primary methods involve expanding the integral, which can be written in terms of the exponential integral, using various series. A varying number of terms from the different series are kept and compared to numerical solutions for the integral. Further commentary on the exact series used and their accuracy can be found in Chen and McKeever (1997).

Plots of first and second-order TL peaks are presented in Figure 2-2. With a change in starting population, a first-order TL peak changes height but not position. A second-order TL peak shifts to higher temperature and becomes broader with decreasing initial population. This characteristic is important for experimentally differentiating the kinetic order of various peaks in a material.

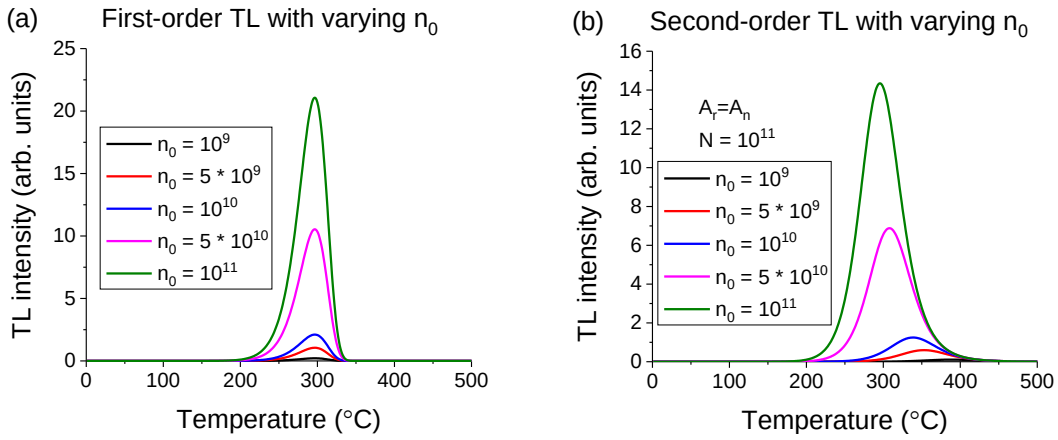

Figure 2-2: Examples of each first-order and second-order TL curves with varying concentration of trapped charges. Parameters used are E = 1.5 eV, $s = 10^{12}$ s^{-1}, and β = 1 °C/s.

In real materials, first-order behavior is far more common than non-first-order (Chen and Pagonis, 2013; Sunta et al., 2001, 2005). Theoretical approaches that avoid the use of the quasi-static equilibrium assumption find that first-order behavior matches observation of real materials, since second-order behavior results in virtually no recombination, as charges are retrapped so strongly, which does not match experimental observation (Lewandowski and McKeever, 1991).

Real materials typically have multiple traps resulting in multiple peaks. To fit a glow curve into a set of glow peaks, linear superposition is assumed. The only case in which linear superposition is justified is for first-order kinetics (Chen and McKeever, 1997). Any amount of retrapping means the traps are somewhat interdependent. Thus, curve fitting for multiple TL peaks that are non-first-order is flawed since this approach ignores the interdependence of the traps.

The analysis shown above is for electron detrapping, but the process for hole detrapping is analogous. The transitions shown in Figure 2-1 and analyzed in equations (2.1) - (2.4) could be defined as hole transitions instead; the same results would be obtained. The transition where this makes a difference is the recombination shown as

transition *d* in Figure 2-1. Whether a hole recombines with an electron or vice versa indicates the type of ionization going on within the recombination center.

The recombination of electron and hole requires the release of energy. Typically, most of the energy of the transition is lost as phonons in the lattice. The remaining energy will place the recombination center in an excited state, and in its transition back to the ground state, it will emit photons. These photons will be characteristic of the defect responsible for the recombination center. The identity and mechanism of the recombination center allows a complete picture of the physics of the material, but also allows for potential engineering of that defect to a desired application.

2.1.2 Optically stimulated luminescence

The theory for OSL process is the same as for TL, with one change: the stimulation for detrapping is now optical rather than thermal (Yukihara and McKeever, 2011). For OSL, the probability of a trapped electron escaping the trap is $p = \sigma\phi$, where σ is the photoionization cross section for the trapping center and is dependent on the wavelength of the incident light, and Φ is the incident photon flux.

The photoionization cross section depends on the trapping center and wavelength of stimulation (Bube, 1960). The photoionization cross section tends to be higher for shorter wavelengths since the photons have more energy. Photoionization is the transition of a localized electron to the conduction band, which has a threshold energy. As there are more energy states within the band than exist at the bottom edge of the conduction band, photons of higher energy will have a higher cross section for photoionization than photons of energy close to the threshold energy.

The results shown in this discussion and this work are for continuous wavelength OSL, constant photon flux, though other stimulation schemes exist (Yukihara and McKeever, 2011).

The same simplifying assumptions can be made, such as quasi-static equilibrium. Again, based on if $(N\text{-}n)A_n$ is much larger or much smaller than mA_r, the two expressions for the OSL intensity, first and second-order, can be derived. The first-order expression is shown in Eq. (2.10) for the slow retrapping case, and the second-order expression is shown in Eq. (2.11) for the fast retrapping case.

$$\mathrm{I_{OSL}} = \boldsymbol{n_0 \sigma\, exp}(-\boldsymbol{t\sigma\phi}) = \boldsymbol{I_0\, exp}(-\boldsymbol{t/\tau}) \qquad \textbf{(2.10)}$$

$$\mathrm{I_{OSL}} = \frac{\boldsymbol{n_0^2 \sigma \phi A_n}}{\boldsymbol{N A_m}} \left(\mathbf{1} + \frac{\boldsymbol{n_0 \sigma \phi t A_n}}{\boldsymbol{N A_m}}\right)^{-2} \qquad \textbf{(2.11)}$$

Here, the simplification seen in Eq. (2.10) is the form seen most often since it is of first-order kinetics. The second equation shows a second-order behavior. Examples of both curves for varying initial trapped population are shown in Figure 2-3.

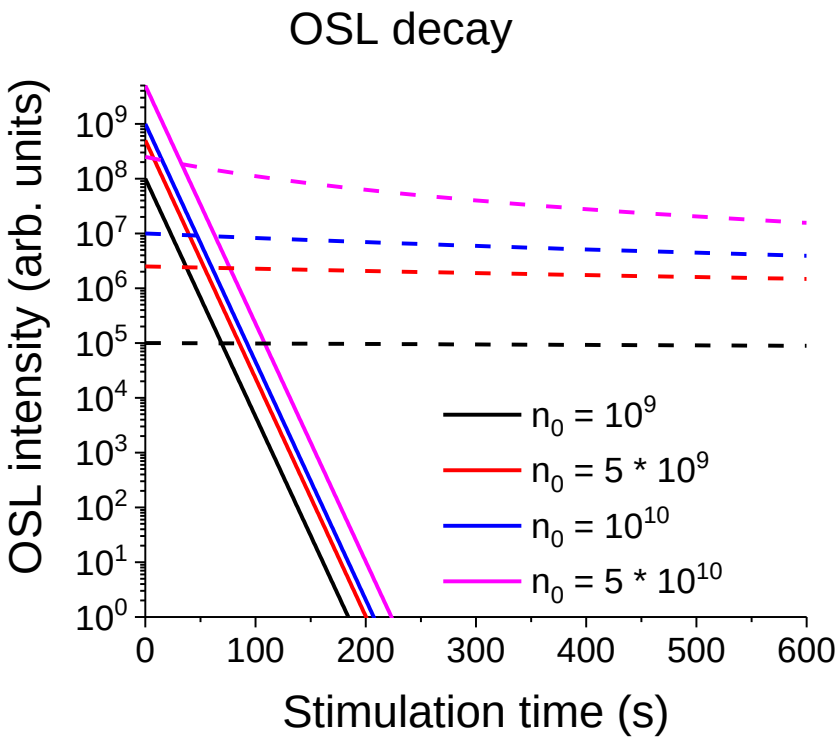

Figure 2-3: Simulated OSL curves for the OTOR model of first-order kinetics (solid lines) and second-order kinetics (dashed lines) for varying initial trapped population (dose). Parameters used were: σ of 10^{-19} cm^2; Φ of 10^{18} cm^{-2}; for second-order N of 10^{12} cm^{-3}; A_n/A_m was 1.

As can be seen, a single OSL decay shows no change in curve shape with varying dose. A second-order OSL decay changes intensity dramatically with dose. For most of the initial populations ($n_0 = 10^9 – 10^{10}$ cm^{-3}), the number of trapping sites was two orders of magnitude larger than the trapped charge, so their curve shapes are similar. However, the highest initial population has a different curve shape due to N and n_0 starting with values close enough to favor recombination over retrapping due to most many traps being filled. Due to retrapping, the depletion for second-order curves is orders of magnitude longer in duration.

As discussed for TL, first-order curves are the only form of curve that allows for valid use of the superposition principle, as non-first-order traps are not fully independent of each other. Thus, curve fitting is only an appropriate approach for first-order peaks. In fitting OSL curves, the presence of multiple decays is indicative of varying response of traps to the stimulating light. With the focus of OSL research being dosimetry, materials with a simple and fast OSL decay have been preferred. As such, non-first-order materials have seen little treatment in literature.

2.1.3 Radioluminescence

Radioluminescence (RL) is the light emitted from a material that is undergoing excitation with ionizing radiation (Bøtter-Jensen et al., 2003). Often, the measurement is done with a spectrometer to discriminate the wavelengths of the luminescence. In theory, the transition observed is transition *d* in Figure 2-1. The RL spectrum indicates the wavelengths of the luminescence centers of the material, some of which are recombination centers for TL or OSL. This emission can be used to identify the defect and transitions from that defect. This information can be used to engineer the recombination

sites at locations that will allow for easier use of optical filters to discriminate from excitation light in OSL or blackbody radiation at higher temperature TL peaks.

2.1.4 Photoluminescence

Photoluminescence (PL) is a way of looking at the luminescence centers in the material, which in some cases can work as recombination centers during the TL or OSL process (Bøtter-Jensen et al., 2003). For PL, material irradiation is not needed beforehand. A luminescence center is excited from ground state, by light, to an excited state and emits light on its return to the ground state. Charges remain localized.

When comparing PL to TL, OSL, or RL, it would be more accurate to show transition *d* of Figure 2-1 as a two-step transition. The first step is non-radiative and occurs as drawn. This puts the recombination center, often an individual atom, into an excited state. The second step is the return of this recombination center to the ground state. This transition is radiative and, in the case of an atomic luminescence center, is characteristic of specific transitions within that atom. The emission from RL, TL, or OSL is from this second step. PL can excite this transition directly without charge delocalization.

PL probes the emission centers by putting them into an excited state and observing the return to the ground state via photon emission. Incident light is absorbed at some wavelengths and emitted by emission centers at longer wavelengths (Stokes shift) (Lakowicz, 2006). One can identify the emission centers and their transitions by changing the excitation wavelength and measuring the emission wavelengths. For a sample with multiple emission centers, PL can show whether the emission centers are entirely independent of each other or if charge or energy can be transferred between them.

2.1.5 Thermal quenching

Thermal quenching is the reduction of luminescence efficiency with increased temperature. The typical mechanism for this is well described with a coordinate diagram of the ground state and an excited state of a luminescence center as shown in Figure 2-4.

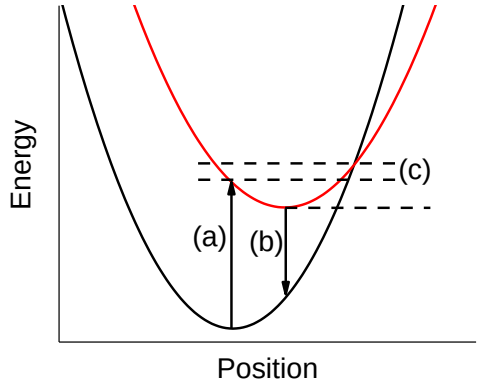

Figure 2-4: Configurational coordinate diagram for a luminescence center ground (black) and excited (red) state. Adapted from Chen and McKeever (1997).

The diagram shows (a) the excitation energy needed to move an electron from the ground state to the excited state, (b) the emission energy given off as a photon by an electron returning to the ground state from the excited state, and (c) the energy above the excitation energy to where the potential energy curves cross. At the energy were the curves cross, an electron may transition between the two states without emission of photons. The return to ground state is non-radiative. As such, the luminescence for the return to the ground state is said to be quenched.

2.2 ***OSL materials***

Historically, the development of synthetic OSL materials has routinely focused on materials investigated for TL that fade with light exposure (Bøtter-Jensen et al., 2003).

Both commercial materials, Al_2O_3 and BeO, were considered as TLDs before being investigated for OSL dosimetry.

The lack of an ideal material is the primary limitation for the adoption of OSL for many applications. Here we describe the advantages and limitations of current commercial materials.

2.2.1 Al_2O_3

The most widely used OSL material is Al_2O_3. Landauer Inc. uses the material in their Luxel and InLight dosimetry systems. Aluminum oxide for OSL is doped with carbon, Al_2O_3:C (McKeever et al., 1999), but a new formulation doped with carbon and magnesium has been used as a fluorescent nuclear track detector and for optical memory storage (Akselrod and Akselrod, 2006; Akselrod and Sykora, 2011; Greilich et al., 2013; Sawakuchi et al., 2016; Sykora et al., 2007; Sykora et al., 2008; Sykora and Akselrod, 2010), as well as for 2D dosimetry (Ahmed et al., 2014; Ahmed et al., 2016a).

Al_2O_3:C was originally developed as a TL material by Akselrod and Kortov (1990); Akselrod et al. (1990). The material showed sensitivity about 50 times greater than LiF:Mg,Ti, widely known by the commercial name TLD-100™ (ThermoFischer Scientific), developed by Harshaw Chemical Company and the University of Wisconsin (Cox, 2004), still today one of the most popular TL dosimeters. Fading in room light of the TL signal resulted in optical stimulation of Al_2O_3:C being studied by Markey et al. (1995). Since then, Al_2O_3:C has undergone in-depth characterization and development as a useful dosimeter for several applications in OSL dosimetry.

Al_2O_3:C has an OSL signal that is about twice its TL signal (Bøtter-Jensen et al., 1997) and good fading characteristics, none observed at room temperature for 100 days (Bøtter-Jensen et al., 1997). It has a broad range of linear dose response, 1 mGy to about 50 Gy, above which it starts saturating (McKeever et al., 1996).

The OSL emission of Al_2O_3:C occurs in two bands, at 335 nm (F^+-center, < 7 ns lifetime (Evans and Stapelbroek, 1978)) and 420 nm (F-center, 35 ms lifetime (Akselrod et al., 1998)), with an optimal stimulation wavelength of about 500 nm (Bøtter-Jensen et al., 1997). This makes for easy excitation with green LEDs or a green laser and readout with a blue or UV bandpass filter.

Nevertheless, the material has some drawbacks. It has a higher effective atomic number ($Z_{eff} \cong 11.3$) than tissue ($Z_{eff} \cong 7.4$), which results in an over response to low energy X-rays. The material's F-center long lifetime makes it a challenge for 2D dosimetry or other methods that rely on fast laser-scanning measurement (Yukihara and Ahmed, 2015). At this point, a large number of corrections are needed to both adjust for the scanner's design and the long luminescence lifetime of the F-centers (Ahmed et al., 2016b). A material that could bypass the need for a pixel bleeding correction would be beneficial to advancing 2D OSL dosimetry. Finally, Al_2O_3:C has weak intrinsic sensitivity to neutrons (small cross section). To be useful for neutron dosimetry, a neutron converter such as Li_2CO_3 enriched with Li-6 is needed (Yukihara et al., 2008).

2.2.2 BeO

BeO produced under the name Thermalox® 995 (Materion Corporation) is attractive for dosimetry, as it has $Z_{eff} \cong 7.1$, which is closer to that of tissue than Al_2O_3. In addition, it has sensitivity comparable to Al_2O_3:C.

BeO was investigated as a TLD by Tochilin et al. (1969) and its light sensitivity was noted. The following year Rhyner and Miller (1970) reported that the material was useful as an OSL dosimeter. Work has continued since then to characterize and use the material in OSL dosimetry.

BeO has OSL emission around310-370 nm and can be stimulated well from 420-525 nm. The OSL curve is comprised of several components, some of which fade at room temperature. The highly unstable components are removable with an annealing of 180 °C (Bulur et al., 2001). However, there remains fading, about 5% in 1 h, in the OSL signal of the more stable components (those components not removable with the annealing). After the first hour following irradiation, the OSL signal shows no more fading for at least 6 months (Bulur and Göksu, 1998; Sommer et al., 2008).

BeO is contributing to several applications. It is used for personal dosimetry (Busuoli et al., 1983; Jahn et al., 2013), explored for 2D dosimetry (Jahn et al., 2010; Jahn et al., 2011), and proposed for environmental dosimetry (Jahn et al., 2014). Currently, the greatest limitation of BeO is that it is not manufactured specifically for dosimetry, which results in large variations from batch to batch. A second weakness is that, like Al_2O_3:C, it needs converters for neutron dosimetry.

2.2.3 Other materials

Several other materials show OSL emission but have not been commercialized. Some, like quartz or feldspar (Godfreysmith et al., 1988), are naturally occurring and useful for luminescent dating. Others show potential as emergency dosimeters, including porcelain (Haskell, 1993), table salt (Nanto et al., 1993b), integrated circuits (Göksu, 2003), and teeth enamel (Godfrey-Smith and Pass, 1997). The remaining group of materials are used for X-ray imaging or were prospective personal dosimetry materials. X-ray imaging materials include KCl (Nanto et al., 1993a), KBr (Douguchi et al., 1999), BaFX where X = Cl, Br or I (Rowlands, 2002; Sonoda et al., 1983; von Seggern, 1999), and RbI (Thoms et al., 1994). The final group of materials are those explored as potential personal dosimeters. This group includes CaF_2 (Bernhardt and Herforth, 1974), $CaSO_4$ (Pradhan and Ayyanger, 1977), $MgSO_4$ (Le Masson et al., 2001), MgO (Bos et al., 2006),

and XS, where X = Mg, Ca, Sr, or Ba (Antonov-Romanovskii et al., 1955; Missous et al., 1991; Rao et al., 1984).

The primary problem with these materials is their effective atomic numbers. The lowest Z_{eff} is that of MgO at 10.8. Some of the materials have low sensitivity or are not practical to synthesize. Thus, it is logical that they are not produced commercially for OSL dosimetry.

2.3 ***Material characteristics for OSL dosimetry***

Desirable properties of an OSL material for dosimetry depend on the application. The requirements for personal dosimetry are different than, for example, for in-vivo dosimetry in radiation therapy. Since there is no perfect material, emphasis can be placed on some properties to the detriment of others, depending on the application. Nevertheless, in general, the desirable properties are as follows.

The material needs to be highly sensitive to ionizing radiation, so only a small amount of material is needed for a dosimeter. The material needs to hold the dose information at room temperature with little to no fading. It is preferable to have a material that emits at shorter wavelengths than the stimulation wavelength, to allow easier optical filtering from the stimulation wavelengths. Finding materials with UV emission is desirable since this allows for stimulation with visible wavelength LEDs and easy optical filtering. For a material to be reusable, the material needs to be resettable. It is best if a single OSL readout can do this. Otherwise, more complicated processes, like annealing or long duration bleaching, are required to reset the detectors for reuse. Finally, good dosimeters measure reliably over a wide dose range.

OSL materials must have a linear relationship between OSL signal and dose to be useful for dosimetry. When a material saturates, the actual dose cannot be determined,

as no additional signal is produced with additional dose. Other non-linear behavior in the dose response hinders the ability to find the dose in a convenient way.

It is important for a material to have an effective atomic number (Z_{eff}) close to that of tissue (~7.4), to ensure it will show similar absorbed dose effects to that of tissue for photons of varying energies. If Z_{eff} is much higher than that of tissue, then the material will show a higher absorbed dose for low energy X-rays than tissue. The overresponse is correctable with knowledge of the material and radiation field, but this introduces additional error into the measurement. Moreover, in practical applications the photon energy spectrum of the radiation field is unknown. Thus, a perfect dosimeter would have an effective atomic number equal to tissue.

For 2D OSL dosimetry systems, it is important for the emission centers to have a short luminescence lifetime. The lifetime influences the scan time per pixel, since the luminescence from the previous pixel readout should be very small compared to the pixel currently being stimulated with the laser. If a long luminescence lifetime center is present in a material, there is signal bleeding from one pixel to the next, or one must wait for the luminescence of the previous pixel to end. This can be addressed by a set of mathematical corrections or optical filters to block the long lifetime center, if there is another luminescence center with a short luminescence lifetime (Ahmed et al., 2014). However, a material with only short luminescence lifetime emission centers would make these corrections moot and eliminate errors introduced by the analysis.

A material with Li or B would be convenient for neutron dosimetry since Li-6 and B-10 have large capture cross-sections for thermal neutrons. Thus, a material containing Li or B could be sensitized to neutrons by synthesis with isotope enriched precursors or desensitized to neutrons by synthesis with isotope enrichment to less sensitive isotopes (Li-7 and B-11). A material allowing for this direct sensitivity to neutrons would be an

improvement over both Al_2O_3 and BeO, both of which need neutron converters for neutron dosimetry applications.

2.4 ***MgB_4O_7***

Recently, MBO has attracted the interest of our research group (Yukihara et al., 2017) as well as other researchers (Souza et al., 2017) as a potential OSL material. MBO is close to tissue equivalent, has Z_{eff} of 8.4 and has boron in its composition, which opens the possibility of neutron dosimetry through enriching with B-10.

2.4.1 MBO as a TL material

Prokic (1980) reported magnesium tetraborate (MBO), MgB_4O_7, to be a useful TL material. The author doped the material with either Dy or Tm and pressed it into sintered pellets. This material served as the basis of commercially produced dosimeters from Vinca Institute of Nuclear Science in Belgrade, Serbia from the 1980s until 2008. A comparable TLD using Teflon to embed the material was produced in Brazil (Souza et al., 2014).

MBO has several physical properties that make it a desirable host material. The primary benefit is a Z_{eff} of 8.4, which is close to that of tissue. Early studies showed the material's TL to have low fading (Driscoll, 1981; Prokić, 1980; Shahare et al., 1993). The TL sensitivity was observed to be around an order of magnitude higher than that of LiF:Mg,Ti (Driscoll, 1981) and higher than the TL from Al_2O_3:C or $CaSO_4$:Dy (Prokić and Bøtter-Jensen, 1993). The annealing procedure for MBO:Dy is simpler than that of LiF:Mg,Ti, allowing simpler reuse (Paluch-Ferszt et al., 2016).

Originally, the material's TL was reported to be stable under light exposure. However, that was incorrect, especially when UV wavelengths were present in the light source used for testing the light sensitivity (Cano et al., 2008; Driscoll, 1981). This opened

the possibility of using UV excitation for PTTL, but the dose response of the PTTL is highly nonlinear (Richmond et al., 1987). The TL of MBO:Dy was reported to be stable after many uses, offering good reusability for sintered samples mixed with Teflon (Campos and Fernandes Filho, 1990). Also attractive, MBO shows a large linear range from microGray to tens of Gray (Driscoll, 1981). MBO was a TLD for personal dosimetry (Prokić, 2007) and environmental dosimetry (Adrovic et al., 2004). MBO, as a TL material, is useful for neutron detection by B-10 enrichment (Price et al., 1998).

One of the first improvements to MBO:Dy was codoping with sodium. This codoping increases the TL signal, shifts the TL peak to slightly higher temperatures, and increases the range of linear dose response (Furetta et al., 1999; Furetta et al., 2000). This could be due to sodium behaving as a charge compensator and allowing easier dysprosium substitution of magnesium. With other dopants, lithium has a similar effect. However, the exact mechanism for the TL emission increase is unknown.

Other dopants explored for TL are manganese (Prokić, 1993), gadolinium (Annalakshmi et al., 2013), cerium (Dogan and Yazici, 2009), thulium (Karali et al., 1999; Prokić, 1980), neodymium (Souza et al., 2015), terbium (Kawashima et al., 2014), silver (Palan et al., 2015), and copper (Rao et al., 2009). As has been found by varying the dopant, the emission tends to be characteristic for the dopant, especially in the case of lanthanides (Yukihara et al., 2014b). Nevertheless, specific TL mechanisms were proposed in only a couple of papers (Annalakshmi et al., 2014; Porwal et al., 2005; Yukihara et al., 2014b).

In MBO:Tm, Porwal et al. (2005) used electron paramagnetic resonance (EPR) to observe the disappearance of BO_3^{-2} at around 150-200 °C. In addition, they related the center's thermal destruction energy, 0.97(3) eV, with the trap depth, 0.98(3) eV, measured using the various heating rate method (see Section 2.5). They proposed that borate ions, BO_3^{-3}, trap holes to form BO_3^{-2}. When heated to around 170 °C, the hole leaves the trap

and recombines with Tm^{2+}, which results in Tm^{3+} in an excited state that emits light. However, the authors proposed that Tm^{2+} enter the lattice in place of Mg^{2+}, since Tm^{2+} is detected by EPR prior to irradiation. This requires Tm^{3+} to return to the ground state of Tm^{2+}. The authors propose that the release of an electron from oxygen vacancies at higher temperatures (~200 °C) that recombine with Tm^{3+} to return it to Tm^{2+}. Thus, following complete heating all Tm in the lattice should be divalent. Optical absorption bands observed suggest that both Tm^{3+} and Tm^{2+} enter the lattice, since Tm^{3+} absorption bands at 360 nm, 465 nm, 658 nm, and 687 nm are present for an unirradiated sample. The Tm^{3+} absorption bands strengthen upon irradiation of the sample. In addition, no fluorescence from Tm^{3+} is observed for irradiated samples following annealing at 500 K. This confirms that Tm^{2+} is the dominant ionization state for Tm entering the lattice.

Annalakshmi et al. (2014) did a similar study with MBO:Dy and MBO:Tb to correlate the observed TL with destruction of signal from ions detected by EPR. As the main TL peaks for Tb-doping and Dy-doping happen at about the same temperature as for Tm-doping, it is probable they are related to a similar trapping center. EPR confirms that the signal from BO_3^{2-} and O_v^- disappear at about the same temperature as the TL signal. The authors here propose that the recombination mechanism involves the hole release by the borate ion, which recombines with a trapped electron at an oxygen vacancy. Some of the energy from the recombination transfers to the lanthanide, which is in its trivalent state. Thus, trivalent lanthanide emission returns the lanthanide to its ground state. PL data shows Gd^{3+} emission at 314 nm and Tb^{3+} emission at 544 nm for their respectively doped version of the material. However, without a comparison of PL with and without irradiation, one is unable to determine the natural ionization state of the dopants in the lattice. With this information, the different interpretations of recombination from Annalakshmi et al. (2014) and Porwal et al. (2005) would be resolved.

Additional study led to a model for the behavior of various lanthanides (Yukihara et al., 2014b). Yukihara et al. systematically doped MBO with various lanthanides. Two types of emission observed were the emission around 550 nm and the lanthanide emission. The 550-nm emission is possibly Mn^{2+}. The evidence provided was both an increase in the TL signal with Mn doping and elimination of the emission when high-purity reagents were used for synthesis. If manganese contamination is responsible for the 550 nm emission band, MBO is highly sensitive to contamination as the magnesium reagent is certified to 2 ppm of manganese. The emission is a broad band and green. This matches the expected characteristics of a d-d transition for Mn^{2+}, specifically the $^4T_1 \rightarrow {}^6A_2$ transition is expected to be broad (Blasse and Grabmaier, 1994). The green emission is consistent with a lower crystal field strength, which would mean the Mn^{2+} would be tetrahedrally coordinated (Blasse and Grabmaier, 1994). If Mn^{2+} is substituting for Mg^{2+}, it would be tetrahedrally coordinated. Thus, Mn^{2+} contamination would be able to enter the lattice and would explain the green emission band.

The lanthanide emission varies according to the particular lanthanide's energy level position within the host's bandgap as well as the impact of the crystal field strength (Dorenbos, 2000a; Dorenbos, 2000b; Dorenbos, 2001, 2003a, 2003d; Dorenbos and Bos, 2008; Dorenbos et al., 2010; Sidorenko et al., 2006). In some cases, this can lead to identification of hole recombination centers or electron recombination centers.

It was observed by Yukihara et al. (2014b) that MBO:Gd,Li has two different recombination mechanisms at play. For the TL peak at 190 °C, the emission is from Gd^{3+}. Paired with the EPR study from Porwal et al. this trap is identified as a hole released from a borate ion and joining with an electron trapped by gadolinium. The 250 °C peak shows as Mn^{2+} emission. This must be manganese behaving as a recombination center for detrapped electrons. If the recombination is delocalized, as the main thrust of TL theory

assumes, then manganese cannot be a recombination center for detrapped holes. Otherwise, Mn^{2+} emission should exist for the 190 °C peak as well.

In the same paper, Ce^{3+} and Mn^{2+} emissions are present for the same TL peaks. This would indicate that the two ions are recombination centers for the same type of trapped carrier. Since Ce^{3+} is usually deep within the band gap, it usually behaves as a deep hole trap. The hole recombines with a thermally liberated electron leaving Ce^{3+} in an excited state. Thus, the emission observed in MBO:Ce is due to the recombination of freed electrons. The exception is TL observed at lower temperatures seen as Ce^{3+} emission only. The authors suggest this may be evidence for localized transitions.

Besides changing dopants, the exact properties of a material change with synthesis type or post-synthesis annealing. Annealing following synthesis is required for complete crystallization of the product. In MBO:Dy, the higher temperature TL peak observed an increase in signal when the sample was allowed to cool naturally following annealing (Karali et al., 2002).

Quality material is synthesizable by a variety of paths. Typically, MBO was sintered with either hot or cold pressing (Prokić, 1980; Shahare et al., 1993; Subanakov et al., 2014). More recently, MBO was synthesized by precipitation wet chemistry, solution combustion synthesis or sol gel (Lochab et al., 2007; Souza et al., 2014; Souza et al., 2017). Solution combustion and sintering remain the lead methods seen in the current literature.

As for dosimetric characteristics, analysis of MBO:Dy has suggested that the main dosimetric peak is a combination of first-order peaks (Souza et al., 1993). The main peak maximum does not shift in temperature over a broad range of doses, indicating first-order behavior (Souza et al., 1993). However, the peak is too broad to be explained by a single first-order peak.

Interest in MBO has been renewed due to its potential for temperature sensing (Doull et al., 2014; Yukihara et al., 2014a; Yukihara et al., 2015). The concept of extracting temperature exposure of a TL particle during a known time after a known dose was given to the material was shown by Doull et al. (2014). The method depends on sequential depletion of the TL curve. It is analogous to a TL curve for a known dose being depleted by some isothermal temperature exposure prior to readout of the TL curve.

2.4.2 MBO as an OSL material

One common observation with MBO since the beginning has been its fading under UV and phototransfer. This observation has led to exploration of the material as an OSL dosimeter. The initial study has recently been published (Yukihara et al., 2017), and the results will be summarized and discussed here.

Preliminary study has shown TL of MBO:Ce,Li is of comparable intensity to LiF:Mg,Ti and the OSL is of the same order of magnitude as Al_2O_3:C. In Figure 2-5, plots are shown comparing TL glow curves for MBO:Ce,Li and LiF:Mg,Ti collected in the same measurement system and OSL decay curves for MBO:Ce,Li and Al_2O_3:C. All samples were powder and 10 mg aliquots were used.

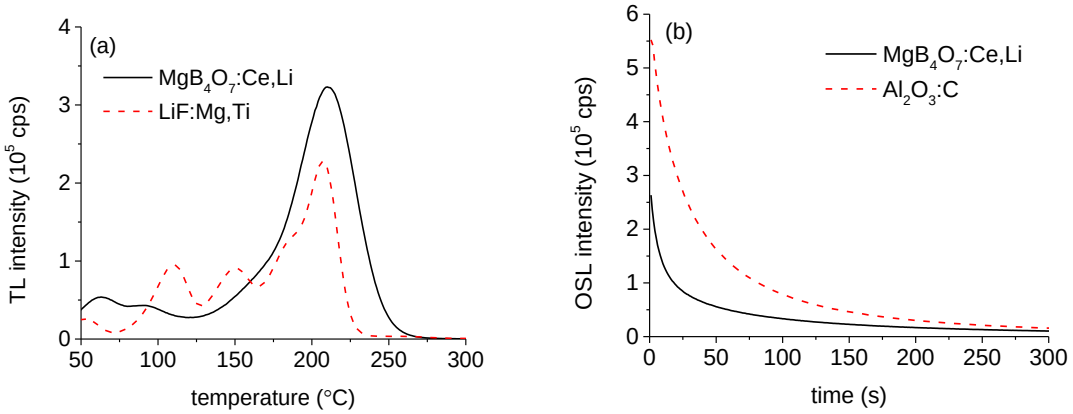

Figure 2-5: (a) TL comparison of MBO:Ce,Li with LiF:Mg,Ti with heating rate of 1 °C/s. (b) OSL comparison of MBO:Ce,Li with Al_2O_3:C. All optical filters used were Hoya U-340 except for LiF:Mg,Ti, which used a Schott BG-39. Each plot is the average of 3 aliquots with less than 10% variation from aliquot to aliquot. Reproduced from Yukihara et al. (2017).

The OSL signal from MBO:Ce,Li is relatively stable, although a long-term study (> 6 days) is not available. The OSL area fades by approximately 10% in 6 days, while the OSL initial intensity fades around 50 % in 6 days. The proposed material shows a linear dose response over a broader range than Al_2O_3:C which may open some other applications. Yukihara et al. (2017) demonstrate sensitivity to neutrons through boron enrichment. Overall, the material warrants more exploration.

A second group has published reporting OSL in MBO:Ce,Li (Souza et al., 2017). However, their RL (emission ~412 nm) and dose response (saturation 100 Gy) disagree with those published by Yukihara et al. (2017). XRD from a previous work from this group showed residual boric acid following synthesis (Souza et al., 2014). If the material was bonded with Teflon like the 2014 study, these two variations combined may account for the difference in emission and dose response observed.

Unpublished studies from our lab have shown MBO:Gd,Li to be a potential OSL material as well. As the trap and recombination model are different than those from

MBO:Ce,Li, the combined study of these two co-dopants may further illuminate the underlying process involved in the OSL process and yield advantageous properties for various applications.

2.5 ***TL/OSL analysis techniques***

Characterization of the trapping and recombination mechanisms is crucial to understand the luminescence properties of a material and allow fine adjustments to the material for other applications. If a specific impurity is responsible for trapping or emission, it may be possible to modify those centers. Knowledge of the trap depth, *E*, and attempt to escape frequency, *s*, allows modeling of the TL process. Some applications like TL thermometry require knowledge of trap depths and frequency factors. Knowledge of trapping parameters may explain the fading in the material.

Over time, several techniques have been developed to find the trap parameters. These methods include initial rise method, various heating rate, and curve fitting, which will be used for analysis in this study. Other methods not used here include isothermal decay and peak shape methods (Chen and McKeever, 1997).

The initial rise method (IRM) stands on the assumption that in the initial part of the TL peak, the trapped population is approximately constant. Many experiments use the region of a peak that is above background and less than 5% of the peak maximum. For this initial region of the TL curve, the signal intensity is essentially an exponential increase, following Garlick and Gibson (1948), for any kinetic order as in Eq. (2.12).

$$\mathbf{I_{TL}} = \boldsymbol{CExp}(-\boldsymbol{E}/\boldsymbol{kT}) \qquad \textbf{(2.12)}$$

A linear fit of a *ln(I)* vs *1/T* plot allows for the finding of the trap depth, *E*. Typically, an experiment for initial rise analysis includes step-annealing, which consists in pre-heating the sample to a specified stopping temperature, allowing the sample to cool, and taking

the final readout of the partially depleted TL. Step-annealing clears lower temperature peaks, so multiple peaks can have their trap depths measured for a material. Challenges arise when peaks overlap, as they may interfere with each other. In addition, the method gives no direct evaluation of the frequency factor. Further discussion of initial rise can be found in McKeever (1985). Thus, other methods are employed find *s* and values of *E*.

A recent modification to the IRM allows for information to be gained about overlapped peaks or a distribution of peaks (Van den Eeckhout et al., 2013). With a step-annealing experiment, many values for *E* are found. These different trap depth values can be assembled into a histogram using the difference in integrated TL compared with the previous step-annealed curve as weighting. This difference in TL intensity is directly related to the number of charges detrapped due to a step-annealed heating of $T_{stop}(i)$ as opposed to a lower heating of $T_{stop}(i-1)$. This is shown in Figure 2-6.

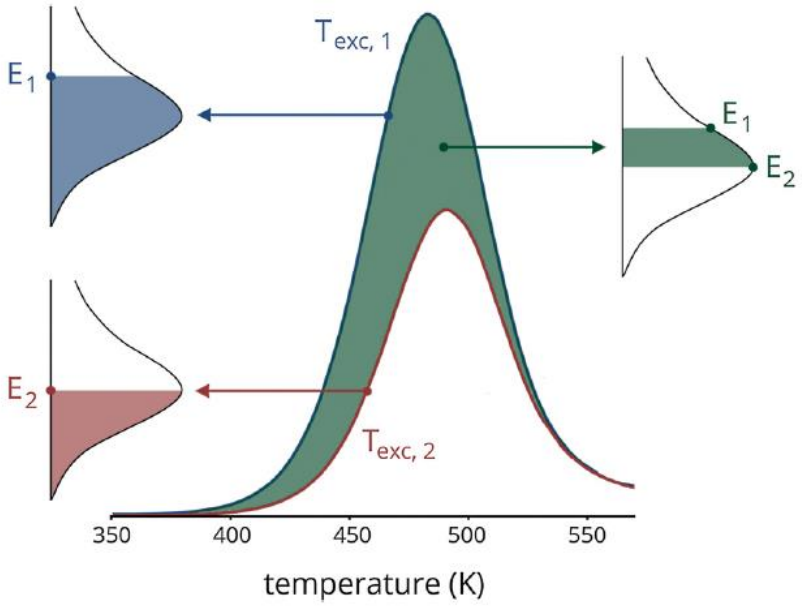

Figure 2-6: The density of a particular trap depth in a distribution can be found by the difference in TL areas from one step-annealed curve to the next. Reproduced from Van den Eeckhout et al. (2013).

The various heating rate method (VHRM) utilizes the change of a peak maximum with varied heating rate. The VRHM discussed here was proposed by Hoogenstraaten (1958) and uses various linear heating profiles. If linear heating rates are used, the relationship between temperature of the peak maximum T_m and the activation energy and frequency factor for a first-order glow curve can be calculated. Taking the derivative of the Randall-Wilkins equation and setting it equal to zero, one can find:

$$\ln\left(\frac{T_m^2}{\beta}\right) = \frac{E}{kT_m} + ln\left(\frac{E}{sk}\right) \quad \textbf{(2.13)}$$

Thus, if a linear fit is calculated for a $ln(T_m^2/\beta)$ vs $1/T_m$, the trap depth can be calculated from the slope and the attempt to escape frequency from the intercept.

The primary weakness of this method is resolution of TL peaks that occur close to each other. When this occurs, the parameters for a peak will be indeterminable if its maximum cannot be resolved from its neighbor. Also, this method is built from the first-order case, although a second-order analog exists. Thus, one needs to know the kinetic order of the peak before choosing the exact VHRM to use.

The remaining method used here will be curve fitting. This technique consists in fitting a TL glow curve with a predetermined number of first-order glow curves superimposed on each other (Mohan and Chen, 1970). As discussed above, linear superposition does not hold true for non-first-order glow curves. The fitting is usually done using a nonlinear least squares method.

The primary weakness is the arbitrary nature of choosing the number of peaks with which to fit a glow curve. For a glow curve with overlapping peaks, it may be difficult to determine an appropriate number of peaks for fitting. Further discussion of the technique and its difficulties can be found in Chen and Pagonis (2011).

Curve fitting can be useful for OSL curves as well. In the context of OSL, the decay curve is fit with multiple exponential decay components. Different decay components will

have different decay constants that will determine how quick that signal will fade for that stimulation. This can also be used to see if different decay components are more temperature stable or fade slower than others.

2.6 ***Other relevant material analysis techniques***

2.6.1 X-ray diffractometry (XRD)

X-ray diffractometry (XRD) is a widely used technique in solid material analysis. It was first observed experimentally in 1912 by Friedrich et al. (1913), for which Max von Laue was awarded the Nobel Prize in Physics in 1914. Crystals are arrays of many atoms in a repeating pattern. For light of short enough wavelength, the gaps in between the atoms behave as a diffraction grating. Since these gaps depend on the atoms within and bond lengths of a material, the diffraction pattern of a material is characteristic to that material. X-rays passing through a crystal are diffracted and form regions of constructive interference following Bragg's law (W. H. Bragg et al., 1913):

$$2d\,sin\theta = n\lambda \qquad \textbf{(2.14)}$$

Here, d is the spacing between diffracting planes, θ is the angle of diffraction, n is an integer that describes the order of diffraction, and λ is the wavelength of the incident X-rays.

2.6.2 Scanning electron microscopy (SEM)

Scanning electron microscopy (SEM) is a technique first demonstrated by von Ardenne (1938). A SEM operates in a manner like that of a conventional optical microscope. An electron gun sweeps a beam of electrons across the surface of a sample

with the aid of a magnetron. Electrons scattered from atoms on the surface of the material are imaged. Detection of these secondary electrons is the most common method of detection though backscattered electrons can be measured also. The SEM takes advantage of having a shorter wavelength than visible light, which results in better resolution than an optical microscope.

2.7 ***Chemical shift model***

A powerful model for engineering defects within materials has been developed in recent years. The Dorenbos model or chemical shift model allows for the prediction of energy levels of lanthanides doped into a material relative to the host's bandgap. Only knowledge of the bandgap width, energy of charge transfer from the valence band to Eu^{3+}, the centroid shift of Ce^{3+}, and energy difference from the Eu^{2+} ground state to the Eu^{3+} ground state is needed to place the energy levels for all lanthanides relative to the bandgap. This section will address the development and particulars of this model, which will be applied in Section 6.3.

The development of the chemical shift model started with the compilation of Ce^{3+} absorption and emission measurements from hundreds of compounds (Dorenbos, 2000a; Dorenbos, 2000b; Dorenbos, 2001, 2002). It was realized that the change in optical absorption and emission for Ce^{3+} only depended on the crystal field depression or spectroscopic redshift. The same was true of the other trivalent lanthanides (Dorenbos, 2000c; Dorenbos, 2000d, 2000e). This meant that the energy of the first 5d→4f could be expressed as:

$$\Delta E(Ln, A) = \Delta E(Ce, free) - D(A) + \Delta E^{Ln,Ce}, \qquad \textbf{(2.15)}$$

where ΔE is the energy of the first 5d→4f transition, *Ln* denotes the lanthanide, *A* represents a host material, *D* is the spectroscopic redshift, and $\Delta E^{Ln,Ce}$ is the energy difference between the Ce^{3+} ground state and the lanthanide's 3+ ground state.

The 4f levels of lanthanides are well shielded electronically from outside influences. The 5d levels, however, are exposed to the influence of the surrounding electric field. In a crystal, the crystal field depresses the 5d levels to lower energies than they are in vacuum. This depression of the 5d states happens equally to all 5d states and does not change with varying the number of ground state 4f electrons (varying lanthanide) in Ln^{3+} ions (Dorenbos, 2000d, 2000e). This meant that the relative energy difference for 5d→4f transitions from lanthanide to lanthanide was constant regardless of host material.

The divalent lanthanides follow the same behavior as the trivalent lanthanides. This was found by compiling excitation and emission data for materials doped with Eu^{2+} (Dorenbos, 2003c). The predictivity of Ln^{2+} transitions was shown in Dorenbos (2003d). Thus, both trivalent and divalent lanthanides could have their excitation/emission predicted in a material if the spectroscopic redshift was known. This redshift could be found with the excitation or emission of one Ln^{2+} or Ln^{3+}.

The next advance related the energies of the Ln^{3+} and Ln^{2+} ground states (Dorenbos, 2003b). The spectroscopic redshift could be described by:

$$[\boldsymbol{D}(\mathbf{2}+,\boldsymbol{A}) = \mathbf{0.64}\boldsymbol{D}(\mathbf{3}+,\boldsymbol{A}) - \mathbf{0.233}]\boldsymbol{eV}, \qquad \textbf{(2.16)}$$

where *D(2+, A)* is the redshift for the 2+ oxidation state, *D(3+, A)* is the redshift for the 3+ oxidation state, and *A* denotes host material. This allows for prediction of all 3+ and 2+ transitions in a solid from the measurement of the ground state transition of one 3+ or 2+ lanthanide. However, the model at this point did not account for the locations of valence and electron bands relative to the ground state energies of the lanthanide ions.

Next, the ground states of trivalent lanthanides show this same systematic behavior for charge transfer of electrons from the valence band to the 3+ ground states of lanthanides in materials (Dorenbos, 2003a). This allows for the placement of the lanthanide ion ground state energy levels relative to the valence band. Again, this can be done from the measurement of one lanthanide. Relating the ground state energies to the band gap of the host material allows prediction of which lanthanides will show 5d→4f emission in a material. If the 5d levels are located within the conduction band, 5d→4f emission is no longer observed.

Relating lanthanide ground state energies also allows prediction of charge trapping behavior for different lanthanides within the same material. A lanthanide with a 3+ ground state close to the conduction band is likely to behave as an electron trap. Whereas, a lanthanide with a 2+ ground state close to the valence band can behave as a hole trap.

Improvements were made both to the relative energy ground state energy difference values (Dorenbos et al., 2010) and the method for finding the energy difference between 2+ and 3+ ground state levels (Dorenbos, 2012). This second refinement presented what is now the current model. Lanthanide ion ground state energies can be placed relative to a host material's band gap with four parameters: the bandgap energy, the charge transfer energy from the valence band to Eu^{3+}, the spectroscopic redshift of Ce^{3+}, and the energy difference between the ground states of Eu^{2+} and Eu^{3+}. A diagram showing this is a vacuum referred binding energy (VRBE) diagram. With the correct equipment, one can measure all these parameters through optical excitation or absorption and plot the ground state energies of 2+ and 3+ lanthanides relative to host band gap.

An example of a VRBE is provided for the reader in Figure 2-7. The material $GdAlO_3$ with the following parameters was used: exciton energy of 7.29 eV, cerium centroid shift of 2.08 eV, europium charge transfer of 4.86 eV, and energy difference of europium ground states of 6.75 eV (Luo et al., 2016).

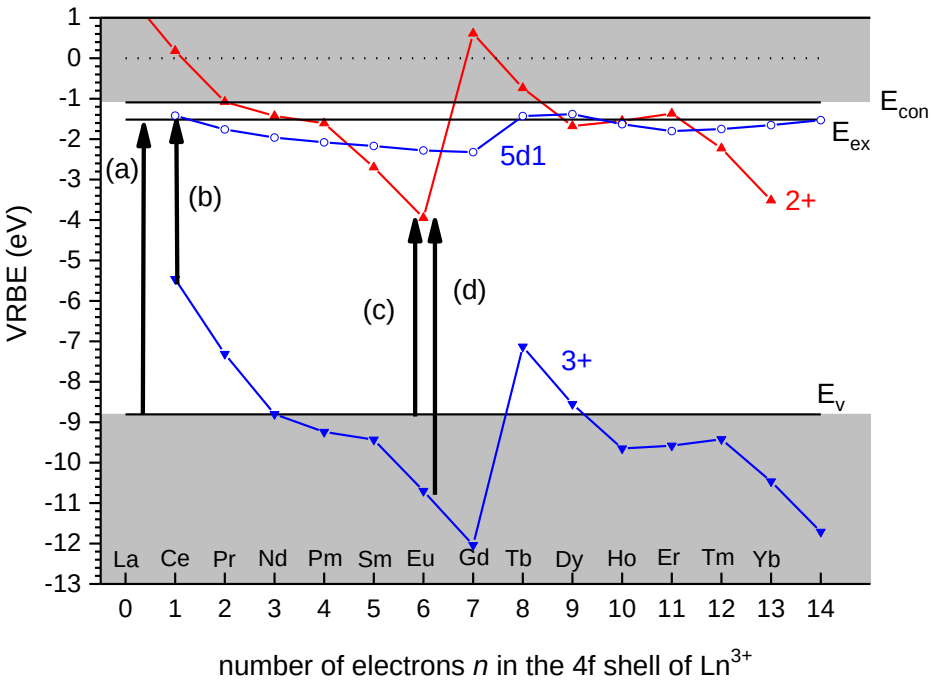

Figure 2-7: Example of VRBE diagram for $GdAlO_3$. Modified from Luo et al. (2016).

For building the diagram, the four important parameters are shown, in Figure 2-7, with arrows: (a) is the exciton energy; (b) is the difference between the free Ce^{3+} emission energy and spectroscopic redshift energy; (c) is the charge transfer from the top of the valence band to europium; (d) is the energy difference between the ground state energies of Eu^{2+} and Eu^{3+}. The Ln^{3+} ground state curve, Ln^{2+} ground state curve, $5d^1$ curve, valence band energy, exciton energy level, and conduction band energy have been labelled also.

The assembly of this diagram allows for predictions to be made about the trapping or recombination role of a lanthanide (Bos et al., 2011; Dorenbos et al., 2013; You et al., 2012). For this material ($GdAlO_3$), Ce is expected to be a deep hole trap. A hole could be trapped by Ce^{3+} (forming Ce^{4+}) with a trap depth of about 3.5 eV (the energy of the ground state above the valence band). Thus, an electron trap in the material would be expected to recombine with the hole at Ce. Nd^{3+}, Sm^{3+}, Dy^{3+}, Ho^{3+}, Er^{3+}, Tm^{3+}, and Yb^{3+} are expected

to trap electrons (forming Ln^{2+}) and would detrap at lower temperatures than a hole trapped at Ce^{3+}. This matches what was observed, except for Sm^{3+} and Yb^{3+} (Luo et al., 2016). This was due to these electron traps being located too deep to be thermally excited easily. Pr^{3+}, Gd^{3+}, and Tb^{3+} are unable to trap electrons, since the ground states of their 2+ levels are within the conduction band.

This model has been successfully applied to explain phenomena in many materials: YPO_4 (Anna et al., 2014; Bos et al., 2008; Bos et al., 2010; Bos et al., 2011), $LiLnSiO_4$ (Ln = Y or Lu) (Sidorenko et al., 2006), AVO (A = La, Gd or Lu) (Andreas et al., 2009), $Y_3Al_5O_{12}$ (Milliken et al., 2012; Ueda et al., 2015a; You et al., 2011), and others.

2.8 ***Objectives of this study***

MBO:Ce,Li has OSL signal and potential advantages over Al_2O_3:C. Nevertheless, the properties of the material need to be determined before further optimizations can be made. Given the results of studies on the properties of the initial material, studies were conducted to improve the brightness of the material through synthesis modification. Finally, models were developed to explain the sensitization observed in the material and the ground state behavior of lanthanides in MBO.

CHAPTER 3

MATERIALS AND METHODS

This chapter describes the material synthesis of MgB_4O_7 and the equipment used in the studies, including: radiation sources, the TL/OSL reader and adjustments for taking TL emission data, the RL reader, the spectrofluorometer used for PL and OSL excitation/emission measurements, the X-ray diffractometer (XRD), and the scanning electron microscope (SEM).

3.1 ***Material synthesis***

MBO was synthesized by solution combustion synthesis (SCS) (Chick et al., 1990; Kingsley and Patil, 1988; Kingsley et al., 1990) as in Doull et al. (2014). In this method, a metal nitrate (oxidizer), fuel, and other precursors are combined in water, and the mixture is heated until combustion, resulting in a foam of fine particulate of the product. In the case of MBO, magnesium nitrate hexahydrate (for low-purity synthesis: 98%, Alfa-Aesar 10329 and for high-purity synthesis: 99.999% metals basis, Alfa-Aesar 10799), boric acid (99.99%, Alfa-Aesar 36771), nitrates of desired dopants (mostly $LiNO_3$ (99%, Alfa-Aesar 13405) and $Ce(NO_3)_3$ (99.5%, Alfa-Aesar 11329)), and urea (99.0-100.5%, Alfa-Aesar 36428) are mixed. Other dopants are used in the codoping study in Chapter 5: $Pr(NO_3)_3$ (99.9%, Alfa-Aesar, 12909); $Tm(NO_3)_3$ (99.9%, Alfa-Aesar, 14579); $Nd(NO_3)_3$ (99.9%, Alfa-Aesar, 12912); $Dy(NO_3)_3$ (99.9%, Alfa-Aesar, 12922); $Yb(NO_3)_3$ (99.99%, Alfa-Aesar, 11196); $Eu(NO_3)_3$ (99.9%, Alfa-Aesar, 15290); $Sm(NO_3)_3$ (99.9%, Alfa-Aesar, 12906);

$Ho(NO_3)_3$ (99.9%, Alfa-Aesar, 14588); $Er(NO_3)_3$ (99.99%, Alfa-Aesar, 11306); $Ag(NO_3)$ (99.2%, Sigmal-Aldrich, SX0205); $Cu(NO_3)_2$ (99.999%, Alfa-Aesar, 10699); $Co(NO_3)_2$ (99.999%, Alfa-Aesar, 10694). To get the desired MBO crystalline phase, an excess of boric acid (25% optimal) is needed (Doull et al., 2014). In addition, the use of high-purity reagent (magnesium nitrate hexahydrate, 99.999% metals basis, Alfa-Aesar 10799) was investigated to improve the material. After synthesis, annealing is needed to fully crystallize the material: the samples were heated to 900 °C at 5 °C/min, soaked at the selected annealing temperature for 2 h, and allowed to cool naturally inside the furnace, unless otherwise noted.

3.2 ***Instrumentation and equipment***

3.2.1 TL and OSL measurements

Risø TL/OSL-DA-15 readers (Risø National Laboratory, Denmark) were used to obtain TL and OSL data. For OSL, green LEDs (emission centered at 525 nm, irradiance of ~10 mW/cm^2 at the sample position) or blue LEDs (emission centered at 470 nm, irradiance of ~30 mW/cm^2 at the sample position) were used at 90% of maximum power unless otherwise noted. A bi-alkali photomultiplier tube (PMT) (model 9235QB, Electron Tubes Ltd.) was used to measure the light emitted from the sample. Hoya U-340 optical filters (7.5 mm thickness, transmission between 290 – 390 nm, Hoya Corp.) placed in front of the PMT were used to eliminate the stimulation light from the OSL signal. OSL measurements were obtained with 600 s of stimulation and 1 s of integration time. For TL, the TL/OSL reader used the same optical filter to measure the light from the same recombination centers as in the OSL measurements (Yukihara et al., 2014b). TL measurements were taken at a heating rate of 1 °C/s in high-purity N_2. Unless otherwise noted, all aliquots used had a mass of (10.0 ± 0.2) mg. Comparison measurements were

also performed using (10.0 ± 0.2) mg powder aliquots of Al_2O_3:C (Landauer Inc.) and (23.8 ± 0.2) mg chips of LiF:Mg,Ti (TLD-100, ThermoFischer Scientific Inc.).

3.2.2 Irradiations

Most irradiations were performed using $^{90}Sr/^{90}Y$ beta source built into the Risø TL/OSL readers, delivering a dose rate of ~70 mGy/s**,** depending on the mass thickness of the sample. In the analysis performed here, precise calibration of the source is not required, since we are interested only in characterizing basic luminescence properties. For applications in dosimetry, however, appropriate calibration for this material and for the form and shape of the detector would be required. For some measurements, a $^{90}Sr/^{90}Y$ beta source with a dose rate of ~100 mGy/s was used.

3.2.3 TL emission

TL emission spectra were measured also using the Risø TL/OSL reader, but replacing the PMT with an optical fiber spectrometer (USB-2000, Ocean Optics Inc.) as described by Orante-Barron et al. (2011). The heating rate was 5 °C/s. An irradiation of 1000 s in the TL/OSL reader (~70 Gy) assured sufficient TL signal for the spectrometer to detect. As there is no synchronization between the spectrometer and the TL reader, the peak positions may be shifted compared to TL data taken using the PMT for light collection. A program in Mathematica (Mathematica 10, Wolfram Research Inc.) was used to apply the correction for the spectrometer to each spectrum and combine the spectra into a matrix that could be represented by a 3D plot or a contour plot. The correction allows for better comparison to other emission measurements (Orante-Barrón et al., 2011).

3.2.4 RL

RL spectra were collected at room temperature using the same Ocean Optics spectrometer used for the TL emission measurements. The instrument, built as described by Orante-Barron et al. (2011), automatically takes a dark (background) spectrum before each readout and subtracts it from the subsequent measured spectrum. The background subtraction is not able to remove fluctuations from some bad pixels in the detector array. Thus, the wavelengths 642.79-646.425 nm and 652.362-655.654 nm were removed manually to avoid the erroneous signal. The spectrometer uses a boxcar integrator for smoothing the spectrum. The boxcar behaves like a mean smoothing. A boxcar setting of some number, n, will behave like a (2n+1)-point mean smoothing. The spectra gathered were corrected for the spectrometer sensitivity (see Section 4.2.1) for better comparison with PL and OSL emission data collected with a different instrument.

3.2.5 PL and OSL emission/excitation

PL data and OSL emission/excitation data were collected using a spectrofluorometer (FL-3-22, Horiba Ltd., Japan). The illumination is an ozone-free xenon lamp (450W/2 OFR, Osram GmbH, Germany) that gives a broad range of wavelengths for excitation, and the emission is measured by the instrument standard PMT (R928P, Hamamatsu Photonics K.K., Japan). The instrument has adjustable double grating spectrometers (blazed to 330 nm) for each selection of excitation wavelength and emission wavelength. Slits at each the entrance and exit of the sample chamber allow adjustment of the bandwidth of allowed wavelengths. Samples were mounted onto a copper solid sample holder using Rusch Silkospray (Teleflex Inc., U.S.A.).

For most measurements, the signal reported is the PMT signal (S) divided by a reference photodiode measurement (R) of the light exiting the monochromator (S/R). For stimulation scans, this accounts for the emission spectrum of the lamp. For emission

scans, this accounts for temporal fluctuations in the lamp brightness. For some stimulation wavelengths, optical filters were needed to block the second-order harmonic of lower wavelength stimulation from exciting the sample (e.g. a 450 nm long pass filter to block the 250 nm second-order harmonic when stimulating the sample with 500 nm).

3.2.6 X-ray diffraction

A powder X-ray diffractometer (XRD), equipped with a LYNXEYE detector (D8-25 ADVANCE, Bruker AXS GmbH, Germany), was used to collect diffractograms to verify phase purity. The X-ray tube is CuKα radiation (X-ray tube operated at 40 kV and 40 mA) and filtered by a 0.02 mm Ni foil to reduce CuKβ. Each diffractogram was scanned in 2θ with step size 0.02042° and 0.5 s per step from 15-80°. Patterns from the International Centre for Diffraction Data (ICDD) PDF 2 Release 2011 Database version 2.1102 were matched to the obtained diffractograms.

In addition to composition matching, percent amorphous composition and percent crystallinity were estimated as was crystal size using DIFFRAC.SUITE EVA (Bruker, Release 2010, v 1.4), referred to as EVA for the duration of this report. Percent amorphous is quantified as:

$$\%\boldsymbol{Am} = \mathbf{100}\frac{\boldsymbol{Global\ area - Reduced\ area}}{\boldsymbol{Global\ area}}. \quad \textbf{(3.1)}$$

The global area is the total XRD area. The reduced area is the background area measured using the software to adjust the curvature and offset of the background to align a background curve to the base of the peaks. After finding the percent amorphous composition, percent crystallinity is calculated by $\%Cr = 100 - \%Am$.

Scherrer analysis was done for peaks at each 19.89°, 22.27° and 25.81° (2θ) to estimate the crystallite sizes. The calculation was done using EVA, which finds the crystal size according to the Scherrer relation (Patterson, 1939; Scherrer, 1918):

$$d = \frac{K\lambda}{FWHM\cos(\theta)} \quad \textbf{(3.2)}$$

Where, d is the crystal size, K is a dimensionless shape factor that varies with crystal shape but is close to 1 (for all calculations here a value of 1 was used); λ is the X-ray wavelength; FWHM is the full width at half maximum of the peak being used, with a correction made for the broadening of the peak due to the instrument; θ is the Bragg angle which is the angle measure of the peak maximum.

3.2.7 SEM

Scanning electron microscope (SEM) images were collected using an environmental scanning electron microscope (Quanta 600, Thermo Scientific). Samples were mounted on aluminum stubs by sprinkling a small amount of the powder onto the stub, which had been coated with carbon double stick tape. The samples were coated with gold-palladium using a Balzers MED 010 sputter coater (40 mTorr argon, 40 mA, 30 s) to reduce charging of the material while imaging. Specifics of the magnification, beam power, and spot size are indicated on each image.

3.2.8 Kinetic parameter evaluation

Various heating rate method

For the various heating rate method (VHRM), TL curves were collected for heating rates of 0.1, 0.2, 0.5, 1, 2, 5, and 10 °C/s. The positions of peak maxima were measured visually in Origin 8.6 to the nearest degree. The linear fit required, from the $ln(T_m^2/\beta)$ vs

$1/T_m$ plot, was also done using the built-in linear least squares fitting from Origin. The results of the fit were used to calculate *E* and *s* from Eq. (2.13).

Initial rise method

Initial rise method was applied to TL data obtained by step-annealing. TL curves were collected following 5 s irradiation (~0.35 Gy) and preheat to a stopping temperature, T_{stop}, varied from 50-350 °C in 5 °C intervals. After each full TL readout, the sample was again irradiated with the same dose and the process was repeated with an increased T_{stop}.

For the analysis of the TL curves, we wrote a script in R (R Core Team 2016). The first part was a peak finding algorithm. A built-in local polynomial fit was used to smooth and interpolate the data. The first peak was identified by locating where the first derivative changes from positive to negative for the first time. To assure that this was not a background artifact, the first peak must have an intensity greater than the background plus 5 times the standard deviation of the background. The first 30 points were used for the calculation of both the mean background and standard deviation of the background. After the first maximum in the smoothed data was identified, a window was taken around that location of plus or minus 10 °C to ensure the maximum value for that peak had been correctly identified. The initial rise region for fitting was the region that was 1%-5% of the peak maximum. The linear fit of the *ln(I)* vs *1/T* plot was conducted using the built-in linear fit and the slope was used to calculate the trap depth according to Eq. (2.12). The trap depths calculated were verified by manual calculations using Origin for the linear fit.

An energy histogram was made for the main TL peak using the Van den Eeckhout method. The weights were found as $T_{stop}(i-1)$-$T_{stop}(i)$ and were the weights for the average energy of the energies found for $T_{stop}(i-1)$ and $T_{stop}(i)$. These were found for T_{stop} of 150-260 °C. 150 °C is the preheat needed to isolate the main peak and 260 °C was the highest

temperature for which an energy was found. Higher temperatures resulted in TL of insufficient intensity to apply IRM.

Curve fitting

TL peak fitting was conducted using a user-defined function in Origin 8.6. Fitting was attempted using 4-7 Randall-Wilkins peaks with the Kitis (Kitis et al., 1998) approximation for the integral as shown:

$$\boldsymbol{I = \sum_i n_{0i} \exp\left(-\frac{E_i}{kT}\right) exp\left(\left(\frac{-s_i\, k\, T^2}{\beta\, E_i}\right)\left(1-\left(\frac{2kT}{E_i}\right)\right) exp\left(-\frac{E_i}{kT}\right)\right) + a.} \qquad \textbf{(3.3)}$$

To aid in constraining the fits, simultaneous fitting was attempted with data sets of multiple curves. In the non-linear curve fitting, values for each n_o were constrained to be positive, values for each *E* were constrained to 0.5-2.5 eV, and values for each *s* were constrained to 10^8-10^{18} s^{-1}. The values for β were fixed according to the data readout. Fits using no weighting, instrumental weighting (uncertainties given by the standard deviation of three aliquots), and statistical weighting (square root of the intensity) were all attempted. The simultaneous fitting shared *E* and *s* values across each data set while allowing n_o and offset to vary for each curve. The fit quality was determined by the R_{adj}^2 value output, which is the adjusted coefficient of determination (Theil, 1958), by the Origin fitting. This is given as:

$$\boldsymbol{R_{adj}^2 = 1 - \frac{residual\ sum\ of\ squares/(n-p-1)}{total\ sum\ of\ squares/(n-1)}.} \qquad \textbf{(3.4)}$$

Where, *n* is the sample size, *p* is the number of parameters in the fit function excluding an added constant, the total sum of squares is the squared difference between data values and the mean value, and the residual sum of squares is the sum of the square of the residuals. A R_{adj}^2 of 0.995 was arbitrarily chosen as the threshold for fit quality.

OSL curve fitting

Some OSL data were fit using three exponential decay functions and an offset. Multiple curves were fit simultaneously to restrict the fitting using Origin. The fit quality was determined by the R_{adj}^2 value output by the Origin fitting.

When the influence of a shallow trap on the fitting was investigated in Section 6.2.2, the second attempt with the differential equation was solved numerically using the NDSolve function in Mathematica. Fitting was still conducted in Origin to remain consistent.

CHAPTER 4

INITIAL CHARACTERIZATION OF MgB_4O_7:Ce,Li

This chapter presents an initial characterization of $MgB_4O_7:Ce_{0.3\%},Li_{10\%}$, originally identified in the laboratory as a promising OSL material. The goal was to identify issues to be solved and obtain data for comparison with optimized material to be developed. Therefore, we examined basic TL and OSL properties, including the relationship between the TL and OSL signals, the TL, RL, and OSL emission spectra, the OSL excitation spectra, and PL data. Also, we reported the problem of sensitization of the TL and OSL signal and fading of the signal. The results presented in this chapter refer to samples synthesized as described by Doull et al. (2014), using low-purity $Mg(NO_3)_2$.

4.1 ***Basic TL and OSL properties***

4.1.1 TL

A basic TL curve was measured using a 10 mg aliquot, 5 s β irradiation, and readout from room temperature to 450 °C using a heating rate of 1 °C/s. A TL curve of LiF:Mg,Ti was taken as well using the same irradiation and readout, but the sample was 23.8 mg in chip form and a Schott BG-39 filter rather than the Hoya U-340 filter was used. The curves for MBO and LiF can be seen in Figure 4-1.

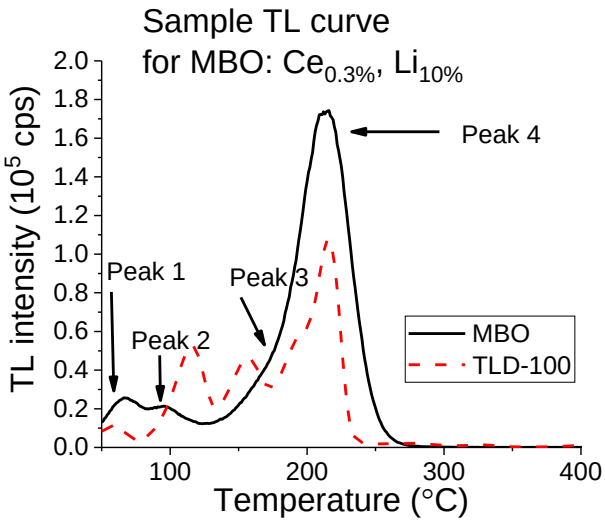

Figure 4-1: Example TL curve of MBO:$Ce_{0.3\%}$,$Li_{10\%}$, measured using Hoya U-340 filters, with the peaks identified. Three peaks (1, 2 and 4) are easy to identify. Peak 3 is a shoulder on the low side of peak 4. The TL from LiF:Mg,Ti (TLD-100, 23.8 mg chip), measure using Schott BG-39 filters, is also shown for comparison.

When doped with Ce and Li, MBO shows a four-peak structure (Figure 4-1). Three peaks are easily discernable, and there is a shoulder on the leading edge of the main peak, which is a fourth peak. This matches what has been reported before (Yukihara et al., 2014b; Yukihara et al., 2017). However, earlier literature for this material used Dy, Mn, or Tm as the dopant, so their curves differ from ours. The TL intensity of MBO:$Ce_{0.3\%}$,$Li_{10\%}$ compared to LiF:Mg,Ti is about 70% more intense despite the larger sample size of the LiF chip. MBO:$Ce_{0.3\%}$,$Li_{10\%}$ was brighter than LiF:Mg,Ti in literature as well (Yukihara et al., 2017). The main peak occurs at ~210 °C. There is a peak present in MBO when doped with Pr, Er, and Gd at the same temperature. This may be an indication that the same trapping center is present in samples doped with these different lanthanides.

4.1.2 OSL

Basic OSL curves of MBO:Ce,Li were measured and compared with Al_2O_3:C readout using the same conditions and shown in Figure 4-2.

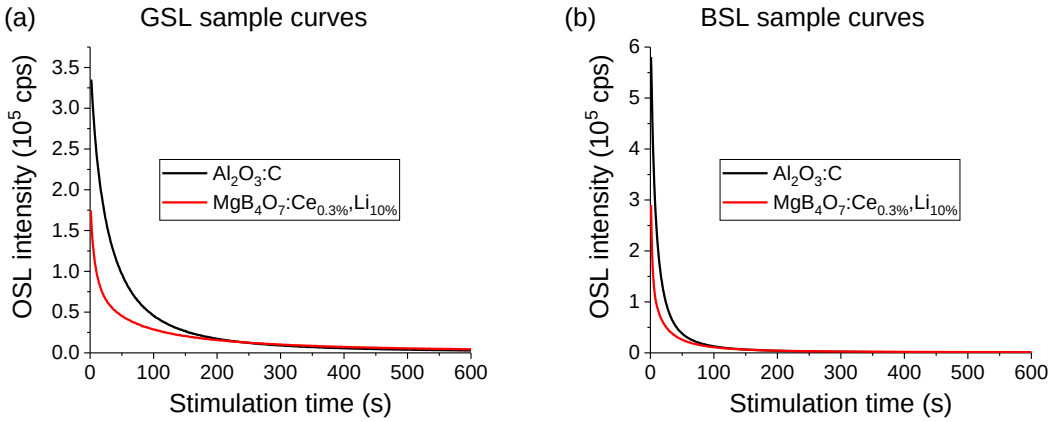

Figure 4-2: OSL curves for single 10 mg aliquots of MBO and Al_2O_3:C. Readout parameters were: 5 s irradiation, 600 s readout, 90% LED power, U-340 filter, and no aperture.

For both stimulations, MBO is about 2-3 times less bright than Al_2O_3. However, the signal may be increased through changes to the synthesis.

4.2 ***Basic luminescence properties***

4.2.1 Radioluminescence

RL data were collected for three 10 mg aliquots of each undoped MBO, MBO:$Ce_{1\%}$, and MBO:$Ce_{0.3\%}$,$Li_{10\%}$. The spectra were collected at room temperature and correspond to the average of five spectra, each obtained with 100 s integration time. A boxcar of 5 was used to smooth the spectra.

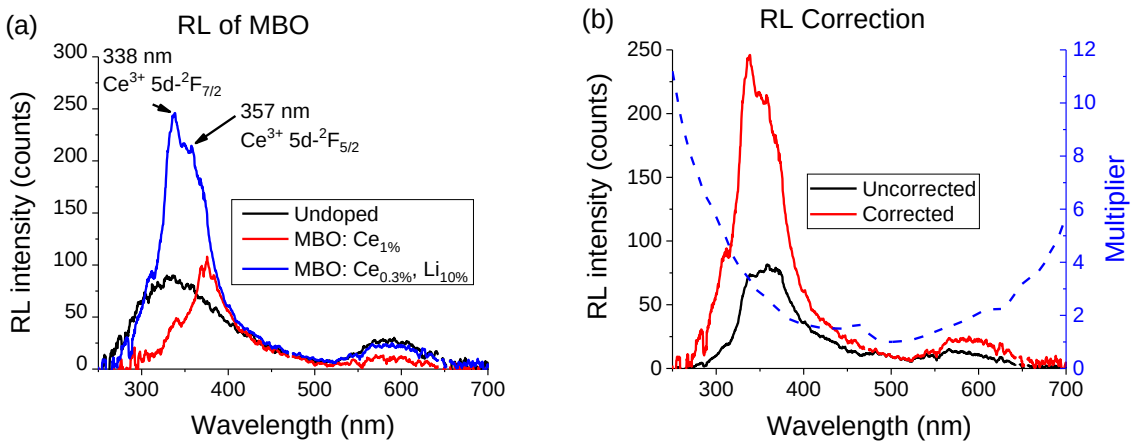

Figure 4-3: (a) RL for 10 mg of undoped MBO, MBO:$Ce_{1\%}$, and MBO:$Ce_{0.3\%}$,$Li_{10\%}$ (experimental details: 100 s integration time, 5 average, 5 boxcar). Ce^{3+} emission or intrinsic emission is observed in the UV region depending on doping. (b) The spectrometer efficiency correction used is shown on the bottom and right axes. The impact of that correction is shown for MBO: $Ce_{0.3\%}$, $Li_{10\%}$.

The undoped sample of MBO shows an intrinsic UV emission, at ~340 nm, from an unknown emission center probably related to an intrinsic defect, and another at ~580 nm which is likely due to Mn^{2+} contaminants (Yukihara et al., 2014b). If Ce^{3+} is introduced, the RL starts to show a two-peak structure in the UV rather than the broad intrinsic band, but the emission at ~580 nm remains. Finally, for the codoped sample, MgB_4O_7:$Ce_{0.3\%}$,$Li_{10\%}$, two emission bands are observed (Figure 4-3a): one at ~350 nm and another at ~580 nm. The UV band (~350 nm) consists of 5d-4f transitions in Ce^{3+}. These transitions are much brighter and sharper with the addition of lithium as a codopant, since lithium helps Ce^{3+} enter the lattice through charge compensation or some other mechanism. The band at ~580 nm is most likely emission from Mn^{2+} (Yukihara et al., 2014b). The emission is likely d-d transitions $^4T_1$-$^6A_1$, and since the emission is yellow, the Mn^{2+} is tetrahedrally coordinated (Blasse and Grabmaier, 1994), which would mean it

is substituting in at a magnesium site. Also, the addition of lithium increased the UV emission, whereas cerium only resulted in a reshaping of the UV emission band.

As mentioned in Section 3.2.4, the data were corrected for the efficiency of the spectrometer. A comparison of uncorrected and corrected RL for MBO:$Ce_{0.3\%}$,$Li_{10\%}$ is shown in Figure 4-3b. Thus, at room temperature, more Ce^{3+} emission was observed than Mn^{2+} for the doped samples.

4.2.2 TL emission spectrum

TL emission data were obtained for 10 mg aliquots, 1000 s β irradiation (~70 Gy), and a 5 °C/s heating rate (see Section 3.2.3). The spectrometer acquired one spectrum per second. A boxcar of 20 was used because of the weak TL intensity and consequent high noise in the data.

TL emission data (Figure 4-4) shows the same emission bands observed in RL: one around 350 nm caused by Ce^{3+} and another around 550 nm attributed to Mn^{2+}. Figure 4-4a shows the contour plot of the TL emission, and Figure 4-4b, the emission spectra at different temperatures during the TL measurement. The main dosimetric TL peak appears at ~250 °C in this measurement because of the higher heating rate (5 °C/s) than that used to obtain the data in Figure 2-5.

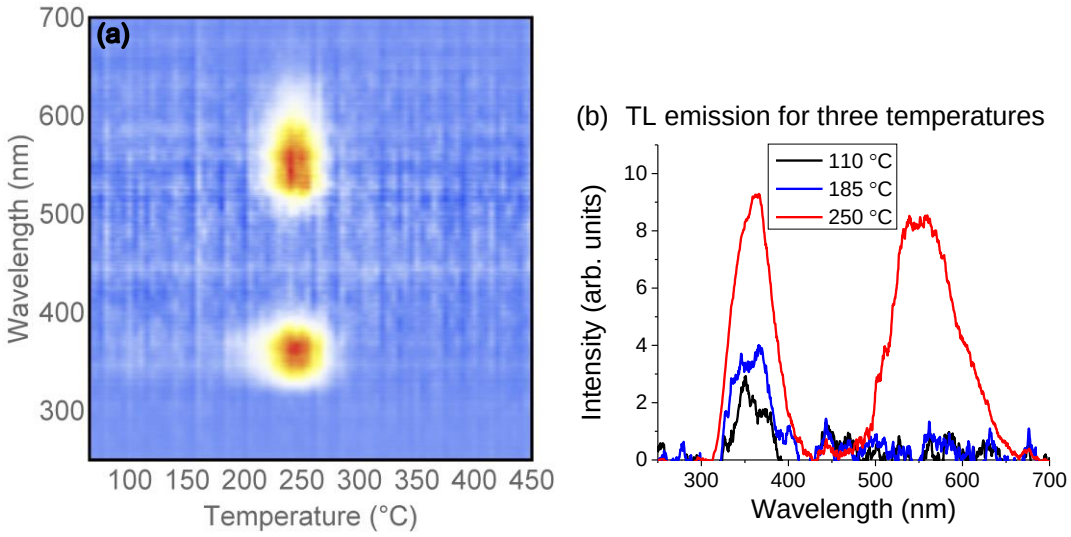

Figure 4-4: TL emission collected for 10 mg of MBO:$Ce_{0.3\%}$,$Li_{10\%}$ after irradiation for 1000 s. Heating rate of 5 °C/s, integration time 1 s, boxcar 20, average 1. The spectra collected have been corrected for the spectrometer efficiency. (a) Contour plot of the TL emission. (b) TL emission spectra at various temperatures.

Both Ce^{3+} and Mn^{2+} bands appear associated with the main dosimetric TL peak, indicating that defects associated with these two dopants act as recombination for the same type of charge carrier. With the use of a U-340 filter, any Mn^{2+} emission is 'lost' from the signal readout in TL or OSL since it is outside the transmission wavelengths of the filter.

Comparison of the TL emission with the RL emission shows three major differences. First, the relative intensities of Ce^{3+} and Mn^{2+} differ between the TL and the RL spectra. Since the same spectrometer/optic fiber and correction for the spectrometer were used for both RL and TL emission measurements, the lower Ce^{3+} emission relative to Mn^{2+} emission in the main TL peak may point to thermal quenching of the Ce^{3+} recombination center. Second, the two-peak structure of the Ce^{3+} emission is obscured in the TL emission plots. This is likely due to the use of a 20-boxcar smoothing and not an actual phenomenon. Lastly, the Mn^{2+} emission is shifted to lower wavelengths for the TL

emission relative to RL. This was observed by Yukihara et al. (2014b), also. The authors demonstrated that this was due to the temperature-dependent wavelength of the emission, verified by measuring the RL at elevated temperatures.

4.2.3 OSL stimulation and emission spectra

For OSL stimulation, emissions at 335 nm and 355 nm, corresponding to Ce^{3+} emissions, were monitored while scanning the stimulation wavelength from 405 nm to 580 nm at 1 nm step size using 0.2 s integration time. The stimulation slit was set to 3 nm bandpass and the emission slit was set to 10 nm bandpass. A 3 mm thick Schott GG-400 long-pass filter was used on the stimulation window to prevent stimulation from the second-order harmonics of 200-300 nm. Five scans were taken with the sample mounted, before irradiation, and the average of those five readouts was used for background subtraction. Then, the sample was irradiated with 1000 Gy. This high dose was needed to ensure emission of enough intensity. The stimulation range was scanned 5 times to verify if the signal remains constant or decreases with each readout. An OSL signal will reduce with light exposure, allowing it to be differentiated from any other luminescence. A 3-point moving average smoothing was used to smooth the spectra.

The OSL stimulation spectra corrected by the reference photodiode (S/R) are shown in Figure 4-5. For both emissions, the stimulation increases as the wavelength decreases. This is intuitive since higher energy photons have a higher probability to cause detrapping (and consequent recombination) than lower energy photons (see Section 2.1.2). Also, no distinct stimulation bands are seen, which suggests that OSL happens through the conduction band rather than direct, localized transitions.

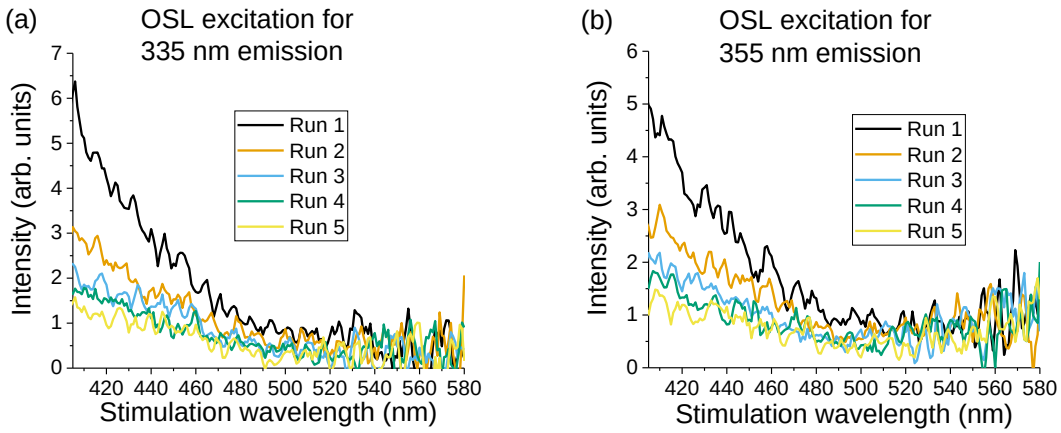

Figure 4-5: OSL excitation for (a) 335 nm and (b) 355 nm emission following 1000 Gy irradiation. All spectra are shown following background subtraction (the average of 5 readouts before irradiation).

As the two options for LED stimulation in the Risø readers are 470 nm and 525 nm, those stimulations for Ce^{3+} emission were compared in the OSL excitation data. A stimulation of 470 nm results in brighter emission than 525 nm for both Ce^{3+} transitions. Thus, the readout procedure for this material can be optimized by using blue stimulation (470 nm) instead of green stimulation (525 nm).

Since 470 nm resulted in more intense Ce^{3+} emission than 525 nm, 470 nm stimulation was used to measure the OSL emission spectra. The emission spectra were measured for wavelengths shorter (300-400 nm with a 1 nm step size using 0.2 s integration time and both slits 10 nm bandpass) and longer (500-750 nm with a 5 nm step size using an integration time of 0.2 s and 10 nm bandpass slits) than the stimulation wavelength. Each scan was repeated 5 times to observe the decrease in the signal, which confirms that the signal is OSL rather than PL. Readouts were done following 1000 Gy irradiation of the sample and with a Schott GG-400 filter on the excitation window to prevent excitation of the sample by the second-order harmonic of 235 nm. The average

of 5 readouts taken prior to irradiation were used as the background and subtracted from the other curves. The resulting curves were smoothed using a 3-point moving average.

Figure 4-6 shows the OSL emission spectra corrected by the reference photodiode (S/R) over the 300-400 nm wavelength range, with 470 nm stimulation. Since the emission spectra are collected by scanning a monochromator while constantly stimulation the material, distortion in the spectrum could be present. No emission was observed in longer wavelength regions, so data are not included here.

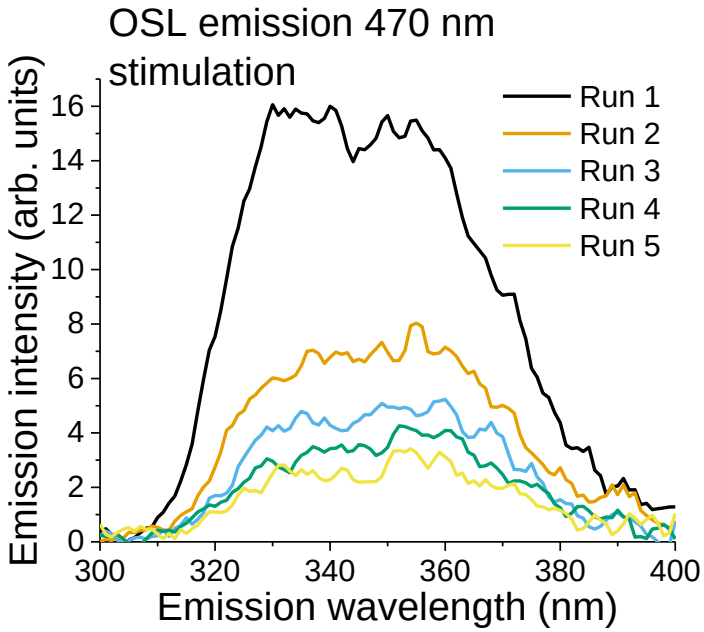

Figure 4-6: OSL emission for blue stimulation (470 nm) following a dose of 1000 Gy. For the lower wavelength portion (300-400 nm), slits were set to 10 nm, and the scanning step was 1 nm with 0.2 s of integration time. A Schott GG-400, 3 mm thick, long-pass filter placed on the stimulation window blocked excitation from the lamp at 235 nm.

The observed OSL emission is consistent with Ce^{3+} emission, showing two bands 1900 cm^{-1} apart. In the UV, the energy difference is about 20 nm in wavelength. For OSL emission, one OSL emission band is present in the lower region centered at about 335 nm,

Ce^{3+} 5d-$^2F_{7/2}$, and another at about 355 nm, Ce^{3+} 5d-$^2F_{5/2}$. The reduction in OSL intensity again attests for the OSL nature of the measured signal.

4.2.4 Photoluminescence signal

PL data were collected for emission and excitation regions of interest. PL excitation spectra were collected for MBO:$Ce_{0.3\%}$,$Li_{10\%}$ at emissions of 330 nm, 340 nm, 350 nm, 360 nm, and 370 nm. For these emissions, the excitation wavelength was scanned from 220 nm to 10 nm less than the emission wavelength. Stimulation spectra (scan from 220 nm to 340 nm) were collected for undoped MBO for emission of 360 nm as well. The low intensity of the undoped sample required the scan to be halted further from the excitation wavelength to prevent scattering from artificially increasing the detected light. For all scans, a step size of 0.5 nm was used and an integration time of 0.5 s. The excitation slit was set to a 1.4 nm bandpass and the emission slit was set to 10 nm bandpass. No optical filter is needed. At these low wavelengths, not enough light is scattered to the reference photodiode. Thus, these spectra are the detected signal from the PMT without correction for the excitation lamp spectrum.

PL excitation/emission spectra for undoped MBO are shown in Figure 4-7. The sample shows weak excitation around 300 nm for emission of 360 nm. This excitation band is so weak, that it may be simply an instrumental artifact (scattered light). The emission spectrum shows no clear band for 320 nm stimulation.

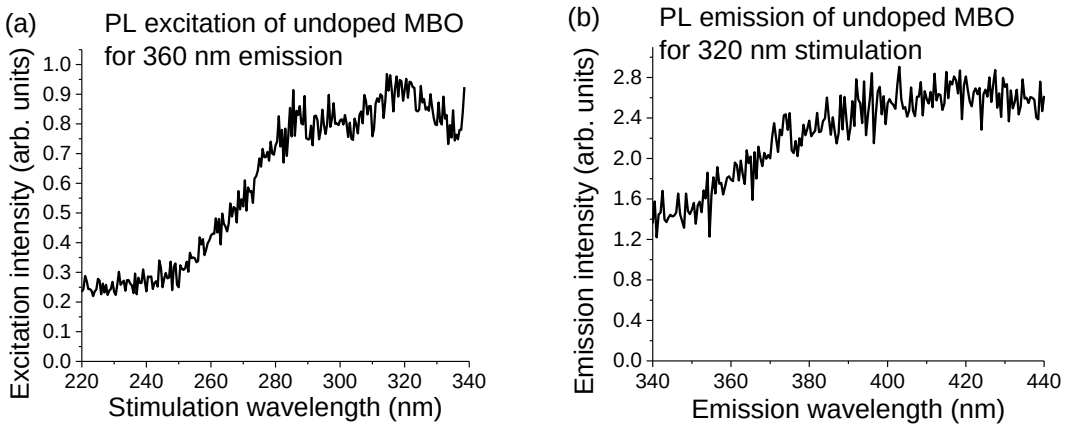

Figure 4-7: PL (a) excitation and (b) emission spectra for undoped MBO.

Excitation/emission spectra for MBO:$Ce_{0.3\%}$,$Li_{10\%}$ are shown in Figure 4-8. MBO:$Ce_{0.3\%}$,$Li_{10\%}$ shows one narrow excitation peak for all emissions at about 320 nm and one broad peak (FWHM ~40 nm) centered at about 285 nm (Figure 4-8a). For cerium, it is expected that five 5d transitions are observable. The lower energy group will form as a triplet and a doublet will form at a higher energy. It is possible that the broad peak is two peaks (~295 nm and ~270 nm) or could be charge transfer to the conduction band.

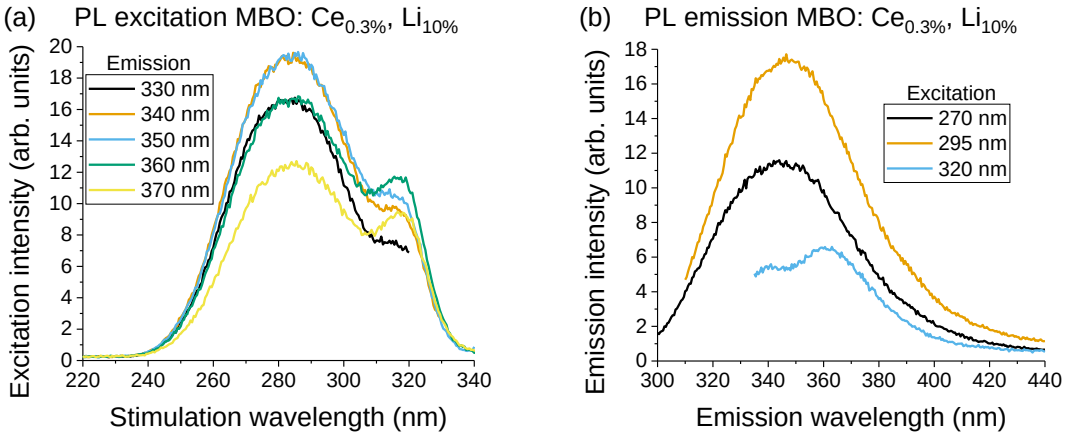

Figure 4-8: PL (a) excitation and (b) emission spectra for MBO:$Ce_{0.3\%}$,$Li_{10\%}$.

The PL emission spectra show varying behavior with different excitation (Figure 4-8b). Exciting with 320 nm, thought to be the lowest 5d state, results in the characteristic two peak Ce^{3+} emission with peaks at 340 nm and 360 nm. Exciting with shorter wavelengths results in a broad (FWHM ~60 nm) emission. As this broad emission and excitation is not seen for the undoped sample, it is most likely due to Ce^{3+}. Charge transfer bands usually are broad, so this remains a possible explanation of this band.

Overall, the Ce^{3+} emissions from RL, TL emission, and OSL emission agree with each other. The undoped material shows an intrinsic UV emission from an unknown recombination center in RL data. The doped material showed Ce^{3+} emission as the dominant emission for all techniques: RL, PL emission, TL emission, and OSL emission. The Ce^{3+} emission in the TL emission shows as one peak due to the heavy boxcar averaging. Mn^{2+} emission is observed in RL and TL emission data though not OSL emission. There is a discrepancy between RL and TL emission for Mn^{2+} by about 40-50 nm which can be attributed to the readout temperature as in Yukihara et al. (2014b).

For stimulation, the OSL intensity showed a typical increase with decreasing stimulation wavelength. PL showed the first 5d state clearly at 320 nm, which indicates a Stoke shift of ~0.174 eV. However, the next excitation band is broader than expected for a 5d energy state and does not show Ce^{3+} 5d-4f emission when stimulating from this band. This band most likely is photoionization from Ce^{3+} to the conduction band.

4.3 ***Dosimetric properties***

4.3.1 Reproducibility

The first of three studies examining the dosimetric properties looked at the reproducibility of TL or OSL (with both blue and green stimulations) readouts.

To investigate the TL reproducibility, three 10 mg aliquots of material were subjected to 10 cycles of 5 s irradiation followed immediately by TL readout to 450 °C at 1 °C/s.

For each readout, we calculated the total and maximum TL intensity. The intensities were normalized to the first run intensity. Then, the three aliquots were averaged, and the standard deviations were calculated. TL curves for the 10 cycles are presented in Figure 4-9a. The TL area and main peak maximum are shown for the average of three aliquots in Figure 4-9b. No background subtraction was done.

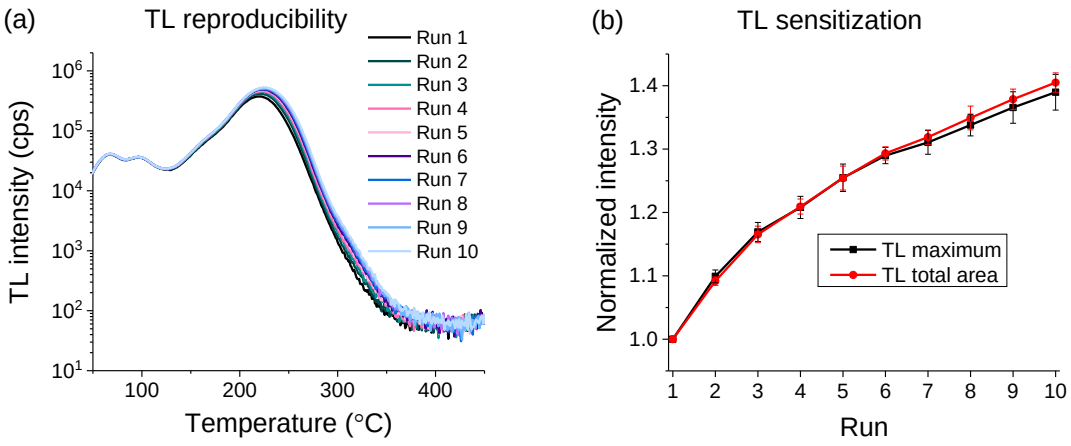

Figure 4-9. (a) Example TL glow curves for repeated irradiation, 5 s, and readout for 10 mg of material from one aliquot. (b) TL area and TL maximum intensity normalized to run 1. The average of three aliquots is presented with error bars indicating the experimental standard deviations of those three aliquots.

Both TL area and maximum increased by ~40% over 10 irradiation/readout cycles. Looking at Figure 4-9a, one can see that most of this sensitization occurred in the main TL peak. The low temperature TL peaks stay relatively constant. The TL sensitization appears to decrease with repeated readout cycles. However, it is unclear from these data

what the mechanism may be. This sensitization will be investigated in more detail in Section 6.1.

Similarly, the OSL reproducibility was investigated subjecting three 10 mg MBO aliquots to cycles of 5 s irradiation with the beta source followed by 600 s OSL readout with either blue or green LED stimulation, BSL and GSL respectively, at room temperature. No heating was done between readouts. GSL and BSL curves obtained for single aliquots are shown in Figure 4-10a and b.

The total and initial (average of first 5 data points) OSL intensity were calculated for each readout. Three aliquots were normalized to their first run intensities. Then, they were averaged, and standard deviations were calculated for the normalized intensities. OSL total areas and initial intensities for both stimulations are presented in Figure 4-10c. No background subtraction was conducted.

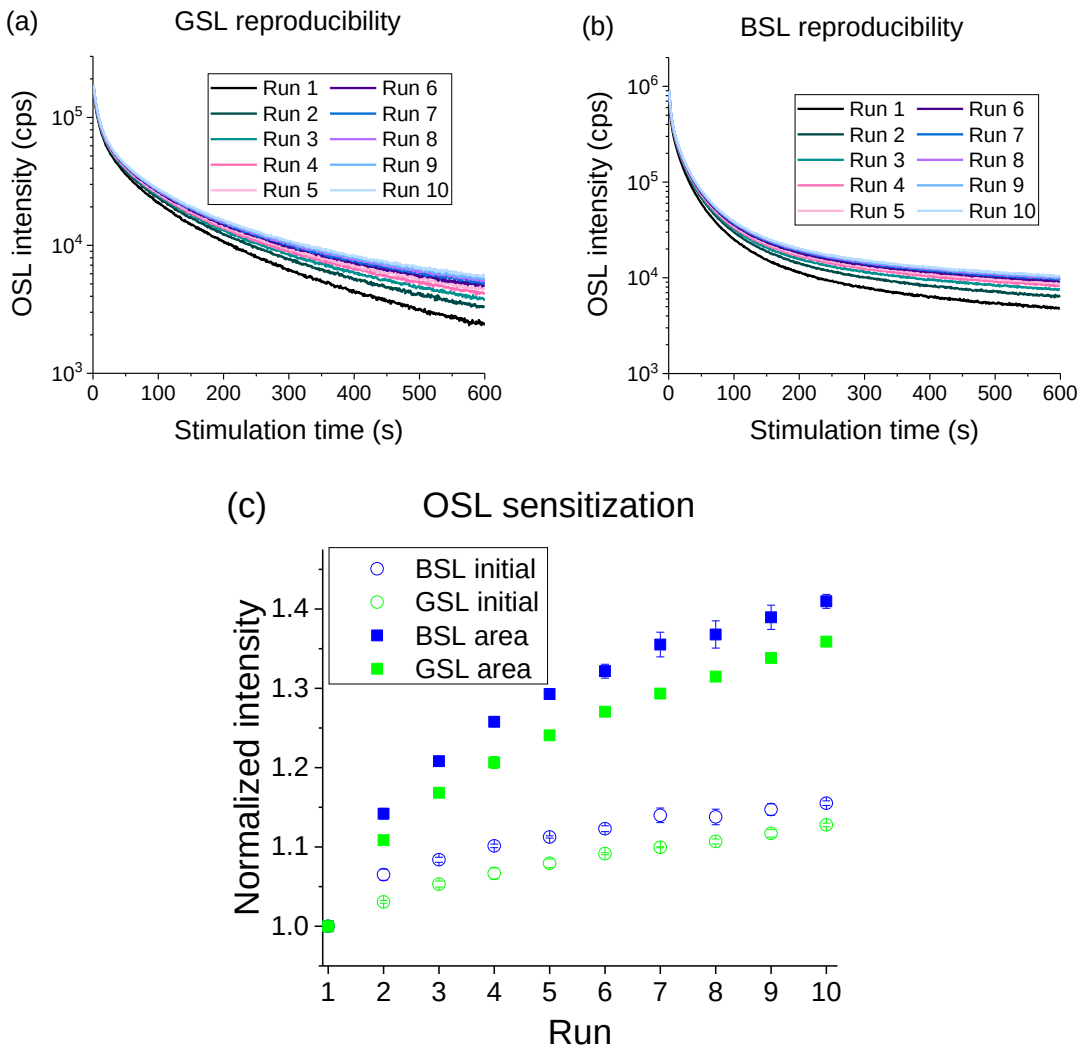

Figure 4-10: Curves for repeated irradiation and readout of (a) GSL or (b) BSL for single aliquots. (c) The sensitization of the initial intensity and total OSL area normalized to run 1. The average of three aliquots is presented with error bars showing the standard deviation between the three aliquots. Readout parameters were: 5 s irradiation, 90% LED intensity, U-340 filter, no aperture, and 10 mg aliquots.

The OSL showed less sensitization than the TL. GSL shows the initial intensity increasing by ~13 % and the total area increasing by ~37 % over the 10 irradiation/readout cycles. BSL shows the initial intensity increasing by ~16 % and the total area increasing

by ~41 % over 10 cycles. For both types of stimulation, the initial intensity sensitizes less than the total OSL area.

To gain further understanding of the components sensitizing, simultaneous fits were performed on the raw data using three exponential decay curves and an offset for each aliquot. Example fits and their residues for run 1 and run 10 of single aliquots are shown in Figure 4-11.

The fits do not seem to describe the behavior of the curves despite R^2 values of over 0.99. The residuals show an organized structure, which suggests that there may be a contribution from a component not described by an exponential decay. The offset is clearly too high and may be trying to help compensate for a component that has a delayed decay. The longest decay component may be trying to fit this unknown component as well. A phototransfer could explain a slight increase of a component and delayed decay. However, these are the wrong data to comment on mechanism or modified line shape. At this point, the fits are sufficient for comparing area contributions but nothing more.

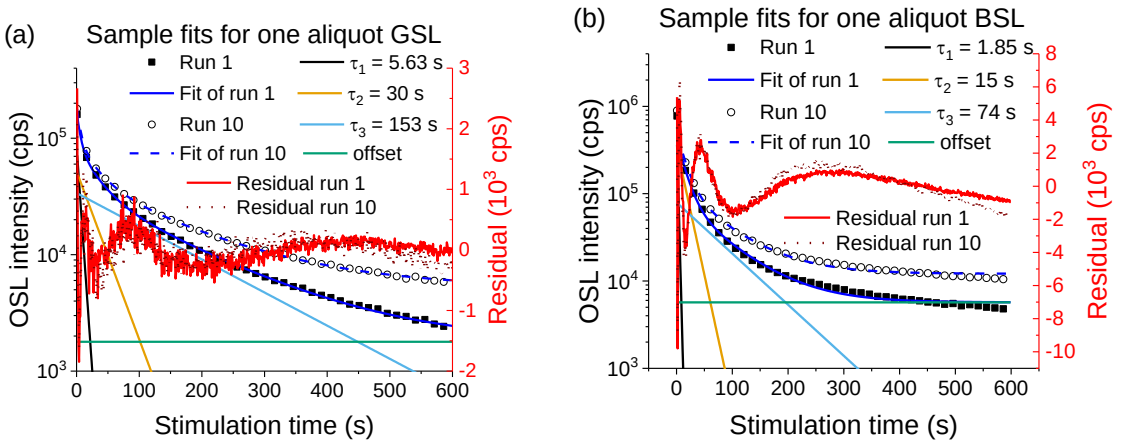

Figure 4-11: Results of simultaneous fitting of reproducibility data with three exponentials for (a) GSL and (b) BSL. The curves and residues presented are for the first and last readouts using either green or blue stimulation.

The areas of the decay components and offset integrated area are presented over 10 cycles. These results are shown in Figure 4-12. The error bars presented are the experiment standard deviations of amplitudes found for three aliquots. The offset shows the most sensitization (a factor of 2-3) over the 10 cycles. As the offset contributes greatly to the integrated OSL signal, the offset is likely the source of the sensitization in this material. An increase in the offset could be due to incomplete bleaching of traps, but the mechanism will be explored in detail in Section 6.1.

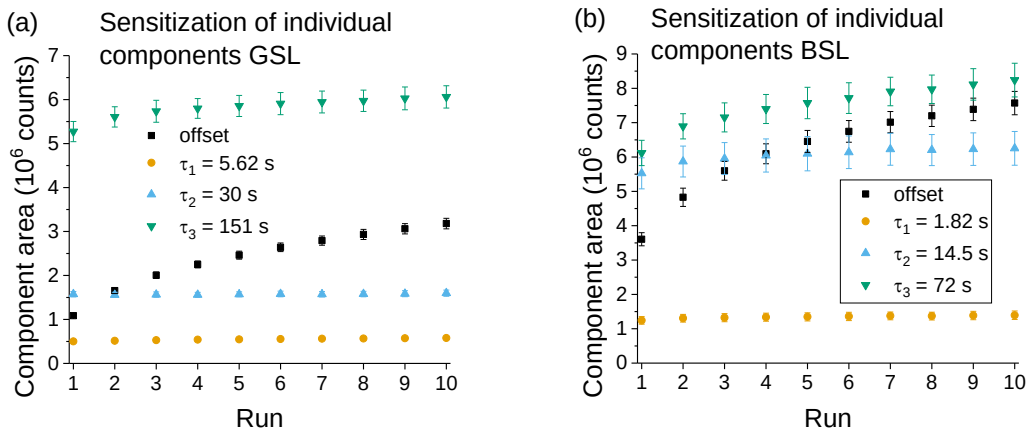

Figure 4-12: The decay component areas from the simultaneous fittings of sensitization data for (a) GSL and (b) BSL. Error bars show the standard deviation for three aliquots.

4.3.2 Dose response

The second dosimetric study looked at MBO's dose response. For each readout modality (TL, BSL, and GSL) three 10 mg aliquots were prepared. Each aliquot was irradiated for 1, 2, 5, 10, 20, 50, 100, 200, 500, and 1000 s and read out going from lowest dose to highest dose. Like in the reproducibility study, TL area and maximum were calculated for each curve. Similarly, OSL initial intensity and area were calculated for each curve. Those intensities were averaged across three aliquots and the standard deviation

was calculated. OSL data were fitted simultaneously with three exponential decay components and an offset. Fewer decay components resulted in poor fits. The three time constants were shared between all curves, but the offset and amplitudes were permitted to vary with each curve.

TL curves of MBO:$Ce_{0.3\%}$,$Li_{10\%}$ were obtained for doses from 0.1 Gy to 100 Gy. An 8 mm aperture was used in front of the PMT to protect it from excess light at high doses. Sample TL curves are shown in Figure 4-13a, and those curves normalized to their maximum intensities are shown in Figure 4-13b.

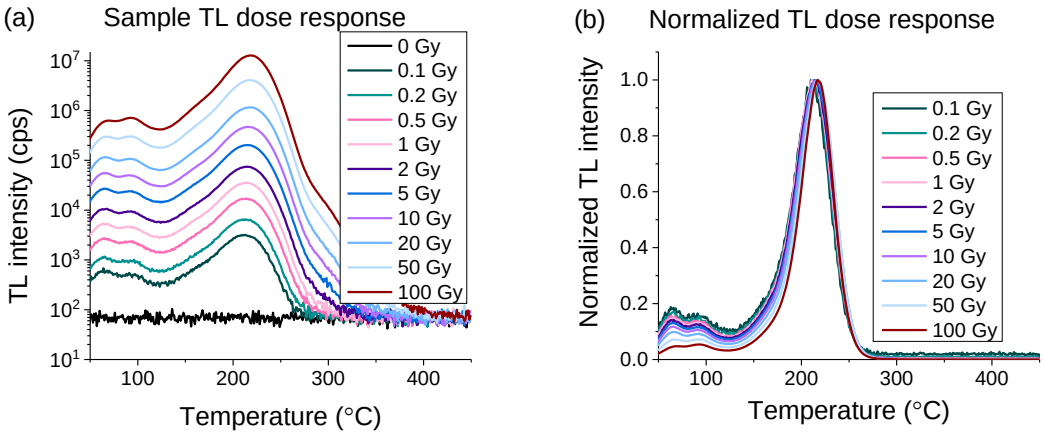

Figure 4-13: (a) TL curves for a 10 mg aliquot of MBO:$Ce_{0.3\%}$,$Li_{10\%}$ for various doses. (b) Same as in (a) but normalized to the maximum intensity of each curve. All readouts use a heating rate of 1 °C/s, an 8 mm aperture, and a U-340 filter. The main TL peak shows first-order kinetics, as the peak does not shift with varying dose.

One can see that the TL peaks remain at approximately the same position with a 1000-fold increase in dose, which supports the interpretation of the TL processes as first-order kinetics. The relative decrease of the intensity of low temperature peaks (50-120 °C) compared to the main peak is related to simultaneous fading of those TL peaks that occurs as irradiation is taking place.

The dose response for the TL maximum and total TL area are shown in Figure 4-14. No background subtraction was done. Dashed lines are provided to show the background plus 3σ of the 0 Gy readout maximum intensities and total areas for 3 aliquots where σ is one experimental standard deviation of three aliquots.

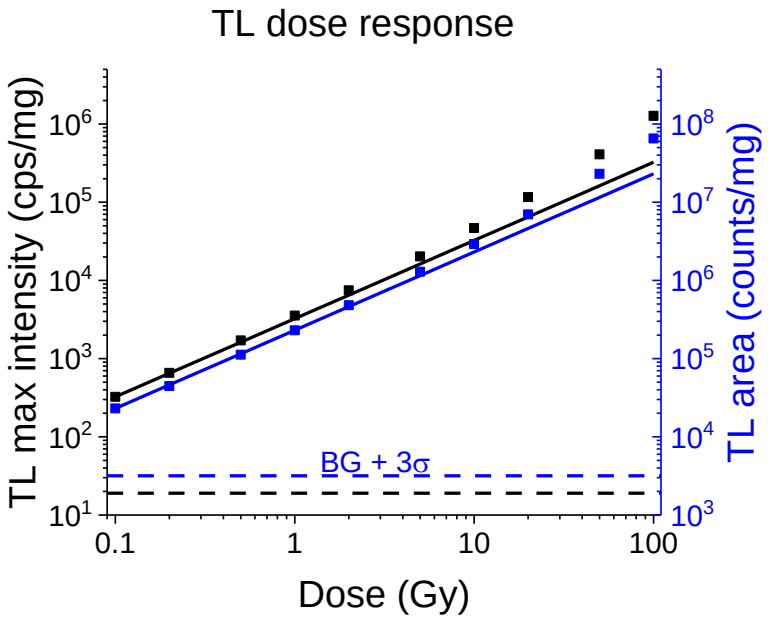

Figure 4-14: Dose response for TL maximum intensity and TL total area with no background subtraction. The solid lines show linear behavior from the lowest dose. Each data point corresponds to the average values for three samples, scaled by each aliquot's mass. Error bars were used to represent the standard deviation of the data, but they are too small to be seen on these scales. BG + 3σ show the average max intensity/TL area for 3 aliquots plus three standard deviations of those three aliquots for 0 Gy dose readouts.

The TL maximum intensity and total TL intensity are linear for low doses becoming supralinear at around 10 Gy (Figure 4-14). It is possible that the supralinear behavior may be related to the sensitization observed in the previous Section. It is anticipated that at higher doses the response will saturate and turn sublinear, as is typical of many materials.

However, the onset of saturation was not observed for MBO:$Ce_{0.3\%}$,$Li_{10\%}$ for the maximum dose used (~100 Gy). The TL for Al_2O_3:C saturates at 30 Gy and BeO saturates at 1 Gy (McKeever et al., 1995).

For GSL, the data were obtained using an 8 mm aperture for the entire dose range. However, BSL benefitted in changing the aperture size when reaching a dose of 1 Gy. For the 0.1 Gy - 1 Gy dose range, no aperture was used. Then, for the 1-100 Gy we used a 4-mm aperture. The duplicate measurement at 1 Gy provided a scaling factor for the 1-100 Gy range, allowing the intensities to be reported as if no aperture had been used. Sample curves are presented for both GSL and BSL in Figure 4-15. The dose responses of the initial intensity and total OSL area with no background subtraction are presented in Figure 4-16. Dashed lines show the background plus three times the experimental standard deviations for the 0 Gy readouts of three aliquots for both initial intensity and total area.

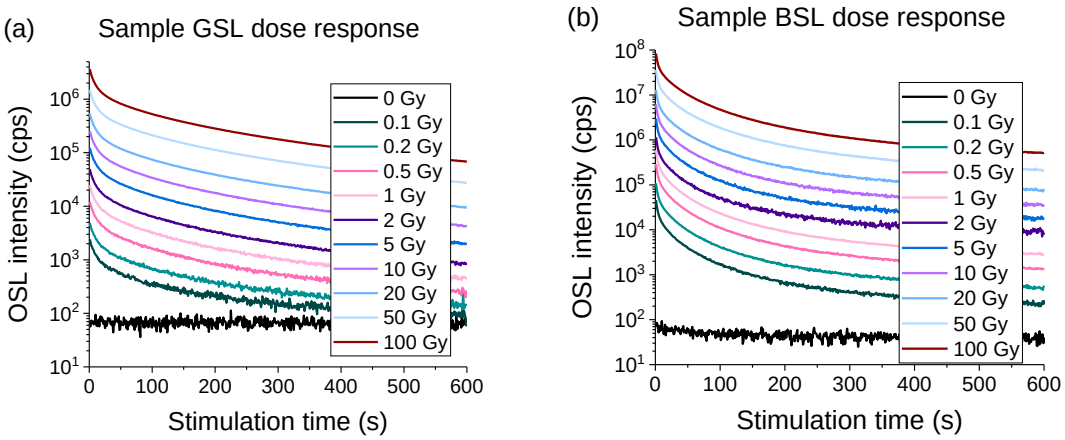

Figure 4-15: (a) GSL and (b) BSL dose response for single aliquots of MBO:$Ce_{0.3\%}$,$Li_{10\%}$. All readouts used 10 mg of material and a U-340 filter.

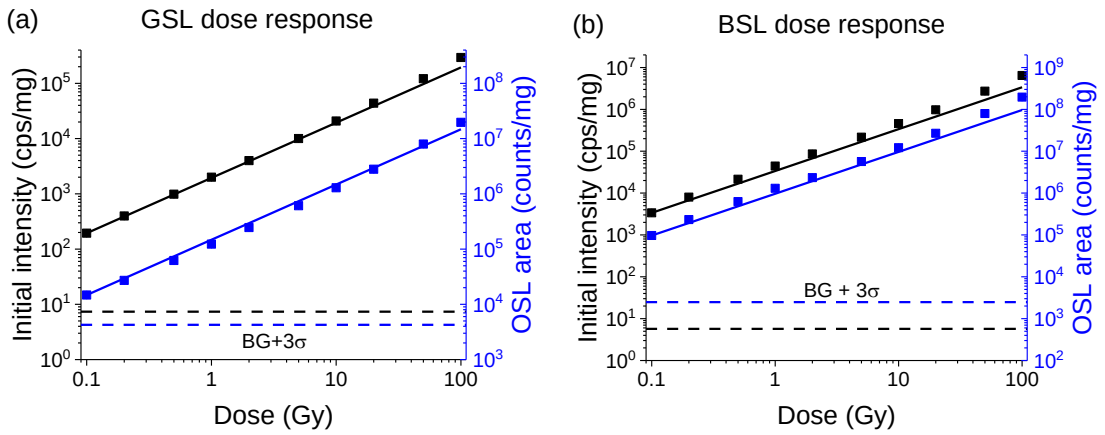

Figure 4-16: (a) GSL and (b) BSO dose response for OSL initial intensity and OSL total area with no background subtraction. The solid lines show the linear behavior from the first data point. Each data point corresponds to the average values for three samples, scaled by each aliquot's mass (10 mg). Error bars were used to represent the standard deviation between three aliquots, but they are too small to be seen on these scales. Dashed lines show the 0 Gy background + 3σ of that background for each initial OSL intensity and total OSL area.

Like TL, the dose response for the initial intensities is linear for low doses for both GSL and BSL. The OSL area for GSL showed sublinear behavior in the low dose region before becoming supralinear at 50 Gy. The area for BSL was supralinear from 0.2-2 Gy, linear to 10 Gy, becoming supralinear above 10 Gy. The low dose supralinearity may be due to the sensitization of the aliquots, since samples were reused. For both initial intensities, the dose response became supralinear above 20 Gy. No saturation was observed, which is an improvement over Al_2O_3:C.

In this Section, it was shown that the OSL dose response does not saturate at doses up to 100 Gy. This is a large improvement over Al_2O_3:C. The dose response was linear up to 50 Gy for the total OSL area of both GSL and BSL. The initial intensity for BSL was linear up to 100 Gy, the highest dose tested. The offsets and longer lifetime components were linear up to lower doses that the shorter lifetime decay components.

4.3.3 TL/OSL dark fading

The final dosimetric study measured the dark fading of the TL and OSL signals for varying durations of time following irradiation. Since sensitization was a known problem from the reproducibility study, three 10 mg aliquots were prepared for each dark fade time for each measurement type (TL, BSL and GSL). Aliquots were irradiated for 5 s and allowed to sit in dark for 0, 0.5, 1, 2, 5, 10, 15, 24, 48, 72, or 144 h. Then, their TL or OSL was measured. Following that readout, the aliquots were irradiated with a reference dose of 5 s β and read out. The maximum intensity of the reference dose curves (each TL and OSL) were used to normalize the faded curves to account for any mass fluctuations. Care was taken to stagger the irradiations and readouts of aliquots so that the three aliquots for each fading duration would experience the same fading time. The TL maximum and area were tracked as in the previous two studies. OSL area and initial intensity were tracked as in the previous two studies.

Example curves are shown in Figure 4-17a, and the TL maximum, from the main peak $T_{max} \approx 210$ °C, and total TL area normalized to reference dose and renormalized to the 0 h fading time readout are shown in Figure 4-17b. This allows the effect of sensitization to be isolated from the fading.

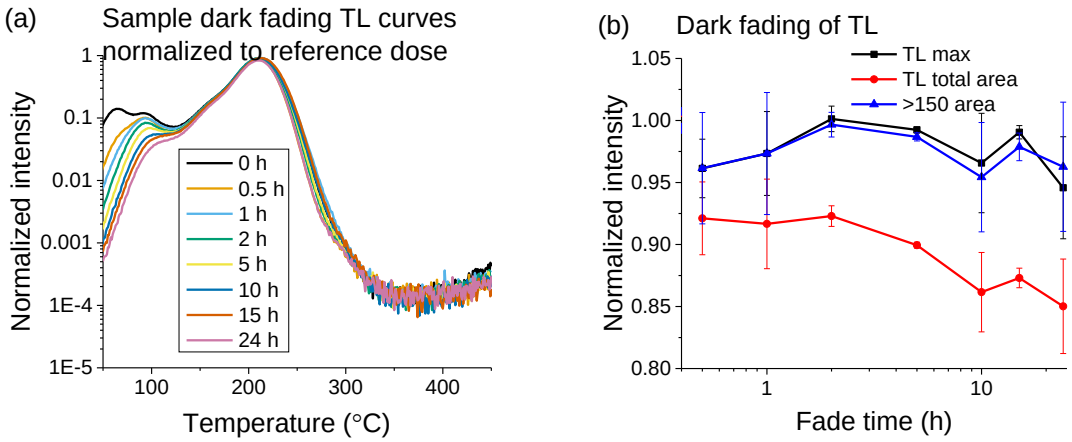

Figure 4-17: TL dark fading for 10 mg material, 0.5 Gy, and normalized to the TL signal after a reference dose (no delay between irradiation and readout). (a) Sample dark faded TL curves normalized to reference dose. (b) TL maximum, TL total area, and area above 150 °C normalized to reference dose and renormalized to the 0 h fading. Error bars show the standard deviations of three aliquots.

TL dark fading showed strong stability in the main dosimetric peak as expected for a peak at T_{max} ≈ 210 °C. The total TL area was less stable due to fading of the low temperature peaks and the shoulder of the main dosimetric peak. The high temperature region, 151-450 °C, remains constant from 0 h to 24 h.

BSL and GSL dark fading were collected for each the initial intensity and area without reusing aliquots. Example curves normalized to the maximum of a reference dose readout are shown for each stimulation in Figure 4-18a and b. The initial intensities and total area normalized to reference dose readouts then renormalized to the 0 h dark fading for each sample are shown in Figure 4-18c and d.

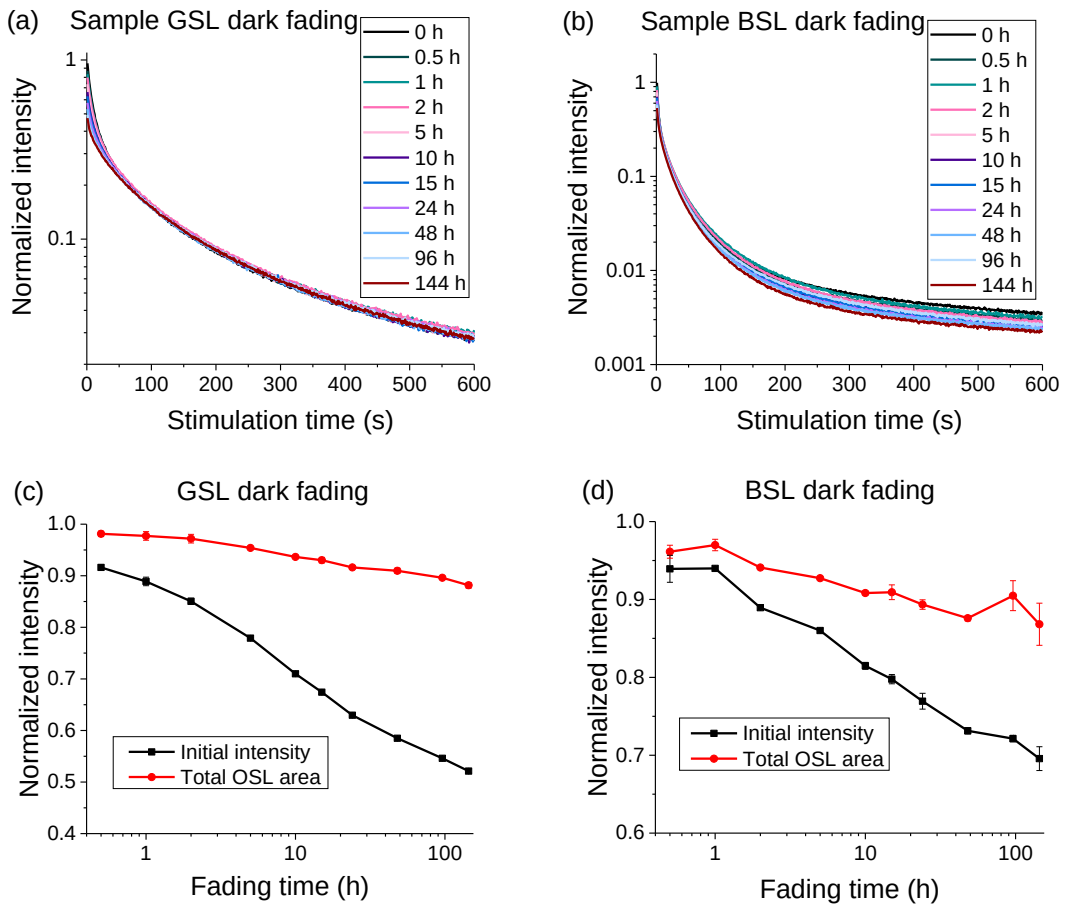

Figure 4-18: OSL dark fading for 10 mg aliquots irradiated with 0.5 Gy. Sample curves normalized to reference readouts are shown for (a) GSL and (b) BSL. Initial intensity and total OSL area normalized to reference dose and renormalized to 0 h are shown for (c) GSL and (d) BSL. Dashed lines show the normalized intensity of a 0 h fade time readout. Error bars show the standard deviations of three samples.

Both stimulations show substantial fading over 144 h. The GSL initial intensity fades to 52% from 0 h to 144 h after irradiation, and the total OSL area fades to 88% from 0 h to 144 h after irradiation. For BSL, the initial intensity fades to 70% from 0 h to 144 h of fading, and total OSL area fades to 87% from 0 h to 144 h of dark fading. The OSL total

area fades the same for both stimulations, but the initial intensity fades more for GSL over 144 h. The fading observed for both stimulations is larger than that from BeO, 6% in 0.5 h then no change for 6 months (Sommer et al., 2007), and Al_2O_3:C, none observed at room temperature for 100 d (Bøtter-Jensen et al., 1997).

Like before with dose response and sensitization, simultaneous fits using three decay components were conducted on the OSL curves. The integrated areas of the decay components are presented in Figure 4-19.

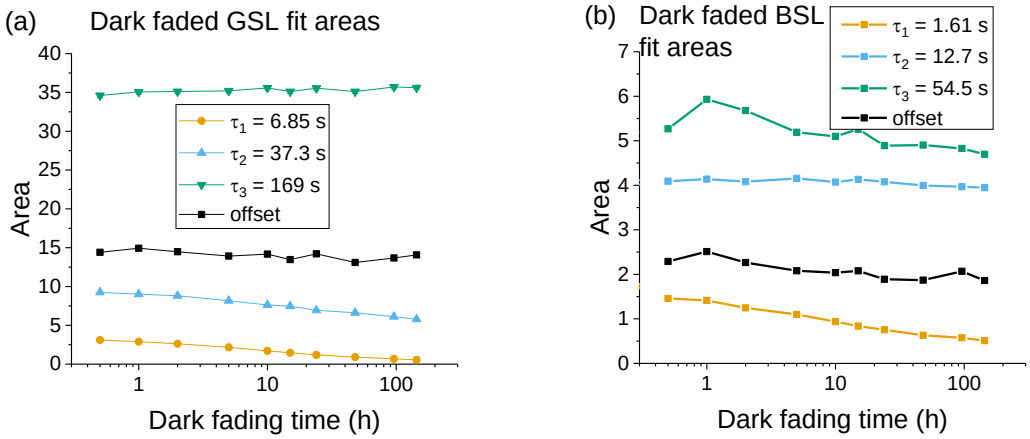

Figure 4-19: Integrated areas of decay components for dark faded (a) GSL and (b) BSL. Error bars show the standard deviations of the amplitudes for three aliquots though are too small to see.

Examining the integrated areas of the decay components gives additional information as to the stability of different traps detrapping. For GSL, the offset remains constant over 144 h, the two shorter lifetime decay components, 6.85 s and 37.4 s, fade with time, and the long lifetime component, 169 s, stays constant. For BSL, the offset and the short lifetime component, 1.61 s, fade over 144 h, but the longer lifetime components, 12.7 s and 54.5 s, are stable.

Overall, dark fading was observed for all measurements. The TL showed heavy fading in the low temperature region, but the high temperature peaks were stable over

24 h. As for OSL, the short lifetime component, which is responsible for most of the initial intensity, fades greatly. This could be an evidence that the short lifetime components correlate with shallow traps that occur at low TL temperatures. This is investigated further in the next Section. The longer lifetime components of OSL are stable up to 144 h. The total OSL area shows much less fading because of the large contribution of the long lifetime components. The initial fading might be diminishable with a preheating or other modification to the readout procedure that would remove the low temperature peaks immediately, so they do not cause perceived fading.

4.4 ***Correlation studies between TL and OSL***

The first correlation study looked at the thermal stability of the OSL signal. This was done by irradiating aliquots for 5 s and pre-heating at 1 °C/s up to a T_{stop} varying from 50 °C to 450 °C in 50 °C intervals. After the pre-heating, the OSL was measured for 600 s, when the aliquot had returned to room temperature. Like the dark fading study, three aliquots were prepared for each T_{stop} to prevent sensitization from confounding the results. Following the OSL readout, a TL readout (T_{stop} = 450 °C at 1 °C/s) removed any residual signal. The aliquots were irradiated for 5 s and their OSL read as a reference. This allowed for the OSL curves obtained after pre-heating to be normalized. Both the OSL area and initial intensities were tracked as a function of the pre-heating temperature.

The results are shown in Figure 4-20. The data shows that the GSL initial intensity and area decrease steadily, reaching negligible values for pre-heating temperatures higher than 250 °C. The main decrease in the OSL area happens in the temperature range around 150 – 250 °C. For the BSL, the initial intensity and total area shows only a small reduction (~10%) until the pre-heating temperature reaches 150 °C. Then, both OSL

intensities decrease rapidly between 200-250 °C, reaching negligible values for pre-heating temperatures above 250 °C.

The difference between GSL and BSL can be explained based on the wavelength dependence of the photoionization cross-section (see Section 2.1.2). For green stimulation, there is likely a larger difference in photoionization cross-section between the shallow traps (unstable <150 °C) and the deeper traps (unstable in the 150 – 250 °C region). Therefore, we see a large difference between the initial OSL intensity, which is dominated by the trapping centers with larger photoionization cross-section (typically shallow traps). Most of the signal, however, comes from the deeper traps and, therefore, the area is stable until pre-heating temperatures above 150 °C are reached.

In the case of the BSL, on the other hand, the photoionization cross-sections at this wavelength are probably more similar. Therefore, both the initial intensity and the total OSL area are dominated by the main contributors to the OSL signal, which is stable until a pre-heating temperature of 150 °C is achieved.

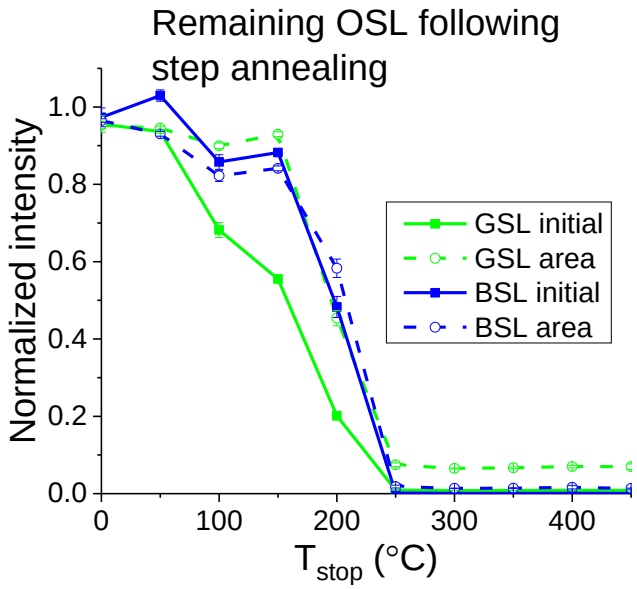

Figure 4-20: Intensity of OSL area and initial when normalized to reference dose. The error bars are the standard deviations based on three aliquots and are mostly too small to see.

The normalized OSL curves were averaged for each preheating and standard deviations were calculated. These curves were fit simultaneously with three exponential components and an offset by fixing the decay constants. Example fits are shown in Figure 4-21. As seen before, the fits do not describe the data, but the areas of those components are the point of interest.

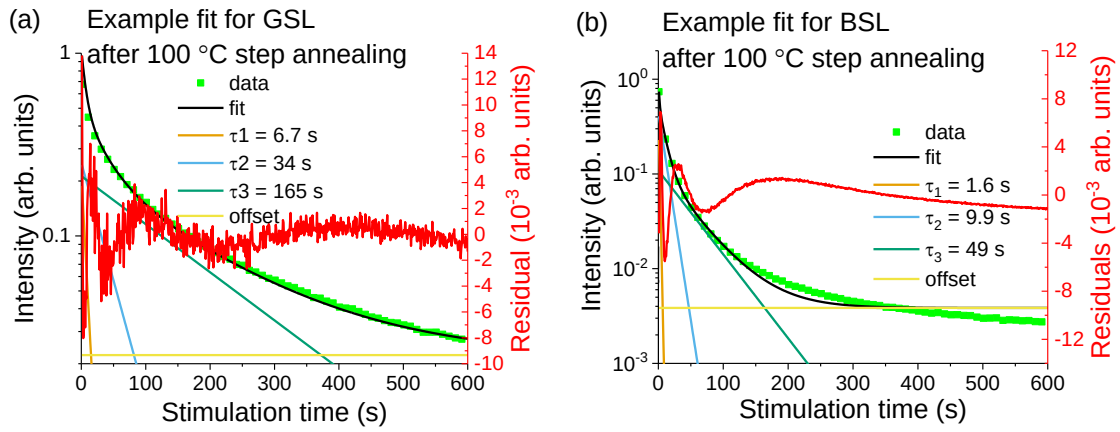

Figure 4-21: Sample simultaneous fits for GSL and BSL following TL depletion.

The integrated areas of the decay components for GSL and BSL are presented in Figure 4-22. As can be seen, the shortest lifetime component is the least thermally stable. The other two components stay constant or increase through a heating of 200 °C for the blue simulated OSL, or 150 °C for the green stimulated OSL. The two slower components are eliminated after a preheating of 250 °C, which corresponds to a complete elimination of the TL signal. Thus, it is likely that the fast OSL component correlates to the lower temperature TL peaks observed. This is confirmed in the dark fading study above. The other OSL components are likely associated with the main TL peak.

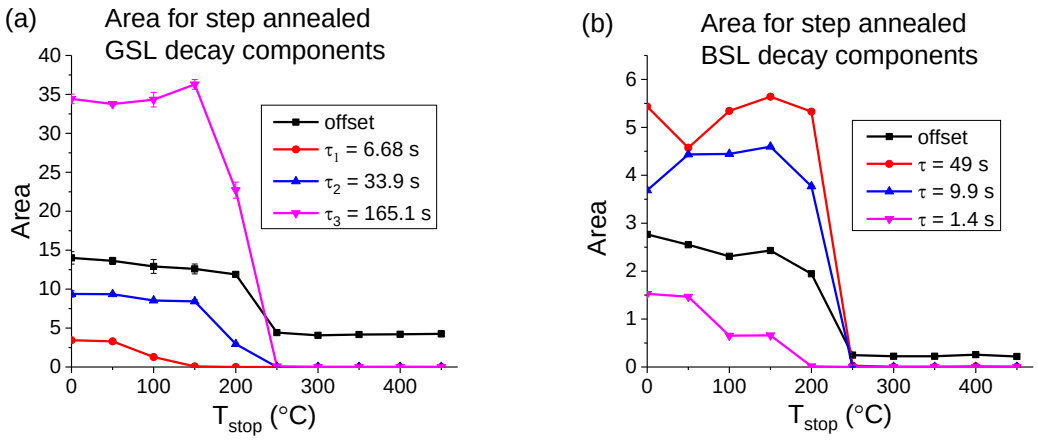

Figure 4-22: Integrated areas of OSL components for (a) GSL and (b) BSL. The error bars are the uncertainties from the fit, mostly too small to see.

4.4.1 TL following optical bleaching

The second correlation study looked at the residual TL following either BSL or GSL. As before, aliquots were not reused to avoid the sensitization problem. The results are presented in Figure 4-23.

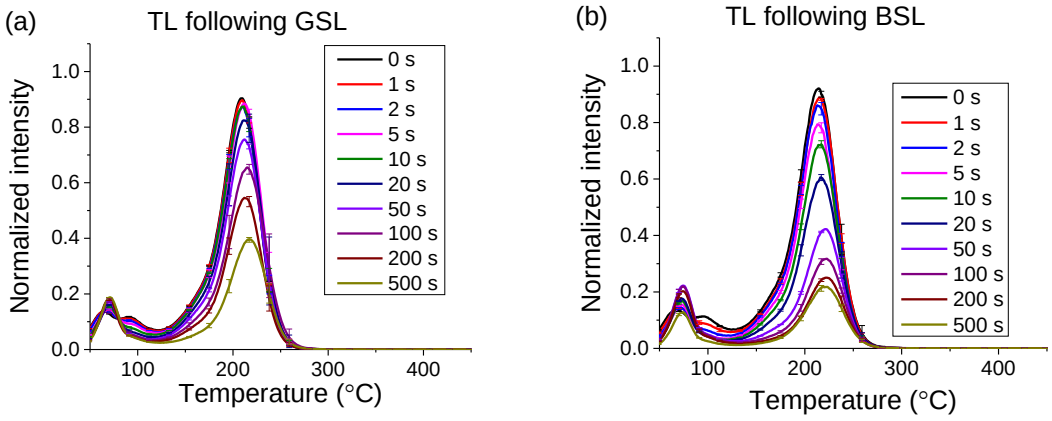

Figure 4-23: (a) TL following various green stimulation times, and (b) TL following various blue stimulation times. A phototransfer to the low temperature peak can be seen in both plots. In both cases the experimental conditions were: heating rate was 1 °C/s, 0.5 Gy, 10 mg of material, 90% power green stimulation, and U-340 optical filter.

These plots suggest a phototransfer of charge from deeper traps (>150 °C) to the shallow traps (< 100 °C), so the TL cleaning runs from the OSL step annealing study (Figure 4-20) were plotted to search for phototransfer. These plots are shown in Figure 4-24 for the TL following a pre-heating up to T_{stop} of 100 °C, 150 °C, 200 °C, and 250 °C, then OSL for 600 s. Despite temperatures of the pre-heating far exceeding the peak at ~75 °C, this peak appears consistently following OSL readouts using either GSL or BSL.

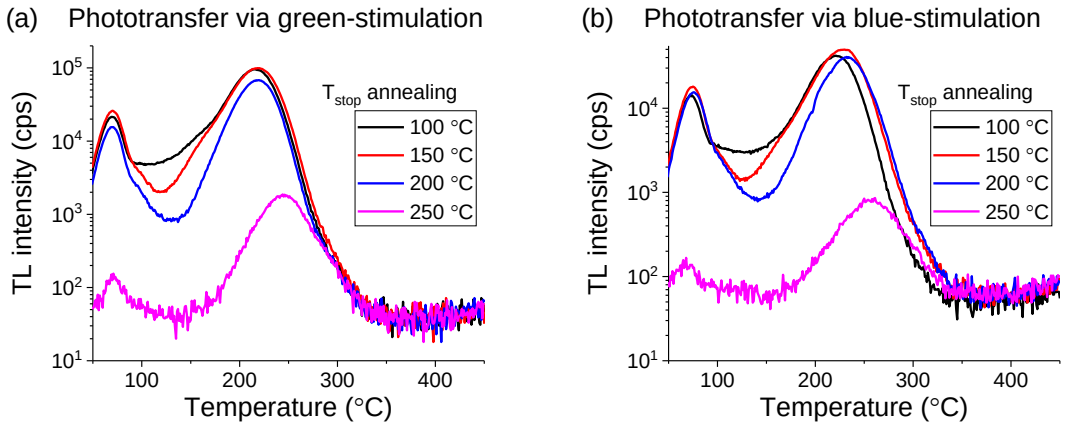

Figure 4-24: TL cleaning runs from the step annealing study which confirm phototransfer. Curves are TL of single 10 mg aliquots following irradiation for 5 s, annealing by TL to a T_{stop} (in the legend), and exposing to 600 s of (a) GSL or (b) BSL.

It appears that green optical stimulation does deplete the main TL peak at 210 °C. However, the low-temperature TL peaks (<100 °C) show slightly different behavior. The peak at about 95 °C fades with optical stimulation, but the peak around 70 °C shows an increase with optical stimulation time. It could be that there is phototransfer from the main TL peak at 210 °C to the TL peak around 70 °C.

Both the TL maximum and TL area were tracked following optical stimulation of varying durations to see if the main peak and area are impacted at the same rate by the

same light stimulation. This will show if there are large variations in the photoionization cross section among the traps. Using the two different stimulations wavelengths gives us some idea of the difference in photoionization cross section between blue and green stimulation.

The results are presented in Figure 4-25. As expected, blue stimulation causes a faster decrease in the TL curve than green stimulation, because of the higher photon energy and higher associated photoionization cross section. There is little difference between the maximum TL intensity and the total TL area, since the TL curves are dominated by the main peak at 210 °C.

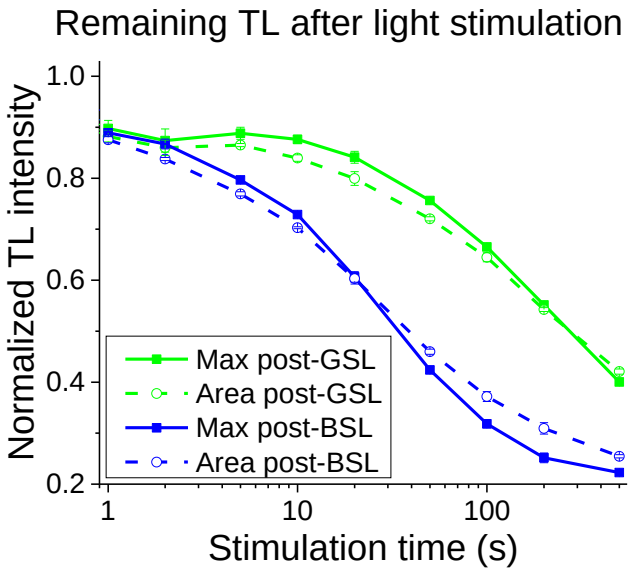

Figure 4-25: TL max and area following (a) GSL or (b) BSL for various durations. The intensities are normalized to the 0 s optical stimulation (not shown). The error bars (mostly too small to see) represent the standard deviation of the data between three aliquots.

As can be seen in Figure 4-25, initially, the TL area decreases slightly more with OSL stimulation than the TL maximum, but after 20 s of BSL or 200 s of GSL, there is more TL area remaining than TL maximum. After 500 s of GSL, just under half of the TL signal remained. Following 500 s of BSL, about a quarter of the TL signal remained. As

much of the TL curve is sensitive to optical excitation, this may be why the OSL sensitizes. A 500 s readout with green or blue light is insufficient to empty all optically sensitive traps. Thus, annealing may be needed to reset the material before reuse.

4.5 ***Kinetic parameter characterization***

Characterization of the kinetic parameters of MBO:$Ce_{0.3\%}$,$Li_{10\%}$ was carried out using three methods to check for consistency between the different methods: the various heating rate method, the initial rise method, and curve fitting (see Section 2.5 for theory and Section 3.2.8 for procedure). In addition, each method has its own advantages and disadvantages, favoring the information of different peaks and sometimes missing other peaks altogether. Thus, multiple methods allow for each peak's kinetics to be determined by at least two methods.

4.5.1 Various heating rate method

Figure 4-26a shows an example of the TL curves measured at various heating rates (see Section 3.2.8). The curves presented have been normalized to their heating rates. Figure 4-26b shows the plots of $ln(T_{max}^2/\beta)$ *versus* $1/T_{max}$ for the main TL peak. Results were obtainable for the two low temperature peaks around 100 °C and the main peak at 210 °C. The shoulder around 160 °C could not be resolved for analysis. This analysis was done for three aliquots.

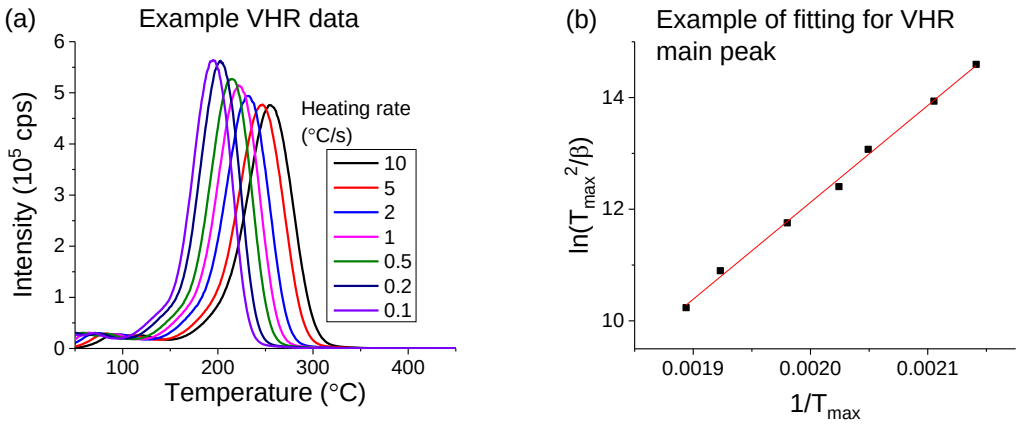

Figure 4-26: (a) TL curves of MBO:$Ce_{0.3\%}$,$Li_{10\%}$ at various heating rates (10 mg material, 0.5 Gy, U340 filters, no aperture); intensities are normalized to heating rate; (b) VRHM plotting and fitting to find *E* and *s* for the main peak.

Base on the VHRM, the peak at ~60 °C has a depth of 0.920(13) eV and frequency factor of 5(2) × 10^{12} s^{-1}. The peak at ~90 °C has a depth of 1.05(3) eV and frequency factor of 4(3) × 10^{13} s^{-1}. The peak at ~210 °C has a depth of 1.55(5) eV and frequency factor of 6(5) × 10^{14} s^{-1}.

4.5.2 Initial rise method

The IRM was applied to step-annealing data. Three 10 mg aliquots were irradiated for 5 s. Then, the aliquots underwent a preheating (1 °C/s) to varying T_{stop} from 50 to 350 °C in 5 °C intervals. The sample was cooled. Then, its partially depleted TL was read a 1 °C/s.

The plot of T_m vs T_{stop} (Figure 4-27a) indicates the presence of two easily found peaks at 110 °C and 225 °C. On this type of plot, glow peaks are seen as plateaus where the T_m values is constant over at least a few T_{stop} values. A plot showing *ln(I)* v *1/kT* and a sample fitting of the initial rise region (this was the region 1-5% of the intensity at T_{max}) is shown in Figure 4-27b. A plot of the energies found for various initial rise regions shows

three plateaus, which likely indicate glow peaks, in Figure 4-27c. The lowest glow peak at around 60 °C was not detected with this method, but the shoulder around 150 °C was observed. The value found for the 110 °C peak is underestimated due to a poor signal to noise ratio. As the initial region used for fitting was 1%-5% of the first peak maximum detected, 1% may have been too low of a threshold for the lower temperature peak to remain unaffected by the background.

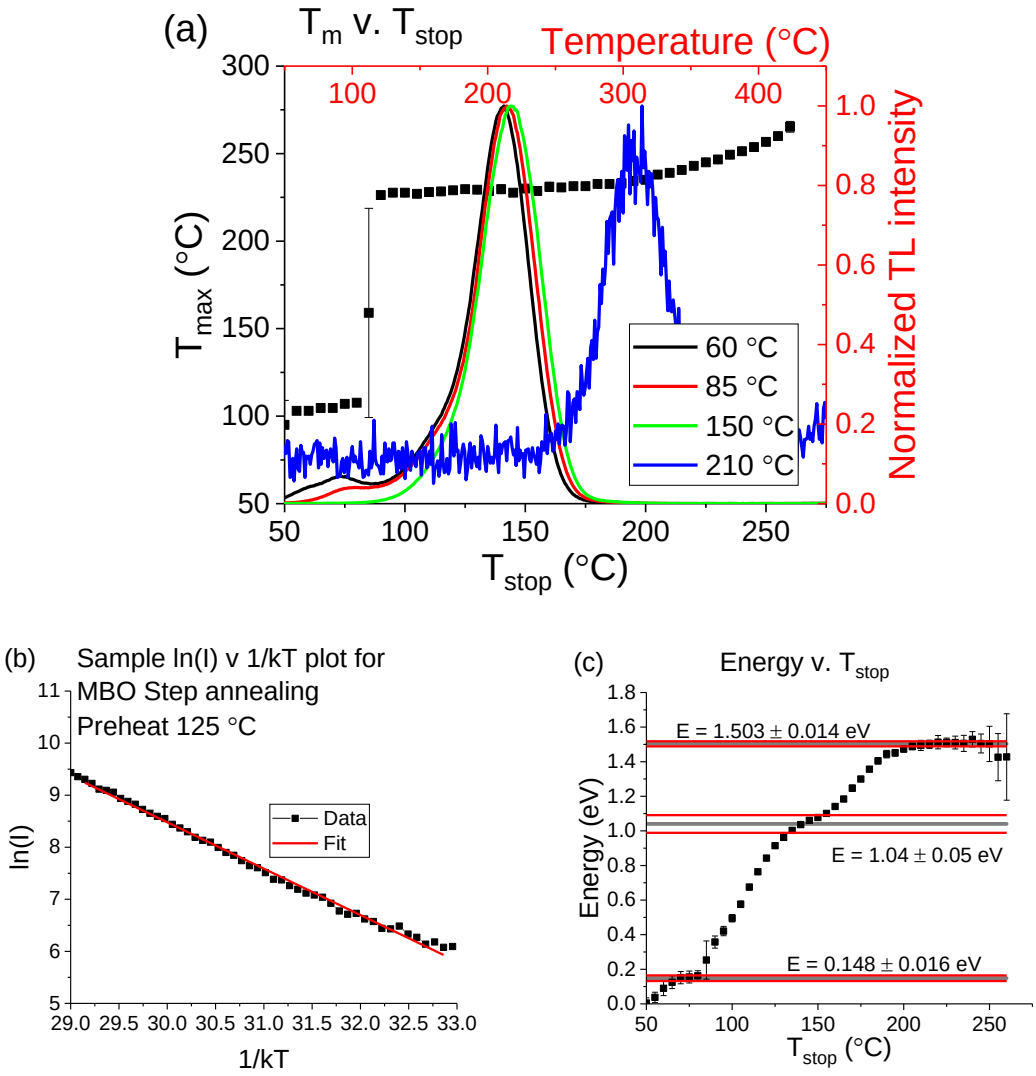

Figure 4-27: (a) T_m vs T_{stop} plot to aid in the identification of peaks and TL curves from step-annealings occurring during plateau regions in either plot shown. (b) A sample

***ln(I)* v *1/kT* plot and fitting for an annealing of 125 °C. (c) Plot of the activation energies found via the initial rise method for various step-annealed curves. Three plateaus were identified and average energies (black lines) and their statistical uncertainties from the points used for their calculation are presented (red lines).**

Three plateaus were identified in the energy plot, whereas two are visible in the T_m *v* T_{stop} plot. The first plateau had an energy of 0.148 eV which is unrealistically low. There are at least two overlapped peaks at <100 °C and interference between the two would result in a lower activation energy. Overlapped peaks result in underestimated energies for the lower temperature peaks (Coleman and Yukihara, 2018). It is possible that the second energy plateau is the shoulder, and the heavy overlap with the main peak is expected to lower its calculated energy also. The main TL peak shows as a large energy plateau, but there is still an increase throughout the plateau. This may evidence of a trap distribution being present. Also, the lack of sharp jumps in energy, but smooth transitions, are likely evidence of trap distributions (McKeever, 1985).

4.5.3 Curve fitting

As the TL curve is obviously comprised of multiple TL peaks, a simultaneous fitting of multiple TL curves is needed to constrain the fit. Otherwise, the fitting will not have a unique solution. The curve fitting was attempted with TL following various durations of blue stimulation, from Section 4.4. These data were fitted with first-order glow peaks (see Section 3.2.8). Because the TL dose response data in Section 4.3.2 show that the peak positions remain constant with dose, first-order peaks are the appropriate choice for fitting. The fits presented are for the fit of each data set using the least number of TL peaks and with a R_{adj}^2 value of over 0.995. The instrumental weighted, where the instrument weights

are from the standard deviation of three aliquots, fit with 7 peaks was the only fit to reach this R_{adj}^2.

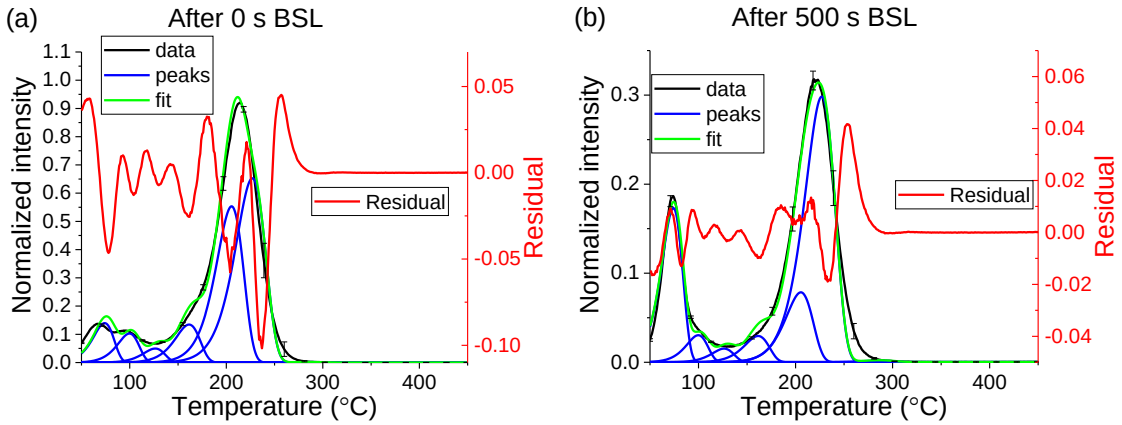

Figure 4-28: Sample fits for simultaneous fitting of residual TL after BSL of varying duration. The data are shown in black, individual peaks are shown in blue, and the fit is shown in green. The residuals are plotted using the y-axis on the right.

Table 4-1: Kinetic parameters found from the simultaneous fit presented with the position of the TL peak.

Peak	**E (eV)**	**s (s^{-1})**	**T_{max} (°C)** **β = 1 °C/s**
1	0.939(2)	$3.9(3) \times 10^{12}$	74
2	1.064(4)	$2.2(3) \times 10^{13}$	100
3	1.196(6)	$1.1(2) \times 10^{14}$	126
4	1.250(8)	$2.4(5) \times 10^{13}$	161
5	1.357(6)	$3.0(5) \times 10^{12}$	227
6	1.38(2)	$2.2(7) \times 10^{13}$	205
7	1.596(11)	$1.4(4) \times 10^{13}$	287

Overall, the fits do not seem to fully describe the behavior of the data. Even with seven curves the low temperature peaks are regularly neglected and the main peak is not fit fully either, as seen by the residuals. It may be better to try fitting with distributions of at least trap energy and maybe frequency factor also. One more fitting attempt is shown in Section 6.2.1 using a mixed data set.

4.5.4 Comparison between the different methods

Table 4-2 compares the kinetic parameters for the TL peaks in MBO:$Ce_{0.3\%}$,$Li_{10\%}$ obtained above using the different analysis methods.

The first peak, at 60 °C, has a trap depth of around 0.93 eV as found by curve fitting and VHR. The frequency factor found was on the order of 10^{11} or 10^{12} s^{-1}. Initial rise was unable to detect the lowest temperature peak.

The second peak, at 90 °C, and third peak, at 161 °C, had mixed results depending on method. Peak 2 shows a trap depth of 1.05 eV with a frequency factor on the order of 10^{13} s^{-1} found by the IRM and curve fitting. The IRM underestimated the energy, since the peaks are heavily overlapped. The third peak had a trap depth of 1.04 eV as found by initial rise method. Curve fitting found this peak to have a trap depth of 1.25 eV. As was discussed, the heavy overlapping from the main peak likely decreased the trap depth estimated using the IRM. Thus, the value from curve fitting is more reasonable. Curve fitting is still not perfect in this region as evidenced by the residuals, so there could be a distribution of traps rather than discrete traps.

The main TL peak (peak 4) has a depth of 1.50 eV and frequency factor on the order of 10^{14} s^{-1}. The IR and VHR agree on this trap depth. The curve fitting finds two traps with depths of about 1.37 eV and 1.65 eV heavily overlapped. The other methods seem to have found the average of this. The peak is broad enough it is certainly a superposition which the VHRM and the IRM are unable to decompose.

Table 4-2: E and s values for the three visible TL peaks and the shoulder found by various methods.

Peak		VHRM	IRM	Curve fitting
Peak 1 (~60 °C)	E (eV)	0.920(13)	Did not resolve	~.95
	s (s^{-1})	$5(2) \times 10^{12}$		
Peak 2 (~90 °C)	E (eV)	1.05(3)	0.148(16)	~1.05
	s (s^{-1})	$4(3) \times 10^{13}$	-	2×10^{13}
Peak 3 (~160 °C)	E (eV)	Did not resolve	1.04(5)	~1.25
	s (s^{-1})		-	3×10^{13}
Peak 4 (~210 °C)	E (eV)	1.55(5)	1.503(14)	1.37-1.65
	s (s^{-1})	$6(5) \times 10^{14}$	-	1×10^{13}

4.6 ***Conclusions***

Overall in this chapter, basic TL and OSL properties of MBO:Ce,Li have been characterized. Luminescence properties have shown that the dominant emission (~340-360 nm) is Ce^{3+} which is observed in RL, PL, OSL emission, and TL emission. Mn^{2+} emission was observed for RL and TL emission at ~590 nm. As this emission is outside of the transmission window for the U-340 filters (290 nm – 390 nm), any light emitted from recombination at this site is lost. One possible improvement to the material may be eliminating this competing recombination center.

Dosimetric properties were observed for the material as well. The dose response showed linearity up to 10's of Gy. The signal for both TL and OSL never saturated for the

dose range checked (up to ~70 Gy). However, sensitization was shown to be an issue. It may be possible to be removed or reduce through modification in the synthesis.

The correlation studies showed a phototransfer to a shallow trap, unstable at room temperature. Retrapping into these shallow traps certainly reduces the OSL intensity to a certain extent, as the process competes with recombination for the capture of charges released during optical stimulation. This phenomenon may also be partially responsible for the OSL sensitization observed. The OSL signal was stable up to about 200 °C.

Finally, the kinetic parameters were found through VHRM, IRM, and curve fitting. The main peak is best described as multiple glow curves. The lack of a shift in the peak positions with varying dose indicates that all peaks follow first-order kinetics. The main peak was found to have a trap depth of about 1.5 eV and a frequency factor on the order of 10^{14} s^{-1}.

CHAPTER 5

MATERIAL ENHANCEMENT VIA SYNTHESIS

This chapter describes attempts to improve the brightness of MBO and decrease its sensitization by changes to the synthesis, namely using high-purity reagent, modifying the post-synthesis annealing treatment, or adding additional codopants. The concentrations of codopants are studied as well. The chapter ends with dosimetric studies of the new best material and compares it with Al_2O_3:C.

5.1 ***High-purity reagent***

The Mn^{2+} emission reported for the MBO:$Ce_{0.3\%}$,$Li_{10\%}$ samples in Chapter 4 indicates a competing recombination process, since the emission occurs outside the Hoya U-340 filter transmission wavelength and, therefore, does not contribute to the OSL signal. The OSL signal can in principle be increased if the charge recombination responsible for the Mn^{2+} emission could occur at a Ce site instead. Thus, one possible way of improving the material would be by eliminating the Mn, unintentionally introduced as a contaminant, by using high-purity reagent.

In this Section, we look at replacing the lower-purity magnesium nitrate hexahydrate with high-purity. All samples were annealed for 2 h at 900 °C and allowed to cool slowly in the furnace. Data were collected for RL, TL, and OSL and compared to data for low-purity reagent MBO.

5.1.1 RL

RL data were collected for three aliquots of each material (Figure 5-1) to examine changes in emission for low or high-purity reagent. Syntheses were also conducted to observe emission for undoped MBO prepared with low or high-purity reagent, as well as Li-doped (10% mol) or Ce-doped (0.3% mol) MBO prepared with high-purity reagent.

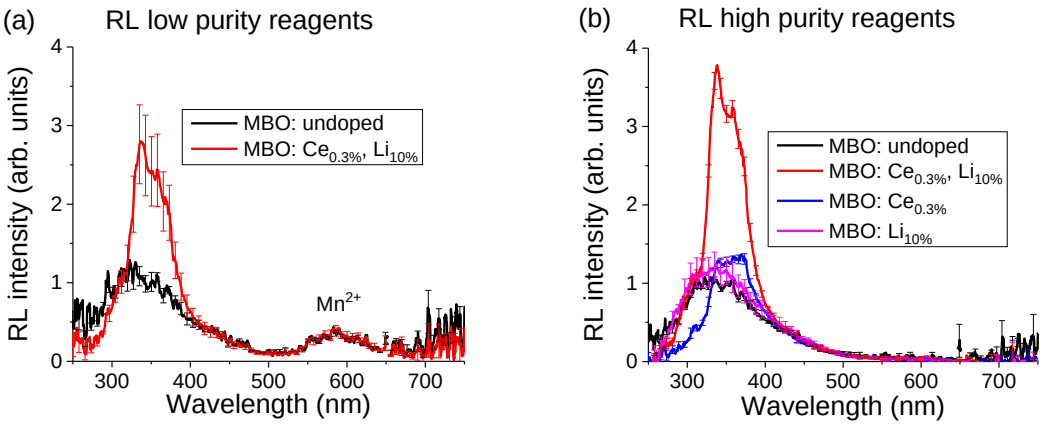

Figure 5-1: RL for (a) low and (b) high-purity MBO. High-purity reagent show no emission around 590 nm indicating elimination of this emission center. 10 mg aliquots, 100 s integration time, 5 boxcar, 5 average. All curves are corrected for the spectrometer efficiency. The error bars are the standard deviations between three aliquots.

Figure 5-1 show that the emission band centered around 590 nm, attributed to Mn^{2+}, is eliminated with the use of high-purity reagent. The addition of lithium as the sole dopant does not change the emission in comparison with the undoped sample.

The UV emission at ~320 nm appears in both undoped samples prepared with either low- or high-purity reagent. The addition of cerium, however, results in a reshaping of the UV emission. The addition of lithium to cerium-doped MBO results in a large increase in the emission and in the shape of the emission resolving to the two-peak emission structure expected for Ce^{3+}.

5.1.2 TL

TL data were collected for three aliquots of high-purity reagent MBO:$Ce_{0.3\%}$,$Li_{10\%}$ and compared to data for low-purity reagent MBO:$Ce_{0.3\%}$,$Li_{10\%}$. Figure 5-2: (a) shows absolute intensities for three aliquots of the high-purity material and one aliquot of the low-purity material, whereas (b) shows the curves normalized to peak maximum for curve shape comparison.

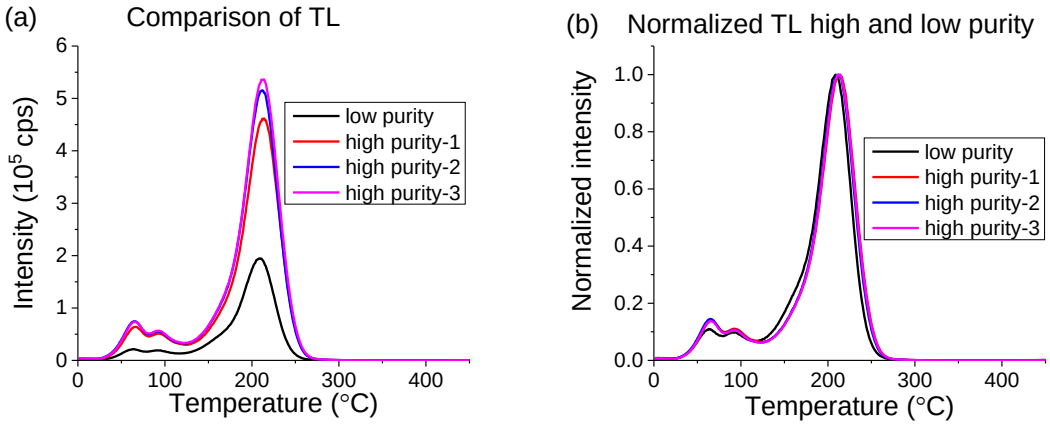

Figure 5-2: TL comparing low-purity and high-purity reagent, presented both as (a) raw data, or (b) normalized to the maximum intensity. No large change in peak shape was observed. Heating rate 1 °C/s, 5 s β irradiation, U-340, no aperture, 10 mg aliquots (three high-purity reagent aliquots and one low-purity reagent aliquot).

Figure 5-2a shows that the use of high-purity reagent results in a large increase in the TL detected with the Hoya U-340 filters. For the high-purity reagent sample, the TL peak maximum and area are about 2.4 - 2.5 times higher than that of the low-purity reagent sample. The normalized TL curves for both high-purity and low-purity reagent samples are nearly identical (Figure 5-2b). There is a small shift in the low-purity reagent sample TL

than can be attributed to cup position in the TL/OSL reader. The only noticeable difference in the curves is a slight increase (~25% greater) in intensity relative to the main peak maximum for TL peak at 65 °C.

5.1.3 OSL

OSL data were collected for three aliquots of MBO:$Ce_{0.3\%}$,$Li_{10\%}$ synthesized using high-purity reagent and compared with the low-purity reagent material. Figure 5-3 compares the (a) green-stimulated OSL, GSL, and (b) blue-stimulated OSL, BSL, for these samples with the OSL from a low-purity reagent sample (three aliquots with high-purity reagent and one aliquot of low-purity reagent).

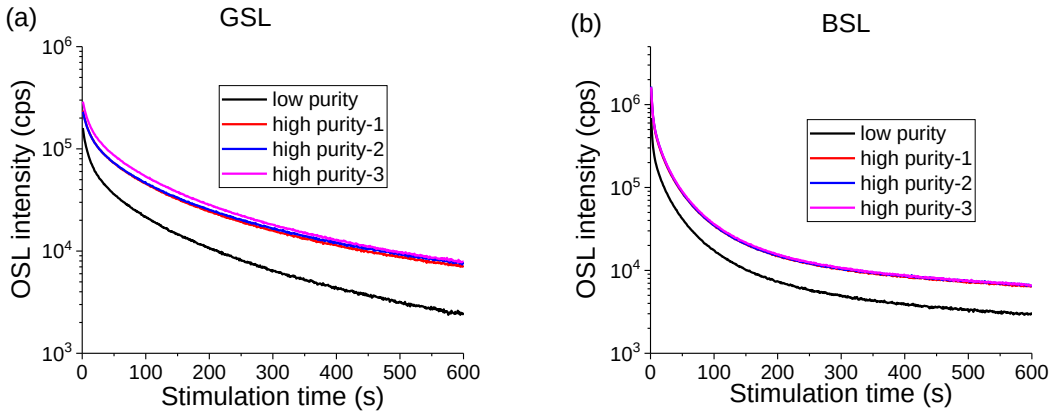

Figure 5-3: (a) GSL and (b) BSL for MBO:$Ce_{0.3\%}$,$Li_{10\%}$ for high and low-purity reagent. Experimental details: 90% LED intensity, 5 s β irradiation, U-340, no aperture, 10 mg aliquots.

Figure 5-3 shows that the OSL intensity increases with use of high-purity reagent. Without background subtraction, the initial intensity and total OSL area for the high-purity reagent samples increase over that of the low-purity reagent sample by ~1.9 times for GSL and ~2.2 times for BSL.

Nevertheless, one can also see the remaining signal after 600 s of stimulation from the LEDs for the high-purity reagent samples is roughly a factor of three greater than the

remaining signal from the low-purity reagent sample. This may be indicative of the phototransfer to a low temperature trap (e.g. the trapping centers responsible for the TL peaks at ~60 °C – 100 °C) that thermally depletes becoming more severe for the high-purity material. Such a phototransfer was observed for the low-purity reagent sample (see Section 4.4). An increase in this phototransfer would be detrimental to the material if the concentration of shallow traps cannot be decreased through additional synthesis modifications.

The curves in Figure 5-3a and Figure 5-3b were fit simultaneously using three exponential decays to see if the high-purity reagent material showed the same decay components as the low-purity material. Since the fits are simultaneous across the four curves, the resulting fit is biased to the high-purity reagent OSL, which contributes three of those curves. The fits are shown with one of the high-purity reagent data curves in Figure 5-4.

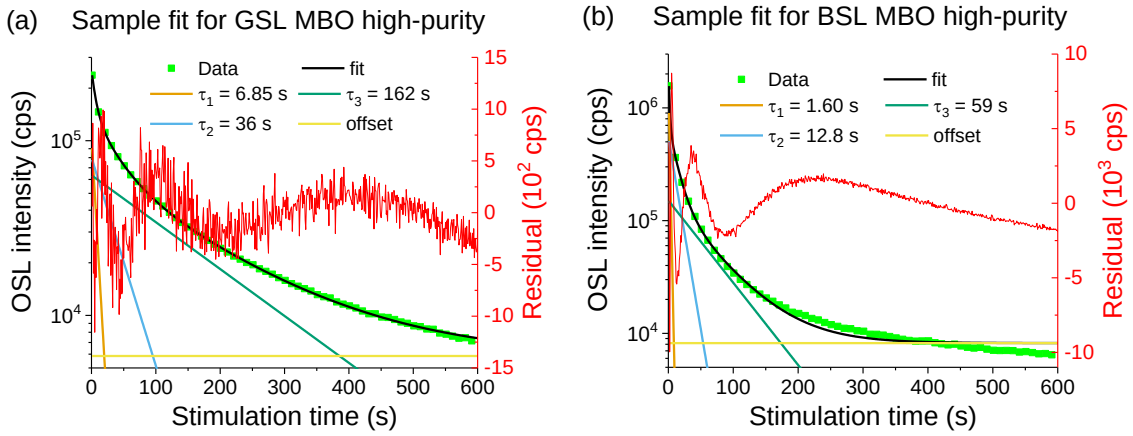

Figure 5-4: Sample fits for simultaneous fitting of three high-purity reagent curves and one low-purity reagent curve for (a) GSL and (b) BSL. The fits are plotted with one of the data curves for high-purity reagent MBO.

Overall, the fits match what was found in Chapter 4. The fit for the GSL has a R_{adj}^2 of 0.9999 with decay components of 6.9 s, 36 s, and 162 s. The fit for the BSL has a R_{adj}^2

of 0.9998 with decay components of 1.6 s, 13 s, and 59 s. This suggests that the trapping centers responsible for OSL could be the same in the low and high-purity reagent materials. However, the phototransfer mechanism is still present and results in fits that do not account for the buildup in the shallow trap appropriately. This is more pronounced in BSL, as commented on in Chapter 4.

5.1.4 Conclusions

The TL and OSL curve shapes stayed constant with the use of high-purity reagent, indicating that the trapping centers were likely not affected. The use of high-purity reagent resulted in the elimination of RL emission from Mn^{2+} and increase in the TL and OSL intensities. The TL was approximately 2.5 times brighter than the TL of material produced with low-purity reagent. The OSL intensity was approximately 2 times greater for both blue and green stimulation. The OSL background showed about a 3-fold increase for the high-purity reagent samples over the low-purity reagent sample. The increase in intensity for TL/OSL and elimination of Mn^{2+} emission was enough reason to conduct all remaining syntheses using high-purity reagent.

5.2 ***Post-synthesis annealing***

Two rounds of studies were conducted to improve the material by changing the post-synthesis annealing. The initial study was conducted using low-purity reagent (and chronologically prior to the high-purity reagent study). The purpose of this study was to observe the morphology of the material with varying temperature. SEM and XRD measurements were taken to observe morphology. The intensity of TL and GSL were tracked as well.

The second study was conducted using high-purity reagent. The focus of the second study was to increase the OSL brightness. As changes in emission are important to OSL, RL data were collected in addition to TL and OSL. The second study looked at fewer temperatures, but varying soak time and cooling treatment. Finally, the second study looked at sensitization of the brightest material to compare with the initial material.

5.2.1 Low-purity reagent

SEM

To examine the morphology of the material with varying annealing temperature, SEM images were collected. Figure 5-5 show SEM images for samples in order of increasing annealing temperatures. The left column shows a direct magnification of 100,000x, and the right column shows a direct magnification of 20,000x.

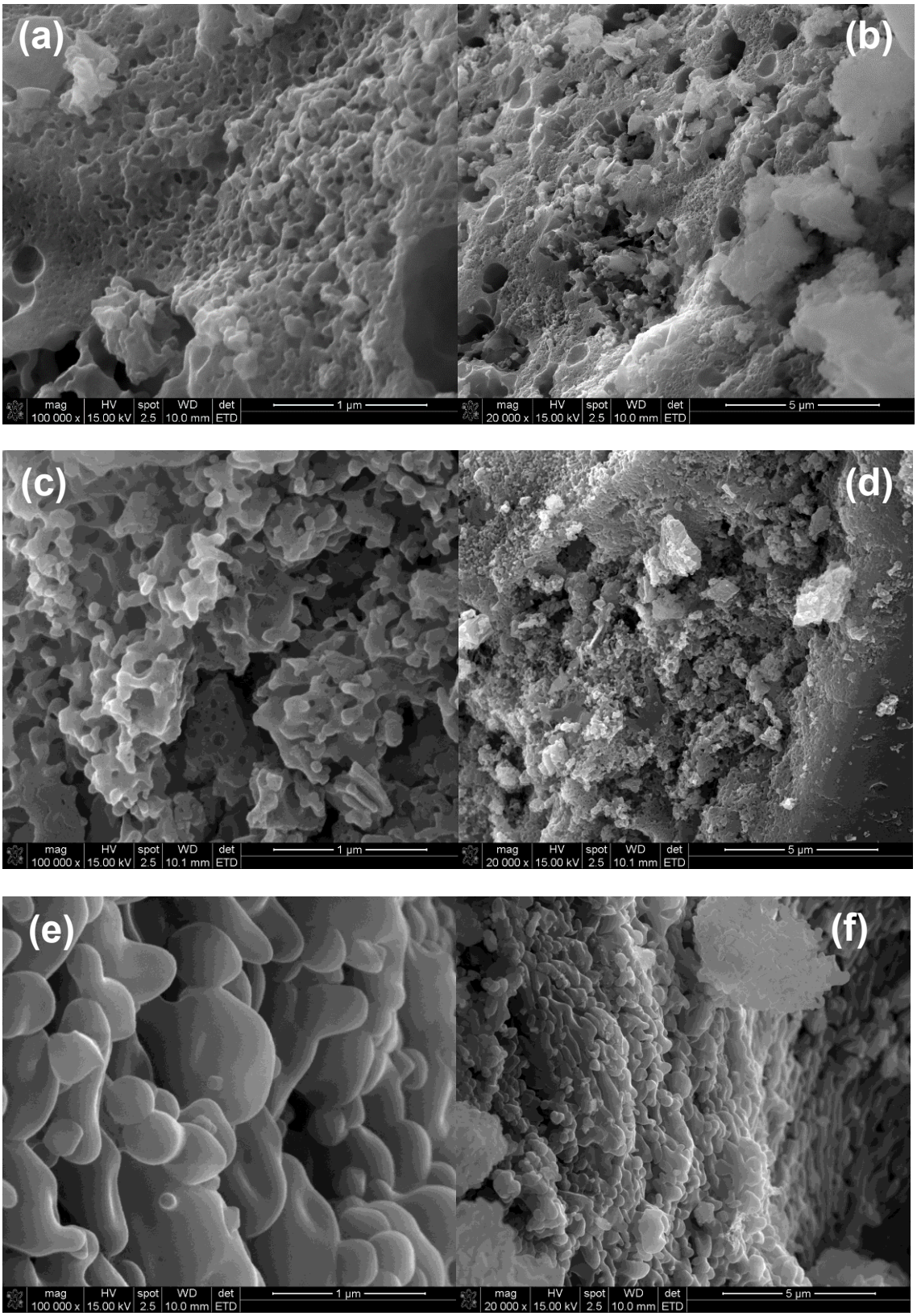
(a)
mag 100 000 x | HV 15.00 kV | spot 2.5 | WD 10.0 mm | det ETD | 1 µm
(b)
mag 20 000 x | HV 15.00 kV | spot 2.5 | WD 10.0 mm | det ETD | 5 µm
(c)
mag 100 000 x | HV 15.00 kV | spot 2.5 | WD 10.1 mm | det ETD | 1 µm
(d)
mag 20 000 x | HV 15.00 kV | spot 2.5 | WD 10.1 mm | det ETD | 5 µm
(e)
mag 100 000 x | HV 15.00 kV | spot 2.5 | WD 10.0 mm | det ETD | 1 µm
(f)
mag 20 000 x | HV 15.00 kV | spot 2.5 | WD 10.0 mm | det ETD | 5 µm

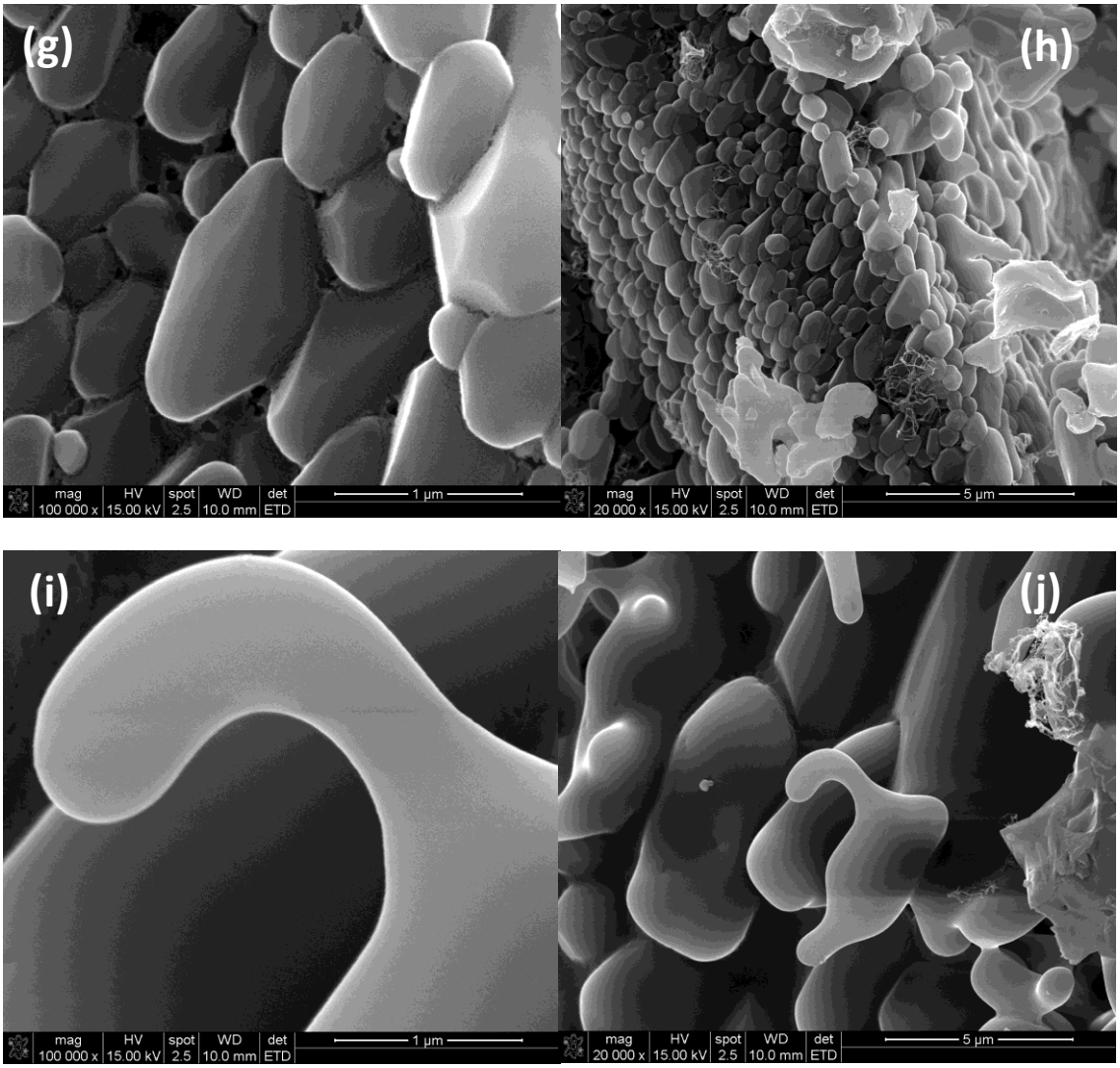

Figure 5-5: SEM for MBO unannealed (a)-(b), annealed at 600 °C for 2 h (c)-(d), annealed at 700 °C for 2 h (e)-(f), 800 °C for 2 h (g)-(h), and 900 °C for 2 h (i)-(j). Magnification of 100000x for (a), (c), (e), (g), and (i). Magnification of 20000x for (b), (d), (f), (h), and (j).

Figure 5-5 shows that the granule size grows by orders of magnitude with increasing annealing temperatures. The raw, unannealed material is comprised of thin films of synthesized material stacked on top each other reminiscent of a sponge. As the annealing temperature increases, those films congeal into granules that increase in size with annealing temperature. This kind of growth is expected, since higher temperatures

allow for greater malleability within the sample. The material, when permitted, attempts to minimize its surface much like a liquid does.

XRD

XRD is a crucial technique for verifying phase purity following synthesis. In this study, XRD was used to provide information regarding the crystallinity of the material for varying annealing soak temperature. Figure 5-6 shows XRD plots for MBO:$Ce_{0.3\%}$,$Li_{10\%}$ following varying annealing soak temperatures, as well as the XRD reference pattern for MBO (PDF reference card 00-031-0787). This describes MBO as having the cell parameters: a = 8.5960(20) Å, b = 13.7290(40) Å, and c = 7.9560(20) Å. The crystallinity is estimated as described in Section 3.2.6. The crystal size was also estimated using the Scherrer method for three different peaks. These two results are presented in Table 5-1.

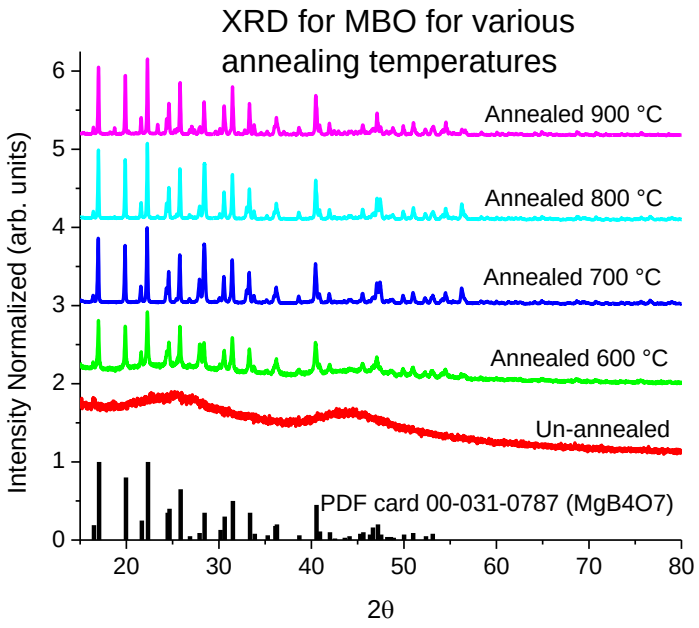

Figure 5-6: Normalized XRD plots for MBO of different annealing treatments with MBO PDF reference card 00-031-0787 shown on same axes. Sample prepared using low-purity reagent.

Table 5-1: XRD analysis for varying annealing soak temperatures, including crystallinity and crystallite size estimated using the Scherrer method in Å for three different peaks (see Section 3.2.6).

	Crystallinity		**Scherrer estimate of crystal size (Å)**		
Annealing temp	Crystallinity	Amorphous	Peak at 2θ 19.89°	Peak at 2θ 22.27°	Peak at 2θ 25.81°
900 ℃	96.4 %	3.6 %	757	719	714
800 ℃	95.5 %	4.5 %	723	712	652
700 ℃	94.1 %	5.9 %	643	613	572
600 ℃	61.4 %	38.6 %	531	513	521
Unannealed	.9 %	99.1 %	-	-	-

The diffractograms show increased sharpness in the peaks with higher annealing temperature, which indicates greater crystallinity. Table 5-1 shows increases in the crystallinity and crystal size with increased annealing temperature. This confirms the increase in granule size with increasing annealing temperature observed with SEM.

TL and OSL

TL measurements were made to investigate changes in intensity and curve shape with the annealing procedure. For TL measurements, background TL readings were obtained using an unirradiated sample for each aliquot. These background readings were subtracted from the measured TL curves. The curves for the three aliquots at each annealing treatment were averaged and the standard deviation was calculated (Figure 5-7a). TL curves normalized to the curve maximum for each aliquot then averaged for

each annealing temperature are shown in Figure 5-7b. The unannealed sample is omitted for this plot, since it shows no discernable TL curve. The maximum for each background corrected curve and total TL area were calculated for each aliquot as well. The averages and standard deviations of TL maximum and TL area for the three aliquots for each annealing treatment are presented in Figure 5-7c.

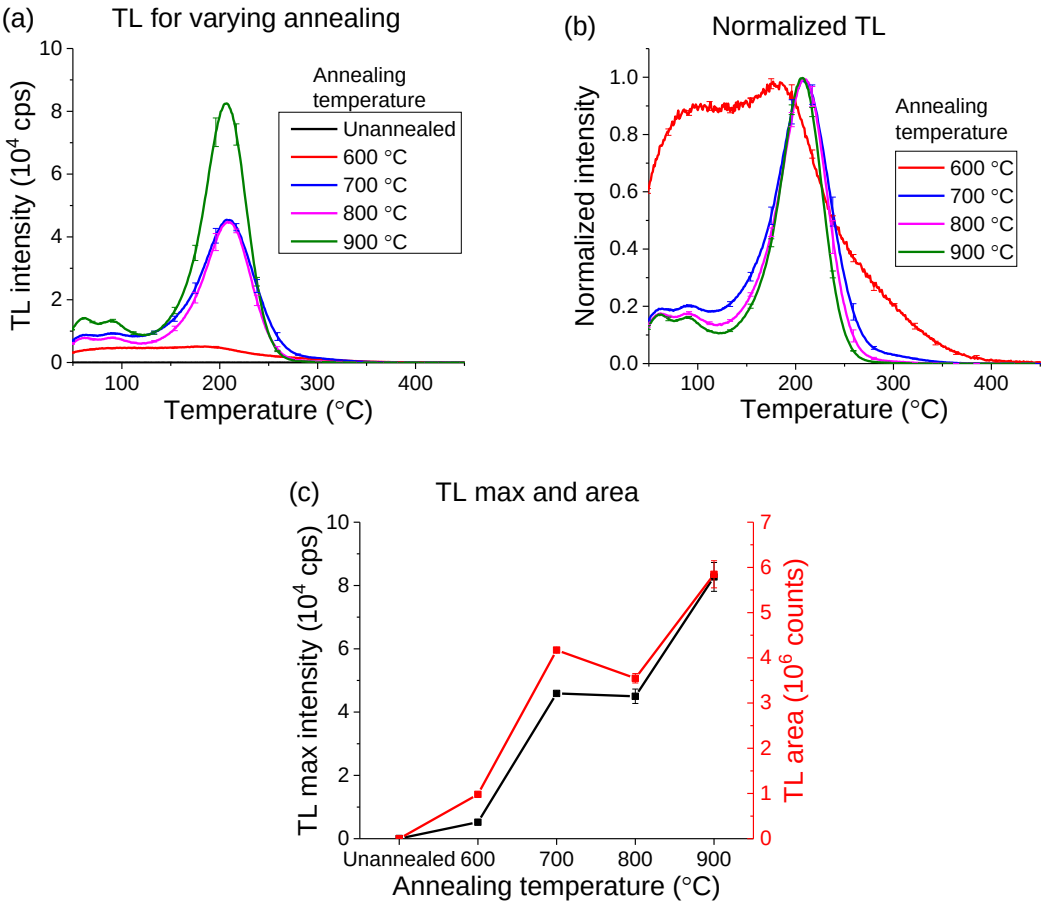

Figure 5-7: (a) Averaged TL curves after background subtraction, (b) TL curves normalized to curve maximum, and (c) TL maximum and total area for MBO:$Ce_{0.3\%}$,$Li_{10\%}$ prepared using low-purity reagent. In both, error bars are experimental standard deviations between the three aliquots for each annealing temperature. Readouts used 10 mg aliquots, 5 s β irradiation, 1 °C/s heating rate, Hoya U-340 filter, and no aperture.

We observe that the TL intensity overall increases with higher annealing temperature. In Figure 5-7b, one can see that the TL peaks narrow with increased

annealing temperature as well. This is likely due to the improved crystallization resulting in better uniformity in the material and better defined energy levels for the TL traps.

For GSL curves, the readouts of three aliquots at each annealing treatment were averaged and the standard deviation was calculated. The data curves are presented in Figure 5-8a**.** For each of the curves, the first five data points were averaged to find the initial OSL intensity, and the total OSL area was calculated for each curve. For both the total OSL intensity and initial OSL intensity, the averages and standard deviations of the three samples for each annealing temperature were calculated (Figure 5-8b).

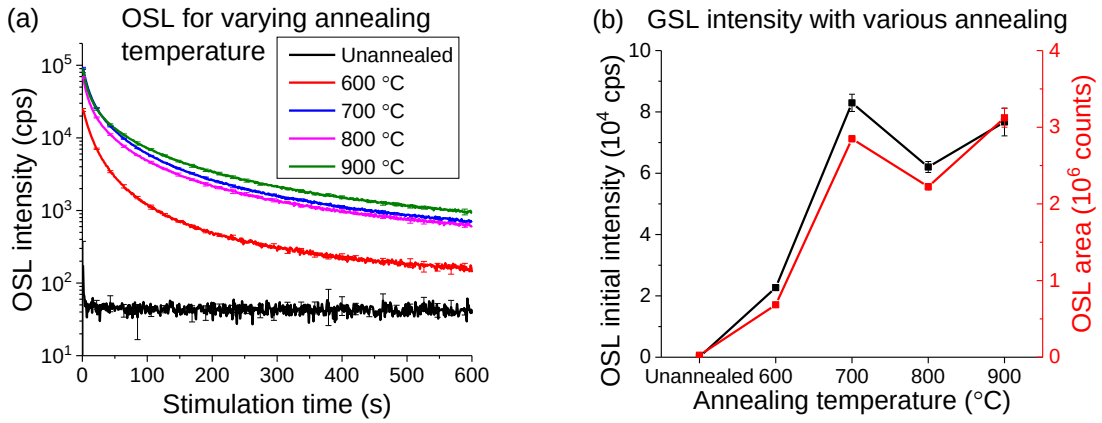

Figure 5-8: (a) Averaged OSL curves. (b) Initial OSL intensity and total OSL intensity versus annealing temperature. In both, error bars are experimental standard deviations between the three aliquots for each annealing temperature. Samples prepared using low-purity reagent.

Annealing at 700 °C and 900 °C resulted in the largest OSL intensity, but annealing at 900 °C resulted in the largest OSL area, Figure 5-8. Annealing at 600 °C or no annealing both resulted in far lower OSL intensities. The study suggests annealing must be at 700 °C or higher to obtain the brightest OSL signal.

Conclusions

Overall, the TL and OSL intensities increase with increased crystallinity of the material. The material synthesized became more crystalized and formed larger crystallites with higher annealing temperature. Annealing at 700 °C or above resulted in crystallinity higher than 90%. The brightest TL was observed for 900 °C annealing. The brightest OSL initial intensity was for 700 °C annealing, and the brightest OSL total area was for 900 °C annealing. In additional studies, annealing temperatures should be 700 °C or higher for brighter TL/OSL signal.

5.2.2 High-purity reagent

The second study was conducted using high-purity reagent in the synthesis. The purpose of this study was to find the annealing treatment that leads to the highest OSL signal. Various annealing temperatures (700 °C, 800 °C, 900 °C, and 1000 °C), durations (2 h and 4 h), and cooling treatments (natural or fast cooling) were tested. Samples that were annealed for 1000 °C melted and were not considered in this study. Data were collected for RL, TL, and OSL (GSL and BSL) to find the brightest TL/OSL material. Finally, data were collected to observe the reproducibility of the TL and OSL signals over 10 irradiation and readout cycles. Two sets of synthesis had 12 aliquots of about 0.5 g treated with each annealing to confirm any trends observed in the brightness of the material.

RL

RL were collected for three aliquots of each sample produced with high-purity reagent and varying annealing. Readouts were conducted using an integration time of 100 s with five readouts averaged and boxcar of five. The spectra were averaged among the three aliquots for each sample and standard deviations calculated to present as error bars. A spectrum for the original low-purity synthesis with 2 h and slow cooling annealing

is shown as reference. Spectra for the first synthesis are shown in Figure 5-9. A second synthesis was performed to verify the results of the first one. The results from the second synthesis are similar to those of the first one, so are not presented here.

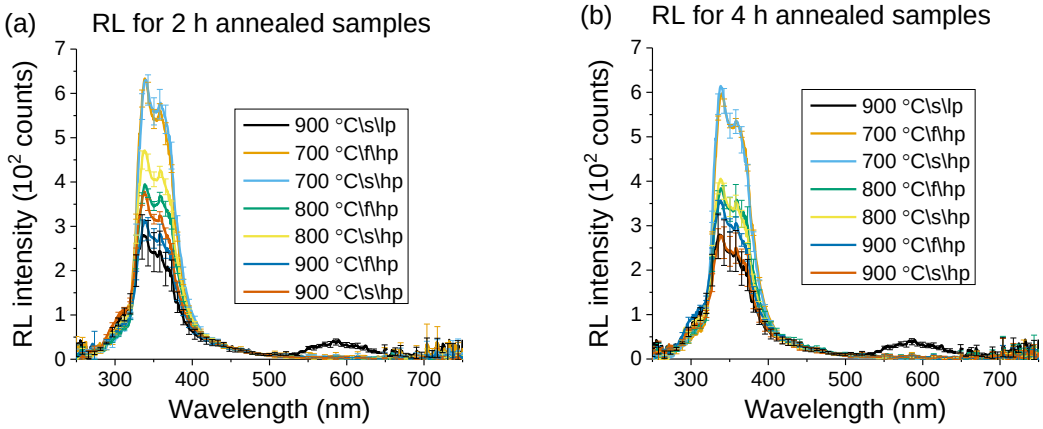

Figure 5-9: RL for various annealing of high-purity MBO for (a) 2 h and (b) 4 h with the exception of the low-purity reagent MBO. The labels in the legend denote annealing temperature in °C, fast (f) or slow (s) cooling, and reagent purity: high-purity (hp) or low-purity (lp). Lower annealing temperature resulted in high emission.

Figure 5-9 shows that the dependence of the emission intensity depends more on the annealing temperature than the rate of cooling or duration of the annealing, at least for the parameters investigated here. The low-purity sample exhibited Ce^{3+} emission intensity similar to that of the high-purity sample for the same annealing treatment. For all high-purity samples, only Ce^{3+} emission is observed. The broad emission band centered at 590 nm has been eliminated. Thus, based on the emission intensity alone, any of the annealing processes with a 700 °C soak temperature would offer improvement over the initial material or its high-purity reagent iteration.

TL

TL data were collected for three aliquots for all samples synthesized. The main characteristics of interest were the curve shape and TL intensity. TL curves for single

aliquots of each annealing are shown in Figure 5-10a and the same curves normalized to the main peak maximum are shown in Figure 5-10b.

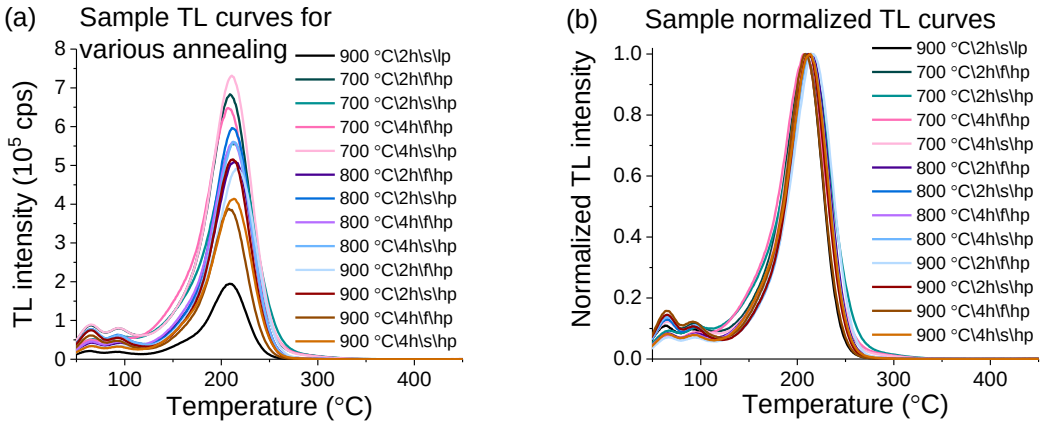

Figure 5-10: (a) TL curves and (b) normalized TL curves for MBO:$Ce_{0.3\%}$,$Li_{10\%}$, for various annealing treatments. The labels in the legend denote annealing temperature in °C, the soak time: fast (f) or slow (s) cooling, and reagent purity: high-purity (hp) or low-purity (lp). Only the first plot used low-purity (lp) reagent. The parameters were: heating rate 1 °C/s, 5 s β irradiation, Hoya U-340 filter, no aperture, 10 mg aliquot.

Figure 5-10a shows that the TL intensities are higher for the high-purity than for the low-purity reagent sample. The curve shape remains unchanged, but the relative intensity of the low temperature peaks varied with annealing (Figure 5-10b).

The maximum intensities and TL areas for the average of three aliquots for each annealing are shown in Figure 5-11. Only data for the first synthesis are shown, since the second synthesis matched all trends.

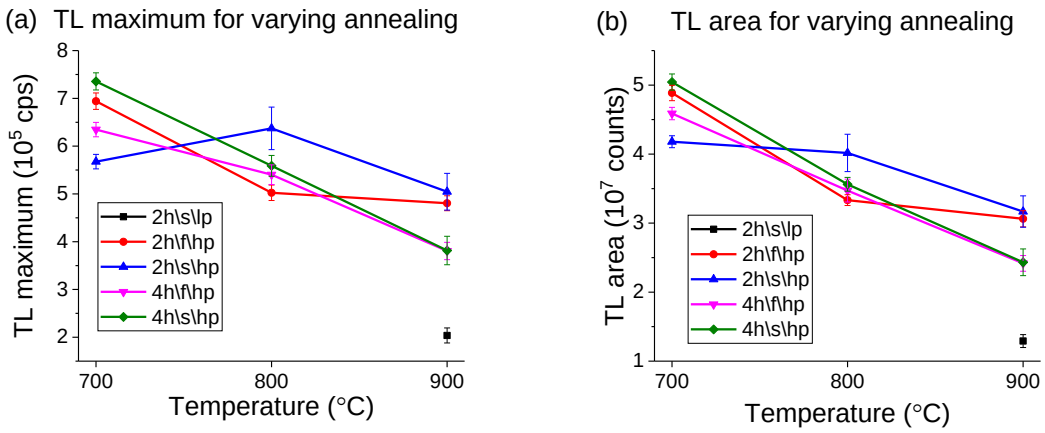

Figure 5-11: (a) TL peak maximum and (b) TL total area for various annealing temperatures, durations and cooling regimes, compared to the MBO:$Ce_{0.3\%}$,$Li_{10\%}$ prepared with low-purity reagent and annealed at 900 °C for 2h with slow cooling. The legend labels denote the annealing duration, fast (f) or slow (s) cooling, and reagent purity: high-purity (hp) or low-purity (lp). The error bars indicate the standard deviations of three aliquots.

The TL maximum intensity and TL area showed improvement over the low-purity, 900 °C, 2 h soak time, slow cooling sample for all high-purity reagent samples. The only trend observed is the larger TL intensity for the 700 °C annealing temperature. There is no clear pattern between either slow or fast cooling or between 2 h or 4 h soak times. Thus, the recommend annealing for quickest annealing and brightest TL is 700 °C for 2 h soak time with either cooling. The increase over the low-purity reagent sample is about a factor of four.

OSL

GSL and BSL were collected for three aliquots of each annealing treatment for two syntheses. OSL curves for a single aliquot of each annealing treatment are shown in Figure 5-12 with the OSL of a low-purity reagent aliquot for reference.

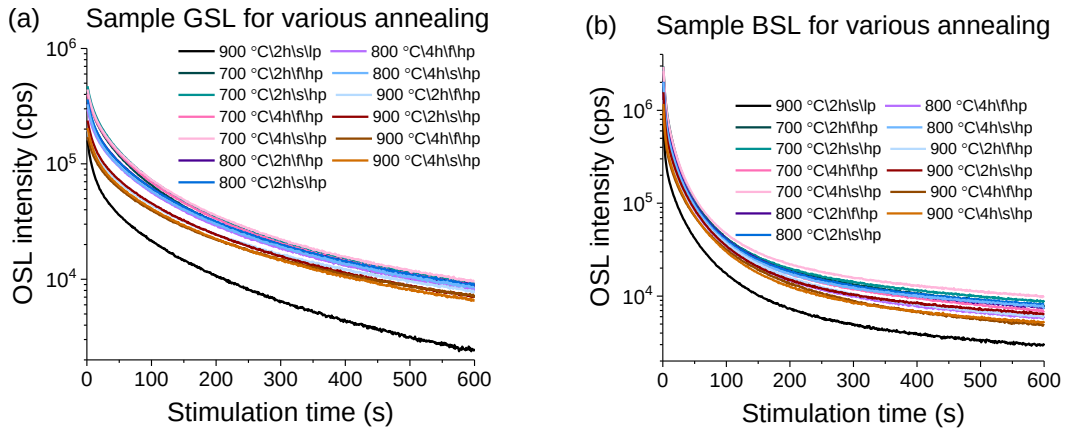

Figure 5-12: Sample raw OSL curves for (a) GSL and (b) BSL. The labels in the legend denote annealing temperature in °C, the soak time: fast (f) or slow (s) cooling, and reagent purity: high-purity (hp) or low-purity (lp). Only the first sample synthesis used low-purity reagent. Readout parameters were: 90% power for each LED, Hoya U-340 filter, no aperture, 5 s β irradiation, and 10 mg aliquots.

No clear patterns appear in the plots of OSL curves, besides the fact that all high-purity reagent samples had more intense OSL than the low-purity reagent sample.

The initial intensities and total OSL areas were calculated for all samples and are presented in Figure 5-13 and Figure 5-14 respectively. The second synthesis confirmed all trends.

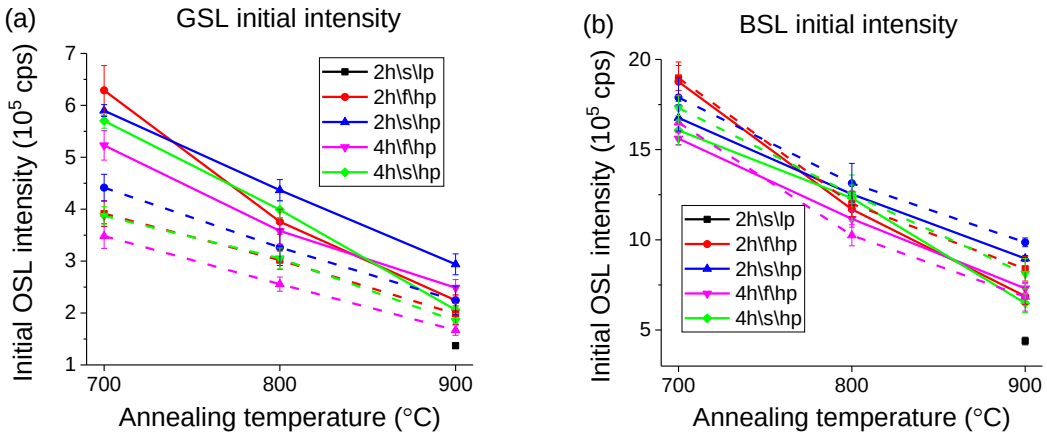

Figure 5-13: OSL initial intensity for (a) green and (b) blue stimulation, for various annealing treatments with high-purity reagent. The first synthesis is shown using solid lines, whereas

the results for the second synthesis is shown with dashed lines. The legend labels denote the annealing duration, fast (f) or slow (s) cooling, and reagent purity: high-purity (hp) or low-purity (lp).

The initial intensities for both green and BSL are higher for 700 °C annealing. There is a variation between the two syntheses for GSL, but the same trends are observed within each synthesis. There may be a trend favoring slow cooling instead of fast cooling, but it is within the margins of error of the data collected. Thus, if there is any advantage in using slow cooling, the increase in initial intensity is small. Likewise, there appears to be no difference in initial intensity for 2 h or 4 h soak time.

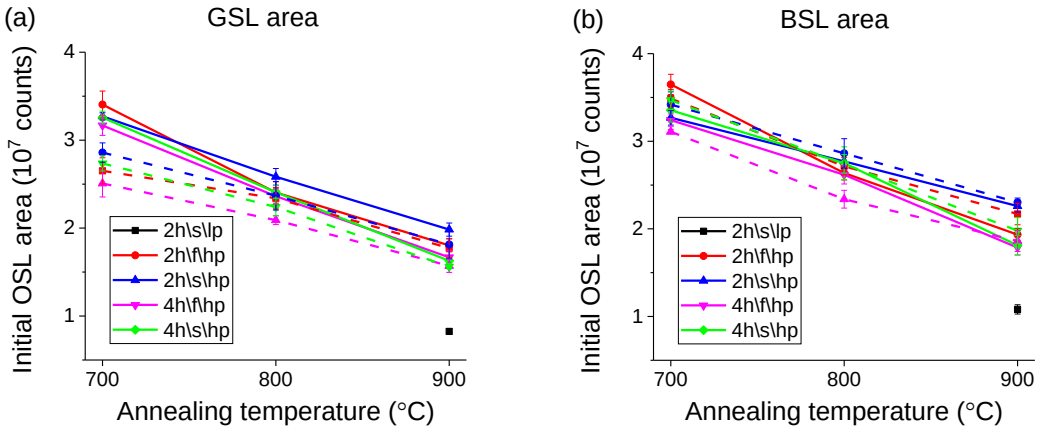

Figure 5-14: OSL area for (a) GSL and (b) BSL, for various annealing treatments with high-purity reagent. The first synthesis is shown using solid lines, whereas the results for the second synthesis is shown with dashed lines. The legend labels denote the annealing duration, fast (f) or slow (s) cooling, and reagent purity: high-purity (hp) or low-purity (lp).

Like the initial intensity, the OSL area showed the greatest improvement with changes in annealing temperature. Differences in OSL area for varying soak time and cooling treatment are both within the margins of error, showing no trend. Thus, the recommended annealing for the most intense OSL signal is 700 °C for 2 h with either

cooling treatment. A 4 h annealing could be used with no detriment to the OSL intensity but adds to the synthesis time with no gain in OSL intensity.

TL/OSL reproducibility for high-purity reagent

As we have seen in Section 4.3.1, one of the biggest challenges to the original material was its sensitization. Thus, reproducibility data were collected for one of the most promising annealing treatments (700 °C, 2 h soak, fast cooling) based on the increased intensity of both TL and OSL. Reproducibility data runs comprised of 10 irradiation and readout cycles. For each reproducibility study (TL, GSL, and BSL), three aliquots were used.

TL reproducibility data are shown in Figure 5-15. In Figure 5-15a, the 10 TL curves are shown for one aliquot. In Figure 5-15b, the intensity for each the TL maximum and TL total area are normalized to the run 1 TL maximum or TL total area. The TL maximum and area are the averages of three aliquots and the standard deviation was calculated.

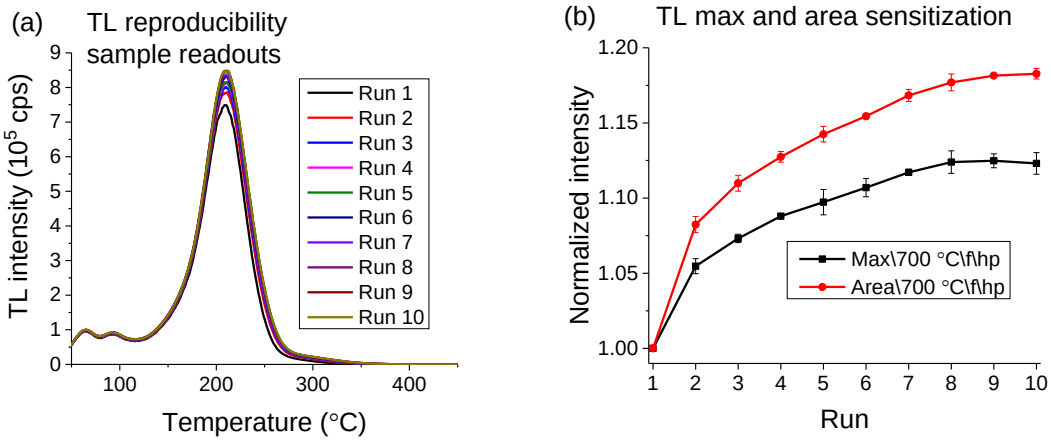

Figure 5-15: (a) TL reproducibility curves for one of the aliquots. (b) TL maximum and total area repeated irradiation and readout normalized to the run 1 maximum or area respectively. Error bars are the standard deviations of three aliquots. Readout parameters were: a heating

rate of 1 °C/s, 5 s β irradiation, Hoya U-340 filter, no aperture, and 10 mg aliquots. Samples prepared using high-purity reagent.

There was a great improvement over the original material. As can be seen in Figure 5-15a, the low temperature peaks (< 150 °C) do not change with repeated irradiation and readout, whereas the main peak at 210 °C increases only about 11% over 10 irradiation/readout cycles, and the TL area increased by about 18% over the same number of cycles. The original material showed sensitization of around 40% for both TL maximum and TL area over 10 irradiation/readout cycles (see Section 4.3.1).

Plots for the sensitization of OSL are seen in Figure 5-16. Figure 5-16a shows BSL curves for one of the aliquots undergoing the reproducibility test. Note that there was no heating to remove residual dose between runs to isolate the OSL reproducibility data from any influence of heating. Curves for GSL are not shown as they were show no additional information. In Figure 5-16b, the initial intensity and total OSL areas are shown normalized to the first readout initial intensity or total area.

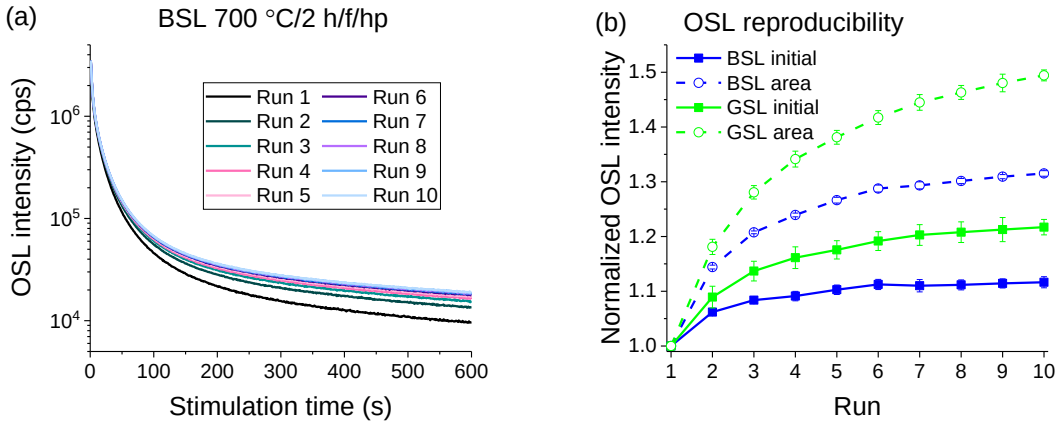

Figure 5-16: OSL reproducibility for high-purity reagent, 700 °C, 2 h soak time, and fast cooling sample. (a) An example of reproducibility data is presented for one aliquot. (b) OSL initial intensity and area normalized to the initial/area average over 10 cycles. Error bars

show the standard deviation of three aliquots. Readout parameters were: 90% power for each LED, Hoya U-340 filter, no aperture, 5 s β irradiation, and 10 mg aliquots.

The OSL reproducibility showed increases of about 10% for the initial BSL intensity, 25% for the BSL area, 20% for the initial GSL intensity, and 50% for the GSL area over the course of 10 irradiation/readout cycles. The BSL results demonstrate an improvement over the original material, which showed 16% for initial and 41% for area. The results for GSL were worse than the original material, which showed an increase of 13% for initial intensity and 37% for OSL area. However, it does appear that the sensitization is saturating within the 10 cycles observed. In the original material, sensitization was still increasing, especially for OSL area, rather than settling on a plateau.

5.2.3 Conclusions

RL data showed that use of high-purity reagent eliminates the emission center characterized by a broad band around 590 nm, as anticipated. The RL was brightest for samples annealed at 700 °C.

The TL intensity was improved with no change to the peak structure. The use of high-purity reagent doubled the OSL intensity, and changing the annealing treatment further increased the OSL factor to a total improvement of a factor between 4 and 5 from the original material. Annealing at 700 °C resulted in the brightest TL and OSL signals.

Reproducibility data were collected for high-purity reagent, 700 °C, 2 h soak, and fast cooling sample. The TL sensitization decreased by a factor of 2-3 compared to the original material. However, the OSL sensitization results were mixed. BSL improved by sensitizing about 60% less than the original material. GSL sensitized more than the

original material by about 50%. The sensitization mechanism for OSL may be due to traps not depleting completely under light stimulation.

5.3 ***Codopants I: transition metals***

Additional codopants provide the potential for the greatest changes in the emission, TL, and OSL properties of a material. Codopants can introduce new emission or trapping centers into the material. The rest of this chapter explores adding a third co-dopant to the MBO:Ce,Li formulation. The first section looks at MBO doped with 0.3% cerium, 10% lithium, and 0.3% of a transition metal: Cu, Ag, or Co. The next section (Section 5.4) explores MBO doped with 0.3% cerium, 10% lithium, and 0.3% of a lanthanide: Pr, Nd, Sm, Eu, Gd, Dy, Ho, Er, Tm, or Yb. The first round of refinement (Section 5.5) looks at changing the dopant concentrations for the new metal in the two most promising candidates from the transition metal and lanthanide codoping attempts: Ag and Gd. Finally, in Section 5.6, the best material, Gd at 1%, has the lithium concentration varied.

To study the codoped material, all codoping was conducted with high-purity reagent and 2 h, 700 °C annealing with fast cooling. For each synthesized material, data were collected for RL, TL, and both GSL and BSL.

The first round of codoping looked at adding 0.3% of another metal to the 0.3% Ce and 10% Li material. Three transition metals were selected as codopants. Copper is known to have TL or OSL signal in MBO (Rao et al., 2009), CaB_4O_7 (Erfani Haghiri et al., 2013), or SrB_4O_7 (Bajaj and Omanwar, 2013). A study showed MBO doped with silver to show TL and OSL signals (Palan et al., 2015). Thus, copper and silver should result in changes to the TL and OSL. It was reasoned that, if Cu and Ag entered at a Mg site in a 2+ oxidation state, they would likely behave as electron traps following irradiation to fill

their d-shell. Cobalt was selected as representative of another transition metal family. Manganese, despite having been used for TL as discussed previously in Section 2.4.1, had been observed to harm the OSL signal in small amounts shown in Section 5.1 above, so it was not an option.

5.3.1 RL

RL data were collected to measure any change in emission for the material. New emissions outside the transmission of the U-340 optical filter is 'lost' signal that would not have been collected if that site behaves as a recombination center. The averages of three aliquots for each transition metal dopant along with the two-dopant material are presented in Figure 5-17.

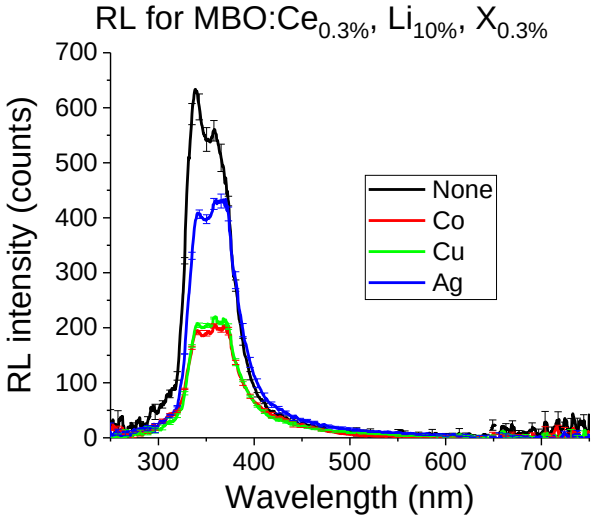

Figure 5-17: RL for MBO:$Ce_{0.3\%}$,$Li_{10\%}$,$X_{0.3\%}$ where X is Co, Cu, or Ag. Shown are averages of three aliquots with the error bars indicating the standard deviation among the three aliquots. Parameters used are: 100 s integration time, average of 5 spectra, boxcar 5, and 10 mg aliquots.

As can be seen, no new emissions were introduced by the new dopants. Also, the RL intensities for the cerium emission were reduced by the addition of codopants. This suggests that the new dopants may be introducing new traps or non-radiative recombination pathways that decrease the luminescence efficiency in the material.

5.3.2 TL

TL curves were collected for three 10 mg aliquots of each material. The average TL curve of the three aliquots is presented in Figure 5-18a with the error bars representing the standard deviation between the three aliquots. The TL maximum and total TL area were tracked in the same manner as previous studies and shown in Figure 5-18b.

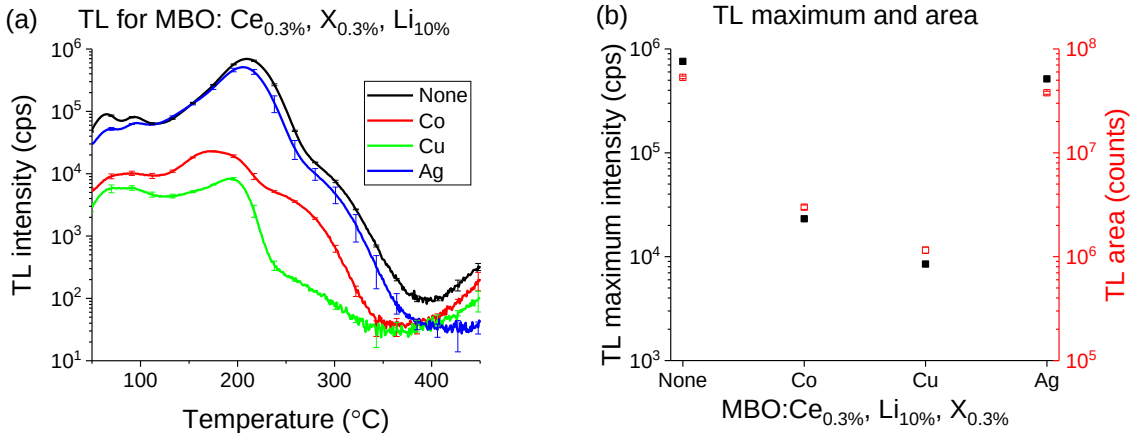

Figure 5-18: TL for MBO:$Ce_{0.3\%}$,$Li_{10\%}$,$X_{0.3\%}$ where X is Co, Cu, or Ag. (a) Shows TL curves for three aliquots averaged of each material. (b) Shows the TL maximum and the TL total area for the average of three aliquots of each material. Error bars are standard deviations for three aliquots (some too small to see). TL parameters used were: 1 °C/s heating rate, 5 s β irradiation, Hoya U-340 filter, no aperture, and 10 mg aliquots.

The TL curves for MBO:Ce,Li changed dramatically with additional dopants. For both Co and Cu, the changes reduce the intensity of the TL glow curve by an order of

magnitude. Ag shows little change in curve shape and intensity (<20%). Thus, for TL, the brightest codopant is Ag.

5.3.3 OSL

OSL curves were taken for three 10 mg aliquots for each GSL and BSL. Raw OSL curves are shown for one of the aliquots for each dopant under each stimulation in Figure 5-19ab. The initial intensity and total OSL area are shown in Figure 5-19c for each codoped material. The error bars indicate the standard deviation of three aliquots.

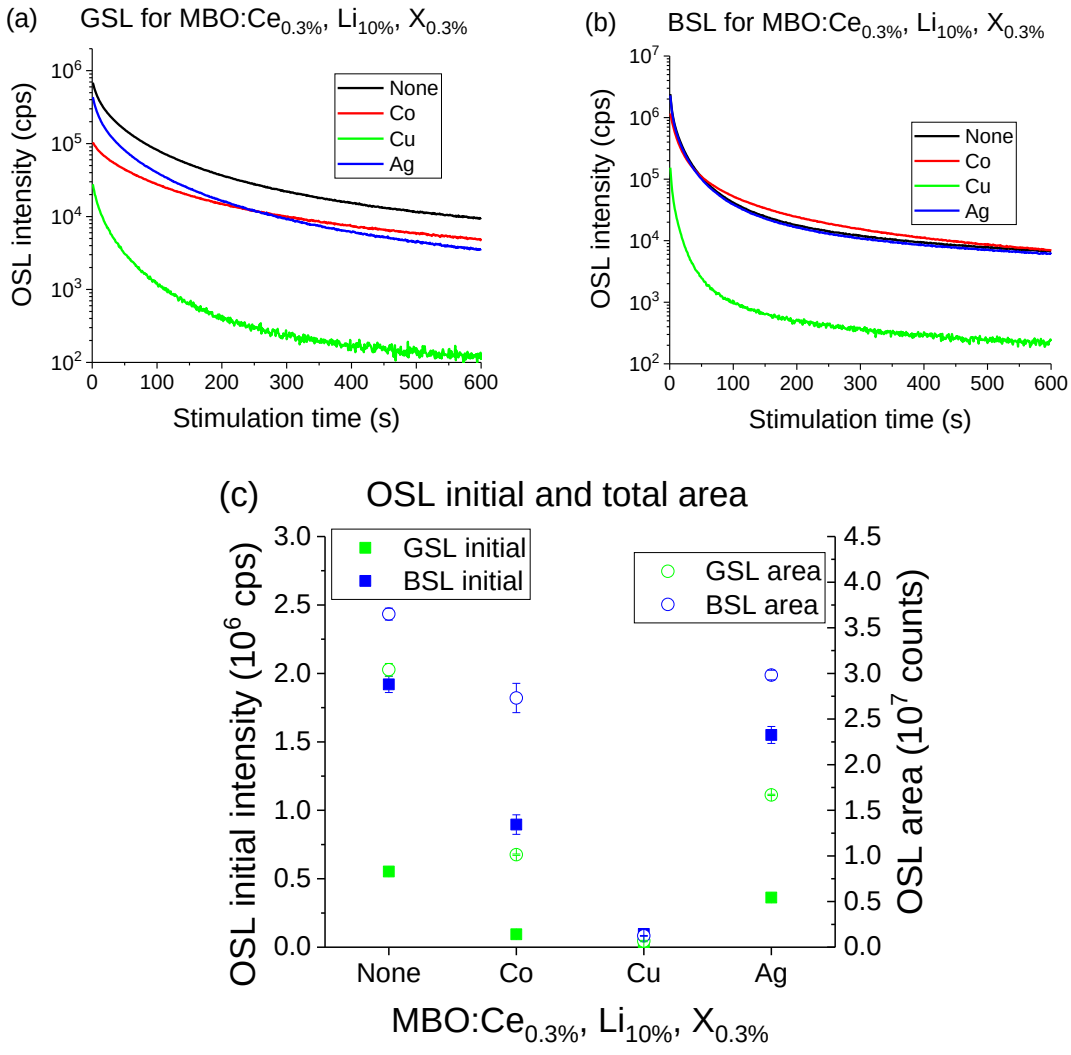

Figure 5-19: (a) GSL and (b) BSL for MBO:$Ce_{0.3\%}$,$Li_{10\%}$,$X_{0.3\%}$ where X is Co, Cu, or Ag. (c) OSL initial intensities and OSL total areas for the average of three aliquots of each material under

each green and blue stimulation. Error bars indicate the standard deviation of the three aliquots (many too small to see). OSL parameters used were: 90% LED intensity, 5 s β irradiation, Hoya U-340 filter, no aperture, and 10 mg aliquots.

Figure 5-19 show that copper destroys most of the OSL signal (orders of magnitude reduction) for both stimulations. Cobalt reduced the OSL intensity moderately (a factor of 2-3). Silver reduced the OSL intensity the least, ~ 40% in comparison with MBO:$Ce_{0.3\%}$,$Li_{10\%}$.

5.3.4 Reproducibility

Reproducibility for both TL and OSL of the new materials were explored using the same procedure as Section 4.3.1. The TL maximum, TL area, OSL initial, and OSL area were measured over 10 irradiation/readout cycles for three aliquots (10 mg, 5 s irradiations). The data for each aliquot were normalized to the first run. Then, the average across the three aliquots was found and standard deviation calculated. Here, the results are shown as the percent increase from run 1 to run 10. Data for each TL and OSL sensitization are shown in Figure 5-20. The results from the original material in Chapter 4, MBO:$Ce_{0.3\%}$,$Li_{10\%}$ with 900 °C anneal for 2 h with slow cooling and low-purity reagent, and the best material from the annealing study in Section 5.2.2, MBO:$Ce_{0.3\%}$,$Li_{10\%}$ with 700 °C anneal for 2 h with fast cooling and high-purity reagent, are shown for comparison.

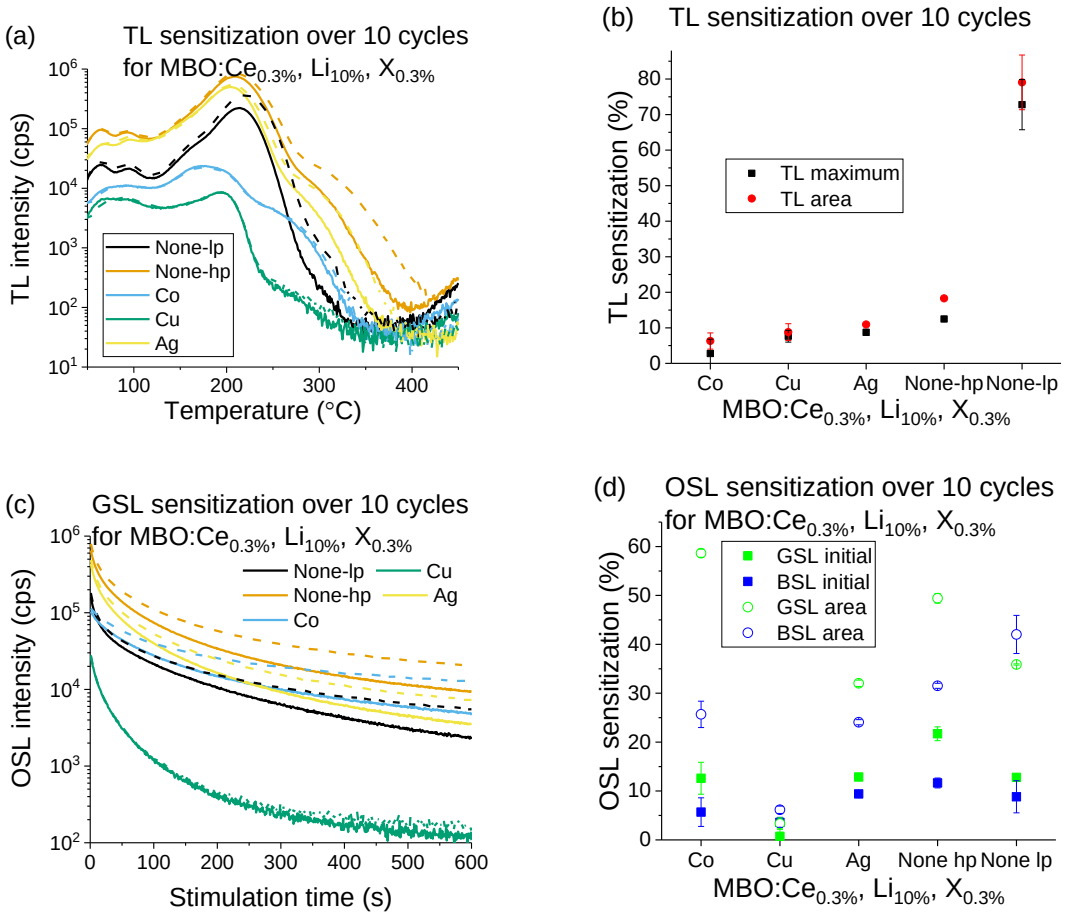

Figure 5-20: The sensitization over 10 irradiation readout cycles for MBO:$Ce_{0.3\%}$,$Li_{10\%}$,$X_{0.3\%}$. (a) TL curves for one aliquot from the first (solid line) and tenth (dashed line) readout. (b) Relative sensitization of the TL maximum and total area. (c) GSL curves for one aliquot from the first (solid line) and tenth (dashed line) readout. (d) Relative sensitization for OSL initial intensity and area. The error bars are the standard deviations of three aliquots. All irradiations were 5 s. Aliquots were 10 mg. TL readout parameters were 1 °C/s, U-340 filter, and no aperture. OSL parameters were 90% LED intensity, U-340 filter, and no aperture.

As can be seen, all the codopants reduced both the TL and OSL sensitizations of the material compared with high-purity reagent material. For OSL, the high-purity reagent material with modified annealing (see end of Section 5.2.2) had greater sensitization than the original low-purity reagent material. The codopant materials have OSL sensitizations

between the high-purity and low-purity reagent materials. The TL sensitization is decreased for all codoped materials compared with both high-purity and low-purity reagent materials.

5.3.5 Conclusions

Transition metal codopants, Co, Cu and Ag, were synthesized in hopes of improving TL and OSL properties of MBO. All codopants reduced RL, TL, and OSL signals. The reductions by Co and Cu are so large that no further investigation of these codopants was warranted.

Ag had TL and OSL intensity close enough to the high-purity reagent material that at least one round of further investigation is logical. The addition of Ag reduced sensitization for both TL and OSL. This is except for GSL area, all other sensitizations are comparable to what was seen in the original low-purity reagent material while maintaining much of the OSL and TL signal increases using high-purity reagent gains. All materials except the silver-doped show a small increase in their TL at around 450 °C. This could be indicative of a deep trap that is not being depleted by a TL readout to 450 °C. The reduced sensitization of the silver-doped sample would support this if the sensitization mechanism is a deep trap for the other materials.

5.4 ***Codopants II: lanthanides***

Codoping with lanthanides was attempted as well. As it was desired to test the VRBE or chemical shift model developed by Prof Dorenbos (Dorenbos, 2012), MBO:Ce,Li was codoped with every lanthanide except La, Pm and Tb. Lanthanum lacks 4f electrons that were desired in doping with lanthanides. Promethium was not used since it is radioactive. Terbium was expected to behave as recombination center for an electron

recombining with a hole which is the same hypothesized mechanism for cerium. As this would be introducing a recombination competitor, terbium was not codoped with cerium. Further discussion of modeling lanthanides in MBO can be found in Section 6.3. In this section, the focus was to find the brightest TL and OSL material. RL data are presented as well. As this section involves many samples, reproducibility data were not taken. The brightest material will have its reproducibility measured in the first refinement section (Section 5.5).

5.4.1 RL

RL were collected for three 10 mg aliquots of all codoped materials. RL without a third dopant are shown for reference. The error bars show the standard deviations between three aliquots. Data are shown in Figure 5-21. The inset shows a zoomed view of 300-400 nm using the same y-scale.

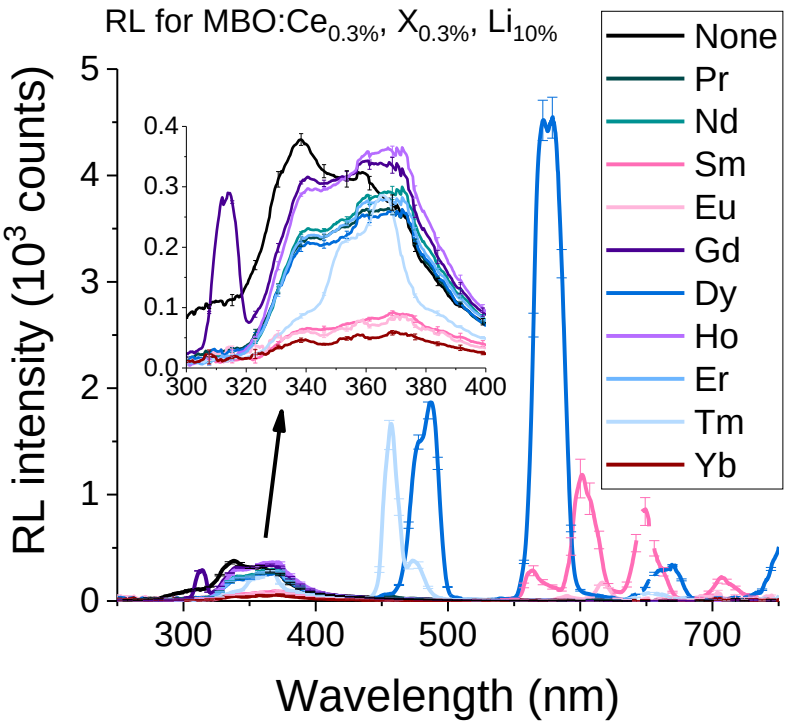

Figure 5-21: RL for MBO:$Ce_{0.3\%}$,$Li_{10\%}$,$X_{0.3\%}$ where X is Pr, Nd, Sm, Eu, Gd, Dy, Ho, Er, Tm, or Yb. Data are presented for the average of three 10 mg aliquots. Error bars show the standard deviation of three aliquots. The inset shows a zoomed view of the emission from 300-400 nm. RL parameters for these data are 100 s integration, 5 boxcar, average of 5. All data are corrected for spectrometer efficiency.

Emission outside of the 300-400 nm region is undesired, since it falls outside the optical filter range needed to detect Ce^{3+}, the intended recombination center. It is hoped that additional dopants can either introduce new traps which, upon stimulation, could feed the cerium recombination center, thus enhancing sensitivity of the material, or introduce new recombination centers that allow charges (holes) that cannot recombine at a cerium site to recombine and emit at wavelengths that would pass through the same filter as cerium.

Many of the dopants introduce new emissions, sometimes being much more intense than the Ce^{3+} emission. These have been summarized in Table 5-2 and an attempt to identify the transitions responsible has been made.

Table 5-2: A summary of RL emissions observed and the possible transitions responsible. Proposed transitions are based on Blasse and Grabmaier (1994).

Lanthanide	Emissions (nm)	Oxidation	Transitions
Ce	338, 358	3+	$5d \rightarrow {}^2F_{7/2}$ and $5d \rightarrow {}^2F_{5/2}$
Pr	460, 615	3+	${}^3P_0 \rightarrow {}^3H_4$ and ${}^3P_0 \rightarrow {}^3H_6$
Nd	300, 400	3+	$5d \rightarrow {}^4F$ and ${}^4G$
Sm	585, 650, 710	3+	${}^4G_{5/2} \rightarrow {}^6H$
Eu	350, 590, 700	3+	${}^5D \rightarrow {}^7F$
Gd	315	3+	${}^6P_{5/2} \rightarrow {}^8S_{7/2}$
Dy	490, 575, 660, 750	3+	${}^4F_{9/2} \rightarrow {}^6H_{15/2}$, ${}^4F_{9/2} \rightarrow {}^6H_{13/2}$, and other ${}^4F \rightarrow {}^6H$
Ho	None	NA	NA
Er	None	NA	NA
Tm	350, 470, 660	3+	${}^1D_2 \rightarrow {}^3F_4$ and other $5d \rightarrow 4f$
Yb	350, 381, 415, 435, 490, 550, 590, 620, 655, 680	3+	$5d \rightarrow {}^2F_{5/2}$

5.4.2 TL

TL curves were taken for all the new codoped materials using three 10 mg aliquots of each. The data presented here show emission through the U-340 filter, since this is the desired emission region. The average of the three TL curves of each material

are presented, in Figure 5-22a, with the error bars representing the standard deviation of those three curves. Normalized TL curves are shown in Figure 5-22b so that the position of main peak may be observed. The TL maximum and total area were tracked and are presented in Figure 5-22c.

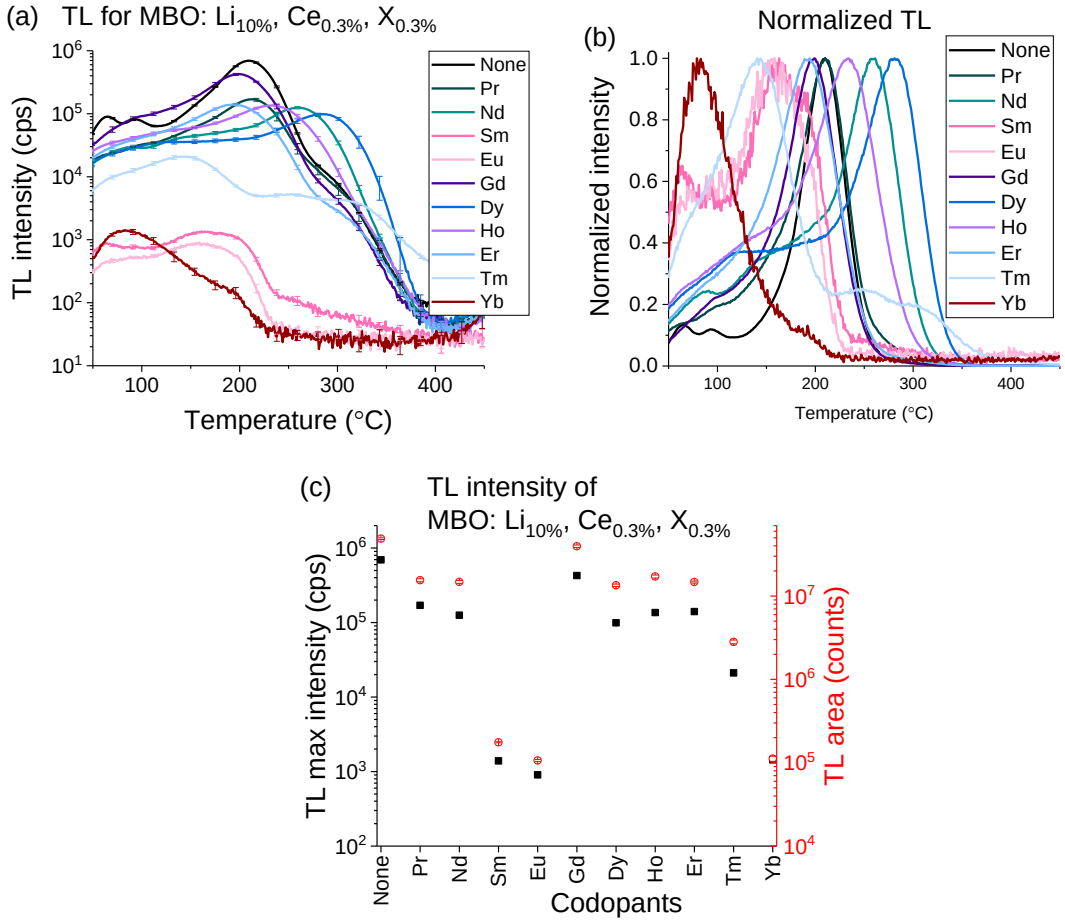

Figure 5-22: TL for MBO:$Ce_{0.3\%}$,$Li_{10\%}$,$X_{0.3\%}$ where X is Pr, Nd, Sm, Eu, Gd, Dy, Ho, Er, Tm, or Yb. (a) The average TL curves for three 10 mg aliquots of each dopant. The error bars indicate the standard deviation of the three aliquots. (b) Normalized TL of one aliquot of each dopant material. (c) TL maximum and total TL area for three aliquots of each material. Error bars (too small to see on these scales) represent the standard deviations of three aliquots of each material. TL parameters were: heating rate of 1 °C/s; 5 s irradiation; U-340 filter; no aperture.

The main peak position changes greatly with codopant varying from about 100 °C with Yb to about 300 °C with Dy. This shift will be discussed later, as the TL intensity is the focus for this Section rather than mechanism or model of the material.

Three of the codopants, Sm, Eu, and Yb, severely reduce the TL signal. This is likely a result of them introducing emission centers outside of the optical filter transmission range. This will be addressed further when developing a model for the behavior of lanthanides in MBO (Section 6.3). Tm reduces the TL by the same mechanism. However, Tm does not reduce the TL as much, since one of the Tm^{3+} transitions is within the transmission window of the Hoya U-340 filter. Pr, Nd, Dy, Ho, and Er show some decrease in the TL. Gd shows TL intensity approximately equal to the material without a third dopant.

5.4.3 OSL

GSL and BSL were collected for three 10 mg aliquots of all codoped material (Figure 5-23ab). The sample curves are of one aliquot of each material. The initial intensities and total OSL areas were tracked and are shown in Figure 5-23c and d. The averages of three aliquots are shown with error bars indicating the standard deviation of the three aliquots.

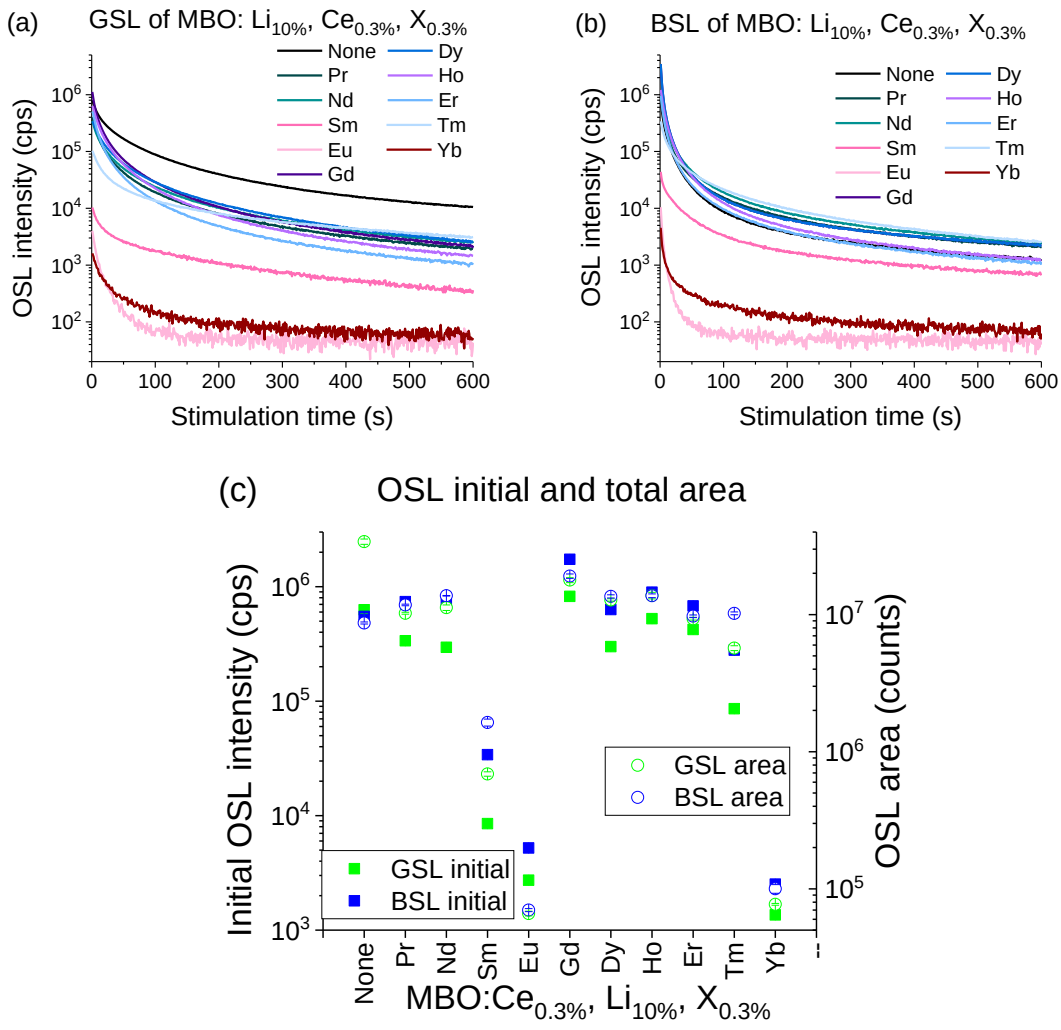

Figure 5-23: OSL for MBO:$Ce_{0.3\%}$,$Li_{10\%}$,$X_{0.3\%}$ where X is Pr, Nd, Sm, Eu, Gd, Dy, Ho, Er, Tm, or Yb. (a) The average GSL curves for three 10 mg aliquots of each dopant. Error bars indicate the standard deviation of the three aliquots. (b) BSL curves for three 10 mg aliquots of each dopant material. (c) GSL and BSL initial intensity and total OSL area for three aliquots of each material. Error bars (too small to see on these scales) represent the standard deviations of three aliquots of each material. OSL parameters were: 90% LED intensity; 5 s irradiation; U-340 filter; no aperture.

For OSL, Sm, Eu, and Yb, showed a decrease in intensity of orders of magnitude. Most of the other dopants showed no change in BSL intensity and a small reduction (<

factor of 2) in GSL intensity. Gd showed a small increase in intensity over the Ce, Li only material.

5.4.4 Conclusions

Gd showed the brightest TL and OSL. Many of the codopants introduced emission outside the transmission of the intended optical filter. If those codopants act as recombination centers, the TL and OSL would be reduced. However, Gd introduced emission that was within the optical window transmission. Further studies will be conducted optimizing the Gd concentration.

5.5 ***Varying dopant concentration of the third dopant***

After testing many different transition metal and lanthanide codopants, the brightest codopant from each group continued to a first round of refinement. In this section, the concentrations of Ag and Gd are varied to further brighten the TL and OSL of the material. Ag was doped in 0.1%, 0.3% and 1% concentrations. Gd was doped in 0.1%, 0.3%, 1%, 2%, and 4% concentrations. RL and reproducibility data were collected as well.

5.5.1 RL

RL were collected for three 10 mg aliquots of each dopant concentration for Ag and Gd. Curves are presented in Figure 5-24, and the error bars represent the standard deviation of the three aliquots. The 0% Gd or Ag sample shown is the material found to be the best in Section 5.2.2.

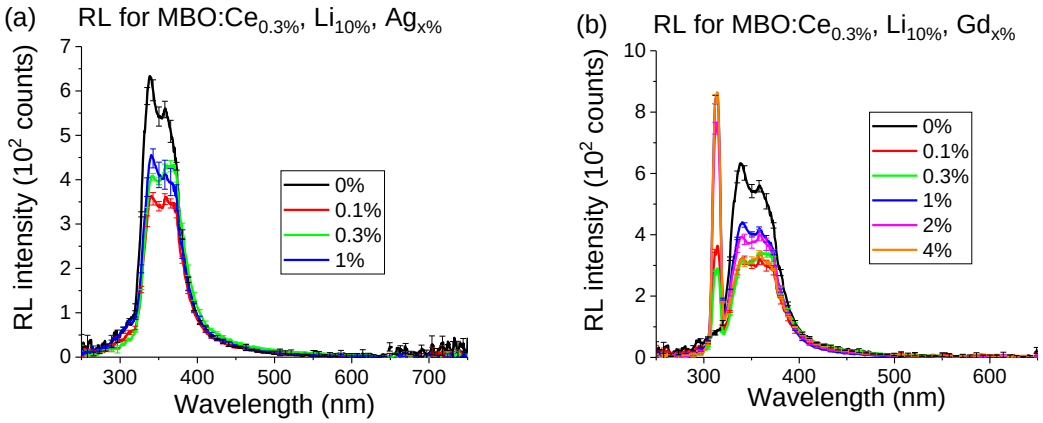

Figure 5-24: RL for (a) MBO:$Ce_{0.3\%}$,$Li_{10\%}$,$Ag_{x\%}$ and (b) MBO:$Ce_{0.3\%}$,$Li_{10\%}$,$Gd_{x\%}$ where X is the dopant concentration of the additional dopant (Ag or Gd). Shown are averages of three aliquots. The error bars indicate the standard deviation among these three aliquots. Parameters used are: 100 s integration time, average of 5 spectra, boxcar 5, and 10 mg aliquots.

Doping with silver does not introduce new emission bands. It is possible it is introducing a new trapping center or modifying an existing trap. Gadolinium shows clear Gd^{3+} emission which is within the transmission window of the U-340 filter. If the recombination mechanism is different for Gd, it may enhance the TL/OSL signal if those traps can be optically excited as well.

5.5.2 TL

TL were taken for the new materials using three 10 mg aliquots of each dopant concentration. TL curves for the silver doping are in Figure 5-25a, and TL curves for the gadolinium doping are in Figure 5-25b. The TL maximum and total area were tracked for each material.

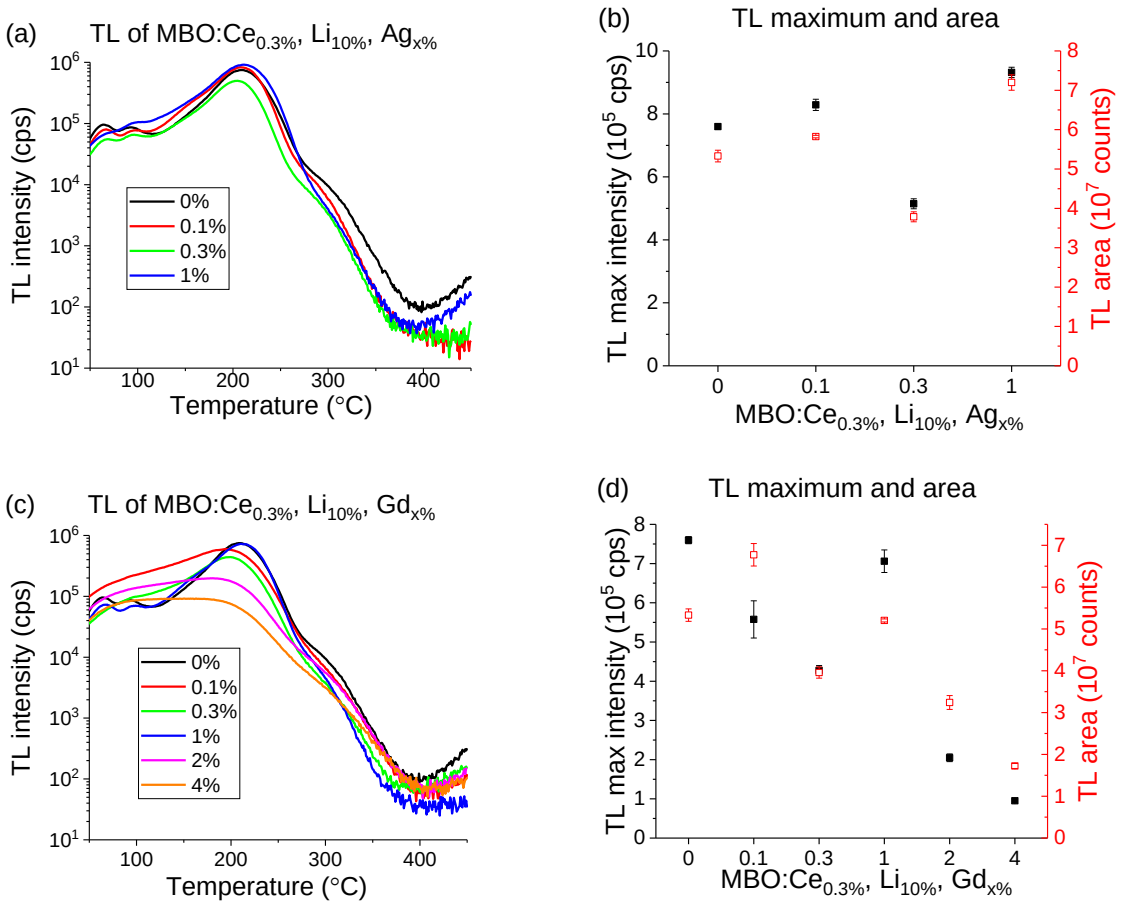

Figure 5-25: (a) Sample TL curves for single aliquots of MBO:$Ce_{0.3\%}$,$Li_{10\%}$,$Ag_{x\%}$ (X = 0, 0.1, 0.3, or 1) and (b) the TL area/maximum for those samples (average of three aliquots). (c) Sample TL curves for single aliquots of MBO:$Ce_{0.3\%}$,$Li_{10\%}$,$Gd_{x\%}$ (X = 0, 0.1, 0.3, 1, 2, or 4) and (d) the TL area/maximum for those samples (average of three aliquots). In (b) and (d), error bars are the standard deviation of three aliquots (many too small to see). TL parameters used were: 1 °C/s heating rate, 5 s β irradiation, Hoya U-340 filter, no aperture, and 10 mg aliquots.

The silver doped material had the brightest TL for 1% Ag concentration. Some of this may be due to the introduction of shoulder peaks around 100 °C and 300 °C. Overall, it was about 20% brighter than the material without silver.

For gadolinium, a concentration of 1% yielded the brightest TL of the Gd-doped material. However, there is no improvement in the brightness over the material without gadolinium.

5.5.3 OSL

GSL and BSL were collected for three 10 mg aliquots of all new materials and compared to a sample with no third dopant. The initial intensity and total OSL areas were tracked, also. Sample OSL curves for Ag doping are shown in Figure 5-26ab while the intensity is shown in Figure 5-26c. Sample OSL curves for Gd doping are shown in Figure 5-27ab while the intensity is shown in Figure 5-27c.

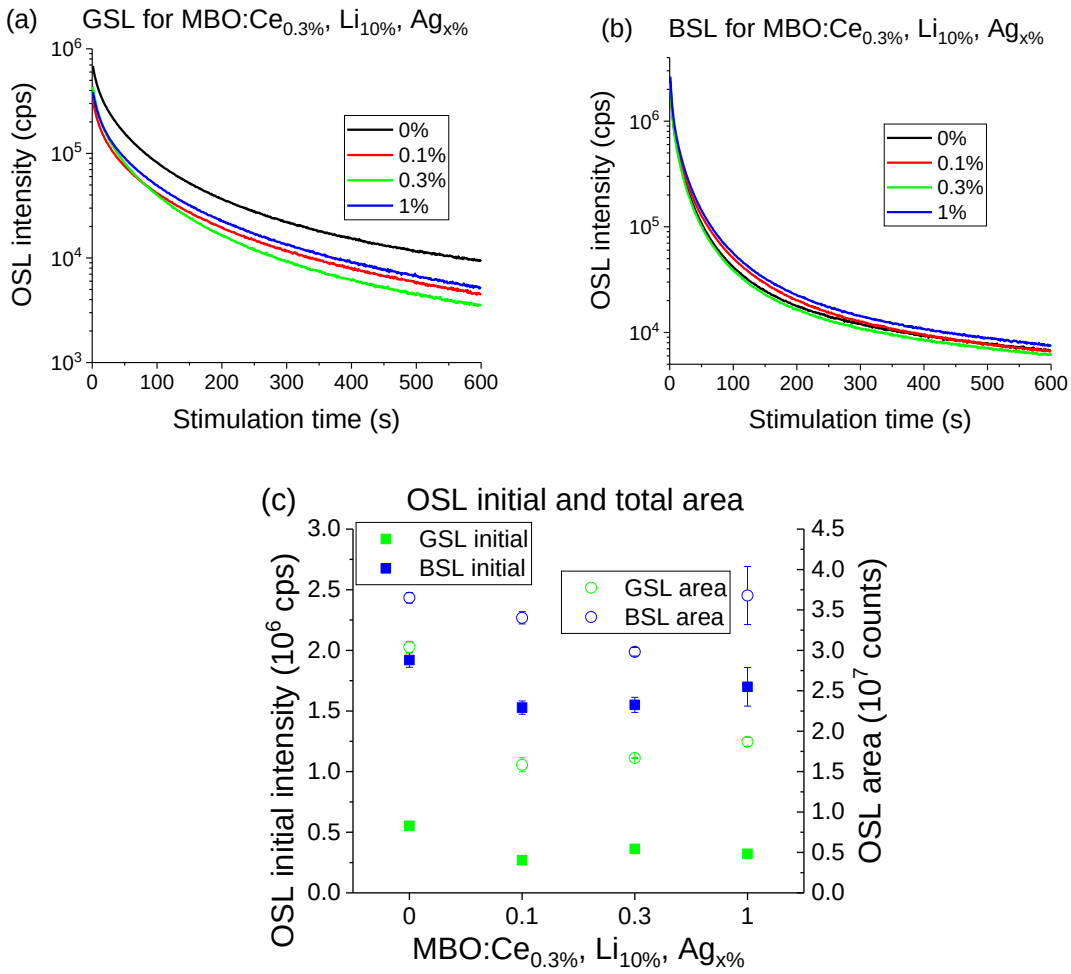

Figure 5-26: (a) GSL and (b) BSL for MBO:$Ce_{0.3\%}$,$Li_{10\%}$,$Ag_{x\%}$ where X is the concentration of Ag doping. (c) Initial OSL intensities and total OSL areas for the average of three aliquots of each material under each green and blue stimulation. Error bars indicate the standard deviation of three aliquots (many too small to see). OSL parameters used were: 90% LED intensity, 5 s β irradiation, Hoya U-340 filter, no aperture, and 10 mg aliquots.

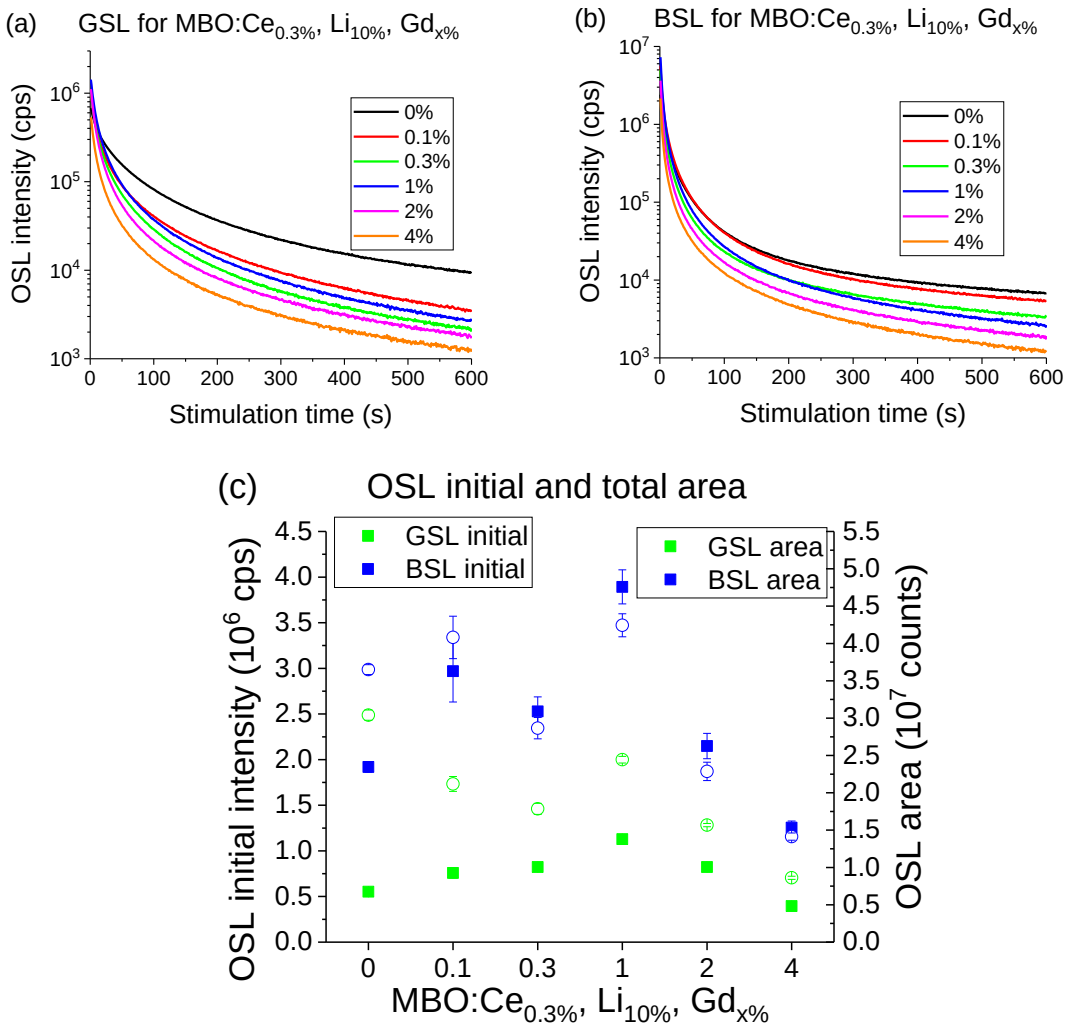

Figure 5-27: (a) GSL and (b) BSL for MBO:$Ce_{0.3\%}$,$Li_{10\%}$,$Gd_{x\%}$ where X is the concentration of Gd doping. (c) Initial OSL intensities and total OSL areas for the average of three aliquots of each material under each green and blue stimulation. Error bars indicate the standard deviation of three aliquots (many too small to see). OSL parameters used were: 90% LED intensity, 5 s β irradiation, Hoya U-340 filter, no aperture, and 10 mg aliquots.

Silver doping did not show a trend of OSL intensity increase with dopant concentration. The brightest OSL was for the sample doped with 1% silver. However, there is no improvement over the material with no silver-doping.

For gadolinium, the curves changed far more visibly. The optimal dopant concentration for Gd is 1%. Compared with the material without Gd-doping both initial

intensities approximately doubled and the BSL area increased about 20% while the GSL area decreased about 25%. The remaining signal after 600 s of stimulation was about a third of what the material without Gd shows.

5.5.4 Reproducibility

Reproducibility for both TL and OSL of the new materials were explored using the same procedure as Section 5.3.4. The TL maximum, TL area, OSL initial, and OSL area were found over 10 irradiation/readout cycles for three aliquots (10 mg, 5 s irradiations). The data for each aliquot were normalized to the first run. Then, the average across the three aliquots was found and standard deviation calculated. Here, the results are shown as the percent increase in the signal from run 1 to run 10. These data are presented for each codoped material using three aliquots. Data for each TL and OSL sensitization for silver doping are shown in Figure 5-28. Data for each TL and OSL sensitization for gadolinium doping are shown in Figure 5-29. The results from the best material from the annealing study in Section 5.2.2 are shown for comparison.

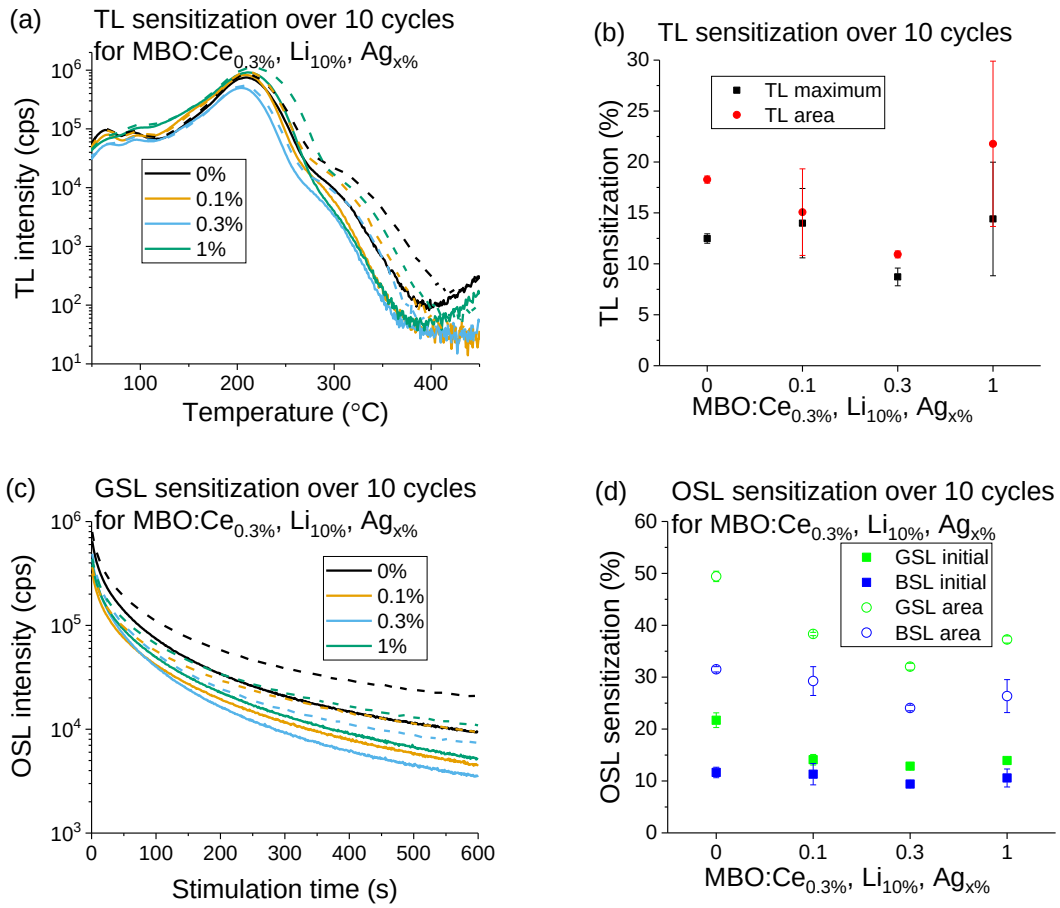

Figure 5-28: The reproducibility over 10 irradiation readout cycles for MBO:$Ce_{0.3\%}$,$Li_{10\%}$,$Ag_{x\%}$: (a) TL curves for single aliquots showing run 1 (solid) and run 10 (dashed); (b) sensitization for TL maximum and total area (average of three aliquots); (c) GSL curves for single aliquots showing run 1 (solid) and run 10 (dashed); (d) sensitization for OSL initial intensity and area (average of three aliquots). The error bars are the standard deviations of three aliquots.

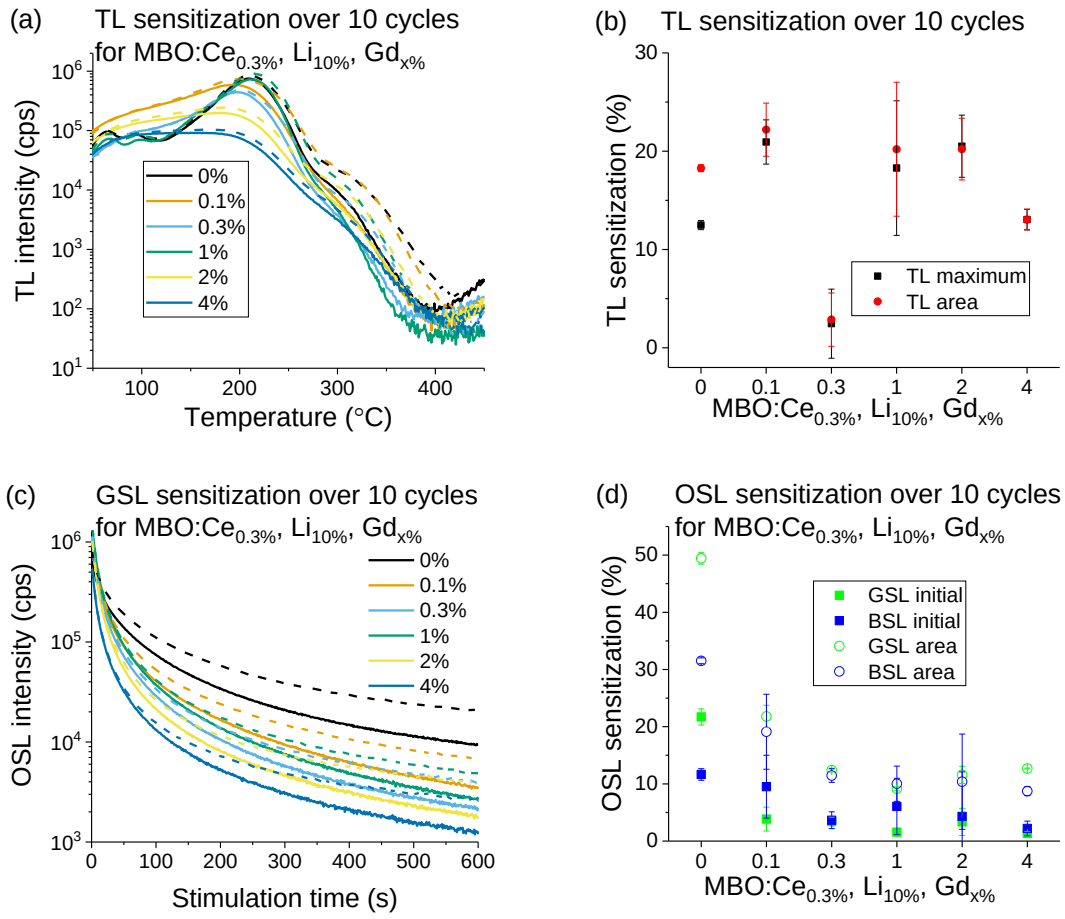

Figure 5-29: The reproducibility over 10 irradiation readout cycles for MBO:$Ce_{0.3\%}$,$Li_{10\%}$,$Gd_{x\%}$: (a) TL curves for single aliquots showing run 1 (solid) and run 10 (dashed); (b) sensitization for TL maximum and total area (average of three aliquots); (c) GSL curves for single aliquots showing run 1 (solid) and run 10 (dashed); (d) sensitization for OSL initial intensity and area (average of three aliquots). The error bars are the standard deviations of three aliquots.

The addition of silver shows no trend for the TL sensitization with doping concentration, but doping with 0.3% reduced the sensitization by about 70% compared with the 0% silver sample. For OSL, silver doping shows little influence on the BSL initial intensity and a modest decrease (<20%) in BSL area going to a higher silver concentration. GSL shows a decrease in sensitization of about 40% when doped with 1% silver rather than no silver.

The addition of gadolinium shows no strong change in the TL sensitization except for 0.3%, which reduces sensitization approximately fourfold. For OSL, all concentrations of Gd dramatically reduce the sensitization. The best improvement was by the material doped with 1% Gd. The BSL sensitization was reduced about threefold from the 0% sample. GSL area sensitization was reduced by almost 2.5 times while the initial intensity sensitization was reduced by more than an order of magnitude.

5.5.5 Conclusions

In this section, Gd has been found to increase the OSL intensity more than Ag, and Gd reduces the sensitization. For TL sensitization, both materials show less of the possible deep trap around 450 °C than the material only doped with cerium and lithium. For OSL sensitization, the intensity after 600 s of stimulation is lower for the Gd-doped and Ag-doped materials compared with the two-dopant material. This may indicate less dose build up than for the two-dopant material. If this mechanism is the cause of the sensitization, it would account for the decreased sensitization of the triple-doped materials.

Silver did not introduce any new RL emission. Silver-doping with 1% increased the TL by about 20% over the material with no third dopant but did not increase the OSL.

The RL for Gd doping show a new recombination center that is within the transition window of the filter used for collecting the Ce emission which likely accounts for the increase in TL and OSL signals. A Gd concentration of 1% showed no change to the TL intensity but increased the OSL by double. The OSL sensitization for the 1% Gd material was improved to less than 10% for all measurements compared with the 13-50% sensitization in the material without Gd. The introduction of Gd may introduce a new radiative transition within the filter for charges that had previously recombined non-radiatively.

5.6 ***Varying lithium concentration***

Now that doping with 1% Gd has been established to have the brightest TL/OSL and show the least sensitization among all tested, a final round of dopant concentration optimization was performed; the lithium concentration was varied. One sample removing Ce as a codopant was synthesized as well. The RL, TL, and OSL are presented for these samples.

5.6.1 RL

RL were collected for three 10 mg aliquots of each dopant concentration for Li and the sample without Ce. A sample with no Gd and 10% Li (best material from Section 5.2.2) is shown for comparison. Curves are presented in Figure 5-30, and the error bars represent the standard deviation of the three aliquots.

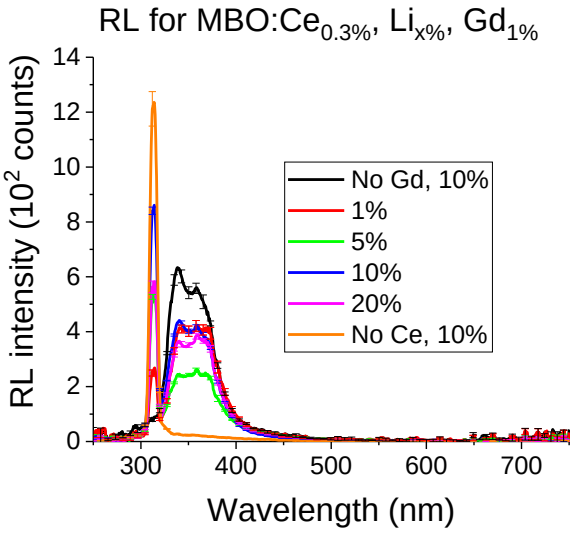

Figure 5-30: RL MBO:$Ce_{0.3\%}$,$Li_{x\%}$,$Gd_{1\%}$ where X is the concentration of lithium doping. Shown are averages of three aliquots. The error bars indicate the standard deviation among these three aliquots. Parameters used are: 100 s integration time, average of 5 spectra, boxcar 5, and 10 mg aliquots.

Changing the concentration of Li from 10% decreases the RL intensity for all concentrations. The sample without Ce shows a 50% increase in the Gd emission and removes the Ce emission. Changing the lithium concentration does not introduce or eliminate any emission centers.

5.6.2 TL

TL were taken for all the new codoped materials and compared with a sample with no Gd doping. Three 10 mg aliquots of each material were prepared. The TL maximum and total TL area were tracked for all samples. Sample TL curves for a single aliquot of each sample are shown in Figure 5-31a, and TL intensity for three aliquots of each sample are shown in Figure 5-31b.

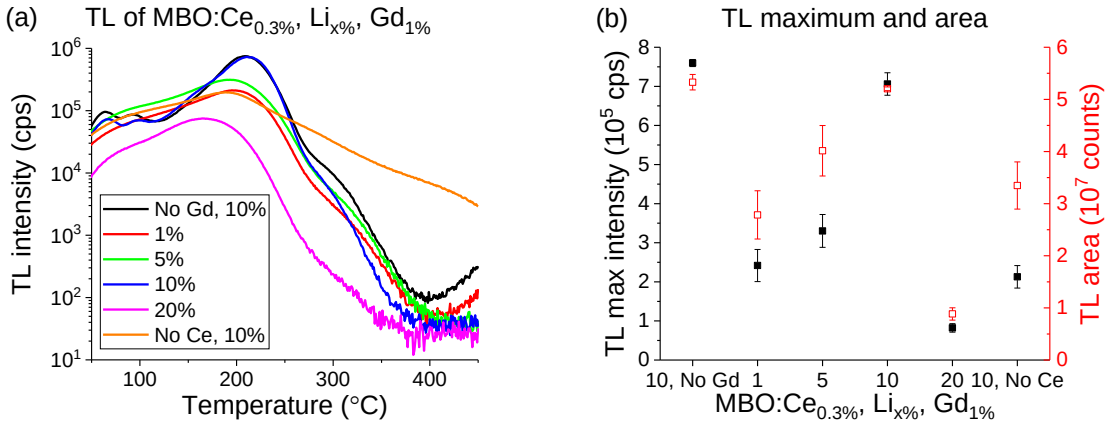

Figure 5-31: TL for MBO:$Ce_{0.3\%}$,$Li_{x\%}$,$Gd_{1\%}$ where X is the concentration of lithium doping. (a) Shows TL curves for single aliquots of each material. (b) Shows the TL maximum and the TL total area for the average of three aliquots of each material. The error bars show the standard deviation of three aliquots. TL parameters used were: 1 °C/s heating rate, 5 s β irradiation, Hoya U-340 filter, no aperture, and 10 mg aliquots.

The TL curve shape is the most well defined for a Li concentration of 10%. For other lithium concentrations, the TL glow peaks melded together into one broad peak. The

sample without Ce shows TL over the entire temperature regime sampled. While interesting, the lack of Ce decreased the TL intensity. The sample doped with 10% Li showed the brightest TL.

5.6.3 OSL

OSL curves were taken for three 10 mg aliquots for each GSL and BSL and compared with curves from material with no Gd-doping. Raw OSL curves are shown for one of the aliquots for each dopant under each stimulation in Figure 5-32ab. The initial intensity and total OSL area are shown in Figure 5-32c for each codoped material. The error bars indicate the standard deviation of three aliquots.

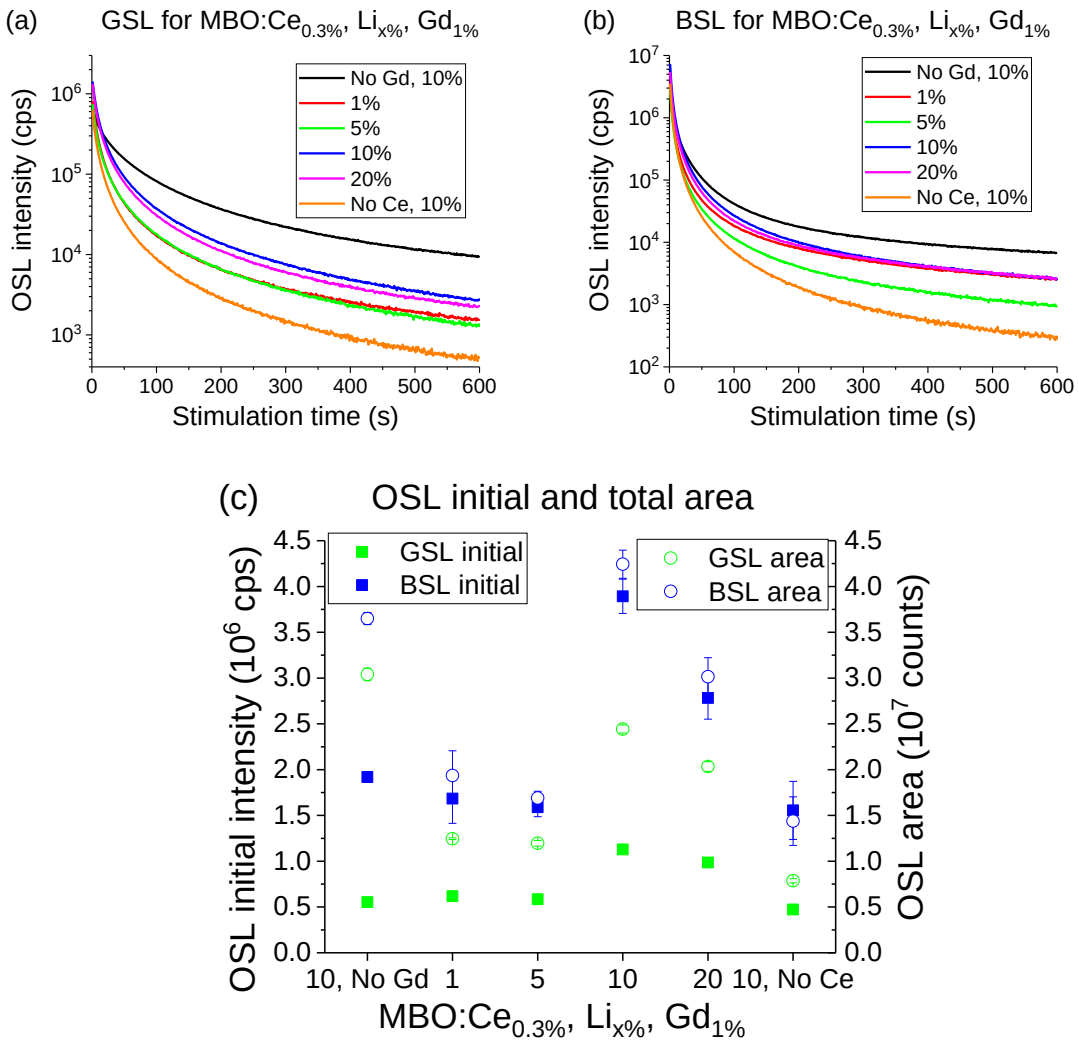

Figure 5-32: (a) GSL and (b) BSL for MBO:$Ce_{0.3\%}$,$Li_{x\%}$,$Gd_{1\%}$ where X is the concentration of Li doping. (c) Initial OSL intensities and total OSL areas for the average of three aliquots of each material under each green and blue stimulation. Error bars indicate the standard deviation of three aliquots (many too small to see). OSL parameters used were: 90% LED intensity, 5 s β irradiation, Hoya U-340 filter, no aperture, and 10 mg aliquots.

The OSL intensity was greatest for 10% lithium doping. Removal of Ce as a codopant harmed the OSL intensity by around a factor of three. Using less than 10% lithium resulted in relatively weak OSL also (reduced by a factor of two).

5.6.4 Reproducibility

Reproducibility for both TL and OSL of the new materials were explored using the same procedure as Section 5.3.4. The TL maximum, TL area, OSL initial, and OSL area were found over 10 irradiation/readout cycles for three aliquots (10 mg, 5 s irradiations). The data for each aliquot were normalized to the first run. Then, the average across the three aliquots was found and standard deviation calculated. Here, the results are shown as the percent increase from run 1 to run 10. These data are presented for each codoped material using three aliquots. Data for each TL and OSL sensitization for varying lithium doping are shown in Figure 5-33. The results from the best material from the annealing study in Section 5.2.2 are shown for comparison.

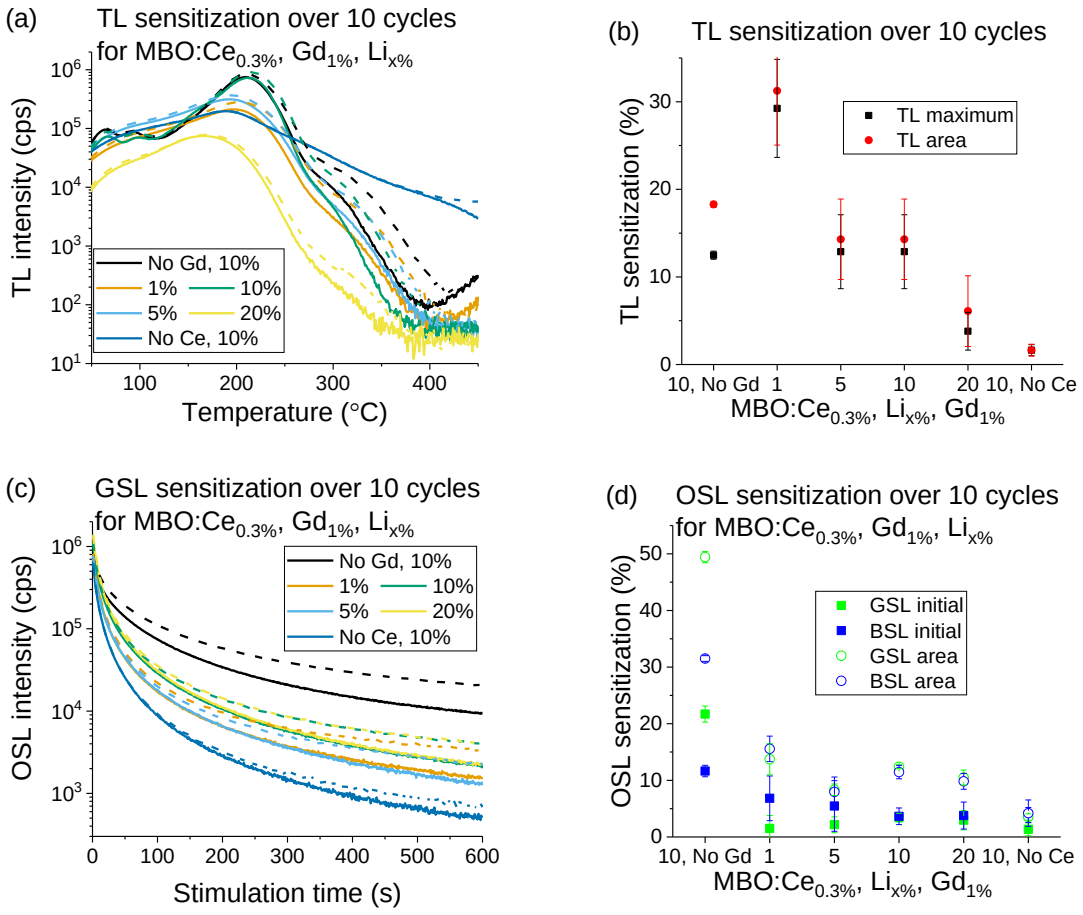

Figure 5-33: The reproducibility over 10 irradiation readout cycles for MBO:$Ce_{0.3\%}$,$Gd_{1\%}$,$Li_{x\%}$: (a) TL curves for single aliquots showing run 1 (solid) and run 10 (dashed); (b) sensitization

for TL maximum and total area (average of three aliquots); (c) GSL curves for single aliquots showing run 1 (solid) and run 10 (dashed); (d) sensitization for OSL initial intensity and area (average of three aliquots). The error bars are the standard deviations of three aliquots.

The TL showed moderate sensitization which was less than the original low-purity reagent material but is more than the high-purity reagent material with no Gd. The OSL sensitization showed no clear change with varying lithium concentration. All OSL sensitizations were less than the original material and the high-purity reagent material.

5.6.5 Conclusions

Overall, the best formulation remains MgB_4O_7:$Ce_{0.3\%}$,$Gd_{1\%}$,$Li_{10\%}$. Changing lithium concentration resulted in minimal change to the RL. Changing the lithium concentration from 10% resulted in a decrease in the TL and OSL signal. Removal of Ce harmed the OSL intensity the most. Lithium concentration did not show a clear impact on the sensitization of the material. Thus, the only changes observed by changing the lithium concentration from 10% were detrimental to the TL/OSL brightness.

5.7 ***Final material additional properties***

Two additional studies were conducted on the brightest material, MBO:$Ce_{0.3\%}$,$Gd_{1\%}$,$Li_{10\%}$. A dose response was conducted using BSL, since BSL resulted in the brightest OSL and lower sensitization than GSL. A dark fading test for BSL was conducted also. With the sensitization data already presented, these studies allow comparison with the initial material, MBO:$Ce_{0.3\%}$,$Li_{10\%}$, from Chapter 4 to determine whether there were improvements in the dosimetric properties.

5.7.1 BSL dose response

A final BSL dose response study was done comparing the brightest codoped material (MBO:$Ce_{0.3\%}$,$Gd_{1\%}$,$Li_{10\%}$), the best high-purity reagent material following the annealing study (MBO:$Ce_{0.3\%}$,$Li_{10\%}$ anneal 2 h at 700 °C and fast cooling from Section 5.2.2), the original material (MBO:$Ce_{0.3\%}$,$Li_{10\%}$ annealed 2 h at 900 °C and slow cooled from Chapter 4), and Al_2O_3:C. Three aliquots of each material were prepared for BSL since blue stimulation had been found preferred for brighter emission. Following a TL run to remove any background dose received aliquots were subject to 10 OSL readouts with no dose. This was used to estimate the minimal detectable dose for the materials in the Risø TL/OSL reader. The readout at 0.5 Gy was used to estimate the sensitivity of the materials.

BSL data were collected for three 10 mg aliquots of each material for doses of 0.1, 0.2, 0.5, 1, 2, 5, 10, 20, 50, and 100 Gy. The LED intensity was 90%, the filter was U-340, and there was no aperture up to 1 Gy. A 4 mm aperture was added for the remaining higher doses. The readout at 1 Gy was repeated to allow a conversion factor for the intensity to be calculated to present all intensities as if no aperture were used. The intensities with dose are shown inFigure 5-34.

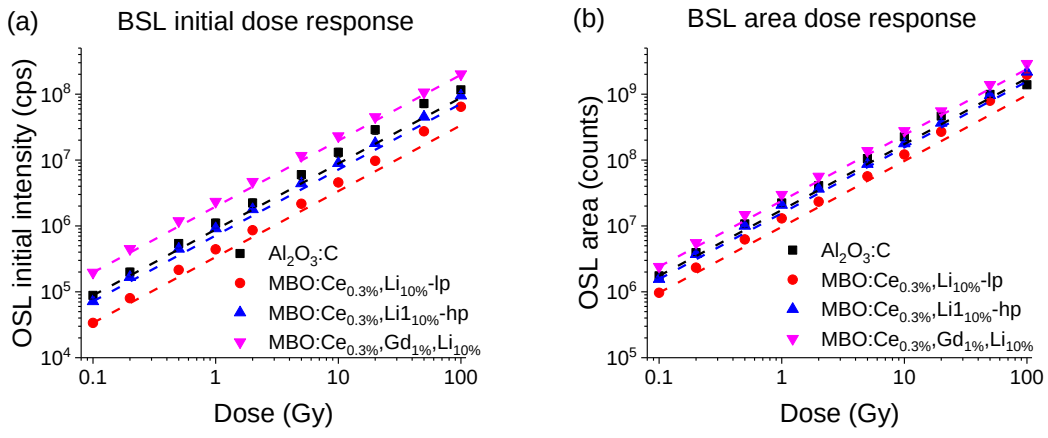

Figure 5-34: Dose response for BSL (a) initial intensity and (b) total area for Al_2O_3:C, the original MBO:$Ce_{0.3\%}$,$Li_{10\%}$ from Chapter 4, the improved MBO:$Ce_{0.3\%}$,$Li_{10\%}$ from Section 5.2,

and MBO:$Ce_{0.3\%}$,$Gd_{1\%}$,$Li_{10\%}$ from Section 5.6. Dashed lines show linearity based on the lowest dose point for each material. Error bars show the standard deviation of three aliquots but are too small to see on these scales.

As expected for this dose range, Al_2O_3:C became supralinear at about 10 Gy. The original material shows the onset of supralinearity around 20 Gy and no saturation. Both improved materials are linear for the full range, with the Gd material having the brighter intensity. Thus, the new materials have improved linear dose ranges over both Al_2O_3:C and the original MBO:$Ce_{0.3\%}$,$Li_{10\%}$ material.

With the background readouts and the 0.5 Gy readout, sensitivity and minimum detectable dose were estimated for each material for initial intensity and area. The minimal detectable dose is taken as 3 standard deviations of the 0 Gy readouts. The results are shown in Table 5-3.

Table 5-3: Estimations of minimal detectable dose for BSL for Al_2O_3:C, the original MBO:$Ce_{0.3\%}$,$Li_{10\%}$ from Chapter 4, the improved MBO:$Ce_{0.3\%}$,$Li_{10\%}$ from Section 5.2, and MBO:$Ce_{0.3\%}$,$Gd_{1\%}$,$Li_{10\%}$ from Section 5.6.

Measurement	Material	3σ of BG	Intensity 0.5 Gy	MDD (μGy)
Initial intensity	Al_2O_3:C	14 cps	$5.2(8) \times 10^5$ cps	14(2)
	MBO-lp	26 cps	$1.94(12) \times 10^5$ cps	68(4)
	MBO-hp	24 cps	$4.21(12) \times 10^5$ cps	28.1(8)
	MBO-Gd	12 cps	$1.14(3) \times 10^6$ cps	5.07(13)
Total OSL area	Al_2O_3:C	6.9×10^3 counts	$1.0(1) \times 10^7$ counts	347(35)
	MBO-lp	7.5×10^3 counts	$5.2(3) \times 10^6$ counts	$7.2(4) \times 10^2$
	MBO-hp	13×10^3 counts	$9.18(18) \times 10^6$ counts	704(14)

	MBO-Gd	4.5×10^3 counts	$1.41(4) \times 10^7$	159(4)

The greatest sensitivity and lowest MDD was found for MBO:$Ce_{0.3\%}$,$Gd_{1\%}$,$Li_{10\%}$. Using the Risø TL/OSL reader, which is not optimized for dosimetry, the MDD was estimated at 5 µGy for initial intensity and 159 µGy for total area. This is an improvement over the next best, Al_2O_3:C, by a factor of two. The MBO:$Ce_{0.3\%}$,$Li_{10\%}$ high-purity reagent material shows MDD worse than Al_2O_3:C by about double, and the original low-purity reagent MBO:$Ce_{0.3\%}$,$Li_{10\%}$ was worse yet. It should be noted that the Risø TL/OSL reader with a U-340 filter is not optimized for Al_2O_3:C (Markey et al., 1995).

5.7.2 Short term fading for BSL

A short term BSL dark fading study was conducted for MBO:$Ce_{0.3\%}$,$Gd_{1\%}$,$Li_{10\%}$. Three 10 mg aliquots were used for each fading time. All aliquots were irradiated for 5 s, allowed to fade varying durations, and read out for 600 s using blue LEDs at 90% intensity. They were re-irradiated and readout as a reference measurement. The faded initial intensity and total OSL area were normalized to those from the reference dose. The intensities were renormalized to the 0 h fading. These results are shown in Figure 5-35.

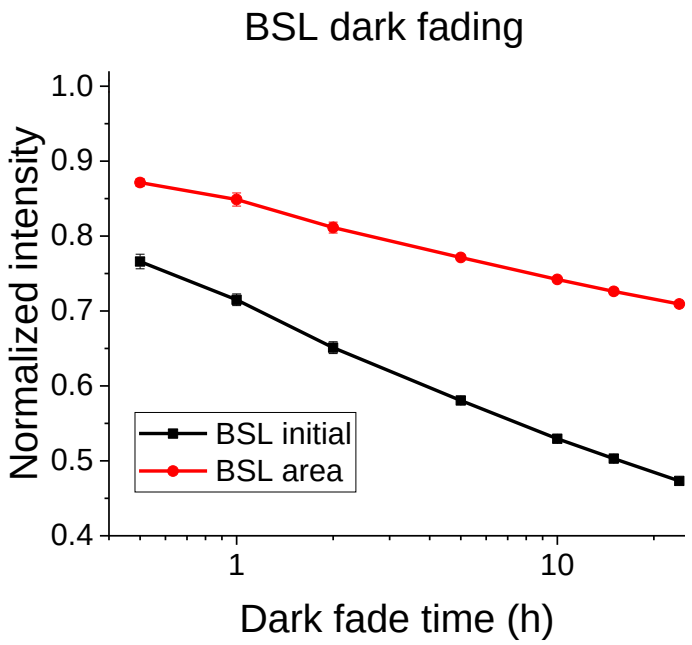

Figure 5-35: BSL dark fading. Intensities are normalized to a reference dose readout taken following the fade time. The points are the average of three 10 mg aliquots. Error bars (mostly too small to see) show the standard deviation of the three aliqouts.

The initial OSL intensity fades by more than 50% in 24 h. This is likely due to the emptying of shallow traps that are responsible for much of the initial OSL intensity. The OSL area fades about 30% in 24 h. The fading of the area is slowing but has not stabilized at the end of 24 h.

A second test was done to see if the fading was a result of the shallow traps depleting at room temperature. OSL fading was done for 0 h, 0.5 h, 1 h, 2 h, 5 h and 24 h with a 120 °C TL readout immediately following irradiation. The intensities were subject to normalization to reference dose and renormalization to the 0 h fading intensity, as in the first study. The results are in Figure 5-36.

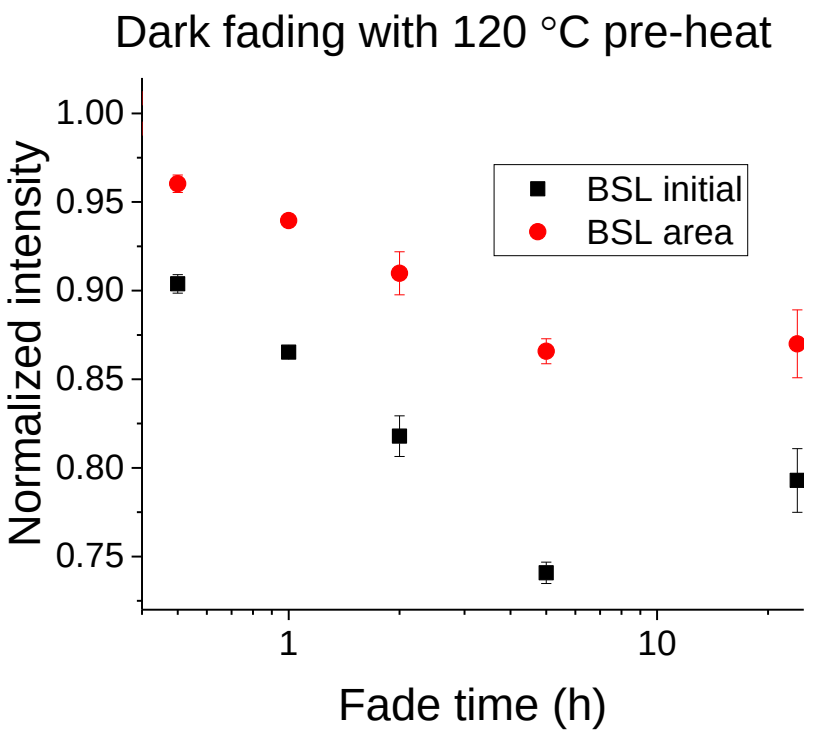

Figure 5-36: BSL dark fading for samples irradiated, pre-heated to 120 °C, allowed to cool, and readout after varying amount (0, 0.5, 1, 2, 5, or 24 h) of dark fading. Intensities are normalized to a reference dose for each aliquot and renormalized to the 0 h fading intensity. Data are the average of three 10 mg aliquots. The error bars show the standard deviation of three aliquots.

As is shown, the dark fading is reduced when the shallow trap is annealed out. The initial intensity fades about 21% and the total area fades about 13% in 5 h and stabilizes. While this is improved over the dark fading with no pre-heat, further study is needed to determine if this fading is constant over long periods of time (10s of days) or if the material continues to fade. Study should be conducted to determine an optimal pre-heating temperature also.

5.7.3 Sensitization comparison

BSL reproducibility data were collected for three 10 mg aliquots of Al_2O_3:C. The same irradiation/readout cycle was used (5 s irradiation with 600 OSL readout). The intensity data are compared with those of the original, low-purity reagent MBO:$Ce_{0.3\%}$,$Li_{10\%}$, the high-purity reagent MBO:$Ce_{0.3\%}$,$Li_{10\%}$ annealed at 700 °C for 2 h and fast cooled, and MBO:$Ce_{0.3\%}$,$Gd_{1\%}$,$Li_{10\%}$. Data are shown in Figure 5-37.

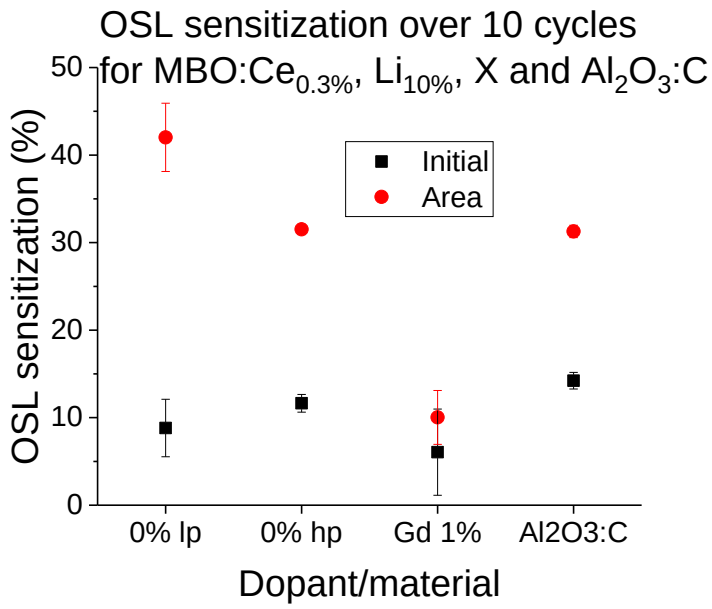

Figure 5-37: Comparison of sensitization for low-purity reagent MBO:$Ce_{0.3\%}$,$Li_{10\%}$, high-purity reagent MBO:$Ce_{0.3\%}$,$Li_{10\%}$, MBO:$Ce_{0.3\%}$,$Gd_{1\%}$,$Li_{10\%}$, and Al_2O_3:C for 10 irradiation/readout cycles of 5 s irradiation and 600 s BSL readout. No background subtraction was done. Error bars indicate the standard deviation of three 10 mg aliquots.

The sensitization of the final, MBO:$Ce_{0.3\%}$,$Gd_{1\%}$,$Li_{10\%}$, was far lower than any of the other materials. Al_2O_3:C showed sensitization about equal to the high-purity reagent MBO:$Ce_{0.3\%}$,$Li_{10\%}$. Al_2O_3:C is known to sensitize at these larger doses (~1 Gy) due to deep traps (Markey et al., 1996). The low sensitization using 5 s irradiations (~0.35 Gy) is encouraging for the use of MBO:$Ce_{0.3\%}$,$Gd_{1\%}$,$Li_{10\%}$ as a dosimeter.

5.8 ***Conclusions***

In this chapter, the initial material was improved through three means: use of high-purity reagent, change of post-synthesis annealing treatment, and addition of Gd as a codopant. Multiple rounds of codoping were conducted to find the brightest material with the lowest sensitization. MBO:$Ce_{0.3\%}$, $Gd_{1\%}$,$Li_{10\%}$ has TL 3-4 times brighter than the original material, OSL area 3-4 times brighter (each stimulation) than the original material, and OSL initial intensity ~8.5 times brighter (each stimulation) than the original material. The increase in intensity could be a result of a new emission center introduced by Gd in the bandpass region of the U-340 filter.

The TL sensitization has been reduced to a quarter of the original material and the OSL sensitizations have been reduced to under 10% over 10 irradiation/readout cycles with the GSL initial intensity showing the best improvement and lowest sensitization at 1.5%.

The dose response for BSL is linear over the full range test 0.1-100 Gy. The minimal detectable dose was estimated at 5 µGy for the initial intensity and 159 µGy for total OSL area which is a lower threshold than Al_2O_3:C by a factor of two in both instances. The sensitivity is sufficiently good that this material may be useful for personal dosimetry as well as medical dosimetry especially with a readout system intended for dosimeters.

The short fading study showed 50% fading of the initial intensity in 24 h and 30% fading of the total OSL area. The fading was reduced to 21% of the initial intensity and 13% of the the total area over 24 h by emptying the shallow traps with a pre-heating to 120 °C. However, a multiple month fading test would be necessary to pursue this material as a personal dosimetry material. The fading is the greatest challenge to the new material.

Finally, the sensitization observed was much lower (2-3 times) than that of Al_2O_3:C.

CHAPTER 6

MECHANISMS FOR VARIOUS EFFECTS IN MgB_4O_7

The aim of this chapter is to study more in depth some of the behaviors of MBO. First, sensitization will be examined to determine mechanisms for both TL and OSL sensitization. Next, curve fitting will be revisited for both TL and OSL to attempt more realistic fits and discuss avenues for further improvements. Finally, the main thrust will be developing an understanding of the traps and recombination centers. The chemical shift model will be used to develop a valence referred binding energy diagram for MBO to understand lanthanide energy states in this material. TL and optical studies were done to improve the model that can be developed from literature values as well as test for consistency.

6.1 ***Model for sensitization***

The results presented in this section are for MBO:$Ce_{0.3\%}$,$Li_{10\%}$ prepared using high-purity reagent and annealed at 700 °C for 2 h with fast cooling (see Section 5.2.2). As shown in Section 5.2.2, TL sensitization was significantly reduced in comparison with the material prepared using low-purity reagent, but remained a problem for both OSL and TL. A more detailed study was conducted to identify the mechanism(s) for sensitization. Mechanisms for sensitization in OSL include the filling of “optically-inactive” trapscompeting with recombination, incomplete trap emptying, and phototransfer to

shallow traps. Mechanisms for sensitization of TL include, deep traps or changes to the material with heating.

OSL sensitization is the primary concern. Phototransfer from deeper traps to traps at about 75 °C has been demonstrated in Section 4.4.1. This trap may have introduced sensitization since OSL readouts were taken shortly after irradiation. Without a preheating or time for the shallow trap to deplete at room temperature, OSL readouts started with the shallow traps at varying degrees of filling. In this case, sensitization with subsequent irradiation/readout cycles can occur for two reasons: (a) phosphorescence from shallow traps increase with dose and can be confounded with the OSL signal measured right after irradiation; (b) shallow traps that compete with the recombination during OSL readout are filled up, resulting in an increase in the recombination probability. If shallow traps are responsible for the apparent OSL sensitization, the sensitization could be removed with allowing aliquots to rest at room temperature, so the shallow traps can empty naturally by thermal fading. The first subsection examines this possible sensitization mechanism.

Another possible sensitization mechanism is residual dose or incomplete bleaching. There is evidence that 600 s of OSL stimulation is insufficient to empty all traps (Section 4.4.1). The second subsection examines this sensitization mechanism.

A third subsection uses the information gained in the first two subsections to modify the OSL readout sequence. This sequence using a pre-heating and TL to remove residual dose is tested to see if it removes sensitization.

A fourth subsection examines the sensitization in TL. Tests were done to determine if the sensitization is caused by simply heating the material.

The increase of the TL signal above 400 °C, seen in many figures includingFigure 4-17, may indicate a thermally quenched deeper trap. This was tested in the fifth subsection.

6.1.1 OSL phototransfer to shallow trap

The ability of the shallow traps in MBO:Ce,Li to cause sensitization depends on the balance between the rate of phototransfer from the optically active trap to the shallow trap, and the rate of thermal stimulation of charges from the trap (responsible for the phosphorescence). To begin testing whether shallow traps cause sensitization, the following experiment was conducted.

Samples were irradiated for 100 s followed by a short OSL readout (0.1 s duration at 10% LED intensity) and phosphorescence readout (10 s duration with no stimulation). A total of 6 OSL/phosphorescence readout cycles were performed. Then, the samples were allowed to rest for 3 h in the dark to allow the population of trapped charges in the shallow traps to decay. Another six cycles of OSL/phosphorescence readout were conducted. So, in the first series the shallow traps were filled, and in the second series the shallow traps were empty. This experiment was performed with either green or blue stimulation, and the OSL integrated intensities were normalized to the first readout of each set of 6 readouts.

The normalized OSL intensities for three aliquots are averaged and presented, in Figure 6-1a, for both experiments using blue stimulation (blue points) and green stimulation (green points). The phosphorescence following OSL stimulation for each aliquot was normalized to the first readout, and the normalized intensities were averaged and presented in Figure 6-1b.

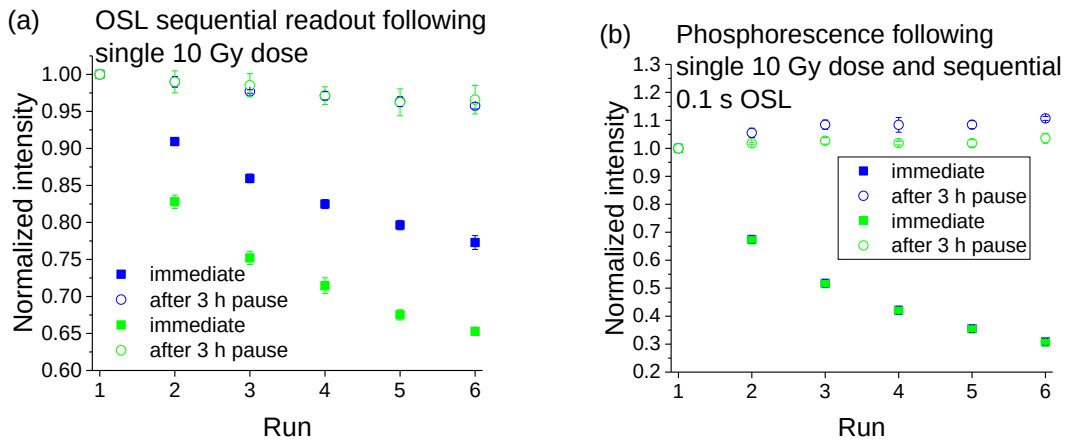

Figure 6-1: (a) OSL intensity normalized to first readout for 10% LED intensity 0.1 s readout time with 10 s pauses between stimulation. (b) Phosphorescence following for 10 s after OSL stimulation. Signal is normalized to first run. Error bars indicate the standard deviation of three aliquots (many too small to see). For both plots, immediate indicates the readouts happened within the first minute following irradiation. The color of the data points indicates color of LED stimulation.

The OSL data in Figure 6-1a show a decline in signal with additional readouts for the data obtained immediately after irradiation. With the low stimulation and short duration, sensitization is not expected. For the data after the pause, the signal is much more stable. This is evidence that phosphorescence is also contributing to the signal immediately after irradiation and confounded with OSL.

The more important data are in Figure 6-1b. Immediately after irradiation, the shallow traps are moderately filled, and phosphorescence dominates. The amount of charge transferred to the shallow trap immediately after irradiation is small compared to the charge already there so no sensitization is observed. However, if the initial shallow trap population is allowed to decay, charges start to build up in this shallow trap when OSL is started again. Thus, a buildup in the intensity following OSL stimulation is observed in Figure 6-1b. The raw intensities for phosphorescence show this also. Immediately after

irradiation, the phosphorescence is about 20% of the OSL signal (both were normalized to cps) and decreases to two orders of magnitude smaller than the OSL by the sixth readout. After the 3 h pause, the phosphorescence is about four orders of magnitude smaller than the OSL signal. This experiment established that phototransfer to the shallow trap can result in a charge build up in the shallow trap. This does not show, however, that the shallow traps are responsible for the sensitization.

A second test of the shallow trap hypothesis looked to remove retrapping to the shallow trap by OSL measurements at elevated temperature. If OSL were collected at a temperature above the temperature of the shallow trap, any charges that may enter that trapping center will be thermally excited out almost instantly. Thus, elevated temperature OSL removes retrapping as a mechanism competing with recombination. The use of elevated temperature OSL has been suggested for quartz using computer simulations (McKeever and Morris, 1994; McKeever et al., 1997) and shown experimentally for Al_2O_3 (Markey et al., 1995; Markey et al., 1996).

OSL were collected using green (GSL) and blue stimulation (BSL). Three 10 mg aliquots were used for each stimulation. The aliquots were irradiated for 5 s then OSL were read out using 90% LED intensity for 600 s with the temperature held at 100 °C. Aliquots were subjected to a total of 13 irradiation/readout cycles. Sample curves for one aliquot are shown for both stimulations in Figure 6-2ab. Also, a phosphorescence curve was included for samples held at 100 °C with no LED stimulation. As in other studies, the initial intensity and total OSL area were tracked. Intensities were normalized to the first readout of each aliquot. The normalized intensities were averaged and presented in Figure 6-2c.

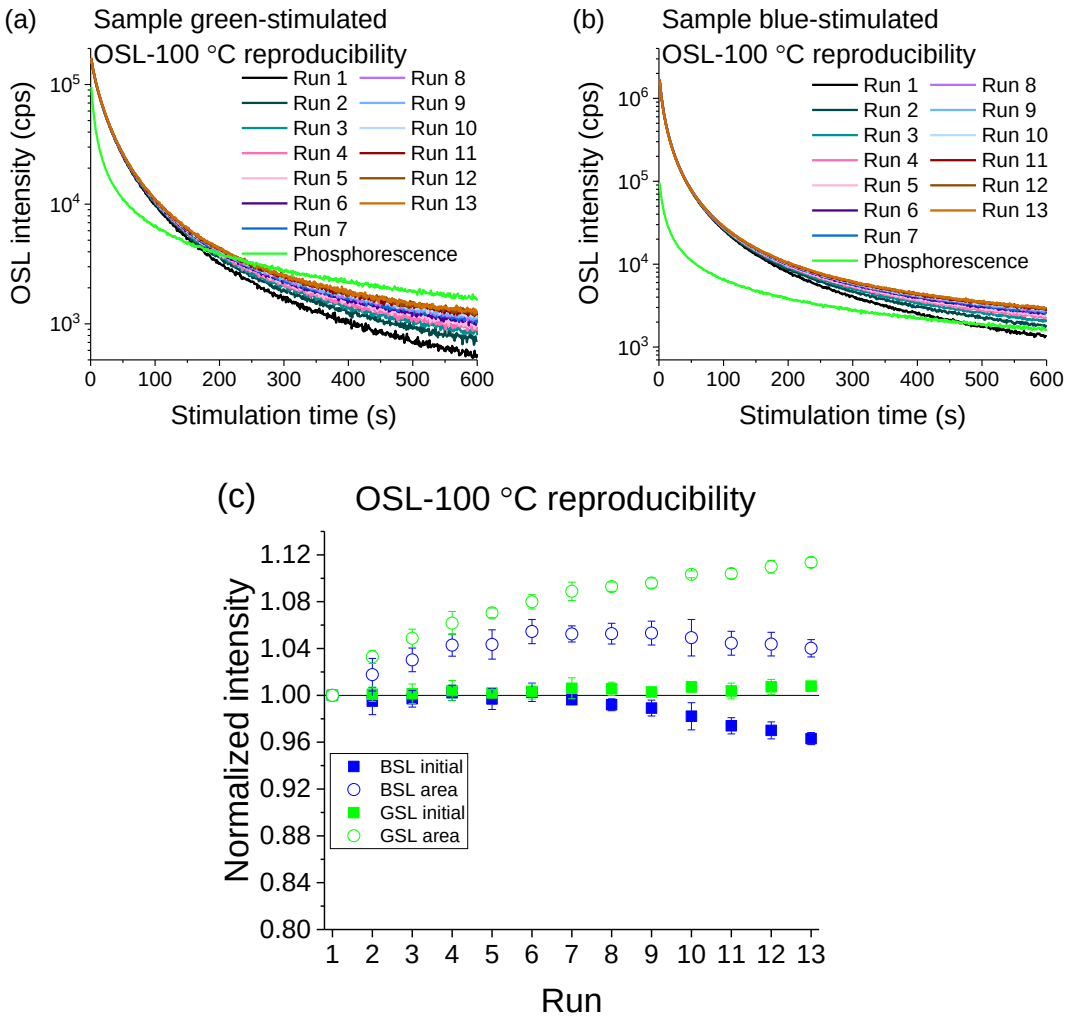

Figure 6-2: Reproducibility data for OSL at 100 °C. (a) Sample GSL curves for one aliquot. (b) Sample BSL curves for one aliquot. (c) The initial intensities and total OSL areas normalized to run 1 intensity for three aliquots. Error bars show the standard deviation of the three aliquots (many too small to see on these scales). Readout parameters were: 90% LED, 100 °C hold temperature, U-340 filter, and no aperture. No background subtraction for all data.

Sensitization is still present for the OSL area. However, sensitization has been removed for the initial intensity. This suggests that the sensitization of the initial intensity is mostly caused by phototransfer to the shallow trap. Other mechanisms such as a TL

annealing or a multi-hour fading time to empty the shallow traps may remove the sensitization of the initial intensity. The sensitization of the total OSL area is not a result of phototransfer.

6.1.2 Thermal cleaning of residual dose

It was presented in Section 4.4.1 that 600 s of OSL stimulation is insufficient to empty all traps. With the previous section showing promise in reducing sensitization, it is important to measure the residual TL following the OSL measurement at 100 °C. This may provide the mechanism by which the total OSL area still exhibited sensitization for OSL collected at 100 °C.

Three fresh 10 mg aliquots were prepared for each GSL and BSL at elevated temperature.

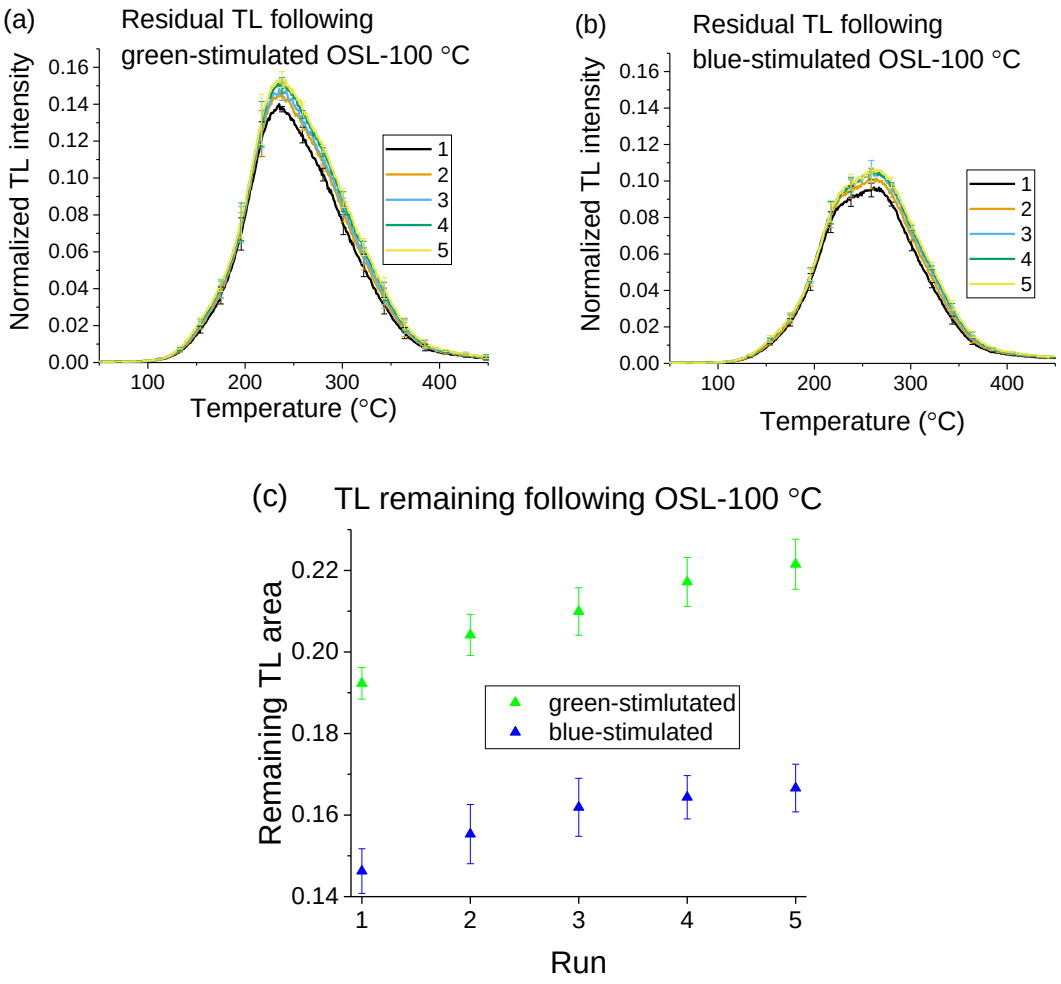

Figure 6-3: Residual TL following repeated irradiation and elevated temperature OSL readouts. Error bars indicate the standard deviation of three aliquots.

Even with OSL at elevated temperature there is a signal build up in the material without a thermal cleaning. This residual TL area is about 16-22% of the original TL area. Thus, OSL sensitization might be reduced with a TL readout following OSL to thermally clean the material.

Thermal cleaning of the material following OSL readouts was examined next. An OSL reproducibility test was run with the addition of a TL readout step following the OSL readout. Three 10 mg aliquots were irradiated for 10 s. Then, OSL was readout using 90% LED intensity (either GSL or BSL). Last, the TL was read to 450 °C at 1 °C/s. The sample

GSL curves are shown in Figure 6-4a. The OSL initial intensity and total area normalized to the first readout are shown in Figure 6-4b.

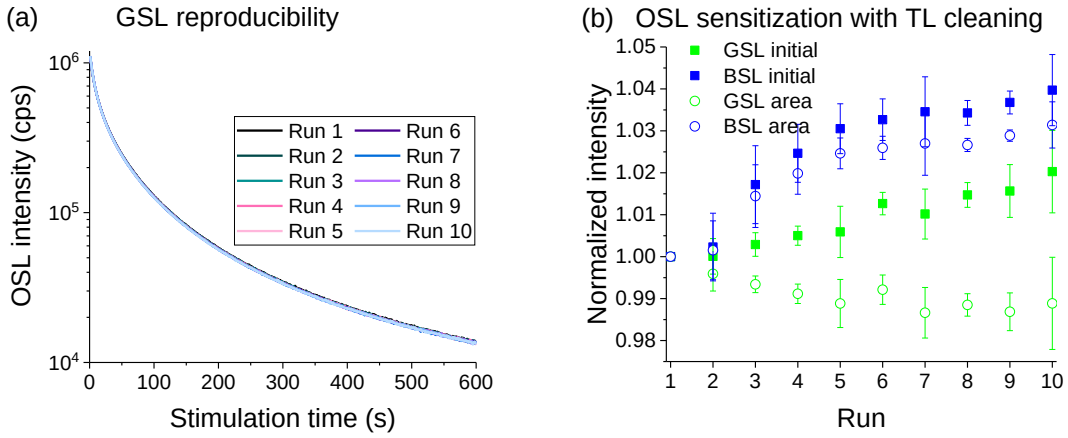

Figure 6-4: Reproducibility for BSL with a TL thermal cleaning step. (a) GSL curves for one aliquot following 10 s irradiation. (b) The OSL initial intensity and total area normalized to the first readout for 10 cycles for the average of three aliquots. Error bars indicate the standard deviation of three aliquots.

With the introduction of the TL cleaning step, sensitization was less than 4%. This is improved greatly from the 10-50% sensitization observed in this material using a smaller dose without a heating step (Section 5.2.2). Thus, the primary mechanism of OSL sensitization in the material has been dose build up due to incomplete emptying of traps by optical bleaching.

6.1.3 Modified readout to remove OSL sensitization

As shown in the previous two sections, the OSL sensitization is caused by both incomplete bleaching of the samples (mostly area sensitization) and phototransfer to shallow traps (mostly initial intensity sensitization). A modified readout was tested to remove both sources of sensitization. Samples were irradiated for 10 s. The higher dose

was used to stress the procedure more than the original 5 s irradiation. Next, a TL readout to 120 °C at a heating rate of 1 °C/s was done to empty the shallow trap. In principle, this step could be replaced with a multi-hour fading time at room temperature. The sample cooled for 120 s. Then, a standard OSL readout was done for 600 s. A TL readout to 450 °C at 1 °C/s cleaned out any unbleached signal. This sequence was done for a total of 10 cycles.

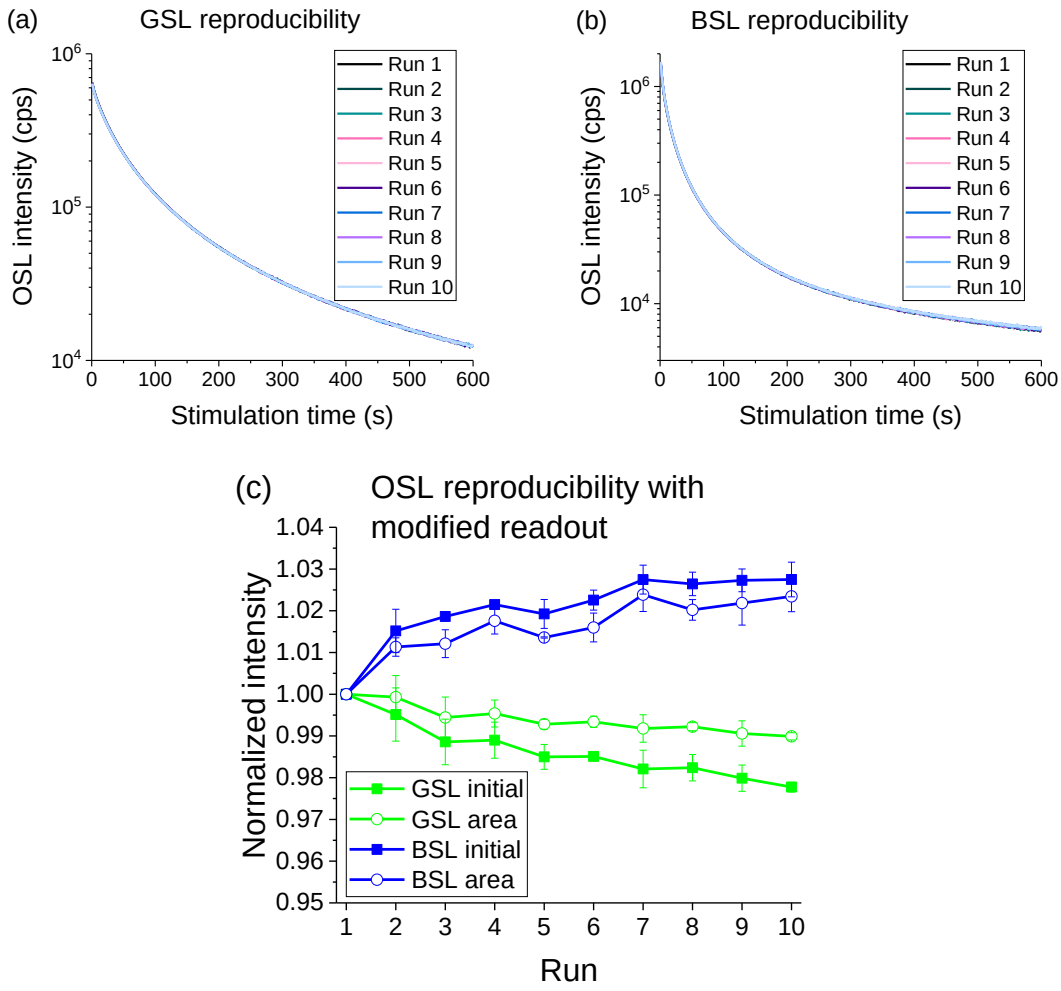

Figure 6-5: OSL reproducibility using the modified readout procedure. Sample curves for one 10 mg aliquot for each (a) GSL and (b) BSL. (c) Reproducibility for OSL initial intensity and OSL area normalized to run 1 for the average of three aliquots. Error bars are the standard deviation of the three aliquots.

The sensitization has been greatly reduced using the modified readout. BSL showed sensitization of less than 3% for both the initial intensity and OSL area. This is an improvement over the original procedure which resulted in sensitization of 10% for BSL initial intensity and 25% for the total OSL area. GSL showed slight desensitization of under 2%. This is much closer to staying constant than the original readout procedure which saw sensitization of 25% for the initial intensity and 50% for the total OSL area.

6.1.4 TL sensitization as a heating effect

To test if the sensitization in TL is a heat-induced effect, samples exposed to repeated heating cycles were compared with conventional TL reproducibility data (irradiation in each cycle). The samples were first given a reference dose of 0.5 Gy and readout. The samples were then heated through 9 more TL readout cycles with no additional dose being given. Then, the samples were given a 0.5 Gy dose and readout. When normalized to the reference dose readout, the sensitization of these samples was compared with the sensitization of 10 irradiation/readout cycles as in a conventional reproducibility test. Sample curves for one aliquot of each the irradiation/readout and repeated heating are shown in Figure 6-6.

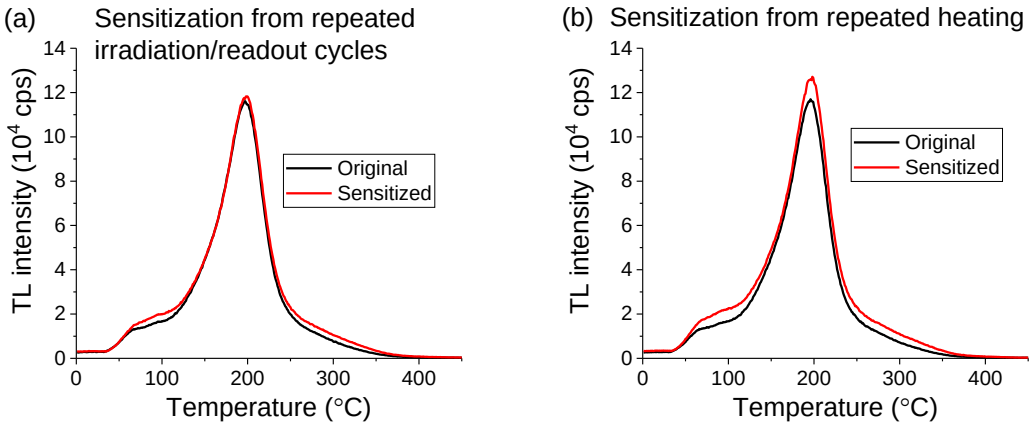

Figure 6-6: Sample curves for single aliquots MBO sensitized by 10 (a) irradiation/readout cycles or (b) repeated heating cycles. The first curve and the last curve (most sensitized) are shown for each.

Table 6-1: The sensitization for three 10 mg aliquots of MBO undergoing irradiation/readout or heating only for 10 cycles. The TL maximum and total area were normalized to the first readout. Presented are the final sensitized values with errors being the standard deviation between three aliquots.

	TL maximum	TL total area
Irradiation/TL cycles	1.0208(34)	1.080(8)
Heating only	1.055(27)	1.126(26)

The data show less than 10% sensitization for the samples that underwent irradiation and readout. The aliquots that only underwent heating show greater sensitization than the samples that were irradiated. This would indicate that TL sensitization, while much less than the original material, is a result of heating the material. No studies have been conducted on MBO to examine the impact of environment especially humidity on the TL/OSL of the material. It is possible that the material may absorb water and dry out over several TL readouts.

To test this, fresh aliquots were prepared from material that underwent post-synthesis annealing the day before the reproducibility test. The short time between annealing and testing should prevent environment driven changes to the material such as the uptake of moisture. Three 10 mg aliquots from this freshly annealed material were subjected to the same irradiation and readout procedure as the irradiated sample above.

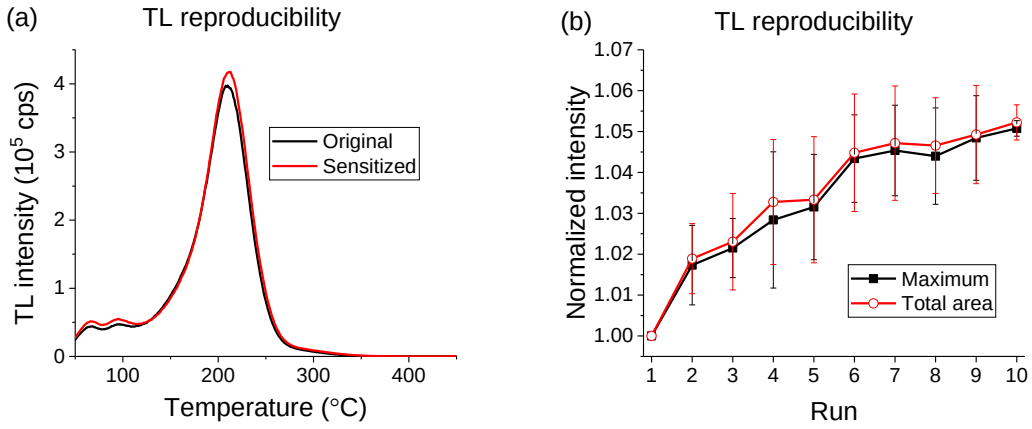

Figure 6-7: (a) Sample TL curves for one aliquot. (b) TL reproducibility for three 10 mg aliquots of material one day after 700 °C, 2 h, post-synthesis annealing. Intensities are normalized to run 1 and the error bars show the standard deviation of three aliquots.

The reproducibility data show the same behavior as the sample tested long after its post-synthesis annealing. The TL maximum sensitization is slightly worse for this new sample (5.1(2)%), but the TL area sensitized slightly less (5.2(4)%). Thus, the results here do not support the heat effect hypothesis unless one day is enough time for the material to change from its annealed state to one that sensitizes.

A further attempt to confirm a heat induced effect was done by annealing aliquots at 400 °C for 1 h, cooling quickly, and immediately running a reproducibility test. Transfer of aliquots from annealing furnace to TL reader was under 10 minutes.

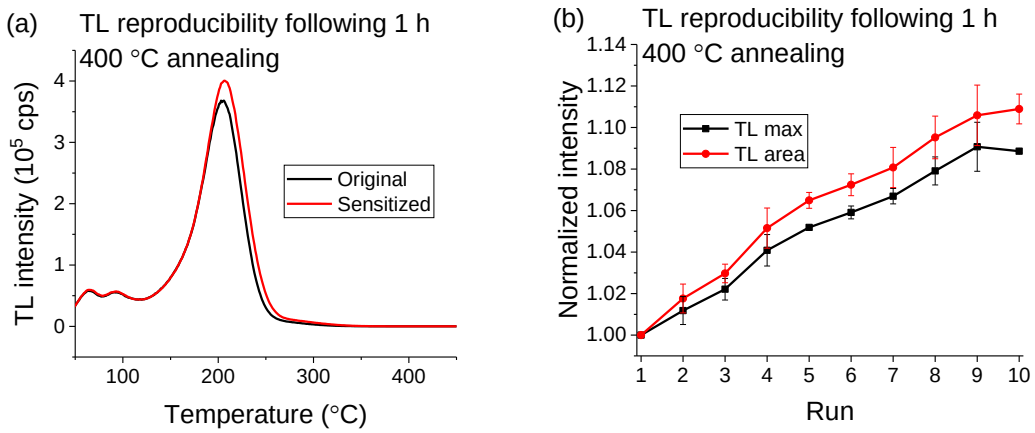

Figure 6-8: (a) Sample TL curves for one aliquot. (b) TL reproducibility for three 10 mg aliquots of material 10 min after 1 h, 400 °C annealing. Intensities are normalized to run 1 and the error bars show the standard deviation of three aliquots.

A 400 °C annealing caused a slight increase in the sensitization. While this is detrimental to reducing sensitization, this treatment maintained the same amount of sensitization (8.9(1)% for maximum and 10.9(7)% for area) previously observed for 10 irradiation/readout cycles of material without annealing.

While these results show possible influence of an effect of heating, the inability to remove this effect by heat treatments suggests that another mechanism is responsible for the sensitization.

6.1.5 TL sensitization due to deep traps

Next, the deep trap hypothesis was tested by performing the same irradiation/readout cycle with the maximum readout temperature now being 600 °C. This was done for three aliquots for 10 cycles. Sample curves for one aliquot are shown in Figure 6-9a, and the sensitization is shown in Figure 6-9b.

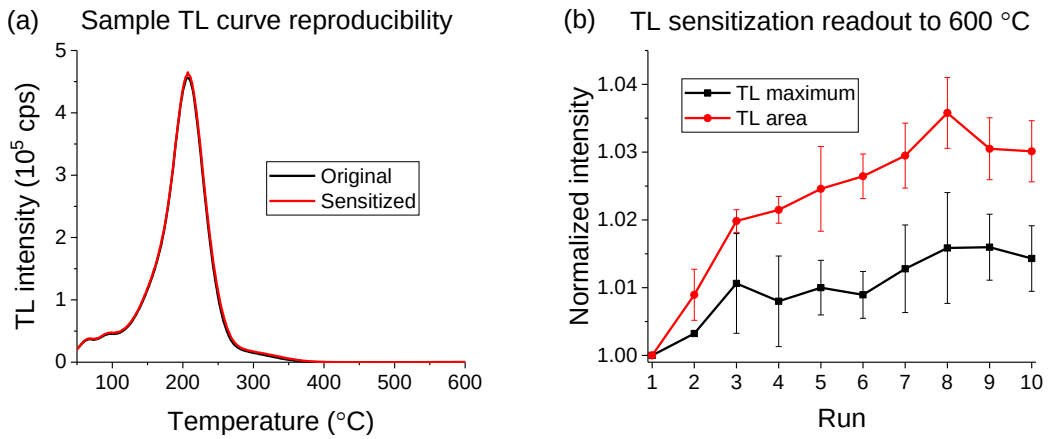

Figure 6-9: (a) Sample TL curves for one aliquot. (b) TL reproducibility for three 10 mg aliquots of material one day after 1 h, 400 °C annealing. Intensities are normalized to run 1 and the error bars show the standard deviation of three aliquots.

Of the attempts to reduce the sensitization in MBO:$Ce_{0.3\%}$,$Li_{10\%}$, this has been most successful. The TL readout to 600 °C reduced in a sensitization of 1.4(5)% for the maximum and 3.0(5)% for the total area. The only other treatment resulting in sensitization close to this was the sample annealed to 700 °C the day before which showed ~5% sensitization. When testing heat effects, the samples that had only been heated to 450 °C at most (including annealing within a day of the testing) showed more sensitization (~10%). These samples likely had residual dose from background radiation that had accumulated over time and was not removed with the TL readout to 450 °C prior to reproducibility data collection. The sample annealed to 700 °C had less time to accumulated background dose.

To confirm the presence of a deep trap, direct observation of the deep trap was desired. However, cerium is known to exhibit thermal quenching, and a trap releasing at 500 °C would likely be heavily thermally quenched. Thus, a sample underwent a TL readout to 600 °C to remove any background dose. Then, it was irradiated for 1000 s. A TL was read out to 450 °C with the PMT disconnected to protect it from high intensity light

emitted from the sample. The sample was cooled. Then, with the PMT connected, a TL curve was read out to 600 °C. That curve and a 0 dose readout for the same, single, aliquot is shown in Figure 6-10.

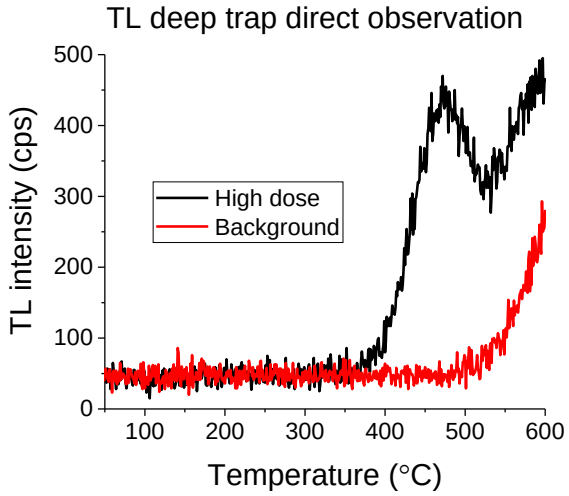

Figure 6-10: TL curve following 1000 s dose and annealing to 450 °C and 0 dose readout of the same single aliquot.

One deep trap is shown at about 480 °C and there may be a second deep trap over 600 °C. The peak at 480 °C is likely deformed due to the preheating to 450 °C. It is possible that this is another trap associated with a distribution in trap depth. Regardless, the direct observation of a deep trap strengthens the argument that TL sensitization is caused by a deep trap.

Overall, OSL sensitization is caused by incomplete bleaching, and TL sensitization is caused by deep traps (one ~480 °C and one deeper).

6.2 ***Curve fitting***

6.2.1 TL

A final attempt at a TL fitting using discrete peaks was made using a hybrid data set. It was hoped that with data from multiple experiment times with varying impacts on the traps would allow for a well constrained fit. Fitting was attempted using a data set comprised of 2 curves each from varying light stimulation (Section 4.4.1), 2 curves from dose response (Section 4.3.2), and 5 step annealed curves (Section 4.5.2) for a total of 11 curves to be fit. These data were fit using 7 RW glow peaks. Sample fits for (a) one post-blue stimulation curve, (b) one dose response curve, and (c) one step annealed curve shown in Figure 6-11.

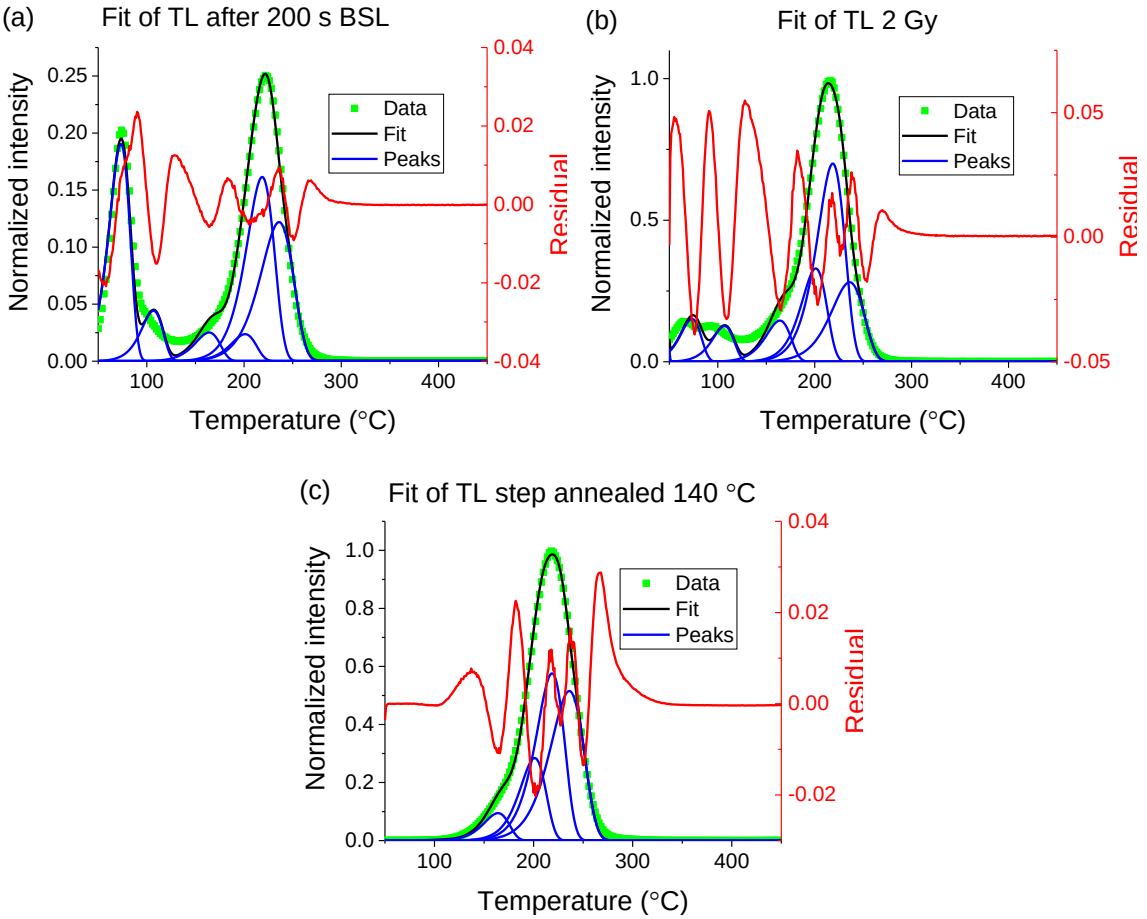

Figure 6-11: Sample fits from the simultaneous fit of hybrid data set: (a) fit for TL after 200 s of BSL; (b) fit for TL of 2 Gy; (c) fit for TL following annealing to 140 °C. 6 peak are visible in (a) and (b), but peak 7 is too small to see on these scales.

As can be seen, the fit is still not convincing. One of the low temperature peaks is fit poorly, and the high temperature side of the main TL peak is not well fit.

A second fitting was attempted on only the main TL peak (128-450 °C). The best fit was found using 7 RW curves. Sample fits for (a) one post-blue stimulation curve, (b) one dose response curve, and (c) one step annealed curve shown in Figure 6-12.

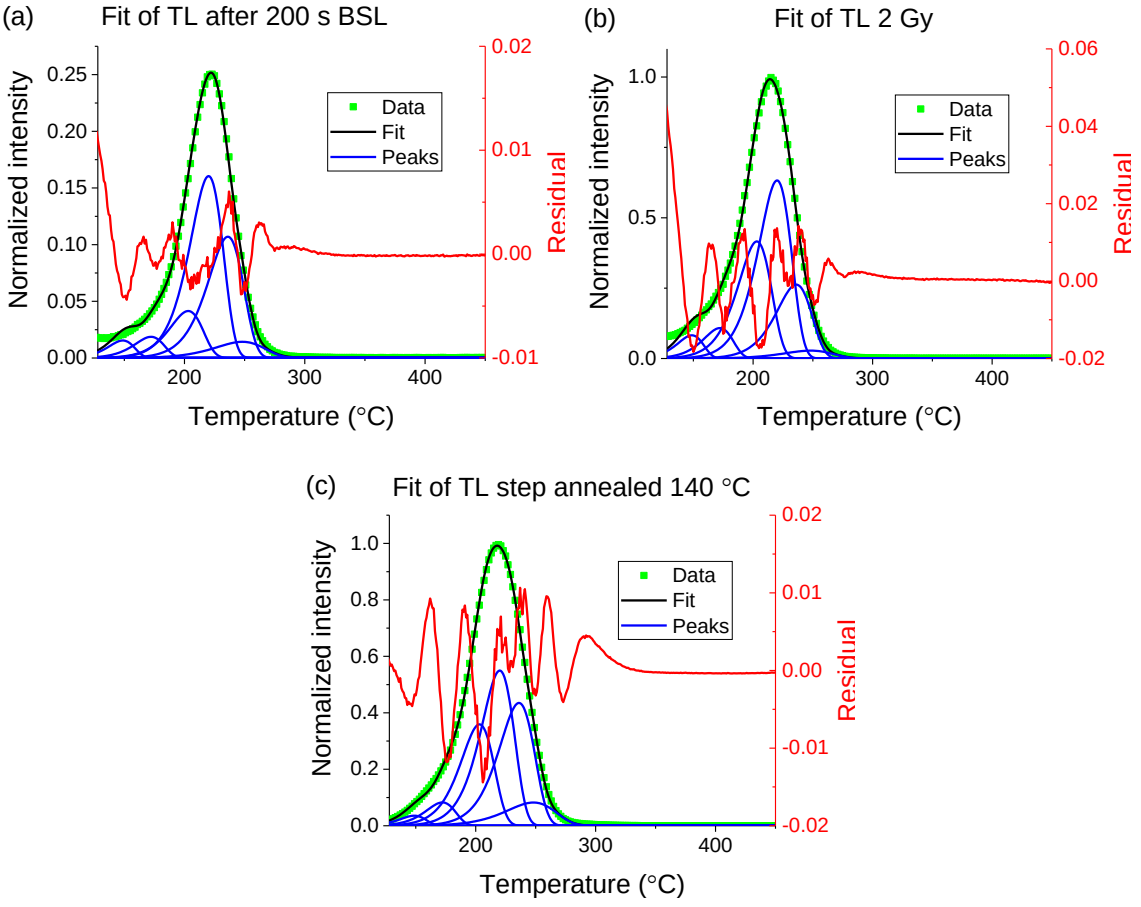

Figure 6-12: Sample fits from the simultaneous fit of hybrid data set over only the main peak (128-450 °C): (a) fit for TL after 200 s of BSL; (b) fit for TL of 2 Gy; (c) fit for TL following

annealing to 140 °C. 6 peak are visible in (a) and (c), but peak 7 is visible in (b). However, this peak is unreasonably wide.

The fit shows a R_{adj}^2 of 0.9995, but it is unlikely that each of these peaks accounts for a separate TL trapping center emptying. Peak 7 seen in (b) is unreasonably broad (a result of a low frequency factor ~10^8 s^{-1}). The fit does not capture the behavior of the leading or trailing edges well. The TL curves might be better fit with a distribution in energy.

Van den Eeckhout method

The suggestion of TL traps with a distribution in energy was tested by revisiting the step-annealing data from the initial rise method in Section 4.5.2. These data were subjected to the method developed by Van den Eeckhout et al. (2013) (theory given in Section 2.5 and method in Section 3.2.8).The results of the Van den Eeckhout method are shown in Figure 6-13 for the main TL peak. Energies were binned by 0.05 eV for the histogram. The amount of TL depletion was used as the weights as described in Section 3.2.8.

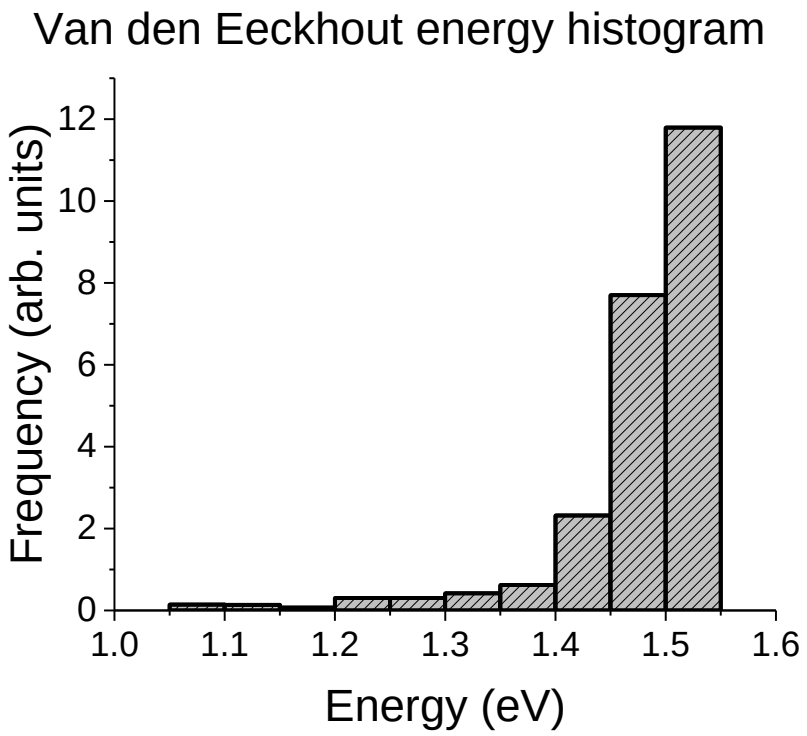

Figure 6-13: Van den Eeckhout method distribution of energies for the main TL peak.

The histogram shows evidence of more than one trap. With this method, discrete peaks tend to have abrupt cutoffs while distributions will show a spread of energies about a mean (Coleman and Yukihara, 2018). The sharp cutoff at the high energy end may suggest a discrete peak around 1.5 eV, and the spread of lower energies may suggest a distribution of traps of slightly lower energy the discrete peak. However, the proposed discrete peak has a greater contribution than the proposed lower energy trap distribution.

Overall, the curve fitting was unable to fit the TL with a meaningful number of peaks, which suggests and energy distribution. Analysis done using the Van den Eeckhout method confirmed that the main TL peak is likely a distribution of traps.

6.2.2 OSL

To try to gain information on the decays present, simultaneous fits using three exponential decays were conducted with data collected at elevated temperature. This technique bypasses the phototransfer, since any charges that enter the shallow trap are immediately thermally excited out of the trap. These data were collected in Section 6.1.1, and a sample fit is shown in Figure 6-14.

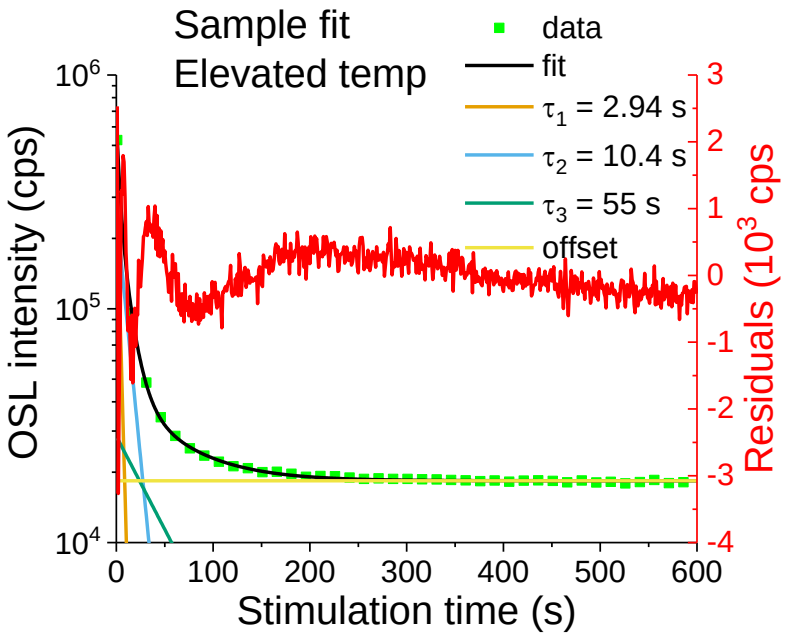

Figure 6-14: Sample fit for BSL taken at 100 °C. One 10 mg aliquot. Readout parameters were: 90% LED, 100 °C hold temperature, U-340 filter, and no aperture. No background subtraction.

While the residuals are improved for this fit, there is still evidence of a non-exponential decay component. At this point, modelling with the differential equations for the system are needed to make further progress.

Model with transfer to shallow trap

If the depletion of the shallow trap is through phosphorescence, the system of differential equations describing one thermally activated trap and two deeper traps depleting through OSL can be written as:

$$\frac{dn_1}{dt} = -\frac{n_1}{\tau_1}$$

$$\frac{dn_2}{dt} = -\frac{n_2}{\tau_2}$$

$$\frac{dn_3}{dt} = -n_2 s * exp\left(-\frac{E}{kT}\right) + A_3(N_3 - n_3)n_c \quad \textbf{(6.1)}$$

$$\frac{dn_c}{dt} = \frac{n_1}{\tau_1} + \frac{n_2}{\tau_3} + n_2 s * exp\left(-\frac{E}{kT}\right) - A_3(N_3 - n_3)n_c$$

$$\frac{dm}{dt} = A_m m n_c.$$

Where n_1 is the population of trap 1, τ_1 is the decay coefficient for trap 1, n_2 is the population of trap 2, τ_2 is the decay coefficient for trap 2, n_3 is the population of trap 3 the shallow phosphorescence trap, s is the attempt to escape frequency for trap 3, E is the trap depth of trap 3, k is Boltzmann's constant, T is the ambient temperature of the readout, A_3 is the capture cross section of trap 3, N_3 is the number of trapping site for trap 3, n_c is the population of the conduction band, m is the population of the recombination center, and A_m is the capture cross section of the recombination site. This set of differential equations is not solvable analytically for all terms, although the solutions to the first two are exponential decays. However, the numerical solution of this system can be found and compared to data. Namely, the numerical solution can be used to produce a simulated data curve which can be compared with data. Further, this simulated curve can be fit with three exponentials and the behavior of the fit and residual compared to the fits found for data. If the behaviors of the simulation and data fits match including residuals, this would be evidence that this model is an improvement over the previous attempt.

The simulation used the following input parameters to obtain the best match with actual data: E = 0.93 eV; s = 7 * 10^{12} s^{-1}; T = 300 K; τ_1 = 2 s; τ_2 = 17 s; N_3 = 10^{15} cm^{-3}; A_3 = 10 cm^{-3}; A_m = $10^{12.5}$ cm^{-3}; $n_1(0)$ = 10^6 cm^{-3}; $n_2(0)$ = 3 * 10^6 cm^{-3}; $n_3(0)$ = 0 cm^{-3}; $m(0)$ = $n_1(0) + n_2(0)$; $n_c(0)$ = 0 cm^{-3}. The parameters for E and s were based on the estimations of

these parameters for the shallowest trap in Section 4.5. The temperature was chosen to be close to room temperature. The decay constants were chosen to be slightly larger than the fastest two found in fits done throughout Chapter 4 for BSL. As was noted, the longest lifetime exponential was likely trying to account for the phosphorescence component. N_3 was chosen to be very much greater than the total charge in the system. The initial trap populations, $n_1(0)$ and $n_2(0)$, were based on fits obtained in Chapter 4 that showed the second fastest decay had an initial intensity about three times the initial intensity of the fastest decay. The value for $n_3(0)$ was chosen to be 0 to match the experimental data following an annealing to empty the shallow trap. Accounting for varying initial populations for this trap would be too complicated for initial development and testing of the model. The initial value for m was chosen to conserve charge. A_3 and A_m were tweaked manually until good agreement with experimental data was gained. The trap populations with time are shown in Figure 6-15.

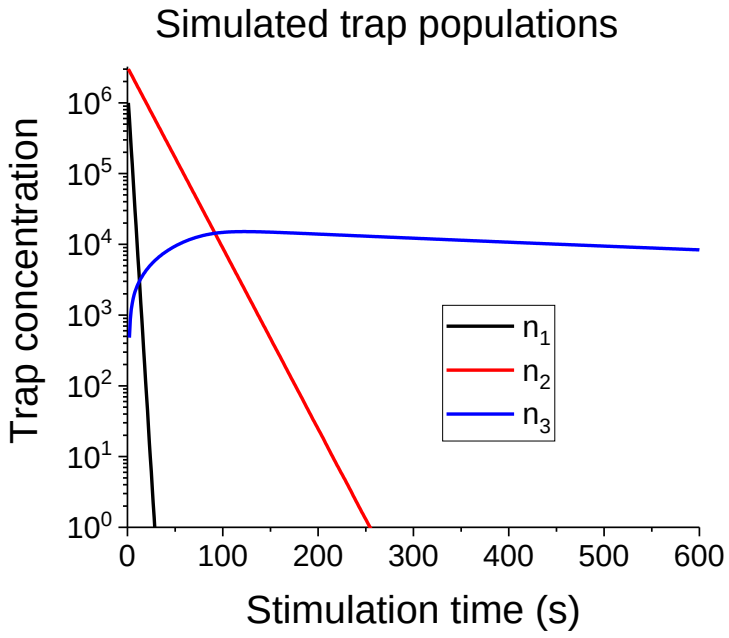

Figure 6-15: Trap concentrations from simulations. Traps 1 and 2 are exponential decays. Trap 3 empties via phosphorescence after receiving charge transfered from traps 1 and 2.

As is shown in Figure 6-15, the first two traps detrap exponentially. The third trap has a competition between trapping charges liberated from the other two traps and thermally releasing charges. Thus, a build up and slow decay is observed for the third trap population.

A fit of the simulated data with three exponential decays and an offset are shown in Figure 6-16.

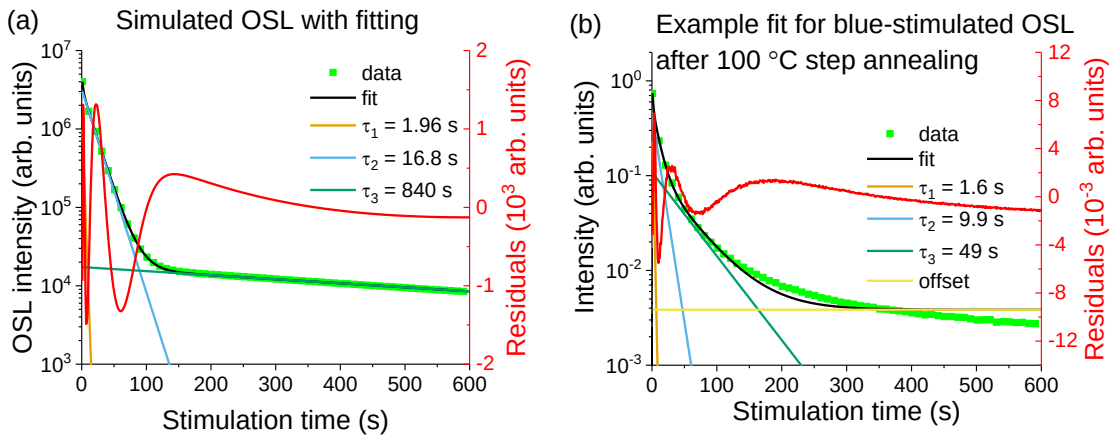

Figure 6-16: (a) Fit of simulated data using 3 exponential decays and an offset. The offset was ~0 so is not seen here. Part (b) of Figure 4-21 reproduced for direct comparison.

As can be seen, the plot of the simulated data matches the same kind of shape shown in of experimental data. Further, the shape of the residuals from the simulated data and fitting shows the same behavior as the residuals for fitting actual data. This is evidence that this model is a step in the right direction. The long lifetime decay components are vastly different as is the offset. This may be since the current model does not account for any optical detrapping from the shallow trap.

To further test the model, the simulation was run with the readout at elevated temperature (375 K). This was done to imitate the readout of data shown in Figure 6-14. The fit of the simulated data is shown in Figure 6-17.

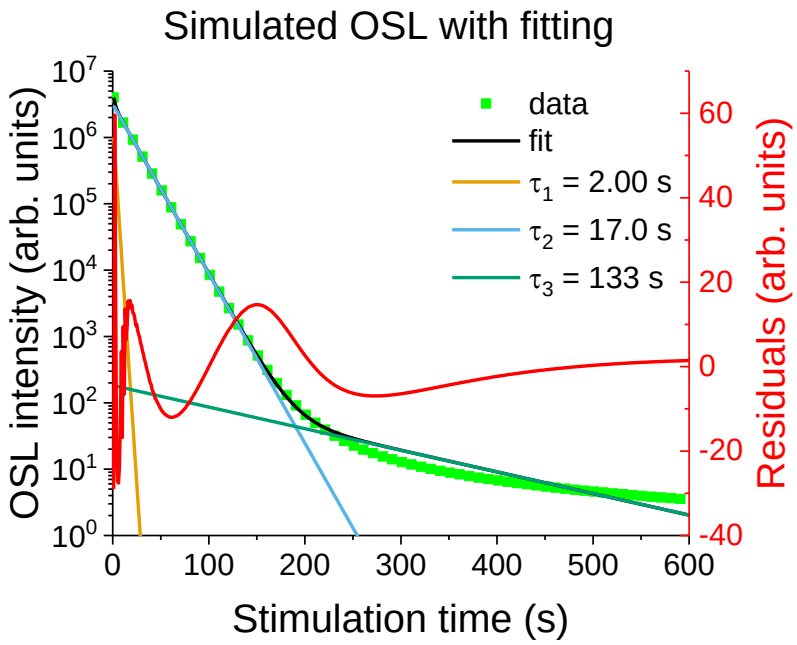

Figure 6-17: Fit of simulated data using 3 exponential decays and an offset. The offset was ~0 so is not seen here.

As can be seen, the curve shape and behavior of the residual imitates that of the real data. The residual is much smaller though shows the same kind of organized oscillation around 0. Again, the longest lifetime components are quite different between simulation and experimental data. This is likely due to exclusion of light depletion of the shallow trap.

Overall, this model explains the behavior observed in experimental data. The transfer of charge to a shallow trap that is thermally active at room temperature is wrongly accounted for in the fits by a longer lifetime exponential decay and the offset. Further improvement to the model could be made through allowing photostimulation of the shallow trap.

6.3 ***Chemical shift model applied to MBO***

The history and development of the vacuum referred binding energy (VRBE) diagram from the chemical shift model or Dorenbos model is discussed in detail in Section 2.7. This model notes that for lanthanides the 4f energy levels are well shielded from any external electric field present in varying compound (the crystal field). However, the 5d levels are depressed by varying amounts according to the strength of the crystal field. The relative energy difference of transitions by varying lanthanide in a material should remain the same regardless of host material as the 5d levels for all lanthanides will be depressed the same.

A VRBE diagram can be established through the knowledge of four parameters for a material: the exciton creation energy at 10 K, E^{ex}, which is about 0.36 eV more than exciton formation at room temperature and a factor of 1.08 less than the band gap (Dorenbos, 2005); the charge transfer from the valence band to Eu^{3+}; the energy difference between the binding energies of Eu^{2+} and Eu^{3+} in the compound, U; the spectroscopic redshift of Ce^{3+} in the material (Dorenbos, 2000d). Exciton creation is measured optically by the onset of fundamental absorption. The charge transfer to Eu^{3+} is a fairly broad (0.6-0.8 eV wide in the 4-6 eV energy range for oxides and borates) optical absorption or excitation band (Dorenbos, 2009). The U parameter can be calculated from the centroid shift of Ce^{3+}, e_c, found by measuring the 5d energy levels (excitation or absorption measurements). U is estimated by:

$$\mathbf{U} = \mathbf{5.44} + \mathbf{2.834} * \mathbf{exp}(-\boldsymbol{e_c}/\mathbf{2.2}) \qquad \textbf{(6.2)}$$

(Dorenbos, 2013). Thus, all needed parameters can be found from optical measurements for a Ce-doped sample and a Eu-doped sample.

In this section, a VRBE diagram will be established from literature values and extrapolations of values for similar compounds. Then, optical measurements will be taken to improve the VRBE diagram. Attempts to verify ground state positions for some lanthanides will be made through TL and optical measurements. TL emission data were collected to aid in explanation for some difficulties encountered in the verification measurements.

6.3.1 First attempt of VRBE for MBO

An initial VRBE diagram was developed for MBO using parameters from literature. This attempt also served as a reality check on measurements to improve the parameter values. The exciton creation energy used is from a computational modeling paper, density-functional theory using CASTEP software, that gives a value of 8.87 eV (this is their band gap value divided by 1.08) (Oliveira et al., 2016). This is consistent with other tetraborate materials. SrB_4O_7 has an exciton creation of energy of 7.80 eV (Dorenbos, 2005). Other borate systems compiled in the same reference show an increase in the exciton creation energy going from Sr borates to Ca borates to Mg borates due to the change in atomic radius. Thus, it is expected that MBO will have an exciton creation energy greater than the 7.80 eV of SrB_4O_7.

The charge transfer to Eu^{3+} is the next parameter needed. In SrB_4O_7, this energy is 4.88 eV (Dorenbos, 2005). Based on values for $M_3N_2(BO_3)_4$ (M = Ba, Sr, or Ca; N = La, Gd, or Y), the typical increase in charge transfer to Eu^{3+} is about 0.15 eV going to each smaller alkaline earth metal (e.g., compound with Ca has charge transfer 0.15 eV greater than the analogous compound with Sr). Thus, adding 0.30 eV to the known charge transfer energy for SrB_4O_7 will result in an estimate of 5.18 eV for the Eu^{3+} charge transfer energy for MBO. This is shown in Figure 6-18a.

The third parameter is the spectroscopic redshift or centroid shift of Ce^{3+}. This redshift is 1.746 eV for SrB_4O_7 and 2.194 eV for CaB_4O_7. If the increase in redshift is the same going from CaB_4O_7 to MBO as SrB_4O_7 to CaB_4O_7, the expected redshift for MBO is 2.642 eV which corresponds to an expected lowest energy excitation of Ce^{3+} of 335 nm. This is shown in Figure 6-18b. However, PL collected in Section 4.2.4 show the lowest wavelength Ce^{3+} excitation to be at 320 nm. Thus, the vacuum absorption of 6.118 eV minus this energy (3.875 eV) gives a redshift of 2.243 eV. This value from measurement of the low-purity reagent material was used for this initial attempt of a VRBE diagram.

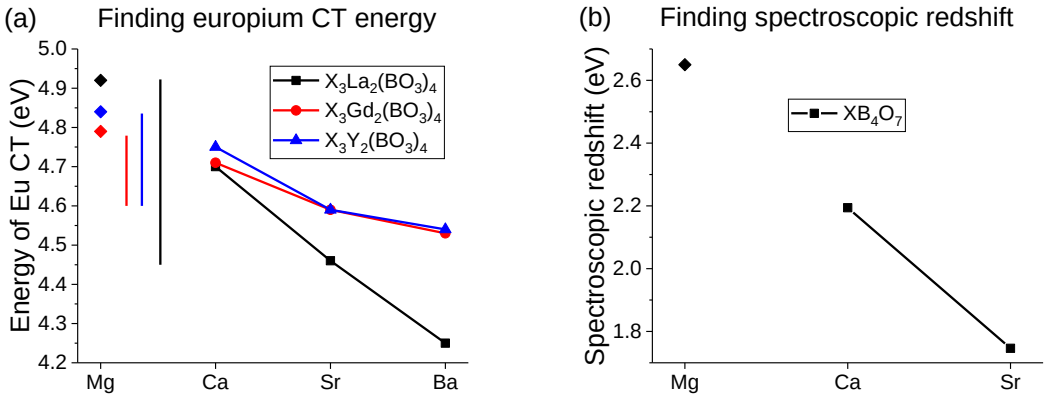

Figure 6-18: (a) Charge transfer energies for Ca, Sr, and Ba borates with the Mg borate transfer energy extrapolated for each borate. The vertical lines show the energy difference from Sr to the extrapolated Mg borate. (b) Spectroscopic redshift energies for CaB_4O_7 and SrB_4O_7 with an estimated redshift for MgB_4O_7 extrapolated.

The final parameter is the difference in binding energies for Eu^{2+} and Eu^{3+}. In vacuum, this value is 18 eV, and in materials, values are typically 6-7.5 eV (Dorenbos, 2013). SrB_4O_7 has a value of U = 7.26 eV (Dorenbos, 2013). This value can be calculated if the centroid shift for Ce^{3+} is known. As shown in the previous paragraph, the centroid shift is 2.243 eV. This value results in U = 6.462 eV.

The following diagram was constructed using a tool in Origin provided by Prof. Dorenbos (2017). The steps to constructing the diagram are detailed in Dorenbos (2013) but will be summarized here. The conduction band is set according to the chemical shift (energy depression) of the 5d levels compared to vacuum. If the vacuum 4f level is set to 0, the conduction band is typically within 1 eV. The exact formulae are in Dorenbos (2012). A second level is identified just below the conduction band. This is the exciton onset level which is approximately the band gap/1.08. The top of the valence band is set according to the charge transfer to Eu^{2+}. This also sets the ground level of Eu^{2+} allowing all the other Ln^{2+} energy levels to be set. The parameter *U* sets the Ln^{3+} levels below the Ln^{2+} with *U* being the energy difference from Eu^{2+} to Eu^{3+}. Then, the spectroscopic redshift is used to place the lowest 5d levels.

The initial attempt of the VRBE diagram for MBO is shown in Figure 6-19. Note that these levels would be for the material at 10 K. The band gap shrinks a few tenths of eV at room temperature in many materials due to a lowering of the mobility edge, the lower edge of the conduction band (You et al., 2011).

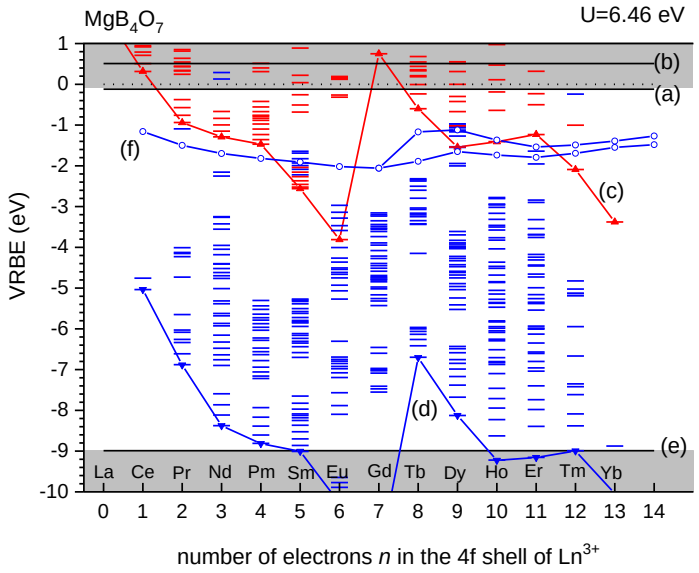

Figure 6-19: Initial attempt of a VRBE diagram for MBO. Parameters used are: exciton creation 8.87 eV; charge transfer to Eu^{3+} 5.18 eV; *U* of 6.462 eV from current centroid shift (excitation of low-purity material); Ce^{3+} redshift of 2.243 eV.

In Figure 6-19, the gray regions are approximations of the upper portion of the valence band and lower portion of the conduction band where charge carriers could travel in a delocalized manner. The dotted line at 0 eV is the vacuum energy level. (a) indicates the exciton energy above the valence band. (b) is the bottom of the conduction band. The jagged red line, (c), shows the ground states of the Ln^{2+} ions. Below, the jagged blue line, (d), shows the ground states of the Ln^{3+} ions. The short lines indicate energy states introduced by lanthanides and are from their Dieke diagrams (Dieke, 1968). The solid black line, (e), at about -9 eV is the top of the valence band. The rounded blue lines, (f), between -1 and -3 eV are the lowest 5d level for the 3+ lanthanides.

This model can be improved by measuring the spectroscopic redshift for Ce^{3+} and attempting to measure the charge transfer to Eu^{3+}. Measurement of the onset of exciton production would require measurement of the fundamental absorption edge.

This model can also be tested by TL or OSL excitation spectra. If various lanthanides enter the lattice in the 3+ oxidation state, they might be able to oxidize and trap an electron in their 2+ state. This can only occur if the 2+ ground state for a lanthanide is within the bandgap. Lanthanides with 2+ ground states within 2 eV of the exciton energy level are prime candidates for introducing new electron traps. If new traps are introduced at these energies, new TL peaks could appear and show trap depths matching the VRBE diagram. For charges trapped deeper than thermal excitation allows, OSL excitation spectra could be used to gain the same information. For OSL, photon energies showing strong OSL excitation (bands of excitation) correspond to the trap depth or the energy below the valence band for a trap. The focus for both studies will be relative trends rather than absolute energy values.

6.3.2 Measurements for model improvement

Now that an estimate from literature has been compiled, optical measurements of MBO:$Ce_{0.3\%}$,$Li_{10\%}$ and MBO:$Eu_{0.3\%}$,$Li_{10\%}$ were taken to acquire the needed values to improve the parameters for the VRBE diagram. Measurement of PL emission and excitation for MBO:Ce,Li allow the spectroscopic redshift and centroid shift to be measured and calculated for a couple of the 5d states.

Measurement of PL excitation for MBO:Eu,Li may show the charge transfer band to Eu^{3+} if the wavelength is low enough for the instrument being used. However, the charge transfer 5.18 eV, as estimated from literature, is at the emission limit of our lamp and the lamp may not be bright enough at that energy. We do not have the equipment to take a fundamental absorption edge measurement as that would require a synchrotron.

Cerium PL excitation and emission

PL emission were collected for MBO:$Ce_{0.3\%}$,$Li_{10\%}$ using an excitation wavelength of 320 nm which had previously been observed as the lowest energy stimulation band. Emission data were taken using the Fluorolog with the following parameters: 0.5 s integration time, 0.5 nm step size, and 1.1 nm bandpass slits. PL excitation was measured for a stimulation of 350 nm, the middle of the emission band. Readout parameters were: 0.5 s integration time, 0.5 nm step size, and 1.1 nm bandpass slits. Both spectra are shown in Figure 6-20.

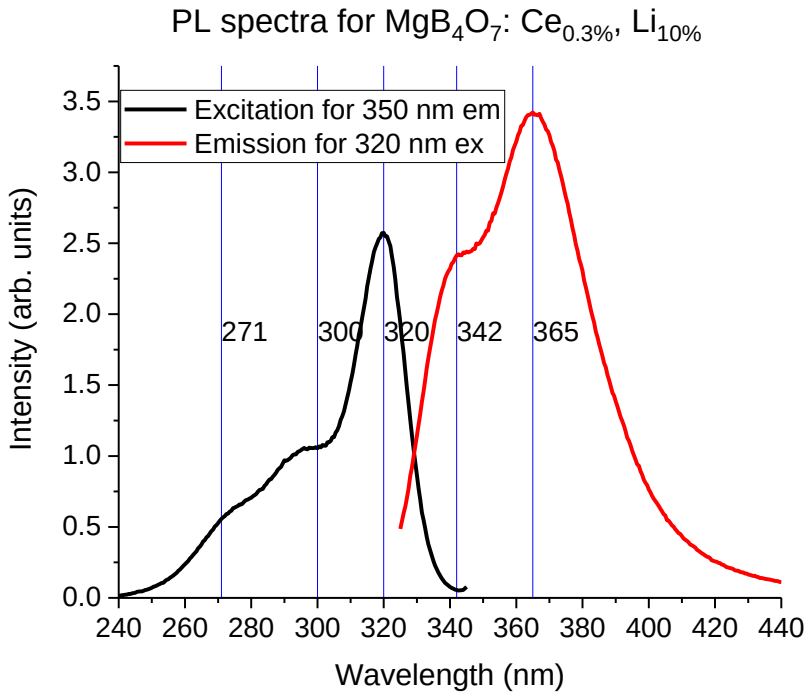

Figure 6-20: PL excitation (black) and emission (red) spectra for MBO:$Ce_{0.3\%}$,$Li_{10\%}$ as synthesized with high-purity reagent and 700 °C annealing for 2 h. Parameters were 1.1 nm bandpass slits, 0.5 nm step size, and 0.5 s integration time.

The emission spectrum shows two distinct emission bands at 342 nm and 365 nm which are attributed to Ce^{3+} emission. The tail above 400 nm is too broad to be part of the Ce^{3+} emission so could be intrinsic emission.

The excitation spectrum shows three distinct excitation bands. These can be attributed to the three lowest 5d energy levels for Ce^{3+}. Two more 5d energy levels are expected at higher energies if they are below the conduction band. Otherwise, the next most energetic excitation band will be a charge transfer band from the ground state of Ce^{3+} to the conduction band. However, this data does confirm that the ground state of Ce^{3+} is at least 4.58 eV below the conduction band (energy of most energetic 5d level).

The energy of the least energetic 5d state can be used to find the centroid shift. The excitation spectrum of the high-purity reagent material confirms the lowest energy excitation to be 320(2) nm. This results in a value for ΔD or ϵ_c of 2.24(2) eV. The value for U calculated from this is 6.46(1) eV.

Europium PL excitation

PL emission and excitation spectra were collected for MBO:Eu,Li. Emission spectra merely helped to find the dominant emission for measuring an excitation spectrum. PL emission parameters were: 2.8 nm bandpass slits, 0.5 nm step size, and 1 s integration time. The 612 nm emission was the brightest. Thus, an excitation spectrum was collected for 612 nm emission. The PL excitation parameters were: 1.8 nm bandpass slit on excitation window and 3.6 nm bandpass slit on emission window, 0.5 nm step size, and 2 s integration time. Both spectra are shown in Figure 6-21.

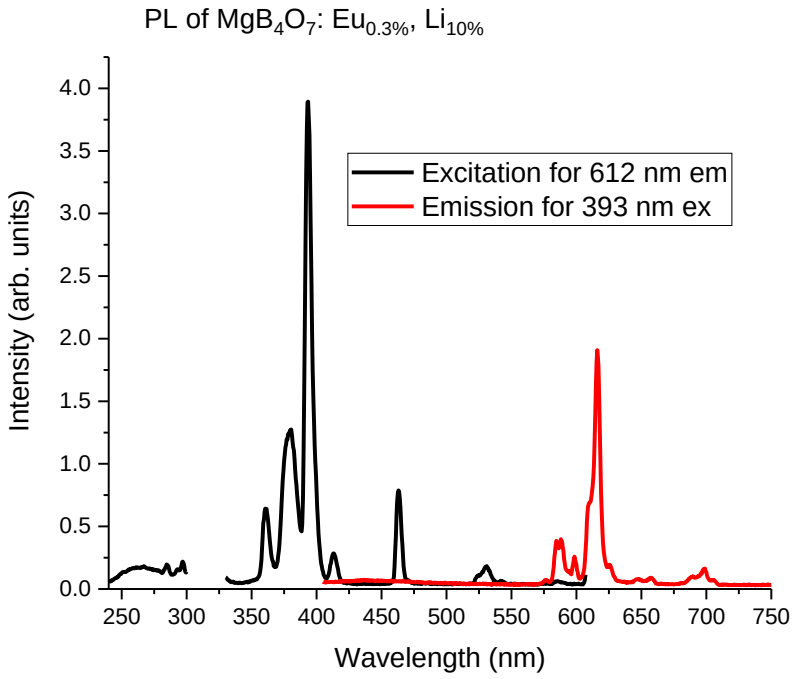

Figure 6-21: PL excitation and emission for MBO:$Eu_{0.3\%}$,$Li_{10\%}$.

No charge transfer band is observed in the excitation spectrum. Papers on SrB_4O_7: Eu show a broad, >50 nm FWHM, excitation band as the charge transfer band. There may be a band at about 260 nm, but it is not broad enough (FWHM ~15 nm). However, this band is not bright enough to draw a firm conclusion due to the low intensity of the lamp in this region. A reason to reject this as the charge transfer band is its low energy (~4.9 eV), lower than that of SrB_4O_7:Eu, which is not expected. It can be concluded from these data that the charge transfer of Eu^{3+} is greater than 4.9 eV. Use of a different lamp with transmission down to 200 nm may allow the charge transfer band to be observed in future studies, but the current measurements could not improve on the estimated value from literature.

6.3.3 TL studies

The initial model shows Ce^{3+} acting as a deep hole trap since it is closer to the valence band than to the conduction band. Therefore, any emission from Ce^{3+} is associated with an electron thermally or optically detrapping and recombining with a hole trapped at a Ce site. Thus, the model could be confirmed by introducing new electron traps by doping with lanthanides such as Nd, Sm, Dy, Ho, Er, Tm, and Yb that have their 2+ oxidation states within the bandgap and relatively close (< 2 eV) to the valence band. If electrons could be trapped at these sites following irradiation, TL could be used to confirm trap depth as has been done in other materials like $LiYSiO_4$: Ce^{3+} (Sidorenko et al., 2006), YPO_4 (Bos et al., 2008), and YAG (Milliken et al., 2012; Ueda et al., 2015a; Ueda et al., 2015b). However, if the traps within the host material dominate, TL may be unable to confirm these energy level placements like $CaLa_4(SiO_4)_3O$ (Dobrowolska et al., 2015).

VHRM for various codopants

An attempt to find trap depths for several lanthanides codoped with Ce was done using the VHRM (Section 3.2.8). The materials used were MBO:$Ce_{0.3\%}$,$Li_{10\%}$,$X_{0.3\%}$ (X = None, Pr, Nd, Sm, Eu, Gd, Dy, Er, Ho, Tm, or Yb) as synthesized in Section 5.4. The analysis is not straightforward as there are clearly multiple peaks and many of the TL peaks are broad enough to be composites.

Data were collected for single 1 mg aliquots of each material. Smaller aliquots were used to improve thermal contact with the TL/OSL cup. Heating rates of 0.1, 0.2, 0.5, 1, 2, 5, and 10 °C/s were used. All data were collected using a U-340 filter with no aperture. The filter was chosen to select recombination occurring through Ce^{3+} which should be a detrapped electron recombining with a Ce^{4+} to form excited Ce^{3+} that relaxes to its ground state. The TL curves for VHR are shown for all materials in Figure 6-22.

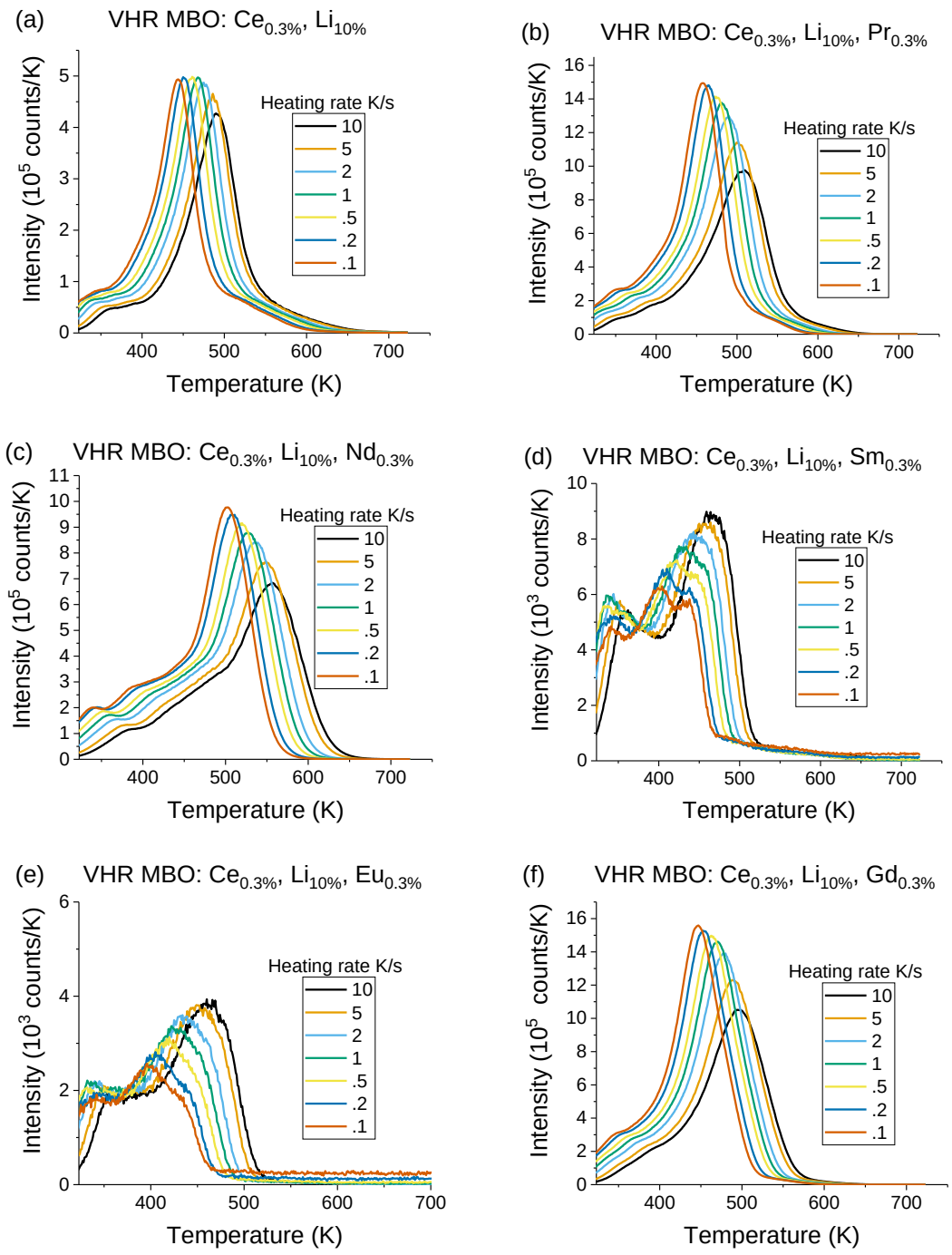
(a) VHR MBO: $Ce_{0.3\%}$, $Li_{10\%}$
Intensity (10^5 counts/K)
Temperature (K)
Heating rate K/s
10
5
2
1
.5
.2
.1
(b) VHR MBO: $Ce_{0.3\%}$, $Li_{10\%}$, $Pr_{0.3\%}$
Intensity (10^5 counts/K)
Temperature (K)
Heating rate K/s
(c) VHR MBO: $Ce_{0.3\%}$, $Li_{10\%}$, $Nd_{0.3\%}$
Intensity (10^5 counts/K)
Temperature (K)
Heating rate K/s
(d) VHR MBO: $Ce_{0.3\%}$, $Li_{10\%}$, $Sm_{0.3\%}$
Intensity (10^3 counts/K)
Temperature (K)
Heating rate K/s
(e) VHR MBO: $Ce_{0.3\%}$, $Li_{10\%}$, $Eu_{0.3\%}$
Intensity (10^3 counts/K)
Temperature (K)
Heating rate K/s
(f) VHR MBO: $Ce_{0.3\%}$, $Li_{10\%}$, $Gd_{0.3\%}$
Intensity (10^5 counts/K)
Temperature (K)
Heating rate K/s

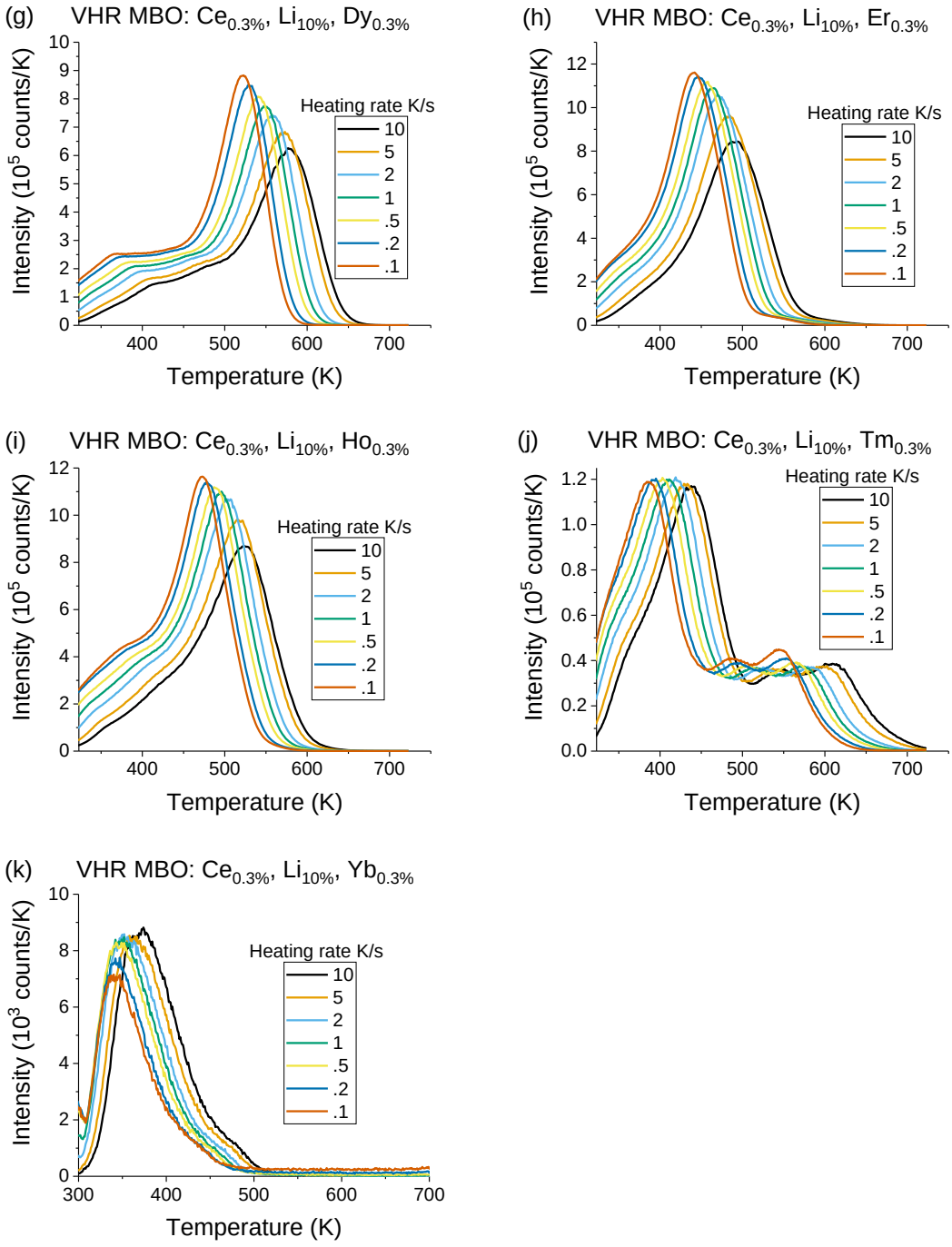

Figure 6-22: VHR data for one 1 mg aliquot of MBO:$Ce_{0.3\%}$,$Li_{10\%}$,$X_{0.3\%}$ where X = (a) None, (b) Pr, (c) Nd, (d) Sm, (e) Eu, (f) Gd, (g) Dy, (h) Er, (i) Ho, (j) Tm, or (k) Yb. A U-340 filter was used with no aperture.

As can be seen, the intensities varied greatly from dopant to dopant. Codoping with Sm, Eu, and Yb resulted in weak TL (on the order of 10^3 cps). If they trap electrons, the trap depths are predicted to be 3-4 eV which is too deep to see in these TL. Most peaks show the expected shift to higher temperature and decrease in intensity with increasing heating rate. However, some show a shift to higher temperature and increase in intensity, as they are sensitized. Regardless, T_{max} does shift to higher temperatures with increasing heating rates, as expected.

A sample plot used for fitting is shown, in Figure 6-23, for MBO:$Ce_{0.3\%}$,$X_{0.3\%}$,$Li_{10\%}$. The results for trap depth are summarized and compared with predicted electron trap depths from the VRBE diagram (ground state energy of Ln^{2+} - conduction band energy) in Figure 6-24.

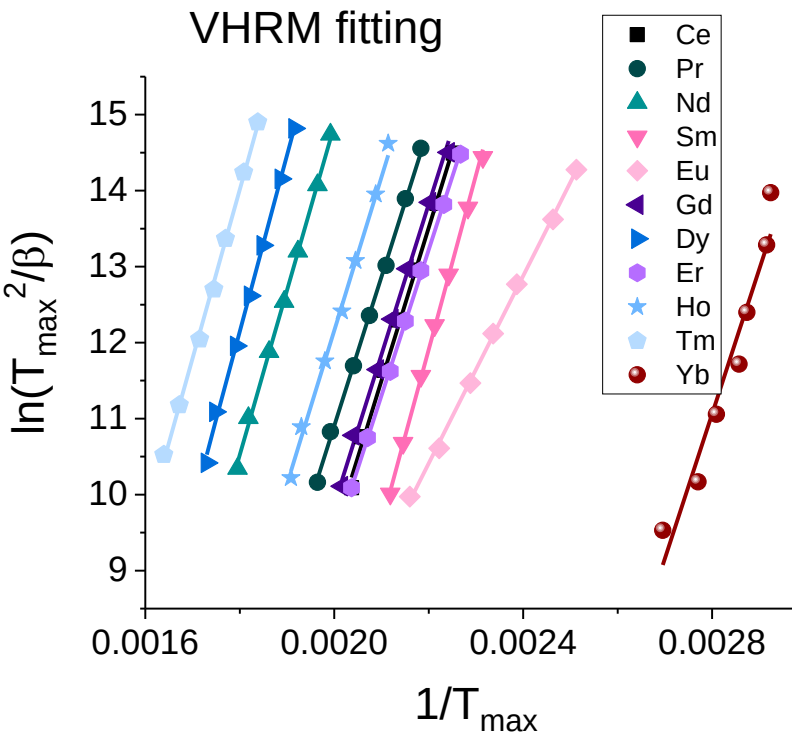

Figure 6-23: Fits required for VHRM for all materials. Data are shown as points and fits are solid lines of color matching data they are fitting. Values for T_{max} were found visually.

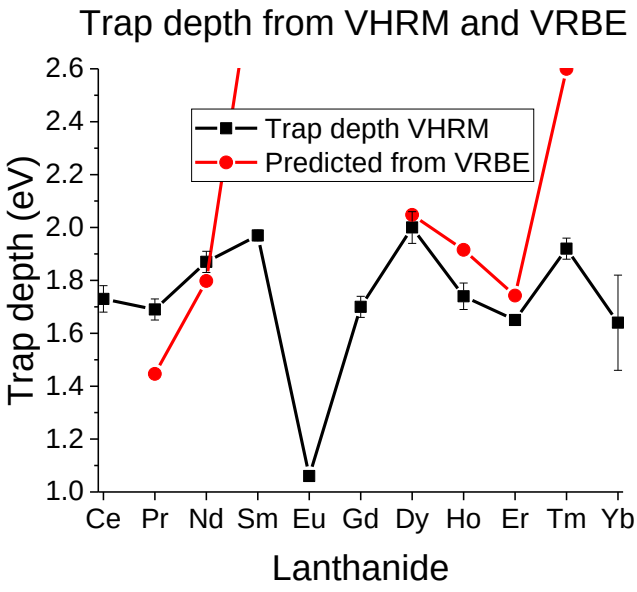

Figure 6-24: TL trap depths found via the VHRM. Electron trap depths predicted from the initial VRBE diagram are shown in red.

These data suggest that Nd, Dy, Ho, Er, and maybe Pr follow the predicted model and behave as electron traps. The energy found for Pr was higher than expected by about 0.2 eV at the energy close to that observed with just Ce doping. This may indicate that Pr did not introduce a new electron trap and the intrinsic electron trap was observed instead.

Eu, Sm, Tm, and Yb were not expected to trap electrons shallow enough to be accessible via TL in the temperature range used. Thus, the peaks observed for Sm, Tm, and Yb are likely related to an intrinsic defect. Eu severely reduces the TL and likely does not behave as an electron trap. Its position in the predicted VRBE diagram is deep enough in the band gap that it would behave as a recombination center for holes.

Overall, these data agree with what was predicted by the original VRBE diagram. This confirms that new electron traps can be added to the material by doping with Nd, Dy, Ho, or Er. Any traps introduced by Sm, Eu, Tm, or Yb were predicted to be too deep for observation by TL which matches the VHR results. Gd was not expected to behave as a

trap, so the trap found by VHR has the same energy as the intrinsic trap seen in the Ce only sample.

TL emission

TL emission were taken for single aliquots of MBO:$Ce_{0.3\%}$,$Li_{10\%}$,$X_{0.3\%}$. If TL emissions outside the transmission of U-340 were introduced, they behave as competing recombination centers with Ce. This is especially important for dopants that trap charges deeper in the band gap where they are more likely to behave as recombination centers than trapping centers.

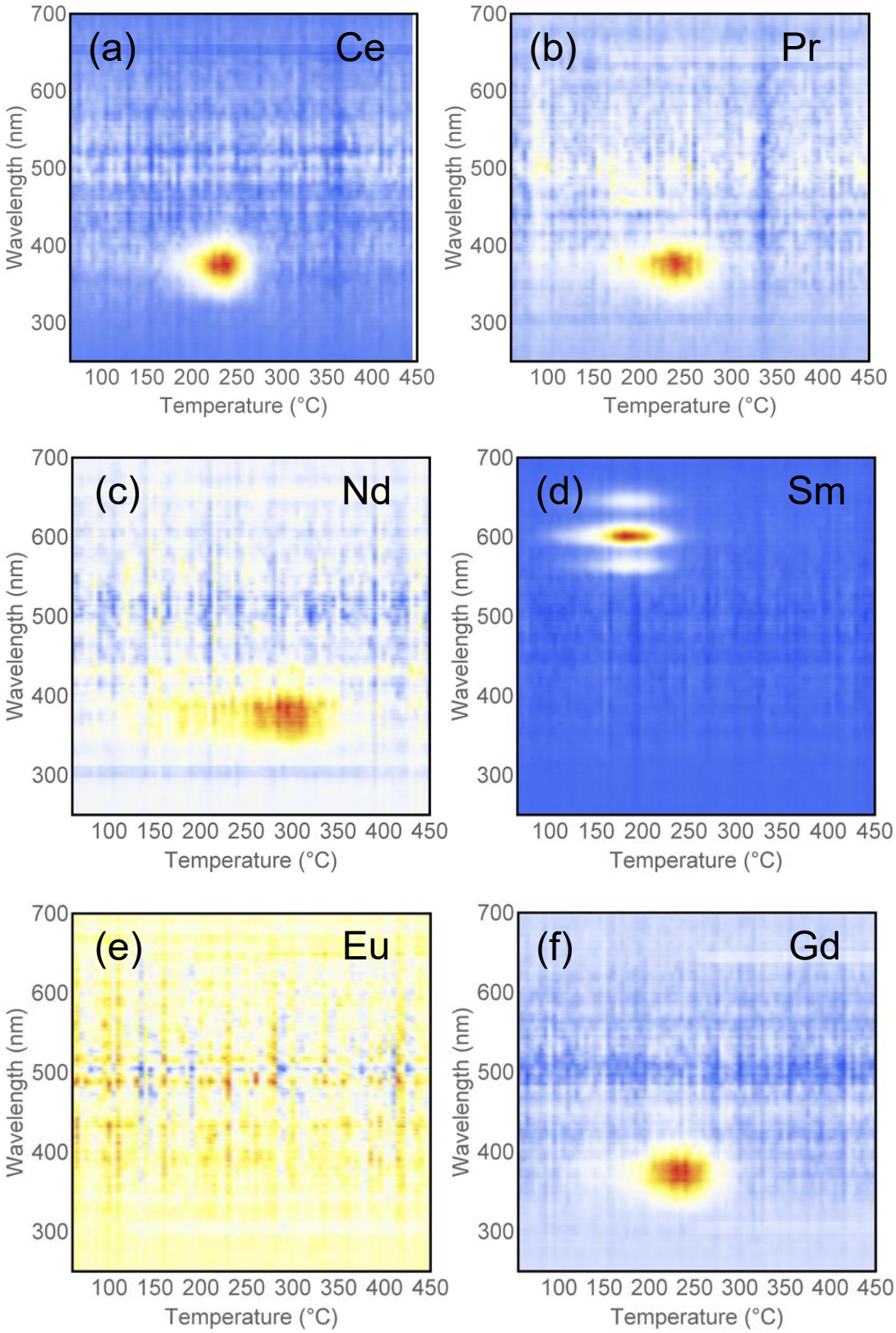
(a)
Ce
(b)
Pr
(c)
Nd
(d)
Sm
(e)
Eu
(f)
Gd
Wavelength (nm)
700
600
500
400
300
100 150 200 250 300 350 400 450
Temperature (°C)

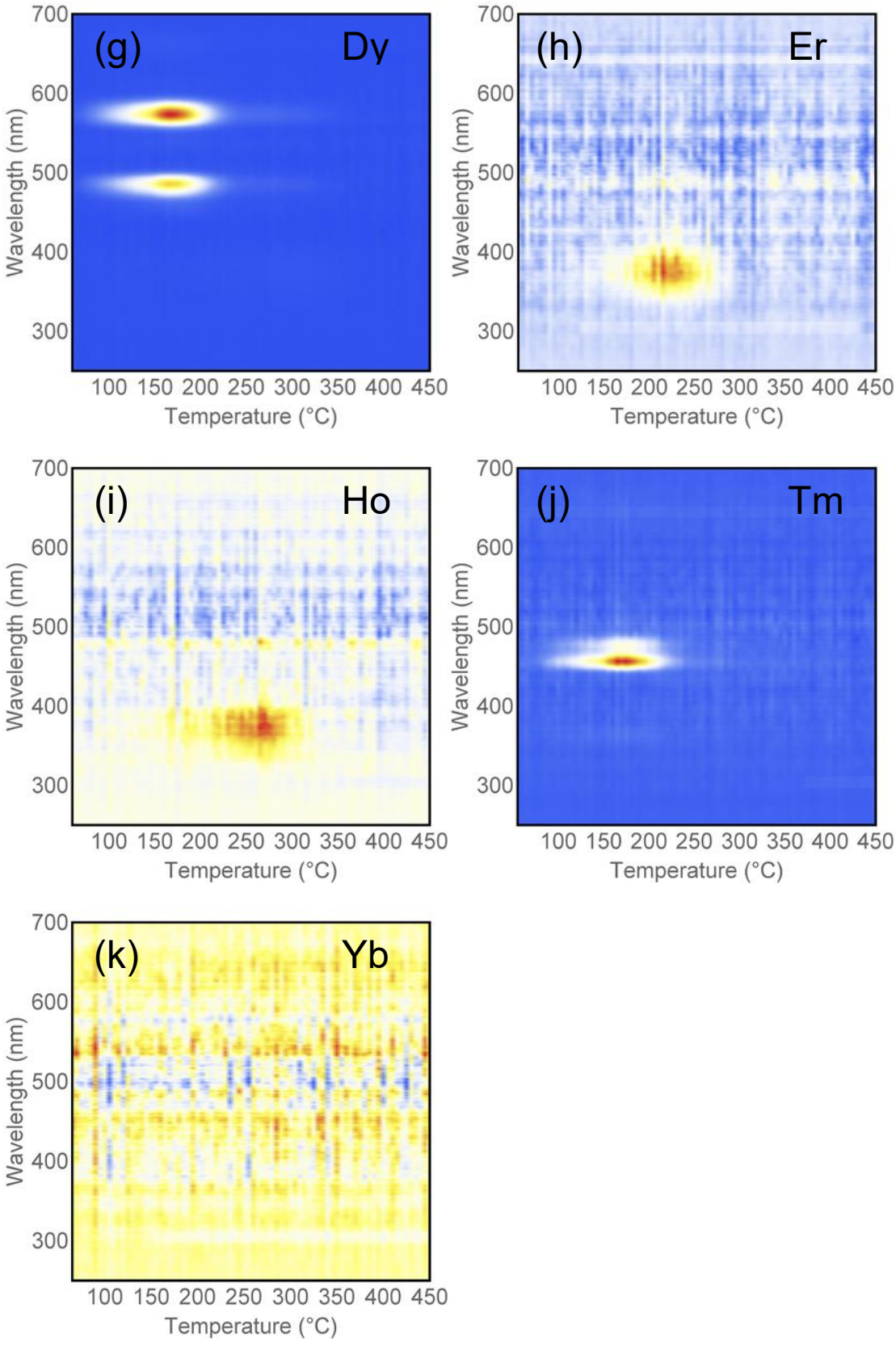
(g)
Dy
(h)
Er
(i)
Ho
(j)
Tm
(k)
Yb
Wavelength (nm)
700
600
500
400
300
100 150 200 250 300 350 400 450
Temperature (°C)

Figure 6-25: TL emission data for MBO:$Ce_{0.3\%}$,$Li_{10\%}$,$X_{0.3\%}$ where X = (a) None, (b) Pr, (c) Nd, (d) Sm, (e) Eu, (f) Gd, (g) Dy, (h) Er, (i) Ho, (j) Tm, or (k) Yb.

Eu and Yb show no TL emission which suggests they may introduce pathways for non-radiative recombination. Tm, Sm, and Dy show emission outside the UV range. This suggests that they are behaving as recombination centers. This behavior is expected for Tm and Sm as argued in Yukihara et al. (2014b).

The emission observed for Dy is from the 3+ oxidation state. This would suggest a hole recombining with an electron trapped by Dy^{2+}. The location of Dy^{2+} ground state is about 2 eV below the conduction band. Thus, for lower temperatures, holes that are released could recombine with Dy^{2+}. However, at higher temperatures, the trapped electrons at Dy^{2+} would be thermally released and no Dy^{3+} emission would be observed. This matches what is observed in the TL emission. Dy^{3+} emission is seen for the lower temperature peaks but is absent for the higher temperature peak.

Ho, Er, Pr, and Gd do not introduce new emissions. This would be evidence that Ho, Er, and Pr behave purely as electron traps. The role of Gd is unknown since the ground states of both 2+ and 3+ states are outside the bandgap.

6.3.4 Refined VRBE for MBO

From the optical measurements taken, the spectroscopic redshift or centroid shift in Ce^{3+} was measured to be 2.24(2) eV. This results in a value for U of 6.46(1) eV. The excitation data for Eu^{3+} do not show a charge transfer band for the measurable region of the instrument. However, it can be concluded that the charge transfer energy must be greater than 4.9 eV which is consistent with what was predicted from literature. As was stated previously, detection of the fundamental absorption edge in MBO is outside the

ability of our lab. Thus, the value derived from literature will still be used. The VRBE diagram for MBO with the revised values is presented in Figure 6-26.

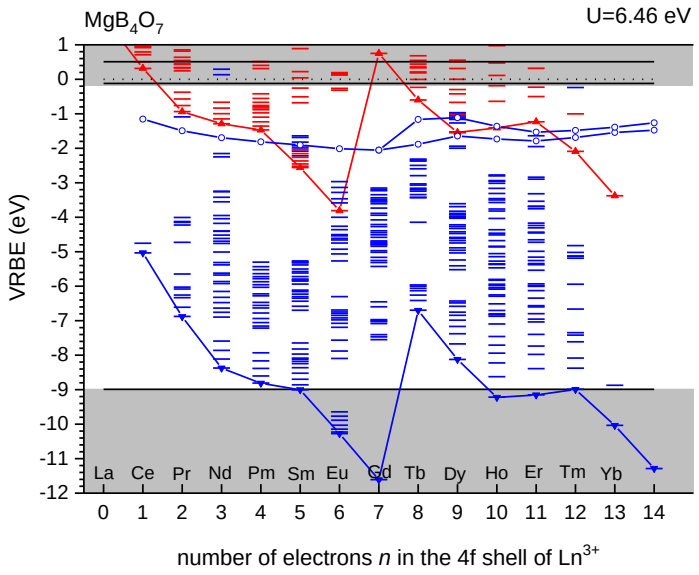

Figure 6-26: Exciton 8.87 eV; CT to Eu^{3+} 5.18 eV; U of 6.46 eV from measured centroid shift; spectroscopic redshift measured 2.24 eV.

In addition to the optical measurements, trap depths found using the VHRM confirmed the location of four Ln^{2+} ground states that behave as electron traps. This model also explains the behavior of Dy as both a recombination center for some temperatures and as a thermally depleting electron trap for higher temperatures.

6.3.5 Possible variations in the chemical shift model for low-purity MBO

In comparing the PL data for the low-purity material in Section 4.2.4 and high-purity material in Section 6.3.2, there are large differences. The relevant plots are reproduced here (Figure 6-27) for the convenience of the reader.

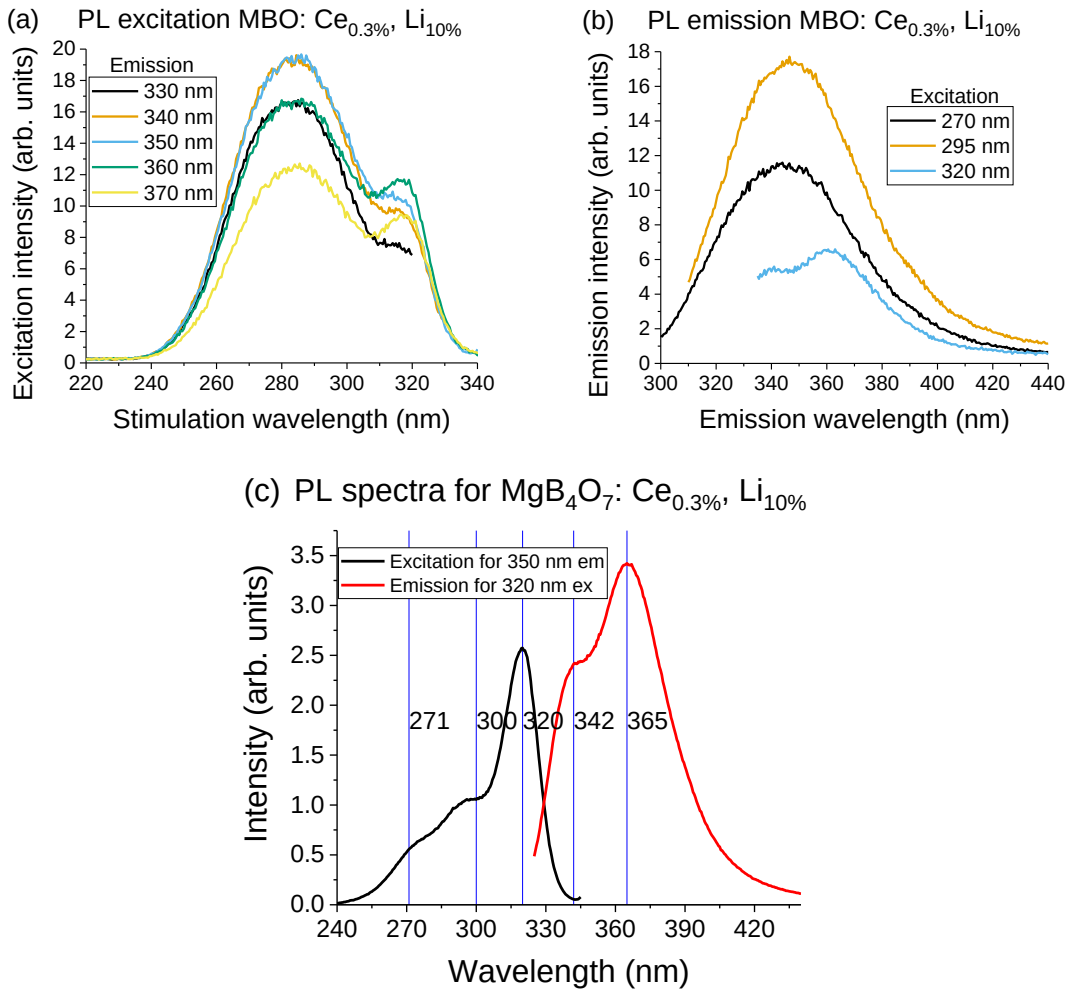

Figure 6-27: PL (a) excitation and (b) emission spectra for low-purity MBO:$Ce_{0.3\%}$,$Li_{10\%}$ and (c) high-purity MBO:$Ce_{0.3\%}$,$Li_{10\%}$.

While the emissions agree for 320 nm excitation, the excitation spectra are greatly different. In the high-purity reagent material, three overlapping peaks that are narrow (FWHM ~15 nm) are evident. These are the transitions to the first three 5d energy levels. However, the low-purity reagent material shows one sharp peak at 320 nm, which matches peak one in the high-purity reagent material, and a broad (FWHM ~50 nm). This peak at 320 nm is likely the transition to the lowest of the 5d levels. The broad peak is most likely charge transfer to the conduction band. This would mean that the conduction band for the low-purity reagent is lower than it is for the high-purity reagent material. The

charge transfer band for the high-purity material is at an energy greater than the $5d^3$ energy level of cerium. This change in structure may be part of the reason that cerium emission was enhanced with the use of high-purity reagent.

6.4 ***Conclusions***

In this chapter, OSL sensitization was shown to be caused by both phototransfer to shallow traps and incomplete bleaching of all trapped charge during an OSL readout. The TL sensitization study showed the influence of heat was uncertain. However, deep traps were present and caused most of the TL sensitization observed. Curve fitting was conducted for both TL and BSL. A hybrid data set used for TL fitting confirmed that the curves cannot be fit with a meaningful number of discrete TL peaks. The Van den Eeckhout method showed evidence of a trap distribution also. The BSL fittings showed that an accounting for phototransfer is needed, but a simplified model for phototransfer is insufficient. Fittings conducted for elevated temperature OSL showed less residual, but the same curve shape was seen for the residual. A second OSL model was developed with two OSL traps and a shallow thermally active trap. When simulated data produced by numerically solving the system of differential equations was fit with three exponential decays, the resulting fit was similar to what was observed with experimental data. The behavior of the residuals for the simulated data fitting had the same behavior as the residuals from fitting experimental data. This suggests that phototransfer to a shallow trap must be accounted for to explain the curve shape of OSL decay in MBO.

Finally, the chemical shift model was used to produce a VRBE diagram that was proposed, improved, and tested. The proposed ground states of four Ln^{2+} were confirmed using VHRM. The chemical shift model was used to explain the dual role of Dy in recombination and as a thermally releasing electron trap. A difference in the positions of energy levels was proposed for the low-purity reagent material and high-purity reagent

material. The proposition explains the difference in PL excitation observed for the two materials and may help explain the increase in Ce^{3+} emission observed for the high-purity reagent material.

CHAPTER 7

CONCLUSIONS

The goal of this work was to characterize MgB_4O_7:Ce,Li, a material originally identified in our group as a potential new OSL dosimeter, find avenues for improving its OSL properties through synthesis, and further elucidate its OSL behaviors and properties.

The initial studies of the original MBO:$Ce_{0.3\%}$,$Li_{10\%}$ material, produced using low-purity reagent, confirmed Ce^{3+} as the main emission center for PL, OSL, TL, and RL. This is important because Ce^{3+} has emission in the UV region in this material (340-360 nm), being therefore suitable for OSL dosimetry with green or blue stimulation. Ce^{3+} has a fast luminescence lifetime (tens of ns), which is desirable for laser-scanning imaging applications (2D dosimetry). The dose response for the material showed no saturation and was linear until about 50 Gy, above which it became supralinear. This is an improvement over both BeO and Al_2O_3:C and allows for application to higher dose applications for which BeO and Al_2O_3:C are unsuitable. These studies identified Mn^{2+} as a competing recombination center, sensitization was a challenge for the material, and both TL and OSL curve fitting did not model the behavior of data well. The identification of a competing recombination center provided one avenue for material improvement. The large OSL sensitization observed in the original material would render MBO useless for typical dosimetric readout. Such readouts rely on reading dose out then irradiating with a reference dose and reading out that intensity. If the reference dose readout is heavily sensitized, the material cannot be used for dosimetry. The TL sensitization made many of

the other studies more difficult, since aliquots could not be reused. This required use of a reference dose readout for each aliquot with the assumption that all aliquots should sensitize by the same amount. The difficulty in TL curve fitting shows that discrete peaks are unable to explain the behavior of MBO. This may indicate the presence of a distribution of trapping centers. The failure of OSL curve fitting shows that the OSL behavior is not merely a superposition of first-order OSL curves. Another mechanism is present during OSL.

We improved the brightness of the original MBO:$Ce_{0.3\%}$,$Li_{10\%}$ material by modifying the original synthesis procedure and achieved a significantly improved material with the use of high-purity reagents. With high-purity reagents the competing recombination at the Mn^{2+} was removed, resulting in increasing emission from the Ce^{3+}-centers as attested by RL and by the increase in TL and OSL emissions by a factor of ~3. Annealing with temperatures in the 700 °C – 900 °C range is essential to achieve high sensitivity, but in this range the temperature, duration and cooling did not influence the sensitivity significantly (<25 %). Nevertheless, for the high-purity reagent the highest OSL sensitivity was achieved with 700 °C annealing, instead of 900 °C as in the case of the original MBO:$Ce_{0.3\%}$,$Li_{10\%}$ material. The final set of material improvements were made through codoping with a third dopant. Gadolinium in a 1% concentration resulted in the brightest OSL, which was about 8 times brighter than the original MBO:$Ce_{0.3\%}$,$Li_{10\%}$, with low-purity reagent, material. This is about twice as bright as Al_2O_3:C under the same readout conditions. Since Al_2O_3:C is sensitive enough for dosimetry, a sensitivity close to that of Al_2O_3:C would allow MBO to be used for many of the same applications as Al_2O_3:C without detriment to sensitivity. Final studies showed the dose response was linear for BSL from 0.1-100 Gy. This is an improvement over the original material, BeO, and Al_2O_3:C, and opens the possibility of application for dosimetry at higher doses than Al_2O_3:C and BeO are capable, since they saturate at lower doses than MBO. The OSL sensitization was

reduced to under 10%. This is better than Al_2O_3:C under the same conditions (~15-30% sensitization). The reduced sensitization would allow for standard readouts utilizing a reference dose to be used. A short dark fading study showed about 30% fading of BSL area in 24 h which was attributed to the emptying of shallow traps and was reduced with a TL pre-heating after irradiation. This is a strong challenge to the new material. If MBO loses much of its signal to fading and continues to fade more with time (>24 h), it is not useful for long exposure applications or applications with a long storage time. However, if the dark fading stabilizes or can be reduced through a sufficient preheating, the material may still be useful in longer duration applications.

The final studies sought to further address some phenomena observed in MBO. Sensitization was shown to be due to residual dose for OSL and likely due to deep traps for TL. This means that OSL sensitization can be removed with a TL readout to remove residual dose. This opens the possibility of aliquot reusability following an annealing or TL heating. A TL heating up to 450 °C was sufficient to remove the residual signal. This is a lower temperature than needed to empty the deep traps in Al_2O_3:C (~900 °C). The TL sensitization showed deep traps responsible and present in the material. Thus, with a sufficient TL readout temperature (~600 °C), TL sensitization is nearly removed (<3%). Thus, aliquots can be reused for IRM or VHRM, which will improve the reliability of the data by removing the need for a reference dose correction. OSL curve fitting showed that exponential decays are insufficient to show the behavior of OSL data, but the behavior was explained by a phototransfer component to a shallow trap. Phototransfer to a shallow trap is a complication. However, a pulsed and time-resolved OSL readout scheme would allow removal of the phosphorescence. Also, if the shallow trap is cleaned out initially, the phosphorescence is much smaller (~4 orders of magnitude) than the OSL signal. Thus, the complication is more in modeling the material rather than in practical application. The TL curve fitting showed that a realistic fitting could not be obtained with a meaningful

number of discrete peaks. A trap distribution was suggested and application of the Van den Eeckhout method supported a distribution of traps. Thus, the traps responsible for TL are likely described by trap distributions. Physically, these trap distributions could be polyatomic ion groups occurring at different positions, orientations, etc. within the lattice resulting in slightly varying trap depth. This contrasts with materials where the TL is described by trapping at the ground state of a dopant or defect that enters uniformly throughout the lattice which results in a discrete TL peak. Lastly, the chemical shift model was applied and was able to explain the trap depths of traps introduced by doping with various lanthanides. This allows for some trap engineering in MBO. The addition of new electron traps via trap engineering with lanthanides was not helpful for OSL, but could be helpful for TL applications such as temperature sensing, where a deeper trap is desired. The deep trap introduced by doping with Dy can be kept while changing the emission from visible to UV by codoping with Ce. This could be an improvement over the MBO:Dy,Li material used in temperature sensing (Doull et al., 2014; Yukihara et al., 2014a; Yukihara et al., 2015).

Future work for the final material, MBO:Ce,Gd,Li, should look at further dosimetric characterization like long dark fading, up to 180 d, and dose response at low dose (~μGy-mGy) and high dose (~100 Gy-10 kGy). If the dark fading of the material does not stabilize, the new material is not useful for dosimetry requiring long exposure or storage time, and the material without Gd should have its fading tested. If the fading could be stabilized through a preheating without losing too much intensity, the material would remain a strong candidate for OSL dosimetry applications. Further testing the dose response would allow for a minimum detectable dose to be verified and show the complete range of linear dose response. If the range of linear dose response is broad, this could offer another improvement for 2D OSL dosimetry where the dose delivered ranges over orders of magnitude spatially.

Further investigation of the deep trap is needed and will require the use of thermally stimulated conductivity measurements, which requires single crystals. The deep traps cannot be studied with TL, since cerium emission is highly quenched at the temperatures needed to activate the deep traps. However, the deep trap concentration is important. If the deep trap concentration is as large as in Al_2O_3:C, TL sensitization should be a small effect at low dose and can be ignored. A large deep trap concentration could open the possibility of phototransfer from the deep trap with the correct stimulating wavelength. Characteristics of the trap may allow it to be used for dosimetry. If the deep trap concentration is small, the material may be improved by delivering a dose to fill the deep traps and presensitize the material.

While progress has been made, the trapping and detrapping within the material needs more study likely with the addition of EPR studies. EPR would be able to help identify ions and, with step annealing or varying bleaching time, show the ion signals depleting with stimulation as they are destroyed. Identification of the trapping ions may allow explanation of the role of Gd. It brightens the OSL and reduces sensitization, but the VRBE diagram shows Gd^{2+} is not stable in the material so cannot act as an electron trap. The 3+ ground state is within the valence band. Thus, Gd is not behaving as a trap and should not behave as a typical recombination center. Its emission may be due to a charge or energy transfer from a neighboring recombination center. To gain further understanding, the VRBE should be improved with exciton energy measurement and europium charge transfer energy. Further, identification of traps through EPR may give more information to show the mechanism by which Gd aids emission.

Thus, while the precise mechanisms for trapping and detrapping remain unknown, progress has been made in characterizing and improving MBO. The brightest material, MBO:$Ce_{0.3\%}$,$Gd_{1\%}$,$Li_{10\%}$, is brighter than Al_2O_3:C under the same readout conditions, has a broader linear dose range, and shows less sensitization under the same readout

conditions. If the fading problem can be solved, this material could be used in every OSL application for which Al_2O_3:C is used. MBO has better tissue equivalence than Al_2O_3:C and intrinsic neutron sensitivity. Also, with the fast luminescence center, Ce, MBO remains a candidate for improving 2D OSL dosimetry, since it would eliminate the need for pixel bleeding corrections.

REFERENCES

2016. *R: A language and environment for statistical computing*. R Foundation for Statistical Computing. https://www.R-project.org/

Adrovic, F., Prokic, M., Ninkovic, M.M. and Glisic, R., 2004. *Measurements of environmental backgroup radiation at location of coal-fired ponaver plaints*. Radiat. Prot. Dosim. 112, 439-442.

Ahmed, M.F., Eller, S., Schnell, E., Ahmad, S., Akselrod, M.S. and Yukihara, E.G., 2014. *Development of a 2D dosimetry system based on the optically stimulated luminescence of Al_2O_3*. Radiat. Meas., in press.

Ahmed, M.F., Shrestha, N., Schnell, E., Ahmad, S., Akselrod, M.S. and Yukihara, E.G., 2016a. *Characterization of Al_2O_3 optically stimulated luminescence films for 2D dosimetry using a 6 MV photon beam*. Physics in Medicine and Biology 61, 7551.

Ahmed, M.F., Schnell, E., Ahmad, S. and Yukihara, E.G., 2016b. *Image reconstruction algorithm for optically stimulated luminescence 2D dosimetry using laser-scanned Al_2O_3:C and Al_2O_3:C,Mg films*. Physics in Medicine and Biology 61, 7484.

Akselrod, A., Akselrod, M.S., Agersnap Larsen, N., Banerjee, D., Bøtter-Jensen, L., Christensen, P., Lucas, A.C., McKeever, S.W.S. and Yoder, C., 1999. *Optically stimulated luminescence response of Al_2O_3 to beta irradiation*. Radiat. Prot. Dosim. 85, 125-128.

Akselrod, M.S. and Kortov, V.S., 1990. *Thermoluminescent and exoemission properties of new high-sensitivity TLD α-Al_2O_3:C crystals*. Radiat. Prot. Dosim. 33, 123-126.

Akselrod, M.S., Kortov, V.S., Kravetsky, D.J. and Gotlib, V.I., 1990. *Highly sensitive thermoluminescent anion-defect α–Al_2O_3:C single crystal detectors*. Radiat. Prot. Dosim. 33, 119-122.

Akselrod, M.S., Agersnap Larsen, N., Whitley, V.H. and McKeever, S.W.S., 1998. *Thermal quenching of F-center luminescence in Al_2O_3:C*. J. Appl. Phys. 84, 3364-3373.

Akselrod, M.S. and Akselrod, A.E., 2006. *New Al_2O_3:C,Mg crystals for radiophotoluminescent dosimetry and optical imaging*. Radiat. Prot. Dosim. 119, 218-221.

Akselrod, M.S. and Sykora, G.J., 2011. *Fluorescent nuclear track detector technology – A new way to do passive solid state dosimetry*. Radiat. Meas. 46, 1671-1679.

Andersen, C.E., Nielsen, S.K., Greilich, S., Helt-Hansen, J., Lindegaard, J.C. and Tanderup, K., 2009. *Characterization of a fiber-coupled Al_2O_3:C luminescence dosimetry system for online in vivo dose verification during ^{192}Ir brachytherapy*. Medical Physics 36, 708-718.

Andreas, H.K., Erik van der, K., Enrico, C., Philippe, B., Marco, B. and Pieter, D., 2009. *Lanthanide 4f-level location in AVO 4 :Ln^{3+} (A = La, Gd, Lu) crystals*. Journal of Physics: Condensed Matter 21, 115503.

Anna, D., Adrie, J.J.B. and Pieter, D., 2014. *Electron tunnelling phenomena in YPO_4 : Ce,Ln (Ln = Er, Ho, Nd, Dy)*. Journal of Physics D: Applied Physics 47, 335301.

Annalakshmi, O., Jose, M.T., Madhusoodanan, U., Venkatraman, B. and Amarendra, G., 2013. *Synthesis and thermoluminescence characterization of MgB4O7:Gd,Li*. Radiat. Meas. 59, 15-22.

Annalakshmi, O., Jose, M.T., Madhusoodanan, U., Sridevi, J., Venkatraman, B., Amarendra, G. and Mandal, A.B., 2014. *Thermoluminescence mechanism in rare-earth-doped magnesium tetra borate phosphors*. Radiat. Eff. Defects Solids 169, 636-645.

Antonov-Romanovskii, V.V., Keirum-Markus, I.F., Poroshina, M.S. and Trapeznikova, Z.A., 1955. *IR stimulable phosphors*. In: Conference of the Academy of Sciences of the USSR on the Peaceful Uses of Atomic Energy, Moscow, USAEC Report AEC-tr-2435, 239-250.

Bailiff, I.K., Sholom, S. and McKeever, S.W.S., 2016. *Retrospective and emergency dosimetry in response to radiological incidents and nuclear mass-casualty events: A review*. Radiat. Meas. 94, 83-139.

Bajaj, N. and Omanwar, S., 2013. *Thermo Luminescence Study of SrB4O7: Cu Phosphor Prepared by Combustion Synthesis*. In: International Journal of Modern Physics: Conference Series, World Scientific, 404-407.

Balarin, M., 1975. *Direct evaluation of activation energy from half-width of glow peaks and a special nomogram*. physica status solidi (a) 31, K111-K114.

Balarin, M., 1977. *Improved approximations of the exponential integral in tempering kinetics*. Journal of Thermal Analysis and Calorimetry 12, 169-177.

Bernhardt, R. and Herforth, L., 1974. *Radiation dosimetry by optically stimulated phosphorescence of CaF_2:Mn*. In: Proceedings of the Fourth International Conference on Luminescence Dosimetry, Krakow, Poland, 1974, T. Niewiadomski (ed.), 1091-1104.

Blasse, G. and Grabmaier, B.C., 1994. *Luminescent Materials*. Springer, Heidelberg.

Bos, A.J.J., Prokić, M. and Brouwer, J.C., 2006. *Optically and thermally stimulated luminescence characteristics of MgO:Tb^{3+}*. Radiat. Prot. Dosim. 119, 130-133.

Bos, A.J.J., Dorenbos, P., Bessière, A. and Viana, B., 2008. *Lanthanide energy levels in YPO_4*. Radiat. Meas. 43, 222-226.

Bos, A.J.J., Poolton, N.R.J., Wallinga, J., Bessière, A. and Dorenbos, P., 2010. *Energy levels in YPO_4:Ce^{3+},Sm^{3+} studied by thermally and optically stimulated luminescence*. Radiat. Meas. 45, 343-346.

Bos, A.J.J., Dorenbos, P., Bessière, A., Lecointre, A., Bedu, M., Bettinelli, M. and Piccinelli, F., 2011. *Study of TL glow curves of YPO_4 double doped with lanthanide ions*. Radiat. Meas. 46, 1410-1416.

Bøtter-Jensen, L., Agersnap Larsen, N., Markey, B.G. and McKeever, S.W.S., 1997. *Al_2O_3:C as a sensitive OSL dosemeter for rapid assessment of environmental photon dose rates*. Radiat. Meas. 27, 295-298.

Bøtter-Jensen, L., McKeever, S.W.S. and Wintle, A.G., 2003. *Optically stimulated luminescence dosimetry*. Elsevier, Amsterdam.

Bube, R.H., 1960. *Photoconductivity of Solids*. John Wiley & Sons, Inc., New York.

Bulur, E. and Göksu, H.Y., 1998. *OSL from BeO ceramics: new observations from an old material*. Radiat. Meas. 29, 639-650.

Bulur, E., Bøtter-Jensen, L. and Murray, A.S., 2001. *LM-OSL signals from some insulators: an analysis of the dependency of the detrapping probability on stimulation light intensity*. Radiat. Meas. 33, 715-719.

Busuoli, G., Lembo, L., Nanni, R. and Sermenghi, I., 1983. *Use of BeO in routine personnel dosimetry*. Radiat. Prot. Dosim. 6, 317-320.

Campos, L.L. and Fernandes Filho, O.O., 1990. *Thermoluminescent characterization of MgB_4O_7:Dy sintered pellets*. Radiat. Prot. Dosim. 33, 111-113.

Cano, A., Gonzalez, P.R. and Furetta, C., 2008. *Further studies of some TL characteristics of MgB(4)O(7): Dy, Na phosphor*. Modern Physics Letters B 22, 1997-2006.

Chen, R. and McKeever, S.W.S., 1997. *Theory of thermoluminescence and related phenomena*. World Scientific Publishing Co., Singapore.

Chen, R. and Pagonis, V., 2011. *Thermally and optically stimulated luminescence: a simulation approach*. John Wiley & Sons, 1119995760.

Chen, R. and Pagonis, V., 2013. *On the expected order of kinetics in a series of thermoluminescence (TL) and thermally stimulated conductivity (TSC) peaks*. Nuclear Instruments and Methods in Physics Research Section B: Beam Interactions with Materials and Atoms 312, 60-69.

Chick, L.A., Pederson, L.R., Maupin, G.D., Bates, J.L., Thomas, L.E. and Exarhos, G.J., 1990. *Glycine-nitrate combustion synthesis of oxide ceramic powders*. Mater. Lett. 10, 6-12.

Coleman, A.C. and Yukihara, E.G., 2018. *On the validity and accuracy of the initial rise method investigated using realistically simulated thermoluminescence curves*. Radiat. Meas. 117, 70-79.

Dieke, G.H., 1968. *Spectra and Energy Levels of Rare Earth Ions In Crystals*. Wiley Interscience, New York.

Dobrowolska, A., Karsu, E.C., Bos, A.J.J. and Dorenbos, P., 2015. *Spectroscopy, thermoluminescence and afterglow studies of $CaLa_4(SiO_4)_3O$:Ln (Ln=Ce, Nd, Eu, Tb, Dy)*. J. Lumines. 160, 321-327.

Dogan, M. and Yazici, A.N., 2009. *Thermoluminescence properties of Ce-doped MgB4O7 phosphor*. Journal of Optoelectronics and Advanced Materials 11, 1783-1787.

Dorenbos, P., 2000a. *5d-level energies of Ce^{3+} and the crystalline environment. I. Fluoride compounds*. Phys. Rev. B 62, 15640-15649.

Dorenbos, P., 2000b. *5d-level energies of Ce^{3+} Chloride, bromide, and II. and the crystalline environment. iodide compounds*. Physical Review B-Condensed Matter and Materials Physics, 62 (23).

Dorenbos, P., 2000c. *Predictability of 5d level positions of the triply ionized lanthanides in halogenides and chalcogenides*. J. Lumines. 87–89, 970-972.

Dorenbos, P., 2000d. *The 5d level position of the trivalent lanthanides in inorganic compounds*. J. Lumines. 91, 155-176.

Dorenbos, P., 2000e. *The $4f^n \leftrightarrow 4f^{n-1}5d$ transitions of the trivalent lanthanides in halogenides and chalcogenides*. J. Lumines. 91, 91-106.

Dorenbos, P., 2001. *5d-level energies of Ce^{3+} and the crystalline environment. III. Oxides containing ionic complexes*. Phys. Rev. B 64, 125117 (125112 pages).

Dorenbos, P., 2002. *5d-level energies of Ce^{3+} and the crystalline environment. IV. Aluminates and "simple" oxides*. J. Lumines. 99, 283-299.

Dorenbos, P., 2003a. *Systematic behaviour in trivalent lanthanide charge transfer energies*. Journal of Physics: Condensed Matter 15, 8417.

Dorenbos, P., 2003b. *Relation between Eu^{2+} and Ce^{3+} f ↔ d-transition energies in inorganic compounds*. Journal of Physics: Condensed Matter 15, 4797.

Dorenbos, P., 2003c. *Energy of the first $4f^7 \rightarrow 4f^6 5d$ transition of Eu^{2+} in inorganic compounds*. J. Lumines. 104, 239-260.

Dorenbos, P., 2003d. *f->d transition energies of divalent lanthanides in inorganic compounds*. Journal of Physics: Condensed Matter 15, 575-594.

Dorenbos, P., 2005. *The Eu^{3+} charge transfer energy and the relation with the band gap of compounds*. J. Lumines. 111, 89-104.

Dorenbos, P. and Bos, A.J.J., 2008. *Lanthanide level location and related thermoluminescence phenomena*. Radiat. Meas. 43, 139-145.

Dorenbos, P., 2009. *Lanthanide charge transfer and related luminescence, charge carrier trapping, and redox phenomena*. J. Alloy. Compd. 488, 568-573.

Dorenbos, P., Krumpel, A.H., van der Kolk, E., Boutinaud, P., Bettinelli, M. and Cavalli, E., 2010. *Lanthanide level location in transition metal complex compounds*. Opt. Mater. 32, 1681-1685.

Dorenbos, P., 2012. *Modeling the chemical shift of lanthanide 4f electron binding energies*. Phys. Rev. B 85, 165107.

Dorenbos, P., Bos, A.J.J., Poolton, N.R.J. and You, F., 2013. *Photon controlled electron juggling between lanthanides in compounds*. J. Lumines. 133, 45-50.

Dorenbos, P., 2013. *Ce^{3+} 5d-centroid shift and vacuum referred 4f-electron binding energies of all lanthanide impurities in 150 different compounds*. J. Lumines. 135, 93-104.

Dorenbos, P., 2017. In E.G. Yukihara (Ed.).

Douguchi, Y., Nanto, H., Sato, T., Imai, A., Nasu, S., Kusano, E. and Kinbara, A., 1999. *Optically stimulated luminescence in Eu-doped KBr phosphor ceramics*. Radiat. Prot. Dosim. 84, 143-148.

Doull, B.A., Oliveira, L.C., Wang, D.Y., Milliken, E.D. and Yukihara, E.G., 2014. *Thermoluminescent properties of lithium borate, magnesium borate and calcium sulfate developed for temperature sensing*. J. Lumines. 146, 408-417.

Driscoll, C.M.H., 1981. *Sensitivity and fading characteristics of thermoluminescent magnesium borate*. Radiat. Prot. Dosim. 1, 135-137.

Erfani Haghiri, M., Saion, E., Soltani, N., wan Abdullah, W.S., Navasery, M. and Hashim, M., 2013. *Thermoluminescence characteristics of copper activated calcium borate nanocrystals (CaB4O7:Cu)*. J. Lumines. 141, 177-183.

Evans, B.D. and Stapelbroek, M., 1978. *Optical properties of the F^+ center in crystalline Al_2O_3*. Phys. Rev. B 18, 7089-7098.

Friedrich, W., Knipping, P. and Laue, M., 1913. *Interferenzerscheinungen bei Röntgenstrahlen*. 346, 971-988.

Furetta, C., Kitis, G., Weng, P.S. and Chu, T.C., 1999. *Thermoluminescence characteristics of MgB4O7 : Dy,Na*. Nucl. Instrum. Methods Phys. Res. Sect. A-Accel. Spectrom. Dect. Assoc. Equip. 420, 441-445.

Furetta, C., Prokić, M., Salamon, R. and Kitis, G., 2000. *Dosimetric characterisation of a new production of MgB_4O_7:Dy,Na thermoluminescent material*. Appl. Radiat. Isot. 52, 243-250.

Garlick, G.F.J. and Gibson, A.F., 1948. *The electron trap mechanism of luminescence in sulphide and silicate phosphors*. Proceedings of the Physical Society 60, 574.

Godfrey-Smith, D.I. and Pass, B., 1997. *A new method of retrospective radiation dosimetry: optically stimulated luminescence in dental enamel*. Health Phys. 72, 744-749.

Godfreysmith, D.I., Huntley, D.J. and Chen, W.H., 1988. *Optical dating studies of quartz and feldspar sediment extracts*. Quaternary Science Reviews 7, 373-380.

Göksu, H.Y., 2003. *Telephone chip-cards as individual dosimeters*. Radiat. Meas. 37, 617-620.

Gorbachev, V.M., 1975. *A solution of the exponential integral in the non-isothermal kinetics for linear heating*. Journal of Thermal Analysis and Calorimetry 8, 349-350.

Greilich, S., Osinga, J.M., Niklas, M., Lauer, F.M., Klimpki, G., Bestvater, F., Bartz, J.A., Akselrod, M.S. and Jäkel, O., 2013. *Fluorescent nuclear track detectors as a tool for ion-beam therapy research*. Radiat. Meas. 56, 267-272.

Haskell, E.H., 1993. *Retrospective accident dosimetry using environmental materials*. Radiat. Prot. Dosim. 47, 297-303.

Hoogenstraaten, W., 1958. *Electron traps in zinc-sulphide phosphors*. Research laboratory of NV philips.

Jahn, A., Sommer, M. and Henniger, J., 2010. *2D-OSL-dosimetry with beryllium oxide*. Radiat. Meas. 45, 674-676.

Jahn, A., Sommer, M., Liebmann, M. and Henniger, J., 2011. *Progress in 2D-OSL-dosimetry with beryllium oxide*. Radiat. Meas. 46, 1908-1911.

Jahn, A., Sommer, M., Ullrich, W., Wickert, M. and Henniger, J., 2013. *The BeOmax system – Dosimetry using OSL of BeO for several applications*. Radiat. Meas. 56, 324-327.

Jahn, A., Sommer, M. and Henniger, J., 2014. *Environmental dosimetry with the BeOSL personal dosimeter – State of the Art*. Radiat. Meas. 71, 438-441.

Karali, T., Townsend, P.D., Prokić, M. and Rowlands, A.P., 1999. *Comparison of TL spectra of co-doped dosimetric materials*. Radiat. Prot. Dosim. 84, 281-284.

Karali, T., Rowlands, A.P., Prokic, M., Townsend, P.D. and Halmagean, E., 2002. *Thermoluminescent spectra of rare earth doped MgB4O7 dosemeters*. Radiat. Prot. Dosim. 100, 333-336.

Kawashima, Y.S., Gugliotti, C.F., Yee, M., Tatumi, S.H. and Mittani, J.C.R., 2014. *Thermoluminescence features of MgB4O7:Tb phosphor*. Radiat. Phys. Chem. 95, 91-93.

Kingsley, J.J. and Patil, K.C., 1988. *A novel combustion process for the synthesis of fine particle α-alumina and related oxide materials*. Mater. Lett. 6, 427-432.

Kingsley, J.J., Manickam, N. and Patil, K.C., 1990. *Combustion synthesis and properties of fine particle fluorescent aluminous oxides*. Bulletin of Material Sciences 13, 179-189.

Kitis, G., Gomez-Ros, J.M. and Tuyn, J.W.N., 1998. *Thermoluminescence glow-curve deconvolution functions for first, second and general orders of kinetics*. J. Phys. D-Appl. Phys. 31, 2636-2641.

Kittel, C., 1996. *Introduction to Solid State Physics*. John Wiley & Sons, Inc., New York.

Lakowicz, J.R., 2006. *Principles of Fluorescence Spectroscopy*. Boston: Springer, Boston.

Le Masson, N.J.M., Bos, A.J.J. and Van Eijk, C.W.E., 2001. *Optically stimulated luminescence in hydrated magnesium sulfates*. Radiat. Meas. 33, 693-697.

Levy, P.W., 1985. *Recent developments in thermoluminescence kinetics*. Nuclear Tracks and Radiation Measurements (1982) 10, 21-32.

Lewandowski, A.C. and McKeever, S.W.S., 1991. *Generalized description of thermally stimulated processes without the quasi-equilibrium approximation*. Phys. Rev. B 43, 8163-8178.

Lochab, S.P., Pandey, A., Sahare, P.D., Chauhan, R.S., Salah, N. and Ranjan, R., 2007. *Nanocrystalline MgB4O7: Dy for high dose measurement of gamma radiation*. Physica Status Solidi a-Applications and Materials Science 204, 2416-2425.

Luo, H., Bos, A.J.J. and Dorenbos, P., 2016. *Controlled Electron–Hole Trapping and Detrapping Process in $GdAlO_3$ by Valence Band Engineering*. The Journal of Physical Chemistry C 120, 5916-5925.

Marfunin, A.S., 1979. *Spectroscopy, Luminescence and Radiation Centers in Minerals*. Springer-Verlag, Berlin.

Markey, B.G., Colyott, L.E. and McKeever, S.W.S., 1995. *Time-resolved optically stimulated luminescence from α-Al_2O_3:C*. Radiat. Meas. 24, 457-463.

Markey, B.G., McKeever, S.W.S., Akselrod, M.S., Bøtter-Jensen, L., Agersnap Larsen, N. and Colyott, L.E., 1996. *The temperature dependence of optically stimulated luminescence from α-Al_2O_3:C*. Radiat. Prot. Dosim. 65, 185-189.

McKeever, S.W.S., 1985. *Thermoluminescence of Solids*. Cambridge University Press, Cambridge.

McKeever, S.W.S. and Morris, M.F., 1994. *Computer simulations of optical bleaching of TL and OSL signals*. Radiat. Meas. 23, 301-306.

McKeever, S.W.S., Moscovitch, M. and Townsend, P.D., 1995. *Thermoluminescence Dosimetry Materials: Properties and Uses*. Nuclear Technology Publishing, Ashford.

McKeever, S.W.S., Akselrod, M.S. and Markey, B.G., 1996. *Pulsed optically stimulated luminescence dosimetry using α-Al_2O_3:C*. Radiat. Prot. Dosim. 65, 267-272.

McKeever, S.W.S., Bøtter-Jensen, L., Agersnap Larsen, N. and Duller, G.A.T., 1997. *Temperature dependence of OSL decay curves: experimental and theoretical aspects*. Radiat. Meas. 27, 161-170.

McKeever, S.W.S. and Akselrod, M.S., 1999. *Radiation dosimetry using pulsed optically stimulated luminescence of Al_2O_3:C*. Radiat. Prot. Dosim. 84, 317-320.

McKeever, S.W.S., Akselrod, M.S., Colyott, L.E., Agersnap Larsen, N., Polf, J.C. and Whitley, V.H., 1999. *Characterisation of Al_2O_3 for use in thermally and optically stimulated luminescence dosimetry*. Radiat. Prot. Dosim. 84, 163-168.

Milliken, E.D., Oliveira, L.C., Denis, G. and Yukihara, E.G., 2012. *Testing a model-guided approach to the development of new thermoluminescent materials using YAG:Ln produced by solution combustion synthesis*. J. Lumines. 132, 2495-2504.

Missous, O., Loup, F., Fesquet, J., Prevost, H., Gasiot, J., Sanchez, J.P. and Dossantos, C.A., 1991. *Optically stimulated luminescence (osl) of rare-earth doped phosphors*. Eur. J. Solid State Inorg. Chem. 28, 163-166.

Mohan, N.S. and Chen, R., 1970. *Numerical curve fitting for calculating glow parameters*. Journal of Physics D: Applied Physics 3, 243.

Murray, A.S. and Wintle, A.G., 2000. *Luminescence dating of quartz using an improved single-aliquot regenerative-dose protocol*. Radiat. Meas. 32, 57-73.

Nanto, H., Murayama, K., Usuda, T., Taniguchi, S. and Takeuchi, N., 1993a. *Optically stimulated luminescence in KCl:Eu single crystals*. Radiat. Prot. Dosim. 47, 281-284.

Nanto, H., Usuda, T., Murayama, K., Nakamura, S., Inabe, K. and Takeuchi, N., 1993b. *Emission mechanism of optically stimulated luminescence in copper-doped sodium-chloride single-crystals*. Radiat. Prot. Dosim. 47, 293-296.

Oliveira, T.M., Lima, A.F., Brik, M.G., Souza, S.O. and Lalic, M.V., 2016. *Electronic structure and optical properties of magnesium tetraborate: An ab initio study*. Computational Materials Science 124, 1-7.

Orante-Barrón, V.R., Oliveira, L.C., Kelly, J.B., Milliken, E.D., Denis, G., Jacobsohn, L.G., Puckette, J. and Yukihara, E.G., 2011. *Luminescence properties of MgO produced by Solution Combustion Synthesis and doped with lanthanides and Li*. J. Lumines. 131, 1058-1065.

Palan, C., Chauhan, A., Sawala, N., Bajaj, N. and Omanwar, S., 2015. *Thermoluminescence and Optically Stimulated Luminescence Properties of*

MgB4O7: Ag Phosphor. International Journal of Luminescence and Applications 5, 408-410.

Paluch-Ferszt, M., Kozlowska, B., de Souza, S.O., de Souza, L.F. and Souza, D.N., 2016. *Analysis of dosimetric peaks of MgB4O7:Dy (40% Teflon) versus LiF:Mg,Ti TL detectors*. Nukleonika 61, 49-52.

Patterson, A.L., 1939. *The Scherrer Formula for X-Ray Particle Size Determination*. Physical Review 56, 978-982.

Porwal, N.K., Kadam, R.M., Seshagiri, T.K., Natarajan, V., Dhobale, A.R. and Page, A.G., 2005. *EPR and TSL studies on MgB4O7 doped with Tm: role of BO32- in TSL glow peak at 470 K*. Radiat. Meas. 40, 69-75.

Pradhan, A.S. and Ayyanger, K., 1977. *Radiation dosimetry by photostimulated luminescence of $CaSO_4$:Dy*. International Journal of Applied Radiation Isotopes 28.

Price, J.L., Guardala, N.A., Riel, G.K. and Mathur, V.K., 1998. *Neutron response of a laser-heated thermoluminescence dosimetry system*. Radiat. Meas. 29, 379-382.

Prokić, M., 1980. *Development of highly sensitive $CaSO_4$:Dy/Tm and MgB_4O_7:Dy/Tm sintered thermoluminescent dosimeters*. Nuclear Instruments and Methods 175, 83-86.

Prokić, M. and Bøtter-Jensen, L., 1993. *Comparison of main thermoluminescent properties of some TL dosemeters*. Radiat. Prot. Dosim. 47, 195-199.

Prokić, M., 1993. *MgB_4O_7:Mg as a new TL dosemeter*. Radiat. Prot. Dosim. 47, 191-193.

Prokić, M., 2007. *Individual monitoring based on magnesium borate*. Radiat. Prot. Dosim. 125, 247-250.

Randall, J.T. and Wilkins, M.H.F., 1945a. *Phosphorescence and electron traps. I. The study of trap distributions*. Proceedings of the Royal Society of London. Series A, Mathematical and Physical Sciences 184, 365-389.

Randall, J.T. and Wilkins, M.H.F., 1945b. *Phosphorescence and electron traps. II. The interpretation of long-period phosphorescence*. Proceedings of the Royal Society of London. Series A. Mathematical and Physical Sciences 184, 390-407.

Rao, M.R., Rao, B.S., Rao, N.P., Somaiah, K. and Murthy, K.V.R., 2009. *Thermoluminescence characteristics of MgB4O7, MgB4O7:Mn and MgB4O7:Cu phosphors*. Indian Journal of Pure & Applied Physics 47, 456-458.

Rao, R.P., Gasiot, J. and Fillard, J.P., 1984. *Optically stimulated luminescence and cathodoluminescence of mgs-eu phosphors*. J. Lumines. 31-2, 213-215.

Rhyner, C.R. and Miller, W.G., 1970. *Radiation dosimetry by optically stimulated luminescence in BeO*. Health Phys. 18, 681-684.

Richmond, R.G., Ogunleye, O.T., Cash, B.L. and Jones, K.L., 1987. *On the phototransferred thermo-luminescence in MgB4O7-Dy*. Appl. Radiat. Isot. 38, 313-314.

Rowlands, J.A., 2002. *The physics of computed radiography*. Physics in Medicine and Biology 47, R123-R166.

Sawakuchi, G.O., Ferreira, F.A., McFadden, C.H., Hallacy, T.M., Granville, D.A., Sahoo, N. and Akselrod, M.S., 2016. *Nanoscale measurements of proton tracks using fluorescent nuclear track detectors*. Medical Physics 43, 6.

Scherrer, P.J.N.G.W.G., 1918. *Estimation of the size and internal structure of colloidal particles by means of röntgen*. 2, 96-100.

Shahare, D.I., Dhoble, S.J. and Moharil, S.V., 1993. *Preparation and characterization of magnesium-borate phosphor*. J. Mater. Sci. Lett. 12, 1873-1874.

Sholom, S., DeWitt, R., Simon, S.L., Bouville, A. and McKeever, S.W.S., 2011. *Emergency optically stimulated luminescence dosimetry using different materials*. Radiat. Meas. 46, 1866-1869.

Sidorenko, A.V., Dorenbos, P., Bos, A.J.J., Van Eijk, C.W.E. and Rodnyi, P.A., 2006. *Lanthanide level location and charge carrier trapping in $LiLnSiO_4:Ce^{3+}$, Sm^{3+}, Ln = Y or Lu*. Journal of Physics: Condensed Matter 18, 4503-4514.

Sommer, M., Freudenberg, R. and Henniger, J., 2007. *New aspects of a BeO-based optically stimulated luminescence dosimeter*. Radiat. Meas. 42, 617-620.

Sommer, M., Jahn, A. and Henniger, J., 2008. *Beryllium oxide as optically stimulated luminescence dosimeter*. Radiat. Meas. 43, 353-356.

Sonoda, M., Takano, M., Miyahara, J. and Kato, H., 1983. *Computed radiography utilizing scanning laser stimulated luminescence*. Radiology 148, 833-838.

Souza, J.H., Ferrari, V.A. and Defreitas, L.C., 1993. *TL peak structure of MgB4O7-Dy*. Radiat. Prot. Dosim. 47, 239-242.

Souza, L.F., Vidal, R.M., Souza, S.O. and Souza, D.N., 2014. *Thermoluminescent dosimetric comparison for two different MgB4O7: Dy production routes*. Radiat. Phys. Chem. 104, 100-103.

Souza, L.F., Antonio, P.L., Caldas, L.V.E. and Souza, D.N., 2015. *Neodymium as a magnesium tetraborate matrix dopant and its applicability in dosimetry and as a temperature sensor*. Nucl. Instrum. Methods Phys. Res. Sect. A-Accel. Spectrom. Dect. Assoc. Equip. 784, 9-13.

Souza, L.F., Silva, A.M.B., Antonio, P.L., Caldas, L.V.E., Souza, S.O., d'Errico, F. and Souza, D.N., 2017. *Dosimetric properties of MgB4O7:Dy,Li and MgB4O7:Ce,Li for optically stimulated luminescence applications*. Radiat. Meas. 106, 196-199.

Subanakov, A.K., Bazarova, Z.G., Nepomnyshchikh, A.I., Perevalov, A.V. and Bazarov, B.G., 2014. *Synthesis and characterization of dysprosium-doped magnesium tetraborate*. Inorganic Materials 50, 485-488.

Sunta, C.M., Ayta, W.E.F., Chubaci, J.F.D. and Watanabe, S., 2001. *A critical look at the kinetic models of thermoluminescence: I. First-order kinetics*. Journal of Physics D: Applied Physics 34, 2690.

Sunta, C.M., Ayta, W.E.F., Chubaci, J.F.D. and Watanabe, S., 2005. *A critical look at the kinetic models of thermoluminescence - II. Non-first order kinetics*. Journal of Physics D: Applied Physics 38, 95-102.

Sykora, G.J., Akselrod, M.S., Salasky, M. and Marino, S.A., 2007. *Novel Al2O3:C,Mg fluorescent nuclear track detectors for passive neutron dosimetry*. Radiat. Prot. Dosim. 126, 278-283.

Sykora, G.J., Akselrod, M.S., Benton, E.R. and Yasuda, N., 2008. *Spectroscopic properties of novel fluorescent nuclear track detectors for high and low LET charged particles*. Radiat. Meas. 43, 422-426.

Sykora, G.J. and Akselrod, M.S., 2010. *Novel fluorescent nuclear track detector technology for mixed neutron-gamma fields*. Radiat. Meas. 45, 594-598.

Theil, H., 1958. *Economic forecasts and policy*. North-Holland.

Thoms, M., Vonseggern, H. and Winnacker, A., 1994. *Optical and thermal-properties of electron-trapping and hole-trapping sites in the x-ray storage phosphor RbI-x (x=Tl(+), In(+), Pb(2+), Eu(2+)*. J. Appl. Phys. 76, 1800-1808.

Tochilin, E., Goldstein, N. and Miller, W.G., 1969. *Beryllium oxide as a thermoluminescent dosimeter*. Health Phys. 16.

Ueda, J., Dorenbos, P., Bos, A.J.J., Meijerink, A. and Tanabe, S., 2015a. *Insight into the Thermal Quenching Mechanism for $Y_3Al_5O_{12}:Ce^{3+}$ through Thermoluminescence Excitation Spectroscopy*. The Journal of Physical Chemistry C 119, 25003-25008.

Ueda, J., Dorenbos, P., Bos, A.J.J., Kuroishi, K. and Tanabe, S., 2015b. *Control of electron transfer between Ce^{3+} and Cr^{3+} in the Y_3Al_5-xGa_xO_{12} host via conduction band engineering*. J. Mater. Chem. C 3, 5642-5651.

Van den Eeckhout, K., Bos, A.J.J., Poelman, D. and Smet, P.F., 2013. *Revealing trap depth distributions in persistent phosphors*. Phys. Rev. B 87, 045126.

Viamonte, A., da Rosa, L.A.R., Buckley, L.A., Cherpak, A. and Cygler, J.E., 2008. *Radiotherapy dosimetry using a commercial OSL system*. Medical Physics 35, 1261-1266.

von Ardenne, M.J.Z.f.P., 1938. *Das Elektronen-Rastermikroskop*. 109, 553-572.

von Seggern, H., 1999. *Photostimulable X-ray storage phosphors: a review of present understanding*. Brazilian Journal of Physics 29, 254-268.

W. H. Bragg, M. A., F. R. S., W. L. Bragg and A., B., 1913. *The reflection of X-rays by crystals*. Proceedings of the Royal Society of London. Series A 88, 428.

Wright, G.T. and Garlick, G.F.J., 1954. *Characteristics of radioluminescence in crystals*. British Journal of Applied Physics 5, 13.

You, F., Bos, A.J.J., Shi, Q., Huang, S. and Dorenbos, P., 2011. *Electron transfer process between Ce^{3+} donor and Yb^{3+} acceptor levels in the bandgap of $Y_3Al_5O_{12}$ (YAG)*. Journal of Physics: Condensed Matter 23, 215502 (215506pp).

You, F., Bos, A.J.J., Shi, Q., Huang, S. and Dorenbos, P., 2012. *Thermoluminescence investigation of donor (Ce^{3+}, Pr^{3+}, Tb^{3+}) acceptor (Eu^{3+}, Yb^{3+}) pairs in $Y_3Al_5O_{12}$*. Phys. Rev. B 85, 115101.

Yukihara, E.G., Mittani, J.C.R., Vanhavere, F. and Akselrod, M.S., 2008. *Development of new optically stimulated luminescence neutron dosimeters*. Radiat. Meas. 43, 309-314.

Yukihara, E.G. and McKeever, S.W., 2011. *Optically stimulated luminescence: fundamentals and applications*. John Wiley & Sons, 0470977213.

Yukihara, E.G., Coleman, A.C. and Doull, B.A., 2014a. *Passive temperature sensing using thermoluminescence: Laboratory tests using Li2B4O7:Cu,Ag, MgB4O7:Dy,Li and CaSO4:Ce,Tb*. J. Lumines. 146, 515-526.

Yukihara, E.G., Milliken, E.D. and Doull, B.A., 2014b. *Thermally stimulated and recombination processes in MgB4O7 investigated by systematic lanthanide doping*. J. Lumines. 154, 251-259.

Yukihara, E.G., Coleman, A.C., Bastani, S., Gustafson, T., Talghader, J.J., Daniels, A., Stamatis, D., Lightstone, J.M., Milby, C. and Svingala, F.R., 2015. *Particle temperature measurements in closed chamber detonations using thermoluminescence from Li2B4O7:Ag,Cu, MgB4O7:Dy,Li and CaSO4:Ce,Tb*. J. Lumines. 165, 145-152.

Yukihara, E.G. and Ahmed, M.F., 2015. *Pixel Bleeding Correction in Laser Scanning Luminescence Imaging Demonstrated Using Optically Stimulated Luminescence*. IEEE Trans. Med. Imaging 34, 2506-2517.

Yukihara, E.G., Doull, B.A., Gustafson, T., Oliveira, L.C., Kurt, K. and Milliken, E.D., 2017. *Optically stimulated luminescence of MgB4O7:Ce, Li for gamma and neutron dosimetry*. J. Lumines. 183, 525-532.

VITA

TIMOTHY DAVID GUSTAFSON

Candidate for the Degree of

DOCTOR OF PHILOSOPHY

DISSERTATION: DEVELOPMENT AND CHARACTERIZATION OF MGB4O4 FOR OPTICALLY STIMULATED LUMINESCENCE DOSIMETRY

MAJOR FIELD: PHYSICS

BIOGRAPHICAL: PERSONAL

Born in Fridley, Minnesota on March 20, 1991

EDUCATION

BACHELOR OF SCIENCE 2012
Bethel University, St. Paul, MN

EXPERIENCE

TEACHING ASSISTANT 2012-2013,
Oklahoma State University, USA 2015-2018

RESEARCH ASSISTANT 2013-2015
Oklahoma State University, USA